Alma Mater Studiorum – Università di Bologna

DOTTORATO DI RICERCA IN

CHIMICA

Ciclo 33

Settore Concorsuale: 03/B1 – FONDAMENTI DELLE SCIENZE CHIMICHE E SISTEMI INORGANICI

Settore Scientifico Disciplinare: CHIM/03 – CHIMICA GENERALE E INORGANICA

NEW METAL TETRAZOLATE COMPLEXES: DESIGN, SYNTHESIS, CHARACTERIZATION AND APPLICATIONS

Presentata da: Nicola Monti

Coordinatore Dottorato

Domenica Tonelli

Supervisore

Stefano Stagni

Co-supervisore

Stefano Zacchini

Esame finale anno 2021

To Alessandro

“Ring the bells that still can ring
Forget your perfect offering
There is a crack in everything
That's how the light gets in.”

Leonard Cohen - Anthem

Declaration

To the best of my knowledge and belief, this thesis contains no previously published material by any other person except where due acknowledgement has been made.

Bologna, 29/12/2020

Abstract

This final thesis is aimed at summarizing the research program I have carried out during my PhD studies, that has been dealing with the design, the preparation, characterization and applications of new Re(I), Ru(II), and Ir(III) metal complexes containing anionic ligands such as 5-aryl tetrazolates $[R\text{-}CN_4]^-$ or their neutral analogues, N-alkyltetrazoles $[R\text{-}CN_4\text{-}R_1]$, that posses an alkyl substituent on the pentatomic ring.

Chapter 1 consists of a brief introduction on tetrazoles and metal-tetrazolato complexes, and on the photophysical properties of d_6 transition metal complexes.

In chapter 2, the synthesis, characterization and study of the photophysical properties of new luminescent Ir(III)-tetrazolate complexes are discussed. The introduction of an electron-withdrawing group – in this case, a cyano group - on the main scaffold of the complexes led to unusual photophysical properties which will be discussed; moreover, the application of one of the new Ir(III)-CN complexes as emissive core in the fabrication of an OLED device is reported.

In chapter 3, the synthesis characterization and study of the antimicrobial activity of a new Ru(II)-alkyltetrazole are reported. The use of N-alkyl tetrazoles as diimine-type chelators in the preparation of trishomoleptic Ru(II)-polypyridyl like complexes eventually led to a new family of fully tetrazole Ru(II) complexes. When the pentatomic ring was substituted with a long alkyl residue, such as a hexyl group, antimicrobial activity toward *Deinococcus radiodurans* was observed.

In chapter 4, the synthesis, characterization, and study of the photophysical properties of a new family of luminescent Re(I)-tetrazolate complexes are reported. In this study, different N-alkyl tetrazoles play the role of diimine (diim) ligands in the preparation of new Re(I) tricarbonyl complexes. In addition, absorption and emission titration experiments were performed to study their interaction with Bovine Serum Albumin (BSA).

In chapter 5, the synthesis and characterization of new luminescent Re(I)-tetrazolate complexes are discussed. The use of sulfonated diimine ligands in the preparation of new Re(I) tricarbonyl complexes led to the first example Re(I) complexes for the luminescent staining of proteins.

In chapter 6, the synthesis, characterization and study of the photophysical properties of a new family of Ir(III)-NO_2 tetrazole complexes are discussed. The introduction of a nitro group on the cyclometalated ligands led to unexpected photophysical properties that will be discussed therein. Moreover, the possibility to tune the luminescent output of such systems upon chemical modification of the pending nitro group was verified by performing reduction tests with sodium dithionite; this represents encouraging evidence for their possible application as hypoxia-responsive luminescent probes in bioimaging.

Commonly used abbreviations and symbols

τ	Excited state lifetime
Φ	Quantum yield
Φ_r	Quantum yield of reference
λ_{abs}	Absorption wavelength
λ_{emi}	Emission wavelength
λ_{exc}	Excitation wavelength
ε	Molar absorptivity
AIE	Aggregation-induced emission
AIQ	Aggregation induced quenching
aq	Aqueous
bpy	2,2’-bipyridine
ACN	Acetonitrile
C^N	Cyclometalating ligand
DCM	Dichloromethane
DMF	N,N-dimethylformamide
DMSO	Dimethylsulphoxide
EtOAc	Ethyl acetate
Et_2O	Diethyl ether
F_2-PPy	2-(2,4-difluorophenyl)pyridine
F_2-PPy-CN	2-(2,4-difluorophenyl)-4-cyano-pyridine
F_2-PPy-NO_2	2-(2,4-difluorophenyl)-4-nitro-pyridine
fac	Facial coordination isomer
HOMO	Highest occupied molecular orbital

Hex	Hexane
IC	Internal conversion
IL	Intra-ligand
ILCT	Intra-ligand charge transfer
ISC	Intersystem crossing
J	Coupling constant (NMR)
k_{ISC}	Intersystem crossing rate constant
k_{nr}	Non-radiative decay rate constant
k_r	Radiative decay rate constant
LC	Ligand-centred
LEEC	Light-emitting electrochemical cell
LLCT	Ligand-to-ligand charge transfer
LUMO	Lowest unoccupied molecular orbital
MC	Metal-centred
mer	Meridional coordination isomer
MeOH	Methanol
MIC	Minimum inhibiting concentration
MLCT	Metal-to-ligand charge transfer
MMLCT	Metal-metal-to-ligand charge transfer
NMR	Nuclear magnetic resonance
OLED	Organic light-emitting device
OD_{600}	Optical density of a sample measured at a wavelength of 600 nm
phen	1,10-phenanthroline 2-phenylpyridine
pyr	Pyridine

TEA	Triethylamine
UV	Ultraviolet
Vis	Visible
VR	Vibrational relaxation

Table of Contents

Chapter 1 Introduction

1.1 Photophysical properties of metal complexes

Fundamental concepts

Photoluminescence consists of the emission of light from an electronically excited state to a ground state, after the absorption of a photon. Absorption phenomena taking place in dilute solution are described by the Beer-Lambert-Bouger law, (**Equation 1**)

$$I = I_0 \times 10^{\varepsilon bc} \qquad \textbf{(eq.1)}$$

where I and I_0 represent the intensity of the transmitted and incident radiation respectively, measured at a given wavelength, ε is the molar attenuation coefficient, b is the optical path length and c is the concentration. The molar attenuation coefficient ε quantifies the ability of a molecule to absorb light. Processes taking place from the interaction of a molecule with light are illustrated in the simplified Jablonski diagram reported in **Figure 1.1**.

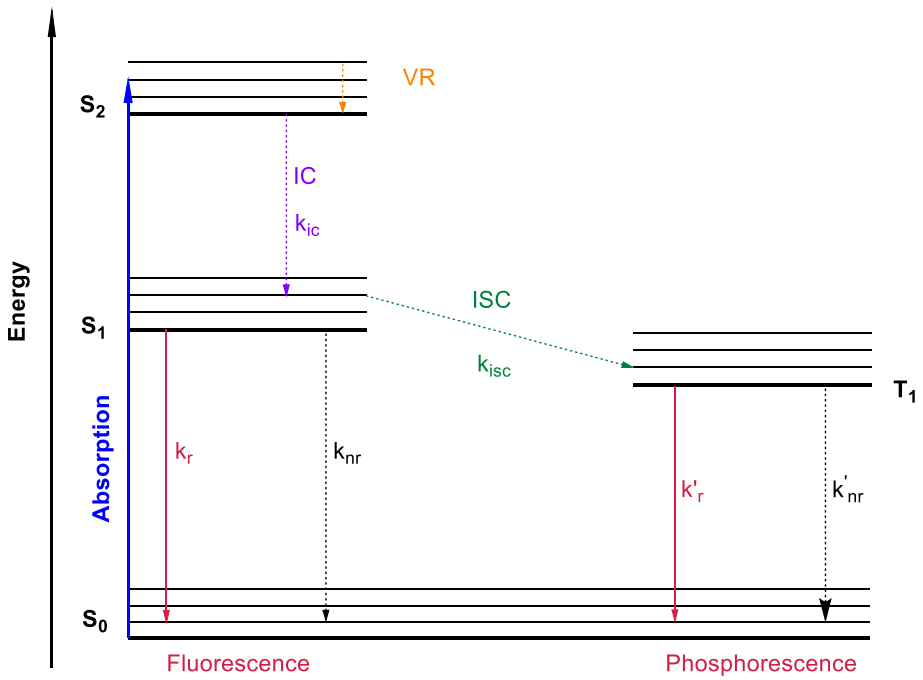

Figure 1.1. Simplified representation of the Jablonski diagram.

The photoexcitation of a molecule with an appropriate wavelength allows the promotion of an electron from the molecule ground state, labelled as S_0, to different electronically excited states (S_1, S_2…S_n) with the same spin multiplicity. Once the electron is excited, several mechanisms allow energy to be dissipated. For each electronic excited state, many vibrational levels are populated upon light absorption vibrational; energy can be dissipated between vibrational levels of the same excited state by vibrational relaxation (VR), whereas internal conversion (IC) takes place between different electronic levels with the same spin multiplicity as a consequence of overlap of vibrational levels. The greater the overlap the fastest the non-radiative decay, implying high values of the process rate constant "k_{ic}". Both VR and IC are fast non-radiative pathways that occur in the order of 10^{-14}-10^{-13} seconds.[1,2] On the other hand, a non-radiative transition between two states of different multiplicity is named intersystem-crossing (ISC) which consists of the conversion of the singlet excited state (S_1) to a more stable triplet state (T_1). Despite ISC violating the spin selection rule, the presence of a heavy element favouring strong spin-orbit coupling, such as a metal centre, results in a relaxation of the spin selection rule thus partially allowing the transition. This process rises from the coupling between the electron spin angular momentum with the electromagnetic field generated by the rotation of the electron around the nucleus. ISC processes are characterized by a rate constant "k_{isc}" which is strictly correlated to the dimension of the considered nucleus and typically occurs with a time scale from 10^{-8} to 10^{-9} seconds.[1,2] As previously mentioned, a non-radiative decay from the excited state to the ground state is favoured by an overlap of vibrational levels, causing the molecule to dissipate energy by moving to the lower energy ground state. The relationship between the entity of this overlapping and the non-radiative decay rate constant k_{nr} is described by the energy gap law. (**Equation 2**)

$$\boldsymbol{k_{nr} = Ae^{-\alpha \Delta E}} \qquad \textbf{(eq.2)}$$

where k_{nr} represents the non-radiative decay constant, A is the pre-exponential coefficient, α is a proportionality constant and ΔE is the energy gap between the two energy states.

Considering such relation, it is possible to notice how a high energy gap between the excited and the ground state is associated with a low rate of non-radiative decay.[3]

Alongside radiationless decays, dissipation of energy from an excited state can be accomplished by spontaneous emission of light, hence by luminescence. Luminescence can be formally divided into two categories according to the nature of the excited state: *fluorescence* ($S_1 \rightarrow S_0 + h\nu$) is the spin-allowed emission of light ($h\nu$) from a singlet excited state (S_1) to a singlet ground state (S_0) within a timeframe of 10^{-9} to 10^{-7} seconds; *phosphorescence* ($T_1 \rightarrow S_0 + h\nu$) takes place from a triplet excited state (T_1) to a singlet ground state (S_0) thus being formally spin-forbidden. The change of spin multiplicity required in the decay of the T_1 excited state to an S_0 ground state is responsible for the slower decay rate of phosphorescent phenomena, hence resulting in elongation in the lifetime of the excited state ($10^{-4} – 10^{-1}$ s).

$$\boldsymbol{\tau = \frac{1}{k_r + k_{nr} + k_{ic} + k_{isc}}} \qquad \textbf{(eq.3)}$$

$$\boldsymbol{\Phi_r = \frac{k_r}{k_r + k_{nr} + k_{ic} + k_{isc}}} \qquad \textbf{(eq.4)}$$

The key parameters that are usually taken into account in the evaluation of the competition between radiationless and radiative decay pathways are the excited state lifetime "τ" and the luminescence quantum yield "Φ_r", being τ the average time the molecule spends in the excited state before deactivation to the ground state and Φ the ratio of emitted photons to the absorbed ones. The terms contributing to the determination of such parameters are gathered in **Equation 3** and **Equation 4**, which represent the entity of the aforementioned parameters in consideration of all the available pathways for the excited state to dissipate energy on going back to the molecule ground state.

Selection rules

Selection rules define the probability of an electron transition between quantum states to occur, and according to such criteria radiative processes can be classified as allowed or as forbidden transitions.

Laporte selection rule

This selection rule, which only applies to centrosymmetric systems, states that a transition occurring between levels with the same parity (g, gerade or u, ungerade) with respect to the inversion centre (e.g. u→u or g→g) is forbidden. Hence, a change of parity must take place for the transition to be allowed (e.g. u→g or g→u). A relaxation of the Laporte rule is found in phenomena like "vibronic coupling". Vibronic coupling in a process arising from the interaction of a vibrational transition with an electronic transition, in which the inversion centre of the molecule is temporarily removed due to asymmetric vibrations of the latter. Thus, the decrease in the overall symmetry of the system allows forbidden transitions to take place, likewise d→d transitions in octahedral (O_h) metal complexes.

Spin conservation rule

According to the spin conservation rule, being ΔS the overall spin multiplicity variation, a transition is to be considered spin-allowed when occurring between states with the same spin multiplicity ($\Delta S=0$), whereas transitions between states of different spin multiplicity ($\Delta S\neq0$) are formally spin-forbidden. On such premises, a singlet (S=0) to singlet transition will be spin-allowed, while a triplet (S=1) to singlet transition will be spin-forbidden. The presence of a heavy element, such as a metal centre, possessing strong spin-orbit coupling that favours interstates mixing, results in a relaxation of the spin selection rule thus partially allowing transitions with $\Delta S\neq0$.

1.1.1 *Electronic structure and transitions of metal complexes*

To better rationalize the possible photophysical processes rising from the absorption of light by a metal complex, several theories describing the electronic structure of these systems can be taken into consideration; among these, one can find the crystal field theory (CFT), the ligand-field theory (LFT) and the molecular orbital theory (MOT).

Crystal Field Theory (CFT)

In CFT, the ligands surrounding a metal centre are considered as negative point charges generating an electrostatic field, and there are no metal-ligand covalent interactions. In transition metal ions, electrostatic interactions with an approaching ligand are possible only for the outer shell d-electrons, being every other atomic orbital empty or completely filled. In a transition metal ion in the gas state, the five d orbitals have the same energy. In a system where the field generated by the approaching ligand is spherically symmetric, the five d orbitals would be higher in energy in comparison to the free ion as a consequence of the repulsion between the metal electron density and the spherical field of the negative charge; despite such interaction, the five d orbitals would be still fivefold degenerate.

In complexes with octahedral geometry, the ligands approach the metal ion along the *x*, *y*, and *z* axes. Therefore, the electrons in the orbitals located on these axes (d_{z2} and d_{x2-y2}) experience greater repulsion in comparison to the one located on orbitals laying between the axes (d_{xy}, d_{xz}, d_{yz}). Now, the five d orbitals are divided into two sets of orbital with different energy: a higher-energy couple of orbital named e_g, and three other orbitals with lower energy named t_{2g}. This is known as crystal field splitting; Δ_o or 10 Dq, which width depends on the central ion and the ligands involved, is generally considered to evaluate the amount of splitting between the e_g and t_{2g} orbitals. (**Figure 2.1**)

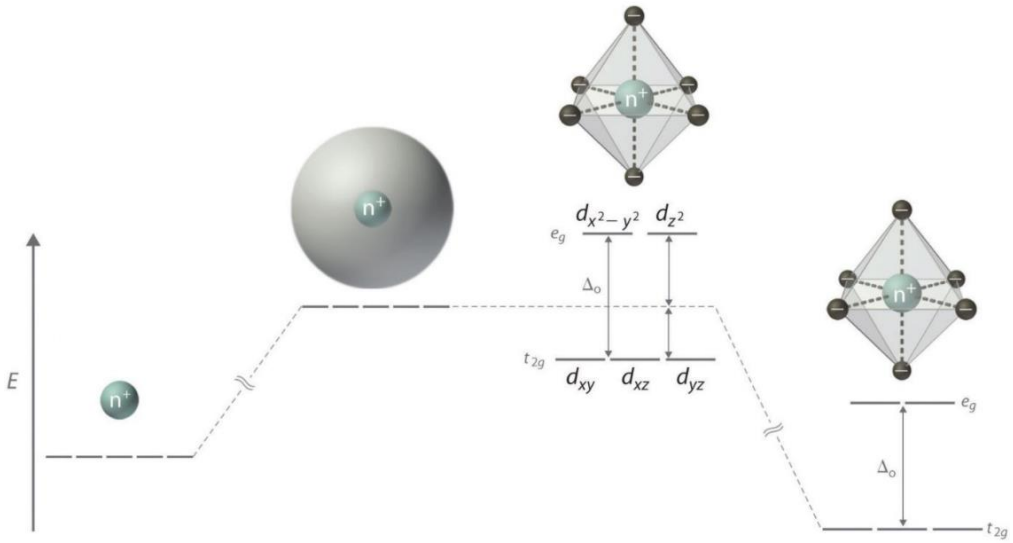

Figure 2.1. Graphical representation of the crystal field splitting of the d orbitals in an octahedral complex.

For the description of the crystal field splitting in tetrahedral complexes, let us consider the metal centre surrounded by a cubic field. In this case, the four ligands do not directly approach the metal centre along the axes, indeed they interact more with orbitals located between the axes (d_{xy},d_{xz}, d_{yz}) which experience greater repulsion in comparison to the one located along the axes (d_{z2} and d_{x2-y2}) As reported in **Figure 3.1**, the splitting of the five d orbital results in a higher-energy set of three degenerate orbitals (t_2) and a low energy couple of orbitals (e); the energy gap is defined as Δ_t. The minor entity of the splitting between the two sets of the orbital is explained by the smaller number of ligand interacting with the metal centre, resulting in a lower repulsion experienced by the five d orbitals. This time no parity terms are involved due to the absence of an inversion centre; this is the reason why transitions in tetrahedral complexes are generally more intense in comparison to octahedral complexes.

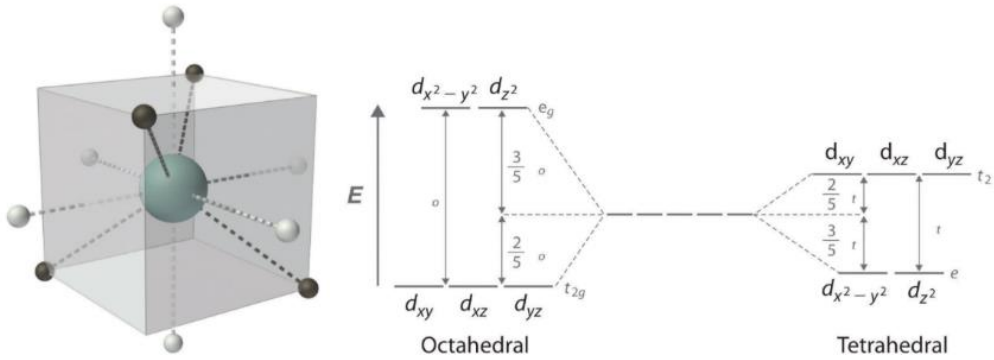

Figure 3.1. Graphical representation of the crystal field splitting of the d orbitals in a tetrahedral complex.

Ligand field theory (LFT)

According to experimental data, the crystal field theory (CFT) represents a rough approximation of the electronic structure of metal complexes. A more representative approach in the description of the electronic structure of these systems takes into consideration a certain extent of covalency in the interaction between the metal centre and the coordinated ligands, thus a certain overlap between the metal-ligand orbitals; this is named as ligand field theory (LFT). According to LFT, the calculation of the energy-level diagrams proceeds analogously to CFT, except that one takes into account that the interelectronic repulsion and spin-orbit coupling parameters are noticeably reduced when going from free to complexed metal ions, because of the delocalization of the ‘metal’ electrons.

Molecular Orbital Theory (MOT)

In molecular orbital theory (MOT) the orbitals involved in the interaction between the metal centre and a coordinating ligand are composed of a linear combination of both metal and ligand orbitals. The ligands orbitals are combined to obtain a set of composite ligand orbitals named ligand group orbital (LGO). Successively, this set of ligands is combined with metal orbitals according to symmetry criteria in the construction of the molecular orbital (MO) diagram of the molecule

Molecular orbital diagram for a d_6 configuration

The molecular orbital diagram reported in **Figure 4.1** is a representation of the electronic structure of a d_6 transition metal complex, showing some of the possible electronic transitions occurring in these systems. In the construction of the diagram, all of the ligands surrounding the metal are assumed to be equivalent and, for simplicity, only the π^* ligand orbitals of t_{2g} symmetry are shown forming molecular orbitals with the metal. Furthermore, in **Figure 4.1** the stability of low spin d_6 metal complexes is highlighted since, as one can notice, they possess completely filled bonding orbitals and empty anti-bonding orbitals.

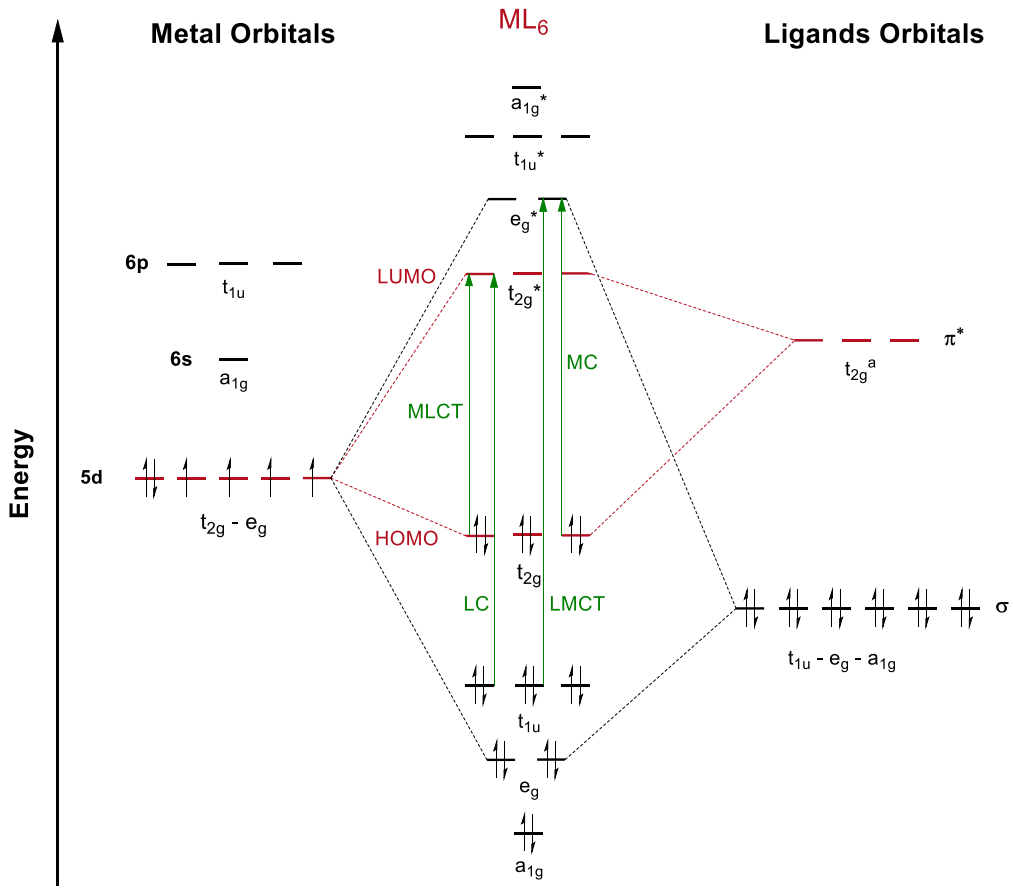

Figure 4.1. Simplified MO diagram for a low spin d_6 transition metal complex, coordinated to six equivalent π accepting ligands. The formation of the relevant molecular orbitals has been indicated with dashed lines. The HOMO and LUMO orbitals are highlighted in red, whereas MC, LC, LMCT, and MLCT transitions are highlighted in green.

For a third-row transition metal ion, the outer coordination sphere consists of 5d, 6p and 6s orbitals, thus these elements will be considered in the construction of the corresponding molecular orbital diagram. In the Oh symmetry point group, metal orbitals may be classified according to symmetry criteria as follows:

$$5d\ (d_{xy}, d_{xz}, d_{yz}) \rightarrow e_g$$

$$5d\ (d_{x2-y2}; d_{z2}) \rightarrow t_{2g}$$

$$6s \rightarrow a_{1g}$$

$$6p\ (p_x, p_y, p_z) \rightarrow t_{1u}$$

The e_g and a_{1g} orbitals are suitable uniquely for σ bonding interaction, t_{2g} orbitals are suitable uniquely for π bonding interaction, whereas t_{1u} orbitals can give rise to both σ and π bonding interactions. As shown in figure 4.1, for a low spin d_6 transition metal complex, the bonding molecular orbitals (a_{1g}, e_g, t_{1u} and t_{2g}) are completely filled, whereas the anti-bonding orbitals (a_{1g}*, e_g*, t_{1u}* and t_{2g}*) are empty. The presence of π accepting ligands generally produces a strong crystal field, thus increasing the entity of the splitting between the metal d orbitals; for such reason, the e_g* molecular orbitals display higher energy in comparison to the t_{2g}*.

In following this approach, the ligands interacting with the metal ion are considered to be all equivalent. Linear combination of their atomic orbital results in the definition of an LGO comprising t_{1u}, e_g, a_{1g} and t_{2g} terms. At this point, the main scaffold of the diagram is built considering the interaction between metal and ligands orbitals with appropriate symmetry requirement. The t_{2g} and t_{2g}* orbitals represent respectively the highest occupied molecular orbital (HOMO) and lowest occupied molecular orbital (LUMO). The separation between such levels is defined as the HOMO-LUMO gap and strictly depends on the π donating/accepting ability of the considered ligands.[4]

In consideration of MOs being linear combinations of atomic orbital with main ligand or metal character, it is possible to define the electronic transitions of an octahedral transition metal complex according to the main character of the orbitals involved in the process as follows:

- Metal Centred transitions (MC). Transitions between MOs with main metal character, these transitions happen between the π (t_{2g}) non-bonding orbital and the σ* (e_g^*) anti-bonding orbital both located on the metallic ion (d-d transitions). These processes are formally spin-forbidden so they are generally associated with small absorptivities.

- Ligand Centred transitions (LC). Transitions between MOs with prevalent ligands character. These processes take place between the ligands orbitals that are not involved in the coordination to the metal. They are directed from the π bonding to the π* anti-bonding system of the ligands. These processes generally represented by intense bands in the UV region. (See CT section for LLCT transitions).

- Charge Transfer transitions (CT). Transitions occurring between MOs with different main character. According to the initial position of the electron undergoing the transition, it is possible to distinguish between three types of transitions: 1) ligand to metal charge transfer (LMCT) for transitions from the π system of the ligands to the σ* (e_g) anti-bonding orbital of the metal; 2) metal to ligand charge transfer (MLCT) when starting either from σ (t_{2g}) non-bonding or σ* (e_g) orbital of the metal to the π* system of the ligands; 3) ligand to ligand charge transfer (LLCT), which are CT transitions between inequivalent ligands. Contrarily to d-d transitions, CT transitions are completely allowed, giving rise to intense absorption bands.

1.2 Luminescent complexes of d_6 transition metal ions

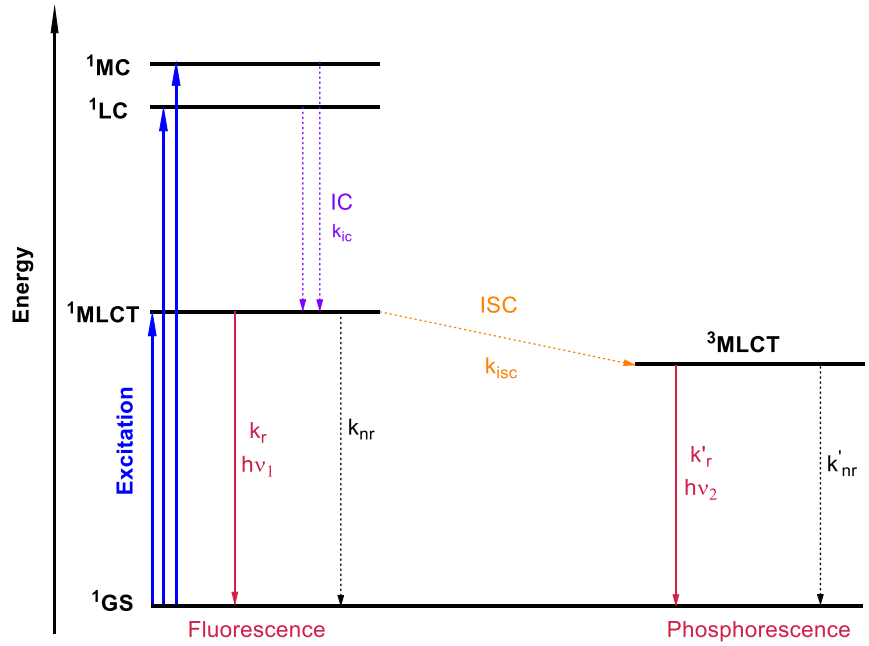

Figure 5.1. Simplified Jablonski diagram for octahedral d_6 transition metal complexes with lowest MLCT excited state. VR and LLCT transitions are not included for simplicity.

The Jablonski diagram reported in **Figure 5.1** is a simplified representation of the possible electronic transition occurring in an octahedral d_6 transition metal complex. The contribution of both the metal and the ligands in the determination of the complex excited states stands behind their much more complicated photophysical properties in comparison to organic fluorophores. In metal complexes, both fluorescence and phosphorescence can be achieved through the right balance of electronic and geometrical requirements. In the ground state electronic configuration of low spin d_6 metal complexes, there are no unpaired electrons, suggesting a singlet spin multiplicity. When using second and third-row transition elements, the presence of heavy metal ions induces high spin-orbit coupling allowing spin-forbidden electronic transitions. The spin-orbit coupling allows efficient ISC from the S_1 excited state to the lowest T_1 excited state, inducing also an admixture between these states (MC, MLCT LC), eliminating the spin-forbidden nature of the phosphorescent transition.

1.2.1 *Ruthenium(II) polypyridyl complexes*

Ruthenium (II) polypyridyl complexes are widely considered the progenitor reference in studies dealing with the photophysical behaviour of transition metal complexes. Indeed, at the beginning, spectroscopic analysis of the archetypal compound $[Ru(bpy)_3]^{2+}$ (**1, Figure 6.1**) evidenced the possibility to populate a ^{3}MLCT emissive state by photoirradiation, leading to a broad phosphorescent emission centred at 620 nm (τ = 900 ns). Although, such emission is generally associated with low values of quantum yield and emission intensity at room temperature due to a low-lying ^{3}MC state, which contributes to radiationless decay by a thermally activated surface crossing process.[5]

Thanks to great research efforts, numerous studies on Ru(II) polypyridyls have been reported all over the years highlighting their great photophysical and electrochemical stability, both in the fundamental and excited state; these reasons stand behind the quite rich applicative scenario Ru(II)-diimine complexes possess nowadays.

Their ability to interact with biological systems is known since the early '50s when Dwyer and coworkers reported the first study on the antimicrobial activity of Ru(II) polypyridyls toward bacteria.[6] Further investigation of the interaction of these complexes with biological moieties led to multiple application of Ru(II) in bioinorganics, where they can act as anticancer drugs,[7] antimicrobial agents,[8] photosensitizer in photodynamic therapy,[9] luminescent probes in bioimaging,[10] and also as staining agents for proteins detection[11]. (**2, Figure 6.1**)

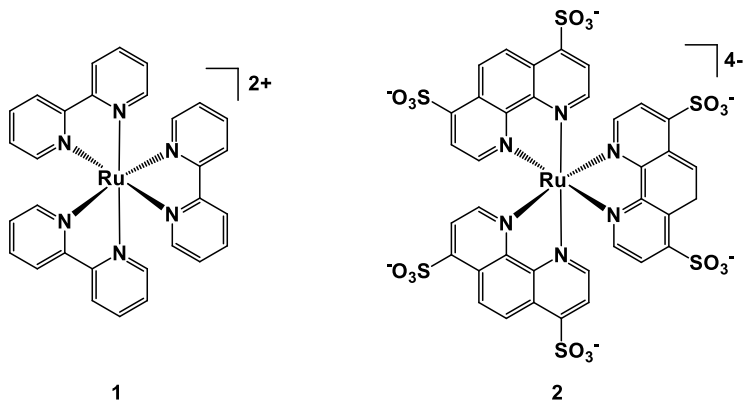

Figure 6.1. (left) Structure of $[Ru(bpy)_3]^{2+}$; (right) Ru SYPRO®, a luminescent protein staining agent.

1.2.2 *Iridium (III) cyclometalated complexes*

During the past 15 years, bis-cyclometalated Ir(III) complexes have been gaining ever-growing attention between luminescent materials. Ir(III) complexes of the form $[Ir(C\hat{}N)(L\hat{}L)]^{0/+}$, where C^N represents a cyclometalating ligand and L^L a chelating ligand, are by far the most commonly investigated type of iridium complexes in this field. They are generally characterized by intense phosphorescent emissions deriving from MLCT or LLCT (or both) excited states.

The chemical nature of these tris-chelate luminophores can be readily tuned by chemical modification of the coordinated ligands. Indeed, it is well know how Ir(III) cyclometalates can be tailored to obtain emissions across the entire range of the visible spectrum, and sometimes even down to the near infra-red (NIR) region.[12] Furthermore, the possibility to obtain both neutral and charged complexes(**3 4 and 5, Figure 7.1**), along with their outstanding photophysical output, makes them great candidates for application in lightning devices such as organic light-emitting diodes (OLEDs, **6 Figure 7.1**)[13] and light-emitting electrochemical cells (LEECs, **7 Figure 7.1**).[14] In the same way, the electrochemical properties of these complexes, in terms of relative position and reversibility of the redox processes the molecule undergoes in both the fundamental and excited state, can be properly modulated by appropriate choice of C^N and L^L ligands. Such a combination of photophysical and electrochemical versatility stands behind the great potential recently displayed by luminescent Ir(III) cyclometalates in photocatalysis, where these systems are responsible for the harnessing of light to promote chemical reactions.[15] (**8**, **Figure 7.1**)

Besides to modification of the photophysical and electrochemical properties, functionalization of the coordinated ligand is a great route to confer these complexes selectivity features. For example, the possibility to achieve localization selectivity toward specific organelles by appropriate choice of the coordinated ligands makes luminescent Ir(III) metal complexes versatile probes in the luminescent bioimaging of live cells. [16] As an example, in **Figure 7.1** an Ir(III) complex (**9**) possessing selectivity towards lysosome is reported.[17]

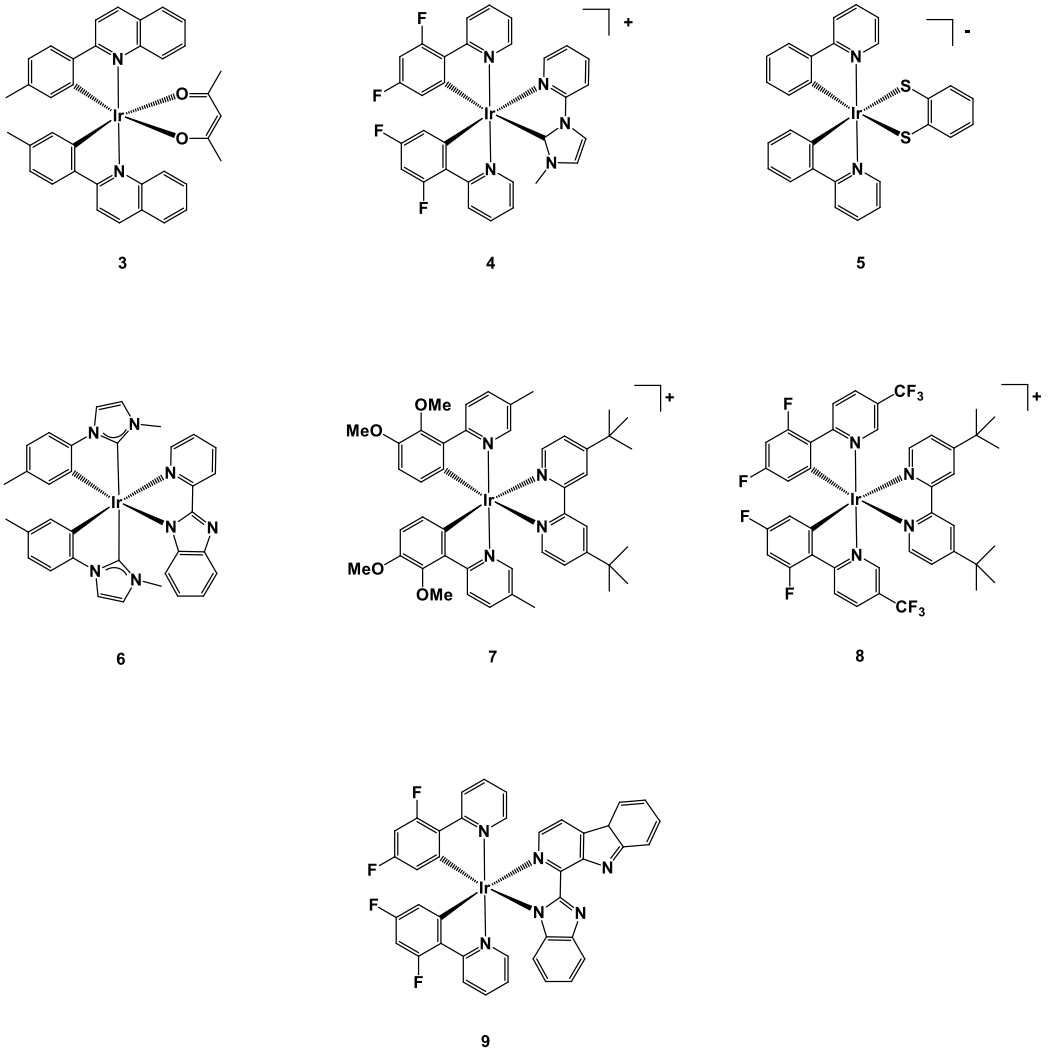

Figure 7.1. Examples of Ir(III) cyclometalated complexes.

1.2.3 *Rhenium(I) tricarbonyl complexes*

Along with Ru(II) and Ir(III) luminophores, isoelectronic Re(I)-tricarbonyl diimine complexes have been extensively studied since the early '70s, when Wrighton and Morse investigated for the first time the luminescent properties of fac-[Re[phen)$(CO)_3$Cl], (**10**, **Figure 8.1**) evidencing their ability to display phosphorescent emission upon the population of an emissive ^{3}MLCT excited state.[18]

The facile synthesis of Re(I)-tricarbonyl diimine complexes, together with the possibility to readily tune their phosphorescent output by a convenient choice of ligands, stand behind the many applications these complexes found through the years. Their use in material sciences sees these systems in lighting devices (OLED, **11 Figure 8.1**).[19,20] More frequently, applications of Re(I) tricarbonyl in life sciences are reported, where they find use in chemical and biological sensing,[21] (**12**) bioconjugation,[22] and as luminescent probes in bioimaging.[23] (**13**)

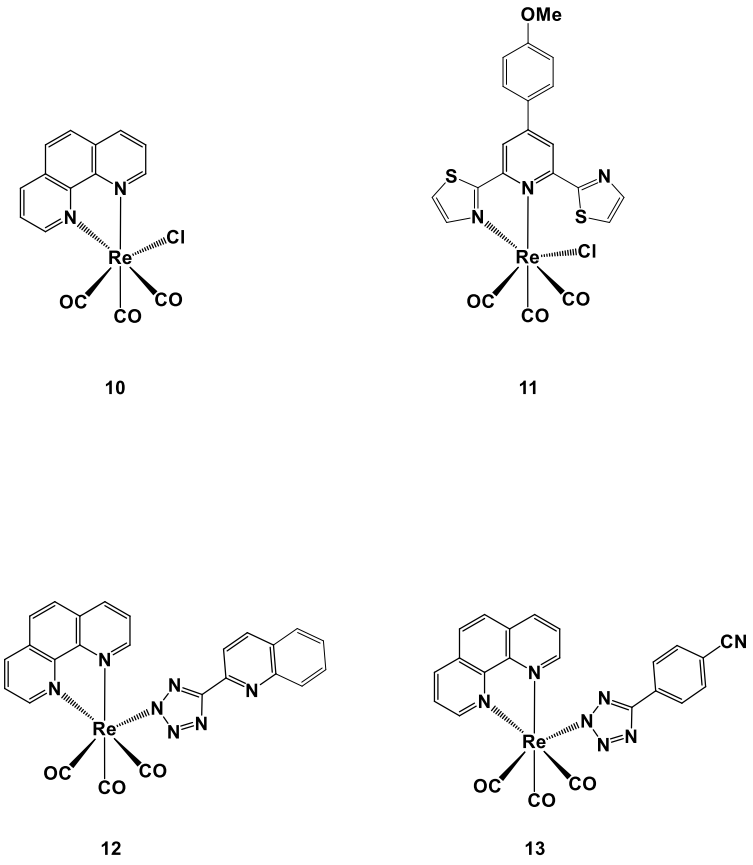

10 11

12 13

Figure 8.1. Examples of Re(I) tricarbonyl complexes.

1.3 Metal tetrazol(at)e complexes

1.3.1 *Tetrazoles: synthetically versatile nitrogen-rich ligands for metal complexes*

Tetrazoles are a class of synthetic organic heterocyclic compounds consisting of an aromatic 5-member ring composed of four nitrogen atoms and one carbon atom. Tetrazoles are carboxylic acid isosteres displaying similar values of pK_a.[24,25] This feature, in combination with their lower toxicity and greater metabolic stability and lipophilicity compared to the -COOH analogues, prompted their use in medicinal chemistry as isosteric substitutes of different carboxylic groups in biologically active molecules. [26]

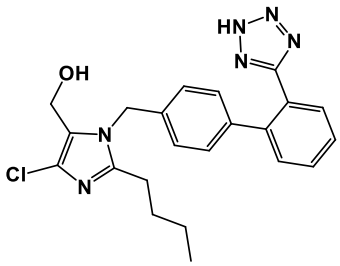

Figure 9.1. Losartan®, the first angiotensin receptor blocker.

Alongside their application in pharmacology, tetrazoles own great potential in coordination chemistry, in light of the presence of four diimine-type nitrogens able to bind transition metal and lanthanide ions. Furthermore, an appropriate design of the main scaffold of the ligand allows the possibility to obtain mono and multinuclear arrays.

Tetrazoles preparation procedures are known since the late ’50s in both organic and aqueous solution.[27] Amidst tetrazole derivatives, 5-aryl tetrazoles are generally obtained by 1-3 dipolar cycloaddition of the azide anion onto an aromatic nitrile. (**Figure 10.1**) Their neutral derivatives, N-Alkyl-5-aryl tetrazoles, can be obtained by substitution with an alkylating agent, such as alkyl halides.[28] (**Figure 10.1**) They are generally obtained as a mixture of regioisomers differing for the substitution on the pentatomic ring. Selectivity towards the unique N2 isomer can be achieved when using bulky functionalities (e.g. a tertbutyl group).

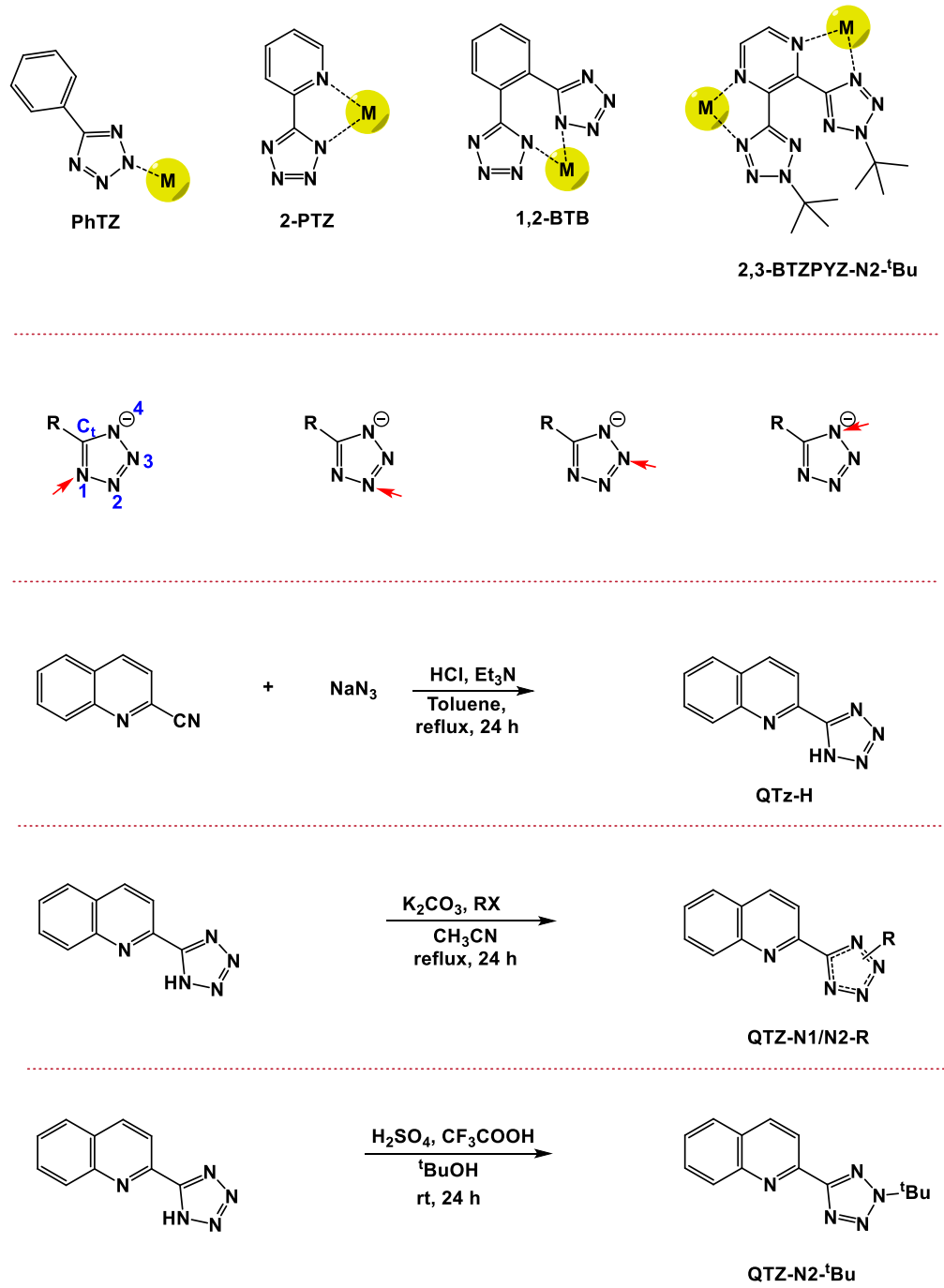

Figure 10.1. Examples of tetrazolates and N-alkyl-tetrazoles presented herein and corresponding acronyms. Coordination modes of 5-substituted tetrazole and numeration. Preparation of QTZ-H using Koguro's procedure. N-alkylation reaction for 5-aryl tetrazolates.

1.3.2 *Metal-tetrazol(at)e complexes*

Since the early 2000s, the research group in which I carried out my PhD is dedicating great research effort to studies dealing with the coordination chemistry of 5-aryl tetrazolates and 5-aryl tetrazoles, their N-alkylated derivatives. At an early stage, the first example of Fe(II)-cyclopentadienyl complexes containing 5 aryl tetrazolates were reported.[29] It is noteworthy how in this case the formation of the pentatomic ring is achieved at room temperature by cyclization of sodium azide onto an already coordinated nitrile, without the addition of any further reagent. (**15**, **Figure 11.1**) Moreover, reactivity studies evidenced the possibility of inducing permanent ($-CH_3^+$) or reversible ($-H^+$) modification on the complex by electrophilic addition on the coordinated tetrazole.

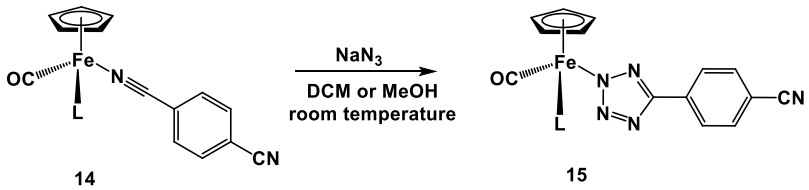

Figure 11.1. Tetrazole formation via cyclization of a coordinated nitrile.

1.3.3 *Ruthenium (II)*

Successively, 5 aryl tetrazolate were employed as mono coordinating or chelating ligand in the preparation of mono and multinuclear Ru(II) polypyridyl complexes. (**16**, **17**, **18 Figure 12.1**) The obtained Ru(II) tetrazolate revealed interesting electrochemiluminescent properties in solution and solid-state, thus prompting further studies on their applicative scenario.[30] Once again, reactivity toward electrophiles was confirmed and photophysical studies revealed a clear and distinguishable variation of the emission properties of the complexes upon addition of electrophile, witnessing for the first time how tetrazolic ligands could actively take part in determining the energy and the composition of the HOMO and/or LUMO levels of the corresponding complexes.[30] More recent applications of these systems in material science see several Ru(II)-tetrazolate complexes as thiocyanate-free dyes as efficient sensitisers in dynamic sensitized solar cells (DSSC).[31] (**19**, **Figure 12.1**) Also, the antimicrobial activity of recently reported tris homoleptic Ru(II)-tetrazoles is discussed in chapter 3.[32]

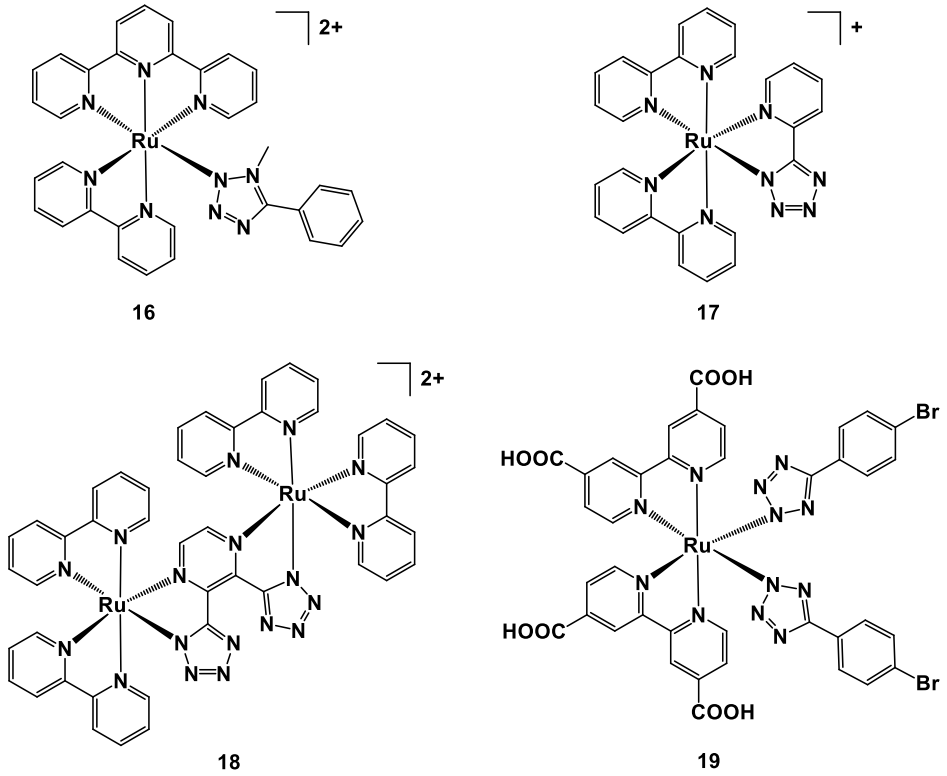

Figure 12.1. Examples of prepared Ru(II)-tetrazolate complexes.

1.3.4 *Iridium (III)*

Alongside Fe(II) and Ru(II) centres, 5-aryl tetrazolate and alkyl-tetrazoles coordination chemistry have been also investigated toward isoelectronic d_6 metal ions such as Ir(III) and Re(I) in the preparation of the corresponding tetrazolate complexes, generally providing luminescent derivatives.

In an early stage, fundamental studies on the reactivity towards electrophiles of luminescent Ir(III)-tetrazolate revealed once again the participation of the tetrazolic ligand in the determination of both luminescence and electrochemical properties of the corresponding complexes.[33] In a successive stage, the first example of luminescent anionic Ir(III)-tetrazolate complexes possessing bright blue or aqua emission were obtained. (**20**, **Figure 10.1**) Then, by the combination of these blu anions with different red-emitting cationic Ir(III)-tetrazole the first examples of fully Ir(III) tetrazolate soft salts were prepared, providing white emitting ion pairs where both the anion and the cation are represented by a luminescent Ir(III) complex.[34, 35]

Along with fundamental studies aimed at getting deeper knowledge on the photophysical and electrochemical behaviour of Ir(III) tetrazolate, their applicative scenario have recently been investigated, leading to interesting results in the field of material and life sciences. Reactivity studies enlightened how the conversion of a neutral Ir(III)-tetrazolate into the corresponding cationic derivative (**21**, **Figure 13.1**) by selective N2-methylation of the coordinated tetrazole results in a switch-on of the complex antimicrobial activity towards *Deinococcus radiodurans*, a gram-positive bacteria.[36]. Later on, different antimicrobial Ir(III)-tetrazolate were supported on a silica matrix,[37] and by coating a cotton textile with the Ir-SiO_2 ceramic nanophase antimicrobial textiles were obtained.[38] More recently, the neutral counterpart of complex **21**, along with other Ir(III)-tetrazolates, found application in the luminescent bioimaging of living bacteria. [39] Furthermore, application of Ir(III)-tetrazolate complex **22** in material science as electroluminescent material in the fabrication of an OLED device will be discussed in chapter 2, and the potential use of newly prepared Ir(III)-tetrazolate complexes possessing NO_2 groups is reported in chapter 6. (**23, Figure 13.1**).

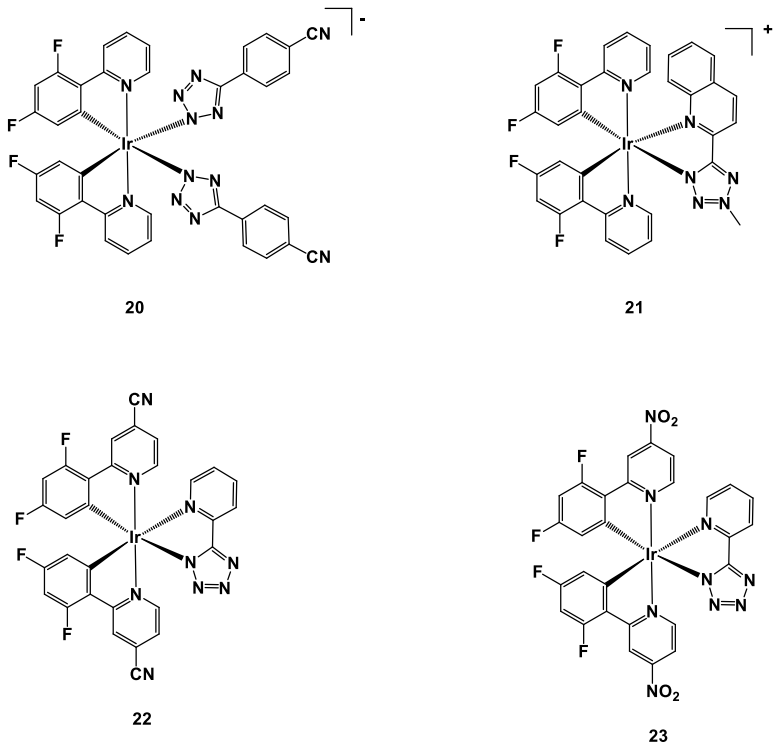

Figure 13.1. Examples of prepared Ir(III)-tetrazolate complexes.

1.3.5 *Rhenium (I)*

Relative to the studies dealing with Re(I) derivatives, the use of 5-aryl tetrazoles as ligands for fac-[Re(CO) (N^N)(X)]-type complexes, (where N^N = diimine such as 1,10 phenanthroline or 2,2' bipyridine, X = Br), initially led to the formation of a new class of phosphorescent neutral compounds which displayed a photoluminescent behaviour congruent with "typical" of Re(I) tricarbonyl complexes. Nevertheless, the emission properties of the Re-tetrazolate complexes appeared to be strongly influenced by the nature of the tetrazolate ligand, which showed a major contribution in the determination of the HOMO level.[40] Analogously to Fe(II), Ru(II) ad Ir(III) tetrazolate systems,[29,30,33] also neutral fac-[Re(N^N)(CO)(L)] tetrazolate complexes undergo electrophilic substitutions at the coordinated tetrazolate ring (reversible/protonation, permanent/methylation). In all cases, the addition of an electrophile led to a marked blue-shift of the emission profile of the Re(I) complex, with a concomitant "boost" of the emission performances, as evidenced by the substantial increase of the PLQY values and the elongation of the phosphorescence lifetimes.[41]

Along with reactivity studies, Re(I) tetrazole complexes were also investigated in biological contexts. A class of neutral Re(I) tetrazolate displayed a particular affinity for the so-called "lipid droplets" (**24**, **Figure 11.2**). The "in vivo" selective localization of Re(I) tetrazolate complexes was recognized through IR and Raman Spectroscopy as well as Confocal Microscopy.[42] Most recently, different Re(I)-tetrazolate complexes found application in the targeting of metal cations,[21] in the preparation of luminescent polymeric materials,[43] and in the luminescent staining o proteins (chapter 5).[44] Moreover, the preparation, characterization and study of the interaction with BSA (bovine serum albumin) of a new family of Re(I)-alkyl tetrazole will be discussed in chapter 4. (**25, Figure 14.1**)[45]

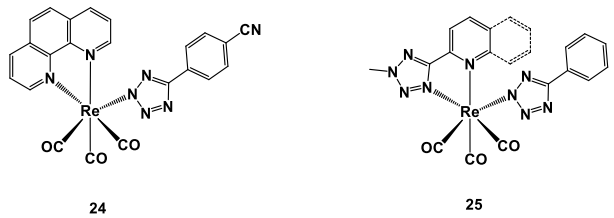

24 25

Figure 14.1. Examples of prepared Re(I)-tetrazolate complexes.

1.4 References

[1] F. P. V. Balzani, G. Bergamini and S. Campagna; *Top. Curr. Chem*., **2007**, 280, 1–36.

[2] J. R. Lakowicz, Principles of Fluorescence Spectroscopy, 3rd Edition, **2006**.

[3] J. V Caspar and T. J. Meyer; *J. Phys. Chem*., **1983**, 87, 952–957.

[4] F. B. L. Flamigni, A. Barbieri, C. Sabatini and B. Ventura; *Top. Curr. Chem*., 2007, 281, 143–203.

[5] a) S. Campagna, F. Puntoriero, F. Nastasi, G. Bergamini and V. Balzani; *Top. Curr. Chem.*, **2007**, 280, 117; b) R. T. F. Jukes, V. Adamo, F. Hartl, P. Belser and L. De Cola; *Coord. Chem. Rev.*, **2005**, 249, 1327; c) S. Welter, N. Salluce, P. Belser, M. Groeneveld and L. De Cola; *Coord. Chem. Rev.*, **2005**, 249, 1360;

[6] a) F. Dwyer, E. C. Gyarfas, W. P. Rogers and J. H. Koch; *Nature*, **1952**, *170*, 190−1. b) F. Dwyer, I. K. Reid, A. Shulman, G. M. Laycock and S. Dixson; *Immunol. Cell Biol.*, **1969**, *47*, 203−18.

[7] S. Li, G. Xu,Y. Zhu, J. Zhao and S. Gou; *Dalton Trans.*, **2020**, 49, 9454.

[8] F. Li, J. G. Collins and F. R. Keene; *Chem. Soc. Rev.***, 2015,**44**,** 2529-2542

[9] a) X M. He, F. Du, W. Zhang, Q. Yi, Y. Wang, H. Yin, L. Bai, Y. Gu andY. Liu; *Polyhedron*, **2019**, 165,97–110. b) S. Paul, P. Kundu, U. Bhattacharyya, A. Garai, R. C. Maji, P. Kondaiah and A. R. Chakravarty; *Inorg. Chem.*, **2020**, 59, 913–924. c) A. Raza, S. A. Archer, S. D. Fairbanks, K. L. Smitten, S. W. Botchway, J. A. Thomas, S. MacNeil and J. W. Haycock; *J. Am. Chem. Soc.*, **2020**, 142, 4639−4647.

[10] C. Lau, C. Chan, K. Zhang, V. A. L. Roy and K. K. Lo; *Eur. J. Inorg. Chem.*, **2017**, 5288–5294.

[11] a) K. Berggren, T. H. Steinberg, W. M. Lauber, J. A. Carroll, M. F. Lopez, E. Chernokalskaya, L. Zieske, Z. Diwu and R. P. Haugland; *Analytical Biochemistry*, **1999**, 276, 129–143. b) M. V. Babak, P. Le Faouder, X. Trivelli, G. Venkatesan, S. I. Bezzubov, M. Kajjout, A. L. Gushchin, M. Hanif, O. Poizat, H. Vezin and C. Rolando; *Inorg. Chem.*, **2020**, 59, 4527−4535.

[12] a) J. C. Deaton, F. N. Castellano, Archetypal Iridium(III) Compounds for Optoelectronic and Photonic Applications: Photophysical Properties and Synthetic Methods. In Iridium(III) in Optoelectronic and Photonics Applications; E. Zysman-Colman, Ed. Wiley-VHC:Weinheim, Germany, **2017**, 1−70 and references cited herein. b) J. Frey, B. F. E. Curchod, R. Scopellitti, I. Tavernelli, U. Rothlisberger, M. K. Nazeeruddin and E. Baranoff; *Dalton. Trans.*, **2014**, *43*, 5667. d) V. H. Nguyen, R. S. H. Khoo, and J. H. K. Yip; *Inorg. Chem.*, **2015**, 54, 2264−2277. e) V. H. Nguyen, H. Q. Chew, B. Su, and J. H. K. Yip; *Inorg. Chem.*, **2014**, 53, 9739−9750.

[13] a) T. Li, J. Wu, Z. Wu, Y. Zheng, J. Zuo, Y. Pan; *Coord. Chem. Rev.*, **2018**, 374, 55–92. b) "Iridium (III) in optoelectronic and Photonics Applications", Wiley, **2017,** chapter 6.

[14] C. E. Housecroft, E. C. Constable; *Coord. Chem. Rev.*, **2017**, 350, 155-177.

[15] J. Twilton, C. Le, P. Zhang, M. H. Shaw, R. W. Evans, D. W. C. MacMillan; *Nature Reviews Chemistry*, **2017**, 1, 0052. b) L. Marzo, S. K. Pagire, O. Reiser and B. Kçnig; *Angew. Chem. Int. Ed.*, **2018**, 57, 10034–10072.

[16] a) C. Caporale, M. Massi; *Coord. Chem. Rev.*, **2018**, 363, 71–91. b) P. Ho, C. Ho, W. Wong; *Coord. Chem. Rev.*, **2020**, 413, 213267.

[17] L. He, Y. Li, C.-P. Tan, R.-R. Ye, M.-H. Chen, J.-J. Cao, L.-N. Ji and Z.-W. Mao, *Chem. Sci.*, **2015**, 6, 5409–5418.

[18] M Wrighton, D. L. Morse; *J. Am. Chem. Soc.*, **1974**, 96, 998–1003.

[19] G. Zhao, J. Zhao, Y. Hu, D. Zhang, X. Lia, *Synthetic Metals*, **2016**, 212, 131–141.

[20] T. Klemens, A. Świtlicka, B. Machura, S. Kula, S. Krompiec, K. Łaba, M. Korzec, M. Siwy, H. Janeczek, E. Schab-Balcerzak, M. Szalkowski, J. Grzelak, S. Maćkowski; *Dyes and Pigments*, **2019**, 163, 86–101

[21] V. Fiorini; A. M. Ranieri; S. Muzzioli; K. D. M Magee; S. Zacchini; N. Akabar; A. Stefan; M. I. Ogden; M. Massi; S. Stagni; *Dalton Trans.*, **2015**, 44, 20597 – 20608.

[22] W. L. Turnbull, E. Murrell, M. Bulcan-Gnirss, M. Majeed, M. Milne, L. G. Luyt; *Dalton Trans.*, **2019**, 48, 14077.

[23] C. A. Bader, A. Sorvina, P. V. Simpson, P. J. Wright, S. Stagni, S. E. Plush, M. Massi and D. A. Brooks, *FEBS Lett.*, **2016**, 590, 3051–3060.

[24] F. H. Allen, C. R. Groom, J. W. Liebeschuetz, D. A. Bardwell, T. S.G. Olsson, P. A. Wood; *J Chem. Inf. Model.*, **2012**, 52, 857−866.

[25] X M. A. Malik, M. Y. Wani, S. A. Al-Thabaiti and R. A. Shiekh, J. Incl. Phenom. Macrocycl. Chem., 2014, 78, 15–37.

[26] C. N. S. S. P. Kumar, D. K. Parida, A. Santhoshi, A. K. Kota, B. Sridhar and V. J. Rao, *Med. Chem. Commun.*, **2011**, 2, 486–492.

[27] a) K. Koguro, T. Oga, S. Mitsui and R. Orita, *Synthesis*, **1998**, 910-914.b) W. G. Finnegan, R. A. Henry and R. Lofquist; *J. Am. Chem. Soc.*, **1958**, 15, 3908. c) V.A. Ostrovskii, E.A. Popova, R.E. Trifonov; *Advances in Heterocyclic Chemistry*, **2017**, 123, 1-62.

[28] a) R. A. Henry, *J. Am. Chem. Soc.*, 1951, **73**, 4470–4470. b) C. Femoni, S. Muzzioli, A. Palazzi, S. Stagni, S. Zacchini, F. Monti, G. Accorsi, M. Bolognesi, N. Armaroli, M. Massi, G. Valenti, M. Marcaccio, *Dalton. Trans.*, **2013**, *42*, 997; c) U. Sheridan, J. McGinley, J. F. Gallagher, A. Fleming, F. Kelleher, *Polyhedron*, **2013**, *59*, 8-16.

[29] A. Palazzi, S. Stagni, S. Bordoni, M. Monari, S. Selva; *Organometallics*, **2002**, 21, 3774-3781. b) A. Palazzi, S Stagni, S. Selva, M. Monari; *J. Organomet. Chem.*, **2003**, 669, 135–140.

[30] a) Stagni, A. Palazzi, S. Zacchini, B. Ballarin, C. Bruno, M. Marcaccio, F. Paolucci, M. Carano, M. Monari, A. J, Bard; *Inorg. Chem.*, **2006**, 45, 695-709. b) S. Zanarini, A. J. Bard, M. Marcaccio, A. Palazzi, F. Paolucci, S. Stagni; *J. Phys. Chem.*, **2006**, 45, 22551-22556. c) Stagni, E. Orselli, A. Palazzi, L. De Cola, S. Zacchini, C. Femoni, M. Marcaccio, F. Paolucci, S. Zanarini; *Inorg. Chem.*, **2007**, 46, 9126-9138.

[31] V. Fiorini, E. Marchini, M. Averardi, L. Giorgini, S. Muzzioli, A. Dellai, R. Argazzi, A. Sanson, N. Sangiorgi, S. Caramori, S.Stagni; , *Dalton Trans.*, **2020**, 49, 14543.

[32] N. Monti, S. Zacchini, M. Massi, A. Hochkoeppler, L. Giorgini, V. Fiorini, A. Stefan and S. Stagni; *Appl Organomet Chem.*, **2020**; e5806.

[33] S. Stagni, S. Colella, A. Palazzi, G. Valenti, S. Zacchini, F. Paolucci, M. Marcaccio, R. Q. Albuquerque and L. De Cola; *Inorg. Chem.*, **2008**, 47, 10509-10521.

[34] V. Fiorini, S. Zacchini, P. Raiteri, R. Mazzoni, V. Zanotti, M. Massi and S. Stagni; *Dalton Trans.*, **2016**, 45, 12884-12896.

[35] V. Fiorini; A. D'Ignazio; K. D. M. Magee; M. I. Ogden; M. Massi and S. Stagni; *Dalton Trans.*, **2016**, 45, 3256 – 3259.

[36] V. Fiorini, I. Zanoni, S. Zacchini, A. L. Costa, A. Hochkoeppler, V. Zanotti, A. M. Ranieri, M. Massi, A. Stefan and S. Stagni; *Dalton Trans*., **2017**, 46, 12328

[37] I. Zanoni, V. Fiorini, M. Rosado, B. Ballesteros, M. Androulidaki, M. Blosi, S. Ortelli, S. Stagni, M. Dondi and A. L. Costa; *New J. Chem.*, **2018**, 42, 9635--9644

[38] I. Zanoni, M. Blosi, V. Fiorini, M. Crosera, S. Ortelli, S. Stagni, A. Stefan, S. Psilodimitrakopoulos, E. Stratakis, F. Larese Filon and A. L. Costa; *Nanomaterials*, **2020**, 10, 1020.

[39] A. M. Ranieri, C. Caporale, V. Fiorini, A. Hubbard, P. Rigby, S. Stagni, E. Watkin, M. I. Ogden, Mark J. Hackett and M. Massi; *Chem. Eur.J*., **2019**, 25, 10566 –10570

[40] M. V. Werrett, D. Chartrand, J. D. Gale, G. S. Hanan, J. G. MacLellan, M. Massi, S. Muzzioli, P. Raiteri, B. W. Skelton, M. Silberstein and S. Stagni; *Inorg. Chem.*, **2011**, 50, 1229-1241.

[41] M. V. Werrett; G. S. Huff; S. Muzzioli; V. Fiorini; S. Zacchini; B. W. Skelton; A. Maggiore; J. M. Malicka; M. Cocchi; K. C. Gordon; S. Stagni and M. Massi; *Dalton Trans.*, **2015**, 44, 8379 – 8393.

[42] C. A. Bader, T. Shandala, E. A. Carter, A. Ivask, T. Guinan, S. M. Hickey, M.V: Werrett, P. J. Wright, P. V. Simpson, S. Stagni, N. H. Voelcker, P. A. Lay, M. Massi, S. E. Plush and D. A. Brooks; *PLoS ONE*, **2016**, 11(8): e0161557. doi:10.1371/journal.pone.0161557.

[43] a) E. Dallerba, M. Massi and A. B. Lowe; *European Polymer Journal*, **2020**, 126, 109559. b) E. Dallerba, M. Massi and A. B. Lowe; *Polymer*, **2020**, 198, 122522

[44] V. Fiorini, L. Bergamini, N. Monti, A. Hochkoeppler, S. Zacchini, M. Massi, A. Stefan and S. Stefano; *Dalton Trans.*, **2018**, 9400-9410.

[45] N. Monti, V. Longo, S. Zacchini, G. Vigarani, L. Giorgini, E. Bonora, M. Massi, Valentina Fiorini and Stefano Stagni; *Inorganica Chimica Acta*, , **2021**, *518*, 1-11.

Chapter 2 Fine colour-tuning of Ir(III) tetrazolato synthesis, photophysical properties and OLED device fabrication

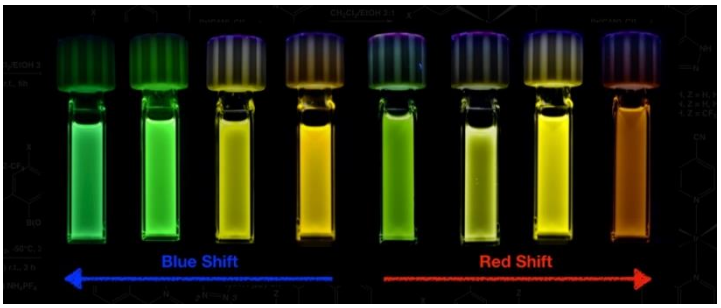

2.1 Abstract

The preparation of a series of both neutrally charged and cationic Ir(III) tetrazole complexes with the general formula **[Ir(C^N)$_2$(N^N)]$^{0/+}$** is described herein. The ancillary ligand (N^N) is represented in turn by 2-pyridyltetrazolato **(PTZ$^-$)**, 2-pyrazinyltetrazolato **(PYZ$^-$)** or 2-pyridyl 5-trifluoromethyl tetrazolato **(F$_3$C-PTZ$^-$)** ligands. The architecture of the cyclometalated ligands (C^N) features an electron-withdrawing group (EWG) such as the cyano (-CN) moiety at the para position of the pyridyl ring, giving rise to 2-phenylisonicotinonitrile **(PPy-CN)** and 2-(2,4-difluorophenyl)isonicotinonitrile **(F2-PPy-CN)**. The photophysical and electrochemical properties of the new Ir(III) cyclometalates have been investigated and the resulting data suggest how the cyclometalating ligands significantly rule the luminescence behaviour of the new complexes, introducing the possibility to blue or red shift the emission maxima of the neutral complexes upon adding a methyl group to the coordinated tetrazolato ring. Lastly, the neutral **[Ir(F2-PPy-CN)$_2$(PTZ)]** was used as emissive phosphor for the fabrication of an **OLED** -type device.

2.2 Introduction

The scientific success of Ir(III)-cyclometalates is reflected by a vast applicative scenario, spanning from bio-inorganics,[1] where they act as biological labels, to the more recent field of photocatalysis,[2a-c] where Ir(III)-based photocatalysts are responsible for the harnessing of visible light to promote several chemical reactions. However, solid-state lightning can be still regarded as the parent and "core business" application for this class of compounds, especially for neutral Ir(III) emitters, which are used in OLEDs (organic light-emitting diodes),[3] and ionic compounds, that are usually employed in LEECs-type devices (light-emitting electrochemical cells).[4] There are several key factors behind the success of Ir cyclometalates, and all of them are closely related to their fascinating photophysical and electrochemical properties.[5] In particular, Ir(III) cyclometalated complexes can be customized for producing the emission of specific colours in the visible range by simply changing the nature of both (C^N) and/or (N^N) ligands. With the aim to modify the relative positions of HOMO and LUMO energy levels, an extensive screening on chemical variations of the ligands has been done, outlining a series of synthetic guidelines that enable the modulation of the emission colours of the corresponding Ir(III) complexes[6a,b] The study of the emission properties and the reactivity of tetrazole and -tetrazolato based Ru(II),[7a-b] Re(I)[8a-c] and Ir(III) complexes was and currently is the main focus of our research activity, enabling us to establish a series of structure-properties (reactivity, emission and redox behaviour) relationships that, in the case of Ir(III) complexes, are closely related to the nature of the tetrazole ligand used (*i.e*. their influence on the composition of the LUMO energy level)[9] and on the net charge of the complex (neutral, cationic or anionic). [8a], [10a-c] Relative to all the Ir(III) complexes we reported so far, in which the set of the cyclometalating ligands (C^N) was invariably constituted by a phenylpyridinato anion (PPy^-) or its fluorinated analogue (F_2-PPy^-), chemical modifications (both permanent and reversible) performed onto the tetrazolato ligand (N^N) did result in the redshift of the emission profiles, with an extent strictly correlated to the nature of the 5-aryl substituent of the tetrazolato ring.[9,10a-c] In this work, we wanted to further investigate the emission properties of a new class of Ir(III) tetrazole-based cyclometalates by altering the nature of the (C^N) ligands, more specifically by introducing an EWG such as the cyano group (-CN) on the

pyridine ring of the cyclometalated ligand, where usually the LUMO level is mainly localized.[5, 6a] To this extent, herein we report the synthesis, the spectroscopic and electrochemical characterization of a new family of **[Ir(PPy-CN)$_2$(N^N)]** and **[Ir(F$_2$-PPy-CN)$_2$(N^N)]**-type complexes, in which (C^N) is 2-phenylisonicotinonitrile (PPy-CN) or 2-(2,4-difluorophenyl)isonicotinonitrile (F$_2$-PPy-CN), while (N^N) represent a 2-pyridyl tetrazolato **(PTZ$^-$)**, its -CF$_3$ substituted analogue **(F$_3$C-PTZ$^-$)** or the 2-pyrazinyl based derivative **(PYZ$^-$)**. By exploiting the peculiar and straightforward reactivity through electrophiles displayed by the coordinated pentatomic ring, we have prepared the corresponding **[Ir(PPy-CN)$_2$(N^N)]$^+$** and **[Ir(F$_2$-PPy-CN)$_2$(N^N)]$^+$** cationic complexes, exhibiting unexpected photophysical behaviour in respect of those previously observed. Furthermore, the neutral **[Ir(F$_2$-PPy-CN)$_2$(PTZ)]** was explored as emissive phosphorescent material in the fabrication of an organic light-emitting diode.

2.3 Results and Discussion

The introduction of one cyano group (-CN) on the cyclometalating ligands was accomplished by performing a standard Suzuki-Miyaura coupling between 4-cyano 2-bromo pyridine and the appropriate boronic acid, represented in turn phenylboronic acid or 2,4 difluorophenyl boronic acid.[11] Then, the formation of the dichlorobridged Ir(III) dimer precursors, namely **[Ir(PPy-CN)$_2$Cl]$_2$** and **[Ir(F$_2$-PPy-CN)$_2$Cl]$_2$**, was achieved by the well-established procedure reported by Nonoyama and coworkers.[12] Light modifications to this latter protocol were introduced for the synthesis of **[Ir(F$_2$-PPy-CN)$_2$Cl]$_2$**, whose preparation required longer reaction time (48 h) and pure ethoxyethanol as the solvent (**Scheme 1.2**).

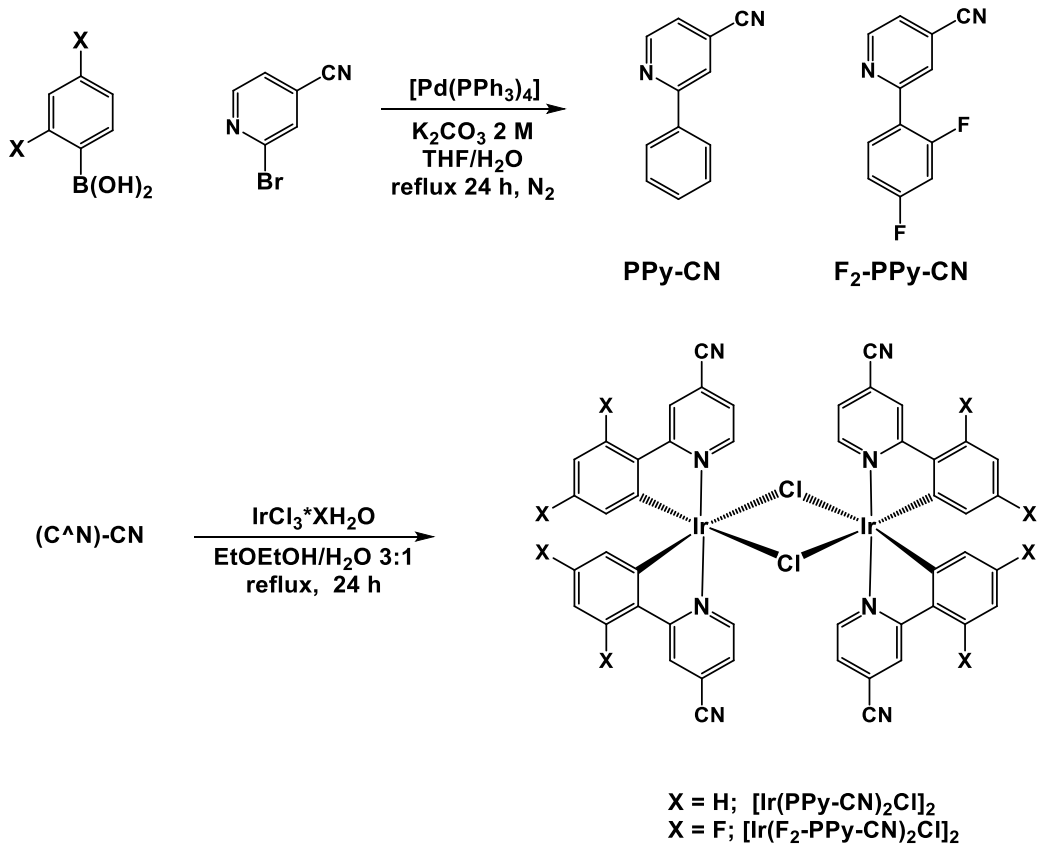

Scheme 1.2. Synthesis of the C^N ligands and of the Ir(III) dimers [Ir(PPy-CN)$_2$Cl]$_2$ and [Ir(F$_2$-PPy-CN)$_2$Cl]$_2$.

In a successive stage, the heteroleptic neutral Ir(III) complexes were obtained under mild conditions by reaction of the Ir(III) precursors with a slight excess of the appropriate tetrazole ligand (**Scheme 2.2**).[9] In all cases, purification was accomplished through column chromatography on neutral Al_2O_3. The identity of each compound was at first confirmed by ESI-Mass Spectrometry. The successive NMR (^1H, ^{13}C) characterization provided results in complete agreement with our past studies about structurally similar Ru(II) and Ir(III) tetrazolato and tetrazole based complexes,[7a-b, 8a, 9] highlighting the formation of the expected tris-chelate Ir(III) complexes with C_1 symmetry. The tetrazolate ligands employed, coordinate the metal centre through the N-1 position of the pentatomic ring, as suggested by the observation of the tetrazolic carbon (C_t) resonating in all cases between 162 and 165 ppm.

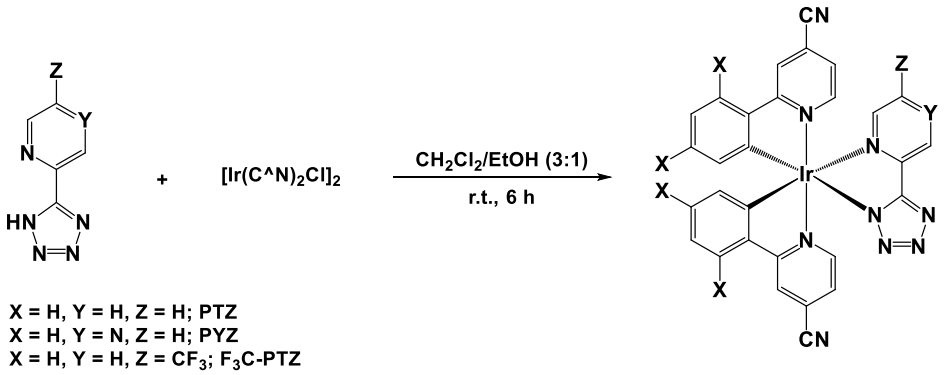

Scheme 2.2. Synthesis of the neutral Ir(III) complexes reported in this work.

Each neutral Ir(III)-tetrazolate complex was converted into the corresponding methylated cationic Ir(III)–tetrazole analogue by reaction with a slight excess of methyl triflate (**Scheme 3.2**). All the methylated complexes displayed one single C_t resonance, that appeared downfield (δC_t = *ca.* 166-168 ppm) to that observed for their neutral precursors. As we demonstrated earlier, this effect is congruent with the regioselective addition of the methyl group to the less sterically demanding N-3 position of the Ir(III)-coordinated tetrazolate ring.[9]

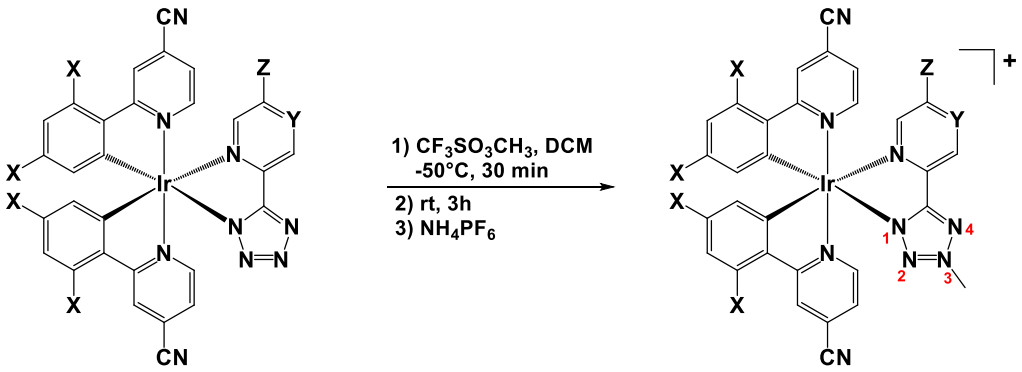

X = H, Y = H, Z = H; [Ir(PPy-CN)$_2$(PTZ)]
X = H, Y = N, Z = H; [Ir(PPy-CN)$_2$(PYZ)]
X = H, Y = H, Z = CF_3; [Ir(PPy-CN)$_2$(F_3C-PTZ)]
X = F, Y = H, Z = H; [Ir(F_2-PPy-CN)$_2$(PTZ)]
X = F, Y = N, Z = H; [Ir(F_2-PPy-CN)$_2$(PYZ)]
X = F, Y = H, Z = CF_3; [Ir(F_2-PPy-CN)$_2$(F_3C-CPTZ)]

X = H, Y = H, Z = H; [Ir(PPy-CN)$_2$(PTZ-Me)]$^+$
X = H, Y = N, Z = H; [Ir(PPy-CN)$_2$(PYZ-Me)]$^+$
X = H, Y = H, Z = CF_3; [Ir(PPy-CN)$_2$(F_3C-PTZ-Me)]$^+$
X = F, Y = H, Z = H; [Ir(F_2-PPy-CN)$_2$(PTZ-Me)]$^+$
X = F, Y = N, Z = H; [Ir(F_2-PPy-CN)$_2$(PYZ-Me)]$^+$
X = F, Y = H, Z = CF_3; [Ir(F_2-PPy-CN)$_2$(F_3C-PTZ-Me)]$^+$

Scheme 3.2. Methylation reaction of Ir(III) compounds with relative acronyms and numeration of the tetrazolato ring used in this work.

2.3.1 *X-ray crystallography*

The evidence deduced from $^{1}H/^{13}C$ NMR experiments were further confirmed from the X-ray diffraction of **[Ir(PPy-CN)$_2$(F$_3$C-PTZ)]**. The molecular structure of **[Ir(PPy-CN)$_2$(F$_3$C-PTZ)]** (**Figure 1.2**) is similar to that of previously reported [Ir(C^N)$_2$(N^N)] complexes,[9] containing a distorted octahedral Ir(III) centre with *cis*-metallated carbons and *trans*-phenylpyridine nitrogen atoms. The Ir-N (N^N) distances (2.108(14) and 2.169(16) Å) are longer than Ir-N (C^N) (2.022(17) and 2.028(18) Å) because of the trans influence of the cyclometalated carbon atoms. The F$_3$C-PTZ ligand is almost coplanar (mean deviation from the least square plane 0.0601 Å).

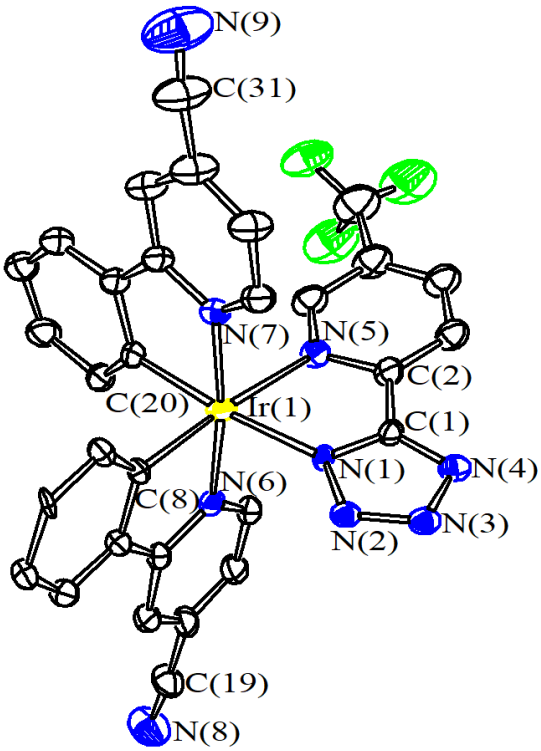

Figure 1.2. Molecular structure of **[Ir(PPy-CN)$_2$(F$_3$C-PTZ)]** with key atoms labelled. H-atoms have been omitted for clarity. Displacement ellipsoids are at the 30% probability level.

2.3.2 *Photophysical properties*

The absorption spectra of all the neutral and cationic Ir(III) species were obtained from the corresponding diluted (10^{-5} M) CH_3CN solutions at room temperature and the collected data are reported in **Table 1.2**.

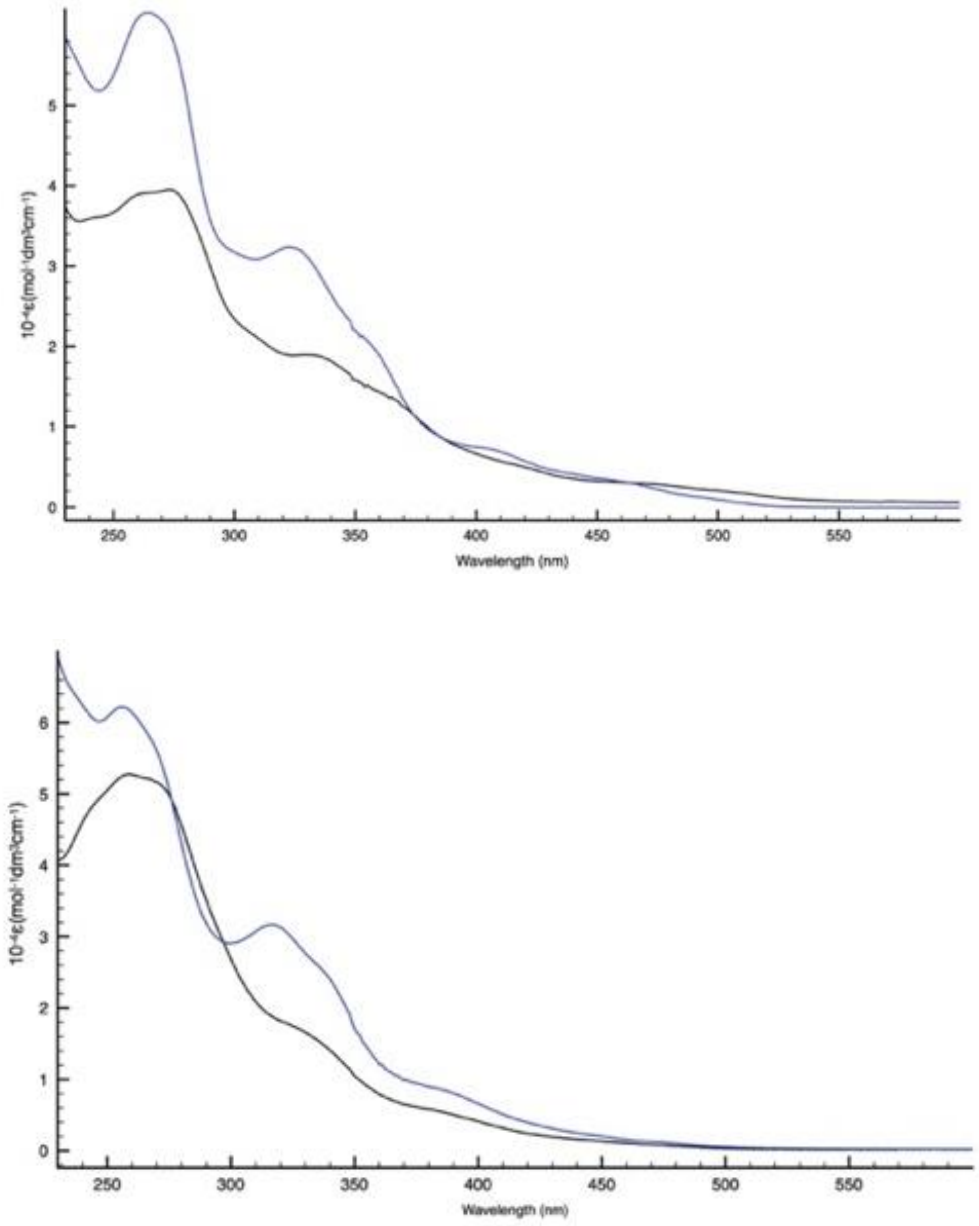

Figure 2.2. Absorption profiles of (Top) **[Ir(PPy-CN)$_2$(PTZ)]** (black line) and **[Ir(PPy-CN)$_2$(PTZ-Me)]$^+$** (blue line); (Bottom) **[Ir(PPy-CN)$_2$(PYZ)]** (black line) and **[Ir(PPy-CN)$_2$(PYZ-Me)]$^+$** (blue line), 10^{-5}M, CH_3CN, 298K.

In all cases, the absorption profile consists of intense ^{1}LC transitions in the UV region (250 - 340 nm) followed by weaker ^{1}MLCT processes at lower energies (380 - 410 nm, **Figure 2.2**). The hypsochromic shift of ^{1}MLCT transitions s observed on passing from neutral to cationic species can be confidently assigned to the introduction of a methyl group to the pentatomic ring, and therefore the saline nature of the latter one (**Figure 2.2**).

Upon excitation of the corresponding dilute CH_3CN solutions, all neutral Ir(III) complexes displayed bright luminescence, with typical ^{3}MLCT-shaped broad and structureless profiles centred in the region between 520 and 590 nm,[5] depending on the nature of both cyclometalating and tetrazolato ligands. In all cases, the triplet character of the excited states was confirmed by the oxygen sensitivity of both quantum yield (Φ) and lifetime values (τ, **Table 1.2**). In contrast with previously reported (PPy)-based complexes,[9] the new Ir(III) complexes described herein appears markedly different along the series where **PTZ$^-$** and **PYZ$^-$** are combined with **(PPy-CN)** and **(F_2-PPy-CN)** as cyclometalated ligands. The use of a more electron-withdrawing substituent at the tetrazole moiety, such as the pyrazine ring, resulted in a blue shift of the emission maxima (Figure 3). Indeed, the resulting emission profiles are centred at 590 and 582 nm for **[Ir(PPy-CN)$_2$(PTZ)]** and **[Ir(PPy-CN)$_2$(PYZ)]**, respectively. The introduction of one trifluoromethyl substituent (-CF_3) on the backbone of the 5-aryltetrazole ligand (**F_3C-PTZ**) led to shift the emission maxima of the corresponding **[Ir(PPy-CN)$_2$(F_3C-PTZ)]** (λ_{max} = 584 nm) in between **[Ir(PPy-CN)$_2$(PYZ)]** and **[Ir(PPy-CN)$_2$(PTZ)]**. A similar trend was observed also for the fluorinated derivatives **[Ir(F2-PPy-CN)$_2$(PTZ)]** (λ_{max} = 540 nm, **Table 1.2**, **Figure 3.2**), **[Ir(F_2-PPy-CN)$_2$(PYZ)]** (λ_{max} = 532 nm, **Table 1.2**, **Figure 3.2**) and **[Ir(F_2-PPy-CN)$_2$(F_3C-PTZ)]** (λ_{max} = 536 nm, **Table 1.2**, **Figure 3.2**). The analyses of the emission spectrum at 77K evidenced, in some cases, the occurrence of structured profiles that might account for the interplay of ^{3}LC/^{3}MLCT type emissive excited states (**Table 1.2**).[5]

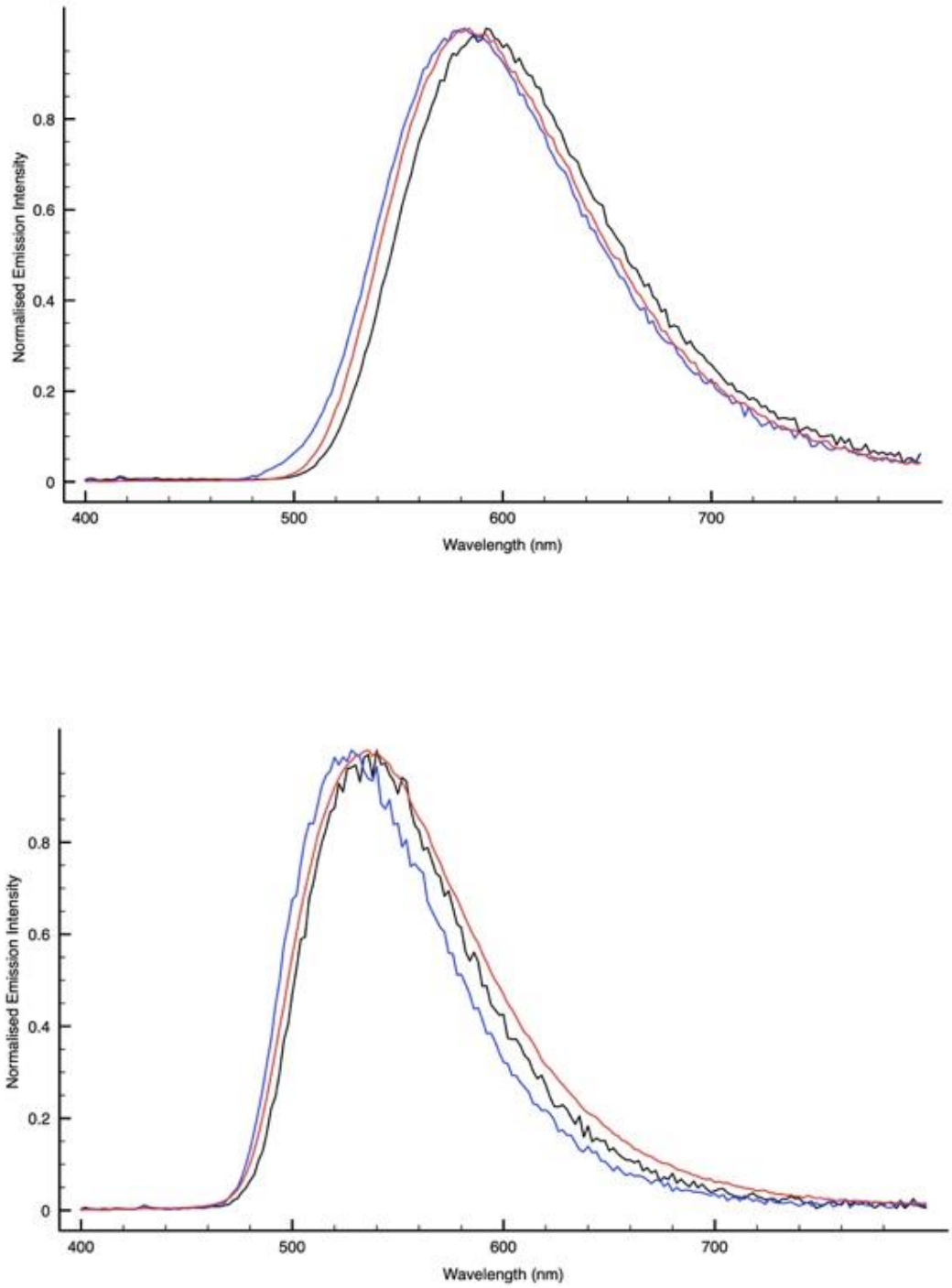

Figure 3.2. (Top) Normalized emission profiles of **[Ir(PPy-CN)$_2$(PTZ)]** (black line), **[Ir(PPy-CN)$_2$(PYZ)]** (blue line) and **[Ir(PPy-CN)$_2$(F$_3$C-PTZ)]** (red line); (Bottom) **[Ir(F$_2$-PPy-CN)$_2$(PTZ)]** (black line), **[Ir(F$_2$-PPy-CN)$_2$(PYZ)]** (blue line) and **[Ir(F$_2$-PPy-CN)$_2$(F$_3$C-PTZ)]** (red line), 10^{-5} M CH_3CN, 298K.

Table 1.2. Photophysical data for neutral and cationic Ir(III) species reported in this work

Complex	Absorption	Emission 298 K[a, b]					Emission 77 K[c]	
CH_3CN as the solvent	λ(nm) $10^{-4}\varepsilon$ ($cm^{-1}M^{-1}$)	λ_{em} (nm)	τ_{ox} (μs)	τ_{deox} (μs)	ϕ_{ox} (%)	ϕ_{deox} (%)	λ_{em} (nm)	τ (μs)
[Ir(PPy-CN)$_2$(PYZ)]	266 (3.83), 330 (2.09), 410 (0.53)	582	0.08	0.96	2.1	23.0	532	3.30
[Ir(PPy-CN)$_2$(PTZ)]	269 (3.94), 338 (1.84), 411 (0.54)	590	0.08	1.02	1.8	26.0	550	4.45
[Ir(PPy-CN)$_2$(F$_3$C-PTZ)]	263 (3.14), 329 (1.61), 418 (0.42)	584	0.07	0.74	2.2	12.2	542	5.57
[Ir(PPy-CN)$_2$(PYZ-Me)]$^+$	270 (6.58), 323 (3.22), 402 (0.98)	614	0.08	0.43	1.0	7.13	548	3.51
[Ir(PPy-CN)$_2$(PTZ-Me)]$^+$	265 (6.18), 323 (3.30), 405 (0.70)	566	0.09	1.22	2.0	25.0	522	2.74
[Ir(PPy-CN)$_2$(F$_3$C-PTZ-Me)]$^+$	267 (2.39), 319 (1.00), 398 (0.24)	568	0.08	0.72	2.6	12.1	540	3.29
[Ir(F$_2$-PPy-CN)$_2$(PYZ)]	255 (4.64), 321 (2.81), 385 (0.81)	532	0.18	1.06	6.2	16.0	490, 518	2.40
[Ir(F$_2$-PPy-CN)$_2$(PTZ)]	262 (5.27), 330 (1.76), 382 (0.58)	540	0.12	1.4	5.0	21.0	524	4.20
[Ir(F$_2$-PPy-CN)$_2$(F$_3$C-PTZ)]	259 (5.25), 322 (2.51), 392 (0.64)	536	0.18	1.26	4.3	44.7	522	4.30
[Ir(F$_2$-PPy-CN)$_2$(PYZ-Me)]$^+$	261 (5.40), 313 (2.99), 383 (0.79)	530	0.28	1.15	8.0	31.0	490, 520	2.48
[Ir(F$_2$-PPy-CN)$_2$(PTZ-Me)]$^+$	258 (6.14), 315 (3.14), 386 (0.94)	520	0.23	1.5	6.0	30.0	482, 514	2.34
[Ir(F$_2$-PPy-CN)$_2$(F$_3$C-PTZ-Me)]$^+$	257 (3.53), 315 (1.79), 391 (0.56)	520	0.22	1.00	5.0	28.1	554	3.32

[a]: "Air" means air equilibrated solutions, "Ar" means deoxygenated solutions under argon atmosphere;[b]: $[Ru(bpy)_3][Cl]_2/H_2O$ was used as a reference for quantum yield determinations (Φ_r = 0.028)[13]; [c]: in frozen CH_3CN.

The photophysical properties of the corresponding cationic derivatives are, in some cases, rather different from those observed earlier for similar tetrazole-based Ir cyclometalates. Indeed, the conversion of **[Ir(PPy-CN)$_2$(PTZ)]** into the positively charged **[Ir(PPy-CN)$_2$(PTZ-Me)]$^+$** was accompanied by a 24 nm blue shift of the emission maxima (from 590 to 566 nm, **Figure 4.2**) and a concomitant elongation of the of lifetime fitting decay (τ) of the phosphorescent emission (from 1 to 1.22 μs for the deoxygenated samples). The same shift through higher energies of the emission profile was observed when going from **[Ir(PPy-CN)$_2$(F$_3$C-PTZ)]** to **[Ir(PPy-CN)$_2$(F$_3$C-PTZa-Me)]$^+$** (from 584 to 568 nm, **Table 1.2**).

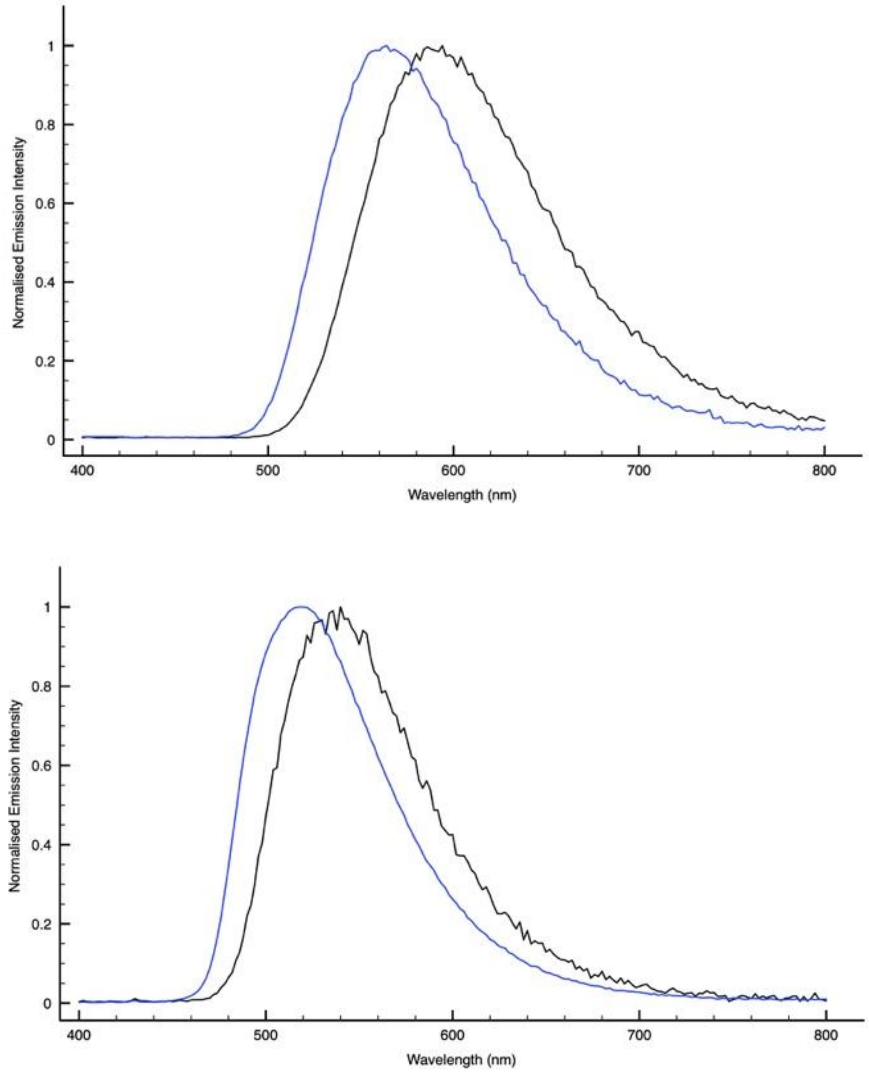

Figure 4.2. Normalised emission profiles of (Top) **[Ir(PPy-CN)$_2$(PTZ)]** (black line) and **[Ir(PPy-CN)$_2$(PTZ-Me)]$^+$** (blue line). (Bottom) **[Ir(F$_2$-PPy-CN)$_2$(PTZ)]** (black line) and **[Ir(F$_2$-PPy-CN)$_2$(PTZ-Me)]$^+$** (blue line); 10^{-5} M solution in CH_3CN.

A quite similar result is deduced when considering their fluorinated analogue **[Ir(F$_2$-PPy-CN)$_2$(PTZ-Me)]$^+$** and **[Ir(F$_2$-PPy-CN)$_2$(F$_3$C-PTZ-Me)]$^+$**, whose emission maxima are *ca.* 20 nm blue-shifted when compared to their neutral precursors. (**Table 1.2** and **Figure 3.2**) While keeping the fluorine-based Ir(III) dimer, the use of **PYZ$^-$** instead of **PTZ$^-$**, produced a similar but less pronounced blue-shift of the emission maxima on passing from **[Ir(F$_2$-PPy-CN)$_2$(PYZ)]** to its cationic analogue **[Ir(F$_2$-PPy-CN)$_2$(PYZ-Me)]$^+$** (from 532 to 530 nm, **Table 1.2** and **Figure 5.2)**.

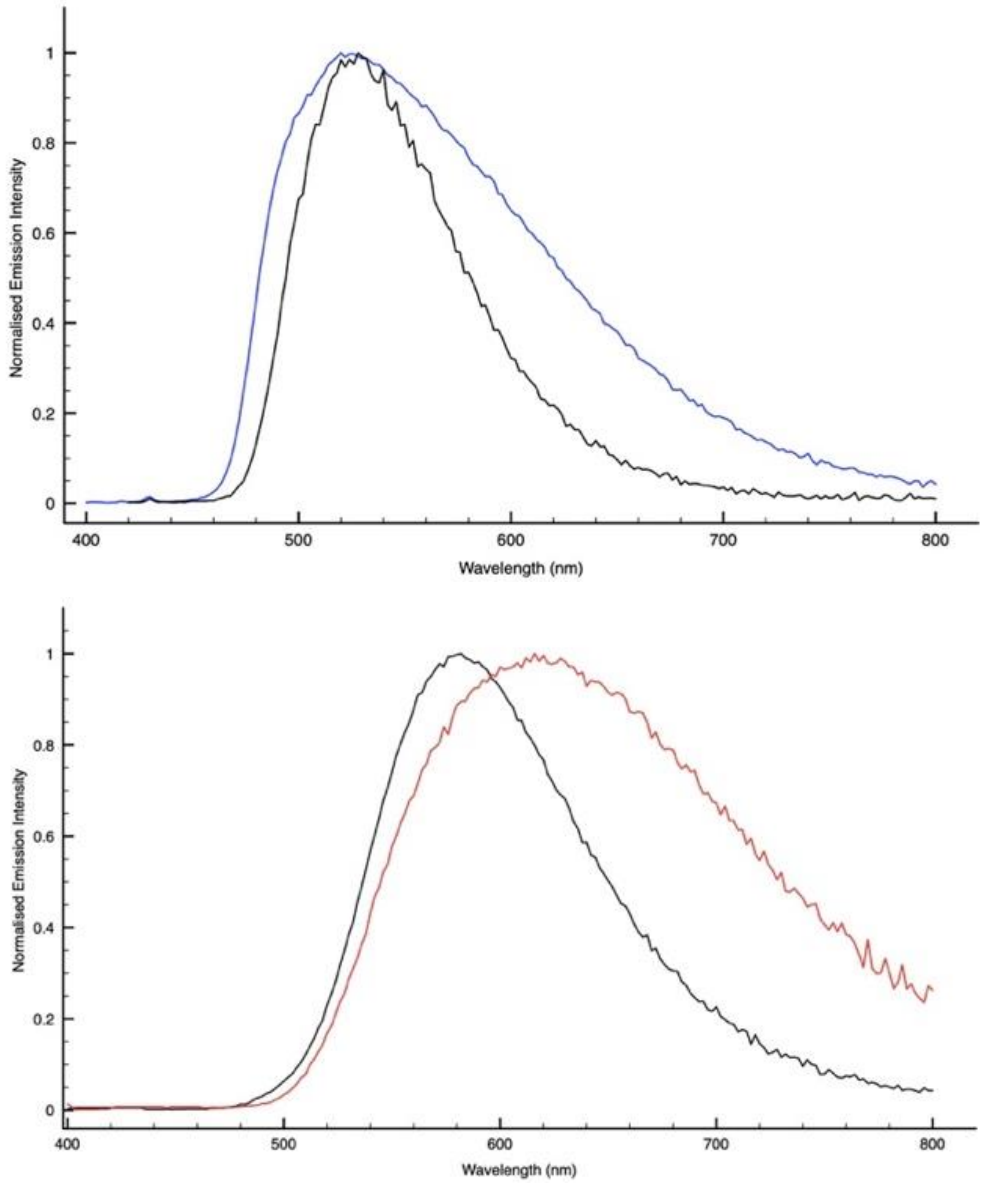

Figure 5.2. Normalised emission profiles of (Top) **[Ir(F$_2$-PPy-CN)$_2$(PYZ)]** (black line) and **[Ir(F$_2$-PPy-CN)$_2$(PYZ-Me)]$^+$** (blue line). (Bottom) **[Ir(PPy-CN)$_2$(PYZ)]** (black line) and **[Ir(PPy-CN)$_2$(PYZ-Me)]$^+$** (red line); 10^{-5} M solution in CH_3CN.

Conversely, the methylation of the **PYZ$^-$**-based derivative **[Ir(PPy-CN)$_2$(PYZ)]** (λ_{max} = 582 nm, **Figure 5.2**) produced a broadening of the emission profile, with a redshift of the emission maxima to 614 nm for **[Ir(PPy-CN)$_2$(PYZ-Me)]$^+$** (**Figure 5.2**), which was also accompanied by the reduction of quantum yield (Φ) and the concomitant shortening of the lifetime decays (**Table 1.2**).[5]

2.3.3 *Cyclic voltammetry*

The electrochemical behaviour of all the neutral and cationic Ir(III) species was investigated in CH_3CN solution by cyclic voltammetry (**Table 2.2**).

Table 2.2. Half-Wave ($E_{1/2}$) Redox Potentials[a] (vs SCE) of neutral and cationic Ir(III) species at 25 °C, CH_3CN.

Complex	Ox	Red		HOMO[c] exp	LUMO[c] exp	GAP[c] exp	HOMO[d] calc	LUMO[d] calc	GAP[d] calc
	$E_{1/2}$ (V)	$E_{1/2}$ (V)		(eV)	(eV)	(eV)	(eV)	(eV)	(eV)
[Ir(PPy-CN)$_2$(PYZ)]	+1.37[b]	-1.34	-1.52	-5.77	-3.06	2.71	-5.92	-2.94	2.98
[Ir(PPy-CN)$_2$(PTZ)]	+1.43[b]	-1.34	-1.55	-5.83	-3.05	2.78	-5.85	-2.90	2.95
[Ir(PPy-CN)$_2$(F$_3$C-PTZ)]	+1.50[b]	-1.26	-1.46[b] -1.80[b]	-5.90	-3.14	2.76	-5.90	-2.93	2.97
[Ir(PPy-CN)$_2$(PYZ-Me)]$^+$	+1.49[b]	-1.04	-1.42 -1.62	-5.89	-3.36	2.53	-6.17	-3.27	2.90
[Ir(PPy-CN)$_2$(PTZ-Me)]$^+$	+1.60[b]	-1.28	-1.47	-6.01	-3.12	2.89	-6.10	-3.04	3.07
[Ir(PPy-CN)$_2$(F$_3$C-PTZ-Me)]$^+$	+1.59[b]	-1.16	-1.45[b] -1.67[b]	-5.99	-3.24	2.75	-6.16	-3.22	2.94
[Ir(F$_2$-PPy-CN)$_2$(PYZ)]	+1.36[b]	-1.25	-1.44	-5.76	-3.15	2.61	-6.31	-3.05	3.28
[Ir(F$_2$-PPy-CN)$_2$(PTZ)]	+1.36[b]	-1.27	-1.47	-5.76	-3.13	2.63	-6.25	-3.00	3.24
[Ir(F$_2$-PPy-CN)$_2$(F$_3$C-PTZ)]	+1.50[b]	-1.24	-1.43	-5.90	-3.16	2.74	-6.29	-3.03	3.27
[Ir(F$_2$-PPy-CN)$_2$(PYZ-Me)]$^+$	+1.47[b]	-1.04	-1.37[b] -1.55[b]	-5.87	-3.36	2.51	-6.58	-2.98	3.60
[Ir(F$_2$-PPy-CN)$_2$(PTZ-Me)]$^+$	+1.85[b]	-1.26[b]	-1.57[b]	-6.25	-3.14	3.11	-6.51	-2.89	3.62
[Ir(F$_2$-PPy-CN)$_2$(F$_3$C-PTZ-Me)]$^+$	+1.48[b]	-1.07	-1.36[b] -1.53[b]	-5.88	-3.33	2.55	-6.56	-3.16	3.39

a) In a 0.1 M $TBAPF_6/CH_3CN$ solution. b) Irreversible process. c) calculated with $E_{HOMO} = -(E_{ox} + 4.4eV)$ and $E_{LUMO} = -(E_{red} + 4.4eV)$.[14] d) see DFT section for further details.

All the neutral Ir(III) species displayed one irreversible process in the region of positive potentials, which is commonly ascribed to the formal oxidation of Ir(III) to Ir(IV). Along the series represented by **[Ir(PPy-CN)$_2$(PYZ)]**, **[Ir(PPy-CN)$_2$(PTZ)]** and **[Ir(PPy-CN)$_2$(F$_3$C-PTZ)]**, this process gradually shifts towards more positive potentials. (**Table 2.2**) Concerning the region of negative potentials, the first reductive processes were observed at the same value for **[Ir(PPy-CN)$_2$(PYZ)]** and **[Ir(PPy-CN)$_2$(PTZ)]** (-1.34 V, **Figure 6.2** and **8.2**, **Table 2.2**), while for **[Ir(PPy-CN)$_2$(F$_3$C-PTZ)]** the first reduction was found at –1.26 V. (**Table 2.2**) Taken together, these data suggested the first reduction process as likely being centred to the cyclometalated ligands. Considering instead the cationic analogues **[Ir(PPy-CN)$_2$(PTZ-Me)]$^+$**, **[Ir(PPy-CN)$_2$(PYZ-Me)]$^+$** and **[Ir(PPy-CN)$_2$(F$_3$C-PTZ-Me)]$^+$**, a shift of the oxidation processes to more positive values was observed (**Table 2.2**), with an extent of 170 mV, 120 mV and 90 mV, respectively. Such differences are probably brought on by charge variations of the complexes rather than changes in the composition of the HOMO level, which still relies on the Ir-phenyl portion. (See DFT section for further discussions)

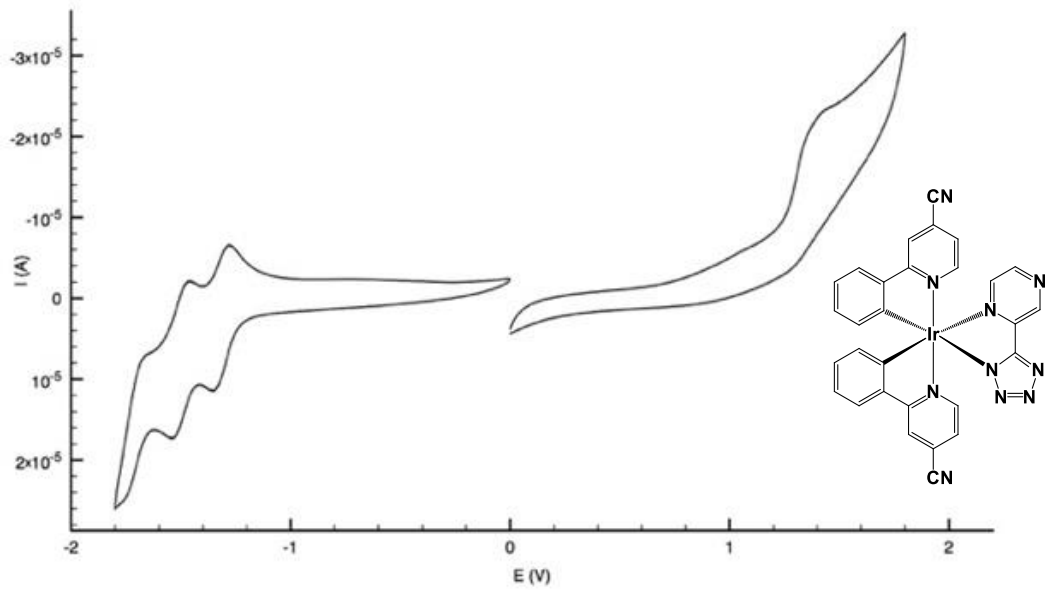

Figure 6.2. CV curves of 10^{-3}M samples of complexes **[Ir(PPy-CN)$_2$(PYZ)]** in a 0.1 M $TBAPF_6$/ CH_3CN solution; working electrode Pt disk; 25 °C; scan rate 0.1 V/s.

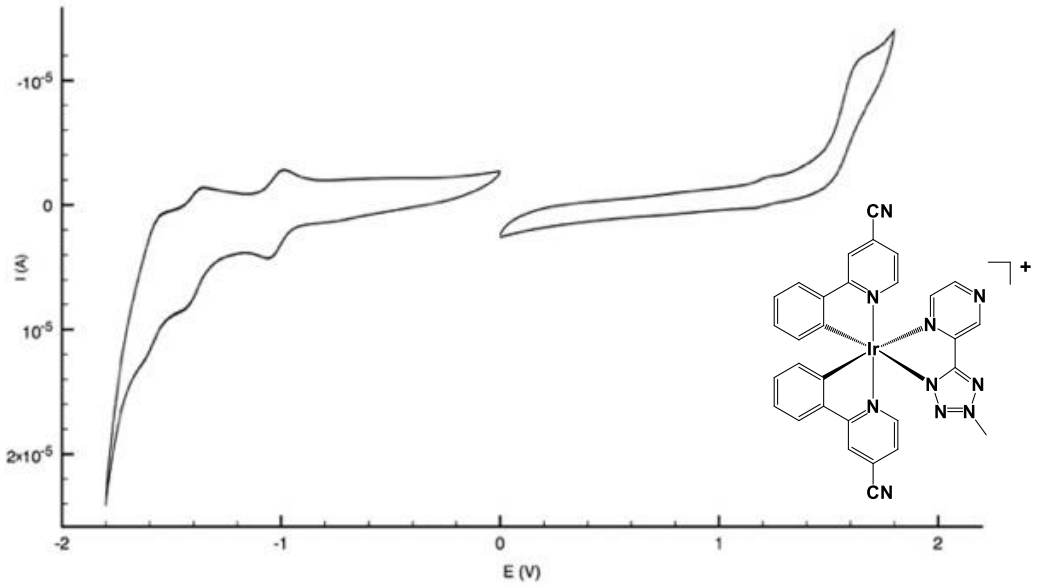

Figure 7.2. CV curves of 10^{-3}M samples of complex **[Ir(PPy-CN)$_2$(PYZ-Me)]$^+$** in a 0.1 M $TBAPF_6$/ CH_3CN solution; working electrode Pt disk; 25 °C; scan rate 0.1 V/s.

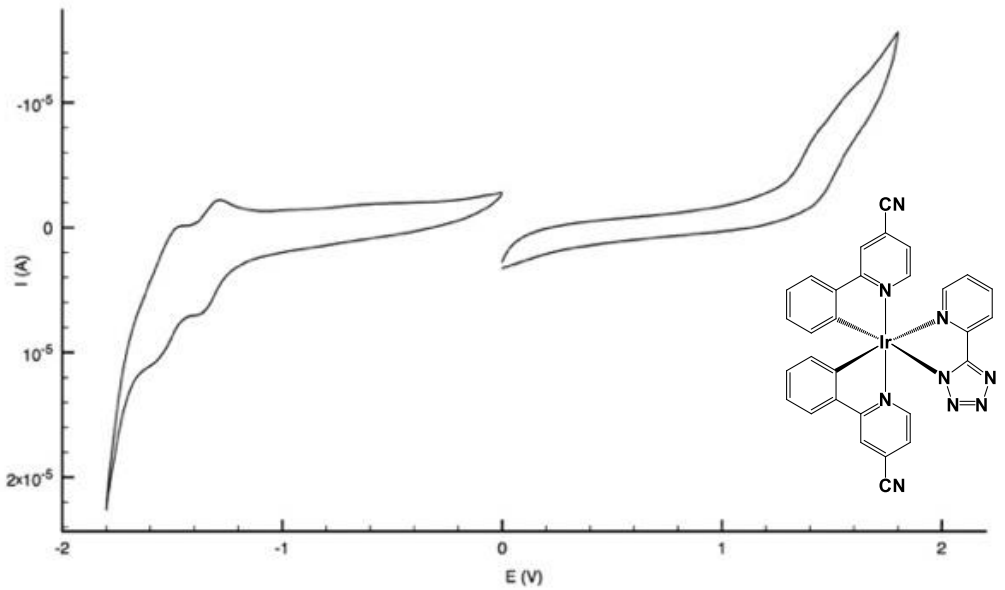

Figure 8.2. CV curves of 10^{-3}M samples of complex **[Ir(PPy-CN)$_2$(PTZ)]** in a 0.1 M $TBAPF_6$/ CH_3CN solution; working electrode Pt disk; 25 °C; scan rate 0.1 V/s.

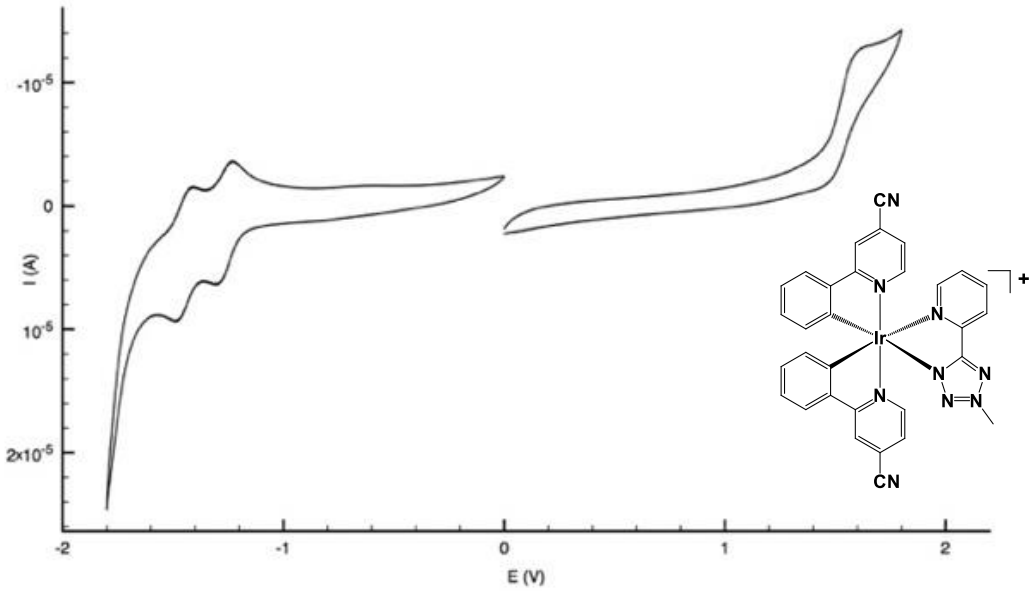

Figure 9.2. CV curves of 10^{-3}M samples of complex **[Ir(PPy-CN)$_2$(PTZ-Me)]$^+$** in a 0.1 M $TBAPF_6$/ CH_3CN solution; working electrode Pt disk; 25 °C; scan rate 0.1 V/s.

The reduction processes of these latter complexes displayed significant changes beyond their neutral counterparts. Indeed, the first reduction of **[Ir(PPy-CN)$_2$(F$_3$C-PTZ-Me)]$^+$** consisted of a process which falls at -1.16 V, a 290 mV displacement through less negative potentials in respect of its neutral precursor. The same trend was observed for the first reduction of **[Ir(PPy-CN)$_2$(PYZ-Me)]$^+$**, which falls at -1.04 V. Concerning **[Ir(PPy-CN)$_2$(PTZ-Me)]$^+$**, the first reduction undergoes a 60 mV positive displacement compared to its neutral analogue, more specifically at -1.28 V. The correlation of these electrochemical data with the observed emission properties, highlights the different impact exerted by tetrazolato or tetrazole ligands in the composition of the LUMO level. In the case of **[Ir(PPy-CN)$_2$(PTZ)]**, the addition of a methyl group produced a shift through higher energies of the emission profile (λ_{max} = 566 nm for **[Ir(PPy-CN)$_2$(PTZ-Me)]$^+$**), attributable to the greater stabilization of the HOMO level rather than the lowest one (**Figure 10.2**). On the other hand, the conversion of **[Ir(PPy-CN)$_2$(PYZ)]** into **[Ir(PPy-CN)$_2$(PYZ-Me)]$^+$** resulted in the previously observed red-shift of the emission maxima (582 to 614 nm) that was rationalized with the preponderant stabilization of the

LUMO level (**Figure 10.2**).[9] The only exception is represented by **[Ir(PPy-CN)$_2$(F$_3$C-PTZ-Me)]$^+$**, in which both HOMO and LUMO levels settles down in energy with the same extent, resulting in a 16 nm (λ_{max} = 568 nm) blueshift emission maximum when compared to **[Ir(PPy-CN)$_2$(F$_3$C-PTZ)]**.

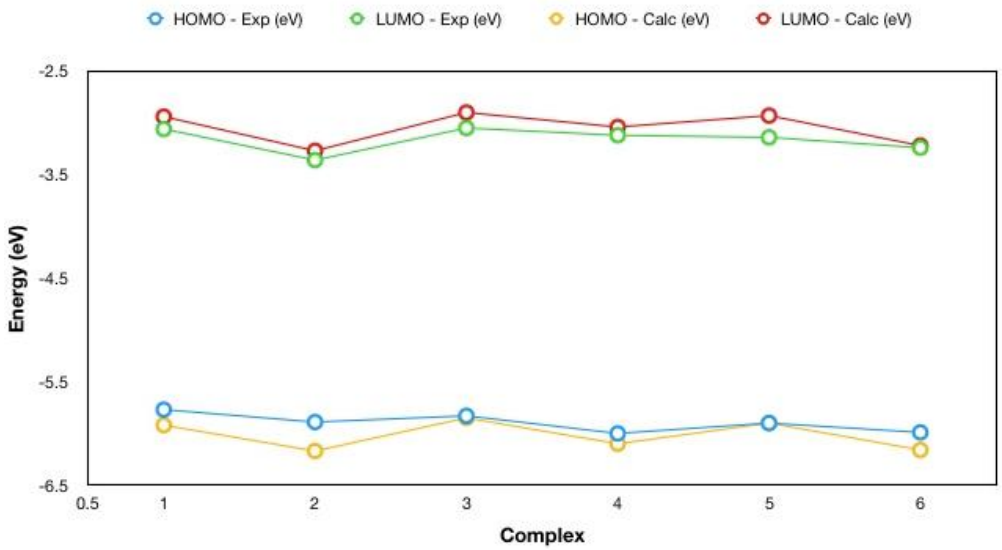

Figure 10.2. Trend of HOMO-LUMO gap for 1) **[Ir(PPy-CN)$_2$(PYZ)]**, 2) **[Ir(F$_2$-PPy-CN)$_2$(PYZ-Me)]$^+$**, 3) **[Ir(PPy-CN)$_2$(PTZ)],** 4) **[Ir(PPy-CN)$_2$(PTZ-Me)]$^+$**, 5) **[Ir(PPy-CN)$_2$(F$_3$C-PTZ)],** 6) **[Ir(PPy-CN)$_2$(F$_3$C-PTZ-Me)]$^+$**.

The replacement of **(PPy-CN)** with the fluorinated **(F$_2$-PPy-CN)** did not substantially shift the potential value at which the oxidation of the neutral Ir(III) compound occurred (**Table 2.2**), but instead had an impact on their first reduction. For **[Ir(F$_2$-PPy-CN)$_2$(PYZ)]** and **[Ir(F$_2$-PPy-CN)$_2$(PTZ)]**, a positive offset of *ca.* 90 mV placed their first reduction at -1.25 and -1.27 V, while for **[Ir(F$_2$-PPy-CN)$_2$(F$_3$C-PTZ)]** this value remains almost unchanged. In its entirety, these findings suggest that for all the neutral Ir(III) compounds discussed so far, both HOMO and LUMO levels are mainly ruled by the nature of the C^N ligands. (**Figure 11.2**)

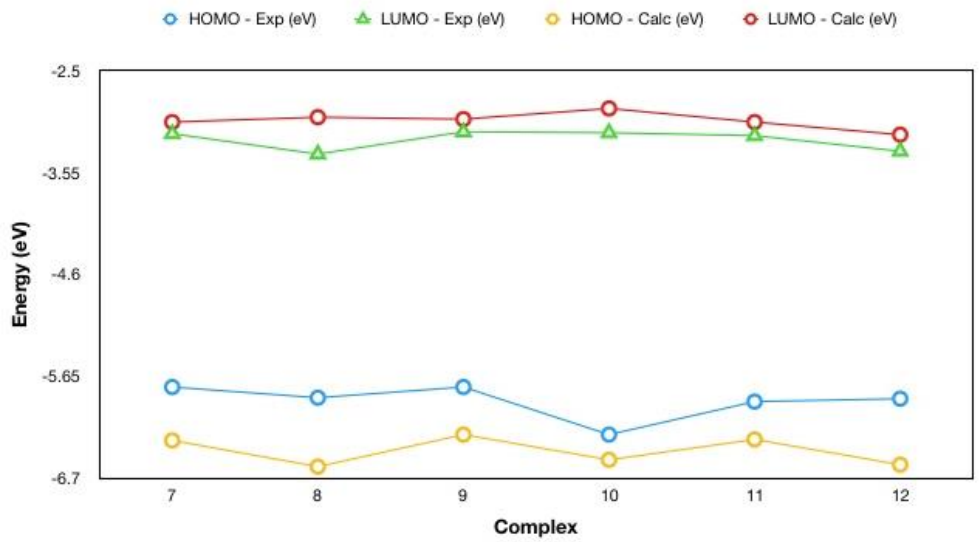

Figure 11.2. Trend of HOMO-LUMO gap for 7) **[Ir(F_2-PPy-CN)$_2$(PYZ)]**, 8) **[Ir(F2-PPy-CN)$_2$(PYZ-Me)]$^+$**, 9) **[Ir(F_2-PPy-CN)$_2$(PTZ)],** 10) **[Ir(F_2-PPy-CN)$_2$(PTZ-Me)]$^+$**, 11) **[Ir(F_2-PPy-CN)$_2$(F_3C-PTZ)],** 12) **[Ir(F_2-PPy-CN)$_2$(F_3C-PTZ-Me)]$^+$**.

The conversion of the Ir(III) -fluorinated complexes into their cationic analogues is accompanied with the expected raise of their oxidation potentials toward more positive values, with the sole exception represented by **[Ir(F_2-PPy-CN)$_2$(F_3C-PTZ-Me)]$^+$**, whose value is roughly identical to that observed from **[Ir(F_2-PPy-CN)$_2$(F_3C-PTZ)]**. Concerning the reductions, for **[Ir(F_2-PPy-CN)$_2$(PYZ-Me)]$^+$** and **[Ir(F_2-PPy-CN)$_2$(F_3C-PTZ-Me)]$^+$**, an appreciable shift toward less negative values is observed. On the contrary, the reduction potential of **[Ir(F_2-PPy-CN)$_2$(PTZ-Me)]$^+$** is almost equivalent to that of **[Ir(F_2-PPy-CN)$_2$(PTZ)]** (**Table 2.2**), resulting in LUMOs with comparable energies. In this case, the remarkable stabilization of the HOMO level might explain the 20 nm blue shift of the emission maxima experienced by **[Ir(F_2-PPy-CN)$_2$(PTZ-Me)]$^+$** (**Table 1.2** and **2.2**).

2.3.4 *DFT calculations*

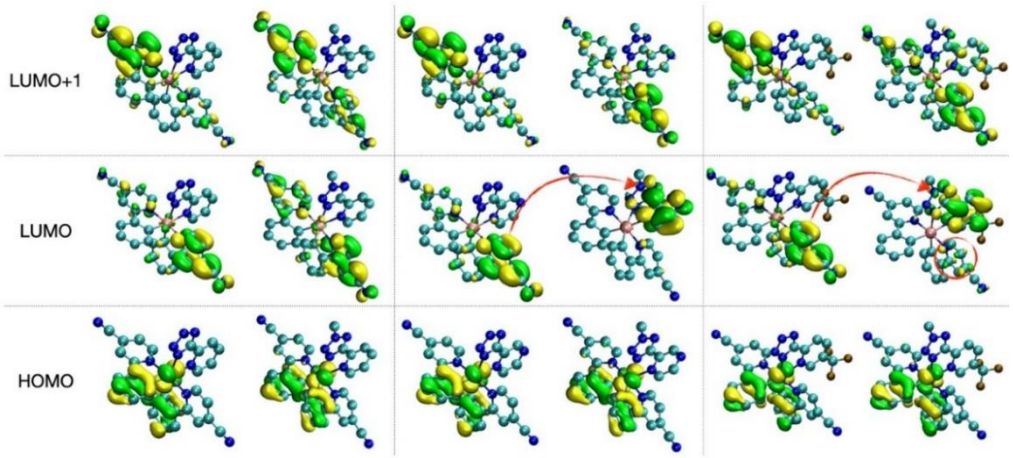

Figure 12.2. Contour HOMO-LUMO for all the neutral and cationic fluorine-free Ir(III) complexes presented in this work; from left to right: **[Ir(PPy-CN)$_2$(PTZ)]**, **[Ir(PPy-CN)$_2$(PTZ-Me)]$^+$**, **[Ir(PPy-CN)$_2$(PYZ)]**, **[Ir(PPy-CN)$_2$(PYZ-Me)]$^+$**, **[Ir(PPy-CN)$_2$(F$_3$C-PTZ)]**, **[Ir(PPy-CN)$_2$(F$_3$C-PTZ-Me)]$^+$** (See ESI and Experimental section for more details on DFT calculations).

To corroborate the experimental findings, DFT calculations were performed to compute the HOMO-LUMO gaps. Unlike photochemical experiments, where the electronic transitions can be assumed to be instantaneous *i.e.* the nuclei do not have time to relax, in the electrochemical experiments the oxidized and reduced molecules have ample time to undergo configurational rearrangements. Hence, we designed our computational experiments to mimic this process. One electron was added or removed for all neutral and cationic Ir(III) complexes and their geometry was allowed to fully relax. The self-consistent reaction field method was also used to partially include solvent effects. The electron affinity and ionization energies of the complexes were then used to compute the values of the HOMO-LUMO gap reported in **Table 2.2** and the molecular orbitals shown in **Figure 12.2**. The preponderant HOMO-LUMO composition for **[Ir(PPy-CN)$_2$(PTZ)]**, and **[Ir(PPy-CN)$_2$(PTZ-Me)]$^+$** consist of (Ir-phenyl) and (pyridine-CN), respectively. As the **PTZ$^-$/PTZ-Me** moiety is not involved in any molecular orbital, the observed blue shift of the emission profile can be confidently assigned to the presence of an EWG in the cyclometalated backbone of the complexes.

On the other hand, the presence of the **PYZ$^-$/PYZ-Me** ring together with the same Ir(PPy-CN) -core, actually recall what was previously observed for Ir(III) -tetrazole based compounds.[9] While the HOMO is still located on the (Ir-phenyl) portion for both **[Ir(PPy-CN)$_2$(PYZ)]**, and **[Ir(PPy-CN)$_2$(PYZ-Me)]$^+$**, the LUMO level is composed by the (pyridine-CN) fragment for the neutral complex, and by **PYZ-Me** for the cationic one. The concomitant lowering of the pyrazine -based LUMO energy explain the observed redshift of the emission profile of **[Ir(PPy-CN)$_2$(PYZ-Me)]$^+$**, together with its being easier to reduce (-1.04 V, **Table 2.2**). With regards to **[Ir(PPy-CN)$_2$(F$_3$C-PTZ)]** and **[Ir(PPy-CN)$_2$(F$_3$C-PTZ-Me)]$^+$**, their HOMOs consist of the same (Ir-phenyl) portion as observed for the other examples. The LUMO level of **[Ir(PPy-CN)$_2$(F$_3$C-PTZ)]** has a preponderant (pyridine-CN) composition, while its cationic analogue is mainly composed by **F$_3$C-PTZ-Me** ligand, with a small contribution stemming from (pyridine-CN). This might account for the observed blue shift of the emission profile upon charge variation and for the observed electrochemical data (**Table 2.2**). These considerations can be extended also to the fluorinated derivatives, both neutral and cationic.

2.3.5 *OLED device with [Ir(F$_2$-PPy-CN)$_2$(PTZ)]*

The relatively high solubility of the selected Ir(III) complex **[Ir(F$_2$-PPy-CN)$_2$(PTZ)]** prompted us to study its application for the preparation of solution-processed OLEDs. This methodology is preferable due to its cost-effectiveness and in light of the recent insights about the inkjet print -OLED technology but, at the same time, it may suffer from several drawbacks that can limit the overall device efficiency.[15] The devices were fabricated by a combination of wet and dry processes (spin coating and sublimation in high vacuum) onto a pre-cleaned indium tin oxide (ITO) glass substrate (see Experimental Section). Holes were injected from the ITO anode and passed through a 40 nm thick transporting layer composed of PEDOT:PSS. Electrons were injected from an Al/LiF cathode and transported to the emitting layer (EML) through a 30 nm thick layer of 2,2′,2"-(1,3,5-benzinetriyl)-tris(1-phenyl-1-H-benzimidazole) (TPBi). Charges recombined in the 40 nm thick EML made of a 4,4’,4’’-tris(N-carbazolyl-triphenylamine (TCTA) matrix, hosting the **[Ir(F$_2$-PPy-CN)$_2$(PTZ)]** 8 wt% as emitter.

The EL spectrum of the OLED and related photo are shown in **Figure 13.2**, left. The OLED emission band is located in the green region and the corresponding CIE coordinates are (0.34, 0.55). The EL spectrum resembles the PL spectrum of the complex in solution media but it's slightly more structured due to rigid media (solid state). No significant contribution to the EL emission bands from the TBPi electron-transporting (hole-blocking) or TCTA binder layers is observed, indicating good charge carrier confinement within the EML and a complete energy transfer from the excited states of TCTA (generated by charge carrier recombination) to the Ir(III) complex. The luminance and external EL efficiency as function of applied voltage and current density of OLED is shown in Figure 10, right. A maximum external EL efficiency of ≈ 5.5% with luminance of ≈ 100 cd/m^2 at about 5 V, and luminance of ≈ 1000 cd/m^2 at about 7.5 V with an external EL efficiency ≈ 4% were obtained for the green OLED based on **[Ir(F$_2$-PPy-CN)$_2$(PTZ)]**. The good OLED performance observed with **[Ir(F$_2$-PPy-CN)$_2$(PTZ)]** as emitter are comparable with respect to those previously reported for solution-processed OLEDs based on Ir complexes.[15]

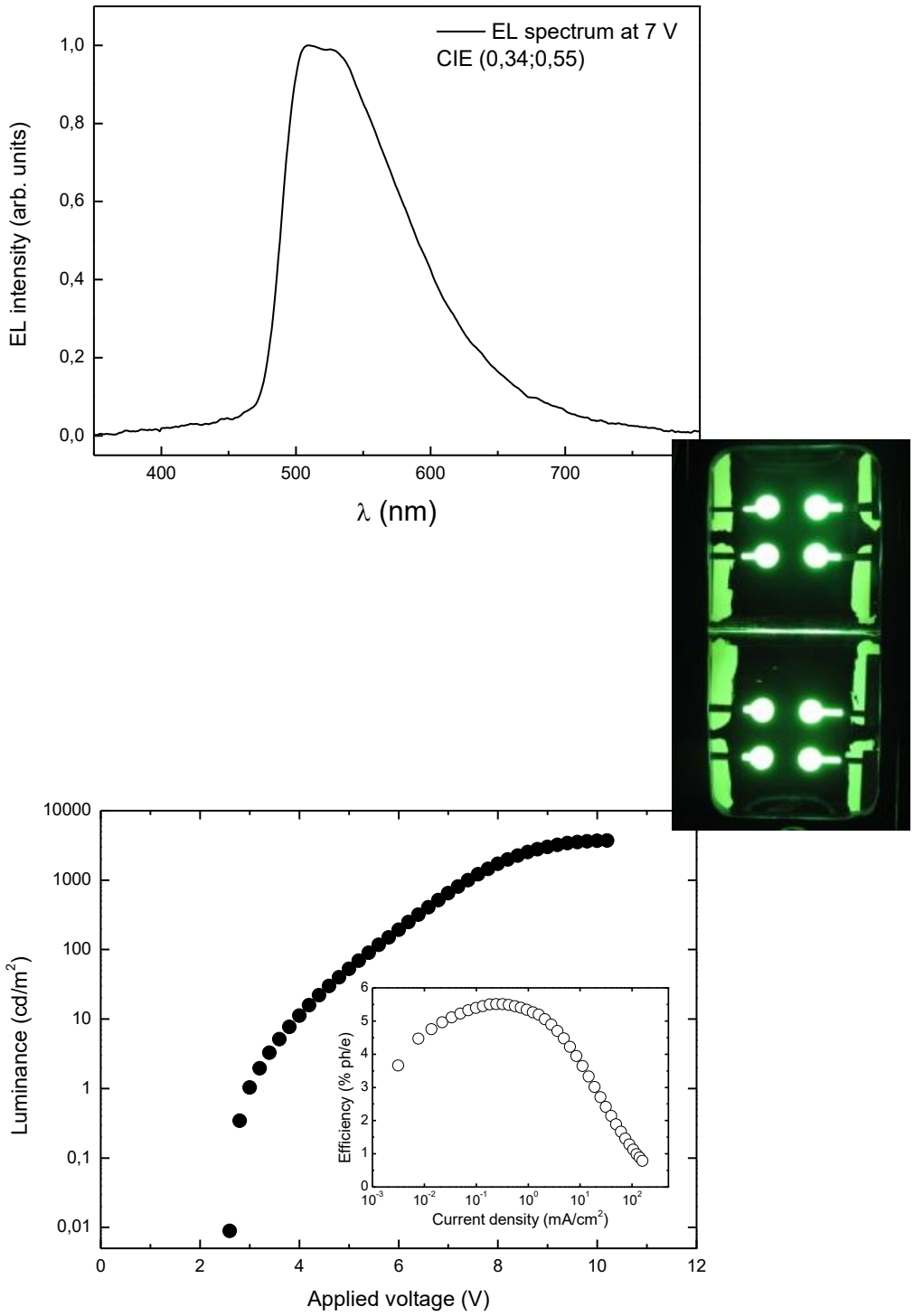

Figure 13.2. (Top) Electroluminescence spectra at 7 V of OLED. (Bottom) Luminance vs applied voltage and external efficiency vs current density (inset) of the OLED. In the inset is reported a photo of green OLED containing complex **[Ir(F_2-PPy-CN)$_2$(PTZ)]**.

2.4 Conclusions

The class of Ir(III)-tetrazole based complexes was further extended through chemical modifications of the cyclometalated phenylpyridine ligands (C^N), which were decorated with one EWG group such as the (-CN) moiety at the -*para* position of the pyridyl ring. The effects of such structural variation upon conversion of the neutrally charged **[Ir(C^N)$_2$(N^N)]** (C^N = **PPy-CN** or **F$_2$-PPy-CN**, N^N = **PTZ$^-$**, **PYZ$^-$** or **F$_3$C-PTZ$^-$**) into the corresponding cationic **[Ir(C^N)$_2$(N^N)]$^+$** -type complexes were reflected at first on their photophysical behaviour, which appeared markedly different in respect of what previously observed for fluorine and fluorine-free based PPy.[9] Surprisingly, the regioselective addition of a methyl group at the N-3 position of the tetrazole ring produced a shift towards higher energies of the emissions stemming from **[Ir(C^N)$_2$(N^N)]** when (N^N) is represented by **PTZ$^-$** and **F$_3$C-PTZ$^-$** ($\Delta\lambda$ *ca.* 20-30 nm). In the case of **PYZ$^-$**, the conversion of the fluorine-free derivative into the cationic **[Ir(PPy-CN)$_2$(PYZ-Me)]$^+$** produced the previously observed redshift of the emission profile ($\Delta\lambda$ *ca.* 20 nm) while remaining almost unchanged in the case of its (**F$_2$-PPy-CN**) -based analogue. All these observations were further rationalized through electrochemical measurements (cyclic voltammetry) and TDDFT calculations, which have highlighted that the emission output of this new class of Ir(III) complexes is mainly regulated by the nature of the cyclometalated ligand (C^N). More precisely, while the HOMO level is invariably composed by the (Ir-phenyl) or (Ir-F$_2$ phenyl) fragment, the lowest unoccupied molecular orbital is located on the (pyridine-CN) portion. The sole exception is represented by **[Ir(PPy-CN)$_2$(PYZ-Me)]$^+$**, in which the LUMO is composed by the tetrazole ligand **PYZ-Me**. The possibility of a straightforward fine colour tuning to both lower or higher energies of such kind of molecules becomes relevant in the field of solid-state lighting, where usually Ir(III) cyclometalates are used as phosphorescent materials in the fabrication of OLED and LEECs devices. In this context, the green **[Ir(F$_2$-PPy-CN)$_2$(PTZ)]** emitter was finally tested for the preparation of solution-processed OLEDs, returning performances in line with those reported for similar compounds.

2.5 Experimental Section

General considerations. All the reagents and solvents were obtained commercially (Sigma Aldrich/Merck, Alfa Aesar, Strem Chemicals) and used as received without any further purification unless otherwise specified. When required, reactions were carried out under an argon atmosphere following standard Schlenk protocols. The purification of the Ir(III) complexes was performed via column chromatography with the use of Al_2O_3 (Brockmann grade I or II) as the stationary phase. ESI-mass spectra were recorded using a Waters ZQ-4000 instrument (ESI-MS, acetonitrile as the solvent). Nuclear magnetic resonance spectra (consisting of ^{1}H and ^{13}C) were always recorded using a Varian Mercury Plus 400 (^{1}H, 399.9; ^{13}C, 101.0 MHz). ^{1}H and ^{13}C chemical shifts were referenced to residual solvent resonances ($^{1}H/^{13}C$: Acetone-d^6 2.05/29.84 ppm; CD_3CN 1.94/118.26 ppm; DMSO-d^6 2.49/39.52 ppm; $CDCl_3$ 7.26/77.16 ppm).

Photophysics. Absorption spectra were recorded at room temperature using an Agilent Cary 100 UV-vis spectrometer. Uncorrected steady-state emission and excitation spectra were recorded on an Edinburgh FLSP920 spectrometer equipped with a 450 W xenon arc lamp, double excitation and single emission monochromators, and a Peltier-cooled Hamamatsu R928P photomultiplier tube (185−850 nm). Emission and excitation spectra were acquired with a cut-off filter (395 nm) and corrected for source intensity (lamp and grating) and emission spectral response (detector and grating) by a calibration curve supplied with the instrument. The wavelengths for the emission and excitation spectra were determined using the absorption maxima of the MLCT transition bands (emission spectra) and at the maxima of the emission bands (excitation spectra). Quantum yields (Φ) were determined using the optically dilute method by Crosby and Demas[16] at excitation wavelength obtained from absorption spectra on a wavelength scale [nm] and compared to the reference emitter ($[Ru(bpy)_3]^{2+}$in H_2O) by the following equation:[17]

$$\phi_s = \phi_r \left[\frac{A_r(\lambda_r)}{A_s(\lambda_s)}\right]\left[\frac{I_r(\lambda_r)}{I_s(\lambda_s)}\right]\left[\frac{n_s^2}{n_r^2}\right]\left[\frac{D_s}{D_r}\right]$$

where A is the absorbance at the excitation wavelength (λ), I is the intensity of the excitation light at the excitation wavelength (λ), n is the refractive index of the solvent, D is the integrated intensity of the luminescence, and Φ is the quantum yield. The subscripts r and s refer to the reference and the sample, respectively. A stock solution with an absorbance > 0.1 was prepared, then a 10 times diluted solution was obtained, resulting in absorbance of about 0.07/0.08 depending on the sample considered. The Lambert-Beer law was assumed to remain linear at the concentrations of the solutions. The degassed measurements were obtained after the solutions were bubbled for 10 minutes under Ar atmosphere, using a septa-sealed quartz cell. Air-equilibrated $[Ru(bpy)_3]Cl_2/H_2O$ solution ($\Phi = 0.028$)[18] was used as reference. The quantum yield determinations were performed at identical excitation wavelengths for the sample and the reference, therefore deleting the I(λr)/I(λs) term in the equation. Emission lifetimes (τ) were determined with the single-photon counting technique (TCSPC) with the same Edinburgh FLSP920 spectrometer using pulsed picosecond LED (EPLED 360, FWHM < 800ps) as the excitation source, with repetition rates between 1 kHz and 1 MHz, and the above-mentioned R928P PMT as the detector. The goodness of fit was assessed by minimizing the reduced χ2 function and by visual inspection of the weighted residuals. To record the 77 K luminescence spectra, the samples were put in quartz tubes (2 mm diameter) and inserted in a special quartz Dewar filled with liquid nitrogen. The solvent used in the preparation of the solutions for the photophysical investigations was of spectrometric grade. Experimental uncertainties are estimated to be ±8% for lifetime determinations, ±20% for quantum yields, and ±2 nm and ±5 nm for absorption and emission peaks, respectively.

Cyclic Voltammetry. $TBAPF_6$ (tetrabutylammonium hexafluorophosphate, Sigma Aldrich) was used as received as the supporting electrolyte, CH_3CN was distilled over CaH_2 and thoroughly degassed under N_2 before each measurement. Electrochemical experiments were recorded with a Metrohm Autolab PGSTAT302N potentiostat-galvanostat using a Calomel electrode as reference (303/SCG/6 – Amel Electrochemistry) and a Platinum solid electrode (492/Pt/2 – Amel Electrochemistry) as working electrode.

Ligand synthesis. Tetrazole derivatives are nitrogen rich molecules that can be used as components for explosive mixtures.[19] The reactions described herein were only run on a few grams scale and no problems were encountered. However, *great caution* should be exercised when handling, knocking or heating compounds of this type. Following the general method reported by Koguro and co-workers,[20] tetrazole ligand [H-**PTZ**], [H-**PYZ**], [H-**PTZ-CF$_3$**] were obtained in almost quantitative yield. [H-**PTZ**] **^{1}H-NMR** (DMSO-d^6, 400 MHz) δ (ppm) = 8.82 (m, 1H), 8.25 (m, 1H), 8.10 (m, 1H), 7.66 (m, 1H). **^{13}C-NMR**, (DMSO-d^6, 100 MHz) δ (ppm) = 155.3, 150.5, 144.1, 138.7, 126.6, 123.1. [H-**PYZ**] **^{1}H-NMR** (DMSO-d^6, 400 MHz) δ (ppm) = 9.42 (d, J = 1.2 Hz, 1H), 8.89 (m, 2H). **^{13}C-NMR**, (DMSO-d^6, 100 MHz) δ (ppm) = 165.1, 147.7, 145.6, 144.6, 143.9. [H-**PTZ-CF$_3$**] (DMSO-d^6, 400 MHz) δ (ppm) = 8.56 (m, 1H), 8.32 (m, 1H), 8.10 (m, 1H), 7.75 (m, 1H). **^{13}C-NMR**, (DMSO-d^6, 100 MHz) δ (ppm) = 163.2, 152.1, 149.9, 136.8, 126.3, 124.7,123.1.

(PPy-CN) and **(F2-PPy-CN)** were obtained by standard Suzuki-Miyaura coupling conditions between 4 cyano 2-bromopyridine and phenylboronic acid or 2,4 difluorophenyl boronic acid in presence of [Pd(pph$_3$)$_4$]. **(PPy-CN) ^{1}H-NMR**, ($CDCl_3$, 400 MHz) δ (ppm) = 8.82 (d, *J = 4.4 Hz,* 1H), 7.97 (m,2H), 7.90 (s, 1H), 7.48 (m, 3H), 7.41 (m, 1H). Y = 0.339 g (86%). **(F2-PPy-CN) ^{1}H-NMR**, ($CDCl_3$, 400 MHz) δ (ppm) = 8.88 (d, *J = 4.8 Hz,* 1H), 8.08 (m,1H), 8.02 (m,1H), 7.48 (d, *J = 5.2 Hz,* 1H), 7.04 (m, 1H), 6.96 (m, 1H). **^{19}F-NMR** ($CDCl_3$, 376 MHz) δ (ppm) = -106.69, -112.11. Y = 0.391 g (83%).

Dichlorobridged Ir(III) dimer **[Ir(PPy-CN)$_2$Cl]$_2$** was obtained according to the Nonoyama protocol;[12] for **[Ir(F2-PPy-CN)$_2$Cl]$_2$** the reaction was carried out over a period of 48h in pure ethoxyethanol.

General procedure for the synthesis of neutral [Ir(C^N)$_2$(N^N)] -type complexes. To a 3:1 solution of DCM/EtOH (15+5 mL) were added the desired dichloro-bridged Ir(III) dimer [Ir(C^N)$_2$Cl]$_2$ (1 eq) and 2.5 eq of [H-**PTZ**], [H-**PYZ**] or [H-**PTZ-CF$_3$**]. The solution was stirred at r.t., for 6h. The solvent was removed by rotary-evaporation and the crude was subsequently purified with Al_2O_3 column chromatography eluted with a 40:1 DCM/CH_3OH or DCM/Acetone gradient from 8:2 to 6:4 mixtures, yielding the desired neutral Ir(III) complex as the second fraction.

[Ir(PPy-CN)$_2$(PTZ)] ^{1}H-NMR (CD_3CN, 400 MHz). δ (ppm) = 8.66 – 8.58 (m, 2H), 8.39 – 8.36 (m, 1H), 8.20 – 8.16 (m, 1H), 8.05 – 8.01 (m, 2H), 7.96 – 7.94 (m, 1H), 7.83 – 7.81 (m, 2H), 7.52 – 7.47 (m, 2H), 7.39 – 7.37 (m, 1H), 7.09 – 7.05 (m, 1H), 6.99 – 6.95 (m, 2H), 6.88 – 6.84 (m, 1H), 6.48 – 6.45 (m, 1H), 6.38- 6.36 (m, 1H). **^{13}C-NMR** (Acetone-*d*^{6}, 100 MHz) δ (ppm) = 170.20, 170.01, 165.34 (Ct), 153.32, 151.12, 150.83, 150.70, 149.87, 148.88, 143.61, 143.00, 140.54, 132.56, 132.37, 131.86, 131.06, 127.08, 126.48, 126.03, 125.48, 124.95, 123.17, 122.49, 122.45, 122.28, 122.16, 121.85, 116.32, 104.20. **ESI-MS** (*m/z*, CH_3CN): [M+H$^+$] = 698; [M+Na$^+$] = 720. Y = 0.090 g (51%). Anal. Calcd. For $C_{30}H_{18}N_9Ir_1$ (696.74) C 51.72, H 2.61, N 18.09. Found: C 49.63, H 2.46, N 17.08.

[Ir(PPy-CN)$_2$ (PYZ)] ^{1}H-NMR (Acetone-*d*^{6}, 400 MHz). δ (ppm) = 9.54 (d, *J* = 1.2 Hz, 1H), 8.68 (d, *J* = 3.2 Hz, 1H), 8.59 (m, 2H), 8.20 (d, J = 6 Hz, 1H), 8.03 (d, J = 8.0 Hz, 1H), 7.94 (d, J = 8.0 Hz, 1H), 7.85 (d, *J* = 3.2 Hz, 1H), 7.80 (d, *J* = 6.0 Hz, 1H), 7.49 (d, *J* = 6.0 Hz 1H), 7.35 (d, *J* = 6.0 Hz, 1H), 7.08 (m,1 H), 7.00 (m, 1H), 6.94 (m, 1H), 6.87 (m, 1H), 6.47 (d, *J* = 7.6 Hz, 1H), 6.36 (d, *J* = 7.6 Hz, 1H). **^{13}C-NMR** (CD_3CN, 100 MHz). δ (ppm) = 170.22, 170.07, 163.63 (C_t) 152.20, 151.94, 151.84, 149.40, 148.71, 145.66, 145.53, 145.19, 144.88, 144.69, 144.47, 143.75, 133.34, 133.05, 132.82, 132.17, 127.23, 126.87, 126.64, 126.10, 124.57, 123.91, 123.76, 123.69, 123.08, 122.97. **ESI-MS** (*m/z*, CH_3CN): [M+Na$^+$] = 721; [M+K$^+$] = 737. Y = 0.101 g (57%). Anal.

Calcd. For $C_{29}H_{17}N_{10}Ir_1$ (697.73) C 49.92, H 2.46, N 20.07. Found: C 49.87, H 2.44, N 20.05.

[Ir(PPy-CN)$_2$(F$_3$C-PTZ)] ^{1}H-NMR (Acetone-*d*^{6}, 400 MHz) δ (ppm) = 8.62 – 8.48 (m, 3H), 8.51 – 8.48 (m, 1H), 8.24 – 8.22 (m, 1H), 8.06 – 8.04 (m, 2H), 7.97 – 7.94 (m, 1H), 7.84 – 7.82 (m, 1H), 7.51 – 7.49 (m, 1H), 7.35 – 7.33,(m, 1H), 7.12 – 7.08 (m, 1H), 7.04 – 6.99 (m, 1H), 6.97 – 6.94 (m, 1H), 6.89 – 6.85 (m, 1H), 6.52 – 6.50 (m, 1H), 6.38 – 6.36 (m, 1H). **^{13}C-NMR** (Acetone-*d*^{6}, 100 MHz) δ (ppm) = 169.34, 169.28, 163.1 (Ct), 152.8, 151.6, 150.8, 150.7, 147.05, 146.99, 146.95, 143.22, 142.43, 137.47, 137.44, 132.12, 131.67, 131.41, 130.57, 128.09, 127.75, 126.03, 125.99, 125.81, 125.56, 125.51, 125.44, 125.11, 124.45, 124.37, 123.91, 122.98, 122.92, 122.89, 122.83, 122.79, 122.13, 122.08, 122.04, 121.98, 121.82, 121.79, 121.73, 121.48, 121.23, 118.62, 118.40, 115.75, 115.73. **ESI-MS** (*m/z*, CH_3CN): [M+CH_3CN] = 806; Y = 0.137 g (95%). Anal. Calcd. For $C_{31}H_{17}N_9F_3Ir_1$ (764.74) C 48.68, H 2.24, N 16.48. Found: C 49.19, H 2.50, N 17.38.

[Ir(F$_2$-PPy-CN)$_2$(PTZ)] ^{1}H-NMR (CD_3CN, 400 MHz) δ (ppm) = 8.51 – 8.48 (m, 2H), 8.37 – 8.34 (m, 1H), 8.11 – 8.07 (m, 1H), 7.81 – 7.78 (m, 2H), 7.71 – 7.69 (m, 1H), 7.41 – 7.37 (m, 1H), 7.30 – 7.26 (m, 2H), 6.77 – 6.66 (m, 2H), 5.92 – 5.89 (m, 1H), 5.84 – 5.81 (m, 1H). **^{13}C-NMR** (CD_3CN, 100 MHz) δ (ppm) = 165.70, 165.58, 165.03, 164.97, 163.85, 156.03, 151.87, 150.82, 150.71, 150.47, 148.37, 140.47, 127.04, 125.70, 125.31, 125.30, 115.66, 115.61, 114.46, 114.43, 114.28, 114.24, 114.15, 113.97, 113.94, 99.26, 98.98, 98.72, 98.46. **^{19}F-NMR** (CD_3CN, 376 MHz) δ (ppm) = -106.24, -107.07, -108.69, -109.59. **ESI-MS** (*m/z*, CH_3CN): [M+H^+] = 769; [M+Na^+] = 790. Y = 0.110 g (63%). Anal. Calcd. For $C_{30}H_{14}N_9F_4Ir_1$ (768.7) C 46.88, H 1.84, N 16.4. Found: C 45.2, H 2.05, N 16.02.

[Ir(F$_2$-PPy-CN)$_2$(PYZ)] ^{1}H-NMR (Acetone-*d*^{6}, 400 MHz) δ (ppm) = 9.53 (s, 1H), 8.72 – 8.71 (m, 1H), 8.59 – 8.58 (m, 1H), 8.29 – 8.27 (m, 1H), 8.04 – 8.03 (m, 1H), 7.81 – 7.80 (m, 1H), 7.62 – 7.60 (m, 1H), 7.47 – 7.45 (m, 1H), 7.23 – 7.15 (m, 1H), 6.85 – 6.71 (m, 2H), 6.05 – 6.02 (m, 1H), 5.88 – 5.86 (m, 1H). **^{13}C-NMR** (Acetone-*d*^{6}, 100 MHz) δ (ppm) = 166.61, 166.48, 165.94, 163.35, 162.79, 161.66, 161.24, 161.11, 156.20, 152.22, 151.31, 149.17, 145.31, 145.13, 144.44, 129.76, 129.03, 126.81, 126.24, 126.11,

126.03, 125.82, 123.77, 123.60, 116.43, 115.59, 115.41, 115.00, 114.82, 100.40, 100.13, 99.86, 99.67, 99.41, 99.14. **^{19}F-NMR** (Acetone-d^6, 376 MHz) δ (ppm) = -105.62, -106.64, -108.58, -109.71. **ESI-MS** (*m/z*, CH_3CN): [M] = 769; [M+Na^+] = 791. Y = 0.123 g (70%). Anal. Calcd. For $C_{29}H_{13}N_{10}F_4Ir_1$ (769.69) C 45.26, H 1.7, N 18.2. Found: C 45.10, H 1.54, N 17.95.

[Ir(F_2-PPy-CN)$_2$(F_3C-PTZ)] **^{1}H-NMR** (Acetone-d^6, 400 MHz). δ (ppm) = 8.47 – 8.42 (m, 3H), 8.19 – 8.18 (m, 1H), 8.03 (m, 1H), 7.69 – 7.67 (m, 1H), 7.50 – 7.48 (m, 1H), 7.32 – 7.30 (m, 1H), 6.75 – 6.59 (m, 3H), 5.97 – 5.94 (m, 1H), 5.74 – 5.71 (m, 1H). **^{13}C-NMR** (CD_3CN, 100 MHz). δ (ppm) = 166.98, 166.86, 166.42, 166.37, 166.21, 166.18, 166.11, 166.05, 164.59, 164.42, 164.30, 164.13, 164.00, 163.73, 163.61, 161.99, 161.87, 161.55, 161.42, 157.01, 156.43, 156.35, 153.17, 152.50, 152.23, 151.74, 151.67, 148.91, 148.86, 139.53, 139.51, 130.11, 129.76, 128.68, 128.21, 127.23, 127.14, 126.94, 126.73, 126.71, 126.54, 126.32, 125.09, 124.71, 124.67, 123.94, 123.90, 122.39, 118.69, 117.00, 116.96, 116.16, 116.13, 115.99, 115.43, 115.40, 115.25, 115.22, 100.96, 100.69, 100.43, 100.35, 100.86, 99.891. **ESI-MS** (*m/z*, CH_3CN): [M+Na^+] = 860; [M+CH_3CN] = 878. Y = 0.09 g (85%). Anal. Calcd. For $C_{31}H_{13}N_9F_7Ir_1$ (836.7) C 44.5, H 1.57, N 15.07. Found: C 41.7, H 1.64, N 13.68.

General procedure for the synthesis of cationic [Ir(C^N)$_2$(N^N)]$^+$[PF_6]$^-$ -type complexes. 1 eq of the desired neutral Ir(III) complex was added to dichloromethane (15 mL) and the mixture was allowed to cool down to -50°C by immersion into an ethanol/liquid nitrogen cold bath. Then, methyl trifluoromethanesulfonate (1.2 eq.) was added. The reaction was stirred under nitrogen for 30 minutes while being kept in the cold bath, and then allowed to warm up to room temperature and stirred for 3 hours. Anion exchange was carried out by adding an excess of NH_4PF_6 to the solution and stirring for 30 minutes. The product was then extracted with H_2O (3×10 mL) and the organic components were combined and dried over anhydrous $MgSO_4$. Subsequent purification by column chromatography on Al_2O_3 eluted with a CH_2Cl_2/acetone 6:4 yielded the desired cationic Ir(III) complex as the second fraction.

[Ir(PPy-CN)$_2$(PTZ-Me)]$^+$[PF$_6$]$^-$ ^{1}H-NMR (Acetone-*d*^{6}, 400 MHz). δ (ppm) = 8.69 – 8.68 (m, 2H), 8.63 – 8.61 (m, 1H), 8.42 – 8.37 (m, 2H), 8.36 – 8.15 (m, 1H), 8.08 – 8.01 (m, 3H), 7.84 – 7.80 (m, 1H), 7.47 – 7.43 (m, 2H), 7.15 – 7.08 (m, 1H), 7.07 – 6.99 (m, 2H), 6.97 – 6.43 (m, 1H), 6.43 – 6.39 (m, 2H), 4.54 (s, 3H). **^{13}C-NMR** (Acetone-*d*^{6}, 100 MHz) δ (ppm) = 170.13, 169.59, 167.76 (C_t), 153.22, 153.06, 152.67, 149.67, 146.43, 146.28, 144.44, 144.34, 142.72, 133.69, 133.29, 133.19, 132.64, 131.69, 127.84, 127.40, 126.77, 126.64, 126.53, 125.11, 124.70, 124.15, 124.07, 123.96, 123.86, 117.23, 117.20, 42.47 (CH_3). **ESI-MS** (*m/z*, CH_3CN): $[M]^+$ = 712; $[M]^-$ = 145. Y = 0.036 g (70 %). Anal. Calcd. For $C_{31}H_{21}N_9F_6P_1Ir_1$ (856.74) C 43.46, H 2.47, N 14.71. Found: C 43.59, H 2.51, N 14.89.

[Ir(PPy-CN)$_2$(PYZ-Me)]$^+$[PF$_6$]$^-$ ^{1}H-NMR (Acetone-*d*^{6}, 400 MHz). δ (ppm) = 9.77 (m, 1H), 8.69 (m, 2H), 8.34 – 8.31 (m, 2H), 8.09 – 8.03 (m, 3H), 7.45 – 7.43 (m, 3H), 7.17 – 6.94 (m, 4H), 6.44 – 6.39 (m, 1H), 6.38 – 6.37 (m, 1H), 4.59 (s, 3H). **^{13}C-NMR** (Acetone-*d*^{6}, 100 MHz) δ (ppm) = 169.82, 169.43, 166.26 (C_t), 151.72, 151.60, 151.51, 146.54, 145.40, 145.33, 144.17, 142.79, 142.62, 139.80, 131.85, 131.68, 131.58, 131.08, 126.20, 125.79, 125.23, 124.98, 123.77, 123.29, 122.59, 122.51, 122.30, 115.49, 42.69 (CH_3). **ESI-MS** (*m/z*, CH_3CN): $[M]^+$ = 713; $[M]^-$ = 145. Y = 0.042 g (64 %). Anal. Calcd. For $C_{30}H_{20}N_{10}F_6P_1Ir_1$ (857.73) C 42.01, H 2.35, N 16.33. Found: C 42.47, H 2.43, N 16.50.

[Ir(PPy-CN)$_2$(F$_3$C-PTZ-Me)]$^+$[PF$_6$]$^-$ ^{1}H-NMR (Acetone-*d*^{6}, 400 MHz). δ (ppm) = 8.86 – 8.85 (m, 1H), 8.73 – 8.67 (m, 3H), 8.39 – 8.37 (m, 1H), 8.33 – 8.31 (m, 1H), 8.22 – 8.21 (m, 1H), 8.11 – 8.09 (m, 1H), 8.05 – 8.03 (m, 1H), 7.45 – 7.40 (m, 2H), 7.19 – 7.15 (m, 1H), 7.10 – 7.04 (m, 3H), 6.99 – 6.94 (m, 1H), 6.49 – 6.47 (m, 1H), 6.40 – 6.38 (m, 1H), 4.56 (s, 3H). **^{13}C-NMR** (Acetone-*d*^{6}, 100 MHz). δ (ppm) = 168.94, 168.54, 166.96 (Ct), 151.70, 151.59, 148.24, 148.13, 148.09, 147.99, 147.11, 143.00, 142.91, 142.75, 138.78, 131.70, 131.61, 131.07, 131.03, 130.72, 126.22, 125.77, 125.28, 124.99, 123.78, 123.42, 123.21, 122.61, 122.54, 122.49, 122.41, 122.32, 122.29, 122.19, 115.55, 115.53, 41.79. **ESI-MS** (m/z, CH_3CN): $[M]^+$ = 780; $[M]^-$ = 145. Y = 0.113 g (87 %). Anal. Calcd. For $C_{32}H_{20}N_9F_9P_1Ir_1$ (924.74) C 41.56, H 2.18, N 13.63. Found: C 42.2, H 2.41, N 13.03.

[Ir(F_2-PPy-CN)$_2$(PTZ-Me)]$^+$[PF_6]$^-$ ^{1}H-NMR (Acetone-*d*^{6}, 400 MHz). δ (ppm) = 8.67 – 8.63 (m, 2H), 8.47 – 8.41 (m, 2H), 8.40 – 8.20 (m, 2H), 7.88 – 7.84 (m, 1H), 7.57 – 7.53 (m, 2H), 6.92 – 6.81 (m, 3H), 5.99 – 5.93 (m, 2H), 4.56 (s, 3H). **^{13}C-NMR** (Acetone-*d*^{6}, 100 MHz) δ (ppm) = 170.19, 169.91, 168.50 (C_t), 153.06, 152.60, 152.45, 145.09, 142.52, 131.35, 126.78, 126.06, 124.30, 124.24, 116.27, 100.94, 100.67, 100.57, 42.67 (CH_3). **^{19}F-NMR** (Acetone-*d*^{6}, 376 MHz) δ (ppm) = -72.03, -73.91, -105.34, -106.09, -108.04, -108.76. **ESI-MS** (*m/z*, CH_3CN): [M]$^+$ = 784; [M]$^-$ = 145. Y = 0.041 g (58 %). Anal. Calcd. For $C_{31}H_{17}N_9F_{10}P_1Ir_1$ (928.7) C 40.09, H 1.85, N 13.57. Found: C 40.12, H 1.98, N 13.55.

[Ir(F_2-PPy-CN)$_2$(PYZ-Me)]$^+$[PF_6]$^-$ ^{1}H-NMR (CD_3CN, 400 MHz). δ (ppm) = 9.64 (d, *J = 1.2 Hz*, 1H), 8.86 (m, 1H), 8.55 (m, 1H), 7.98 (d, *J = 6.4 Hz*, 1H), 7.94 (m, 1H), 7.84 (m, 1H), 7,42 (m, 1H), 7.38 (m, 1H), 6.80 (m, 3H), 5.85 (d, *J = 8.8 Hz*, 1H), 5.78 (d, *J = 8.4 Hz*, 1H), 4.48 (s, 3H). **^{13}C-NMR** (Acetone-*d*^{6}, 100 MHz) δ (ppm) = 169.94, 169.51, 166.89 (C_t), 152.97, 152.90, 150.98, 150.90, 148.60, 148.52, 146.74, 146.54, 140.19, 126.98, 126.83, 126.75, 126.55, 126.44, 126.23, 124.49, 116.24, 115.52, 115.31, 101.29, 101.02, 100.82, 42.91 (CH_3). **^{19}F-NMR** (CD_3CN, 376 MHz) δ (ppm) = -72.03, -73.91, -105.06, -105.78, -107.78, -108.54. **ESI-MS** (m/z): [M^+] = 785; [M^-] = 145. Y = 0.031 g (50 %). Anal. Calcd. For $C_{30}H_{16}N_{10}F_{10}P_1Ir_1$ (929.69) C 38.76, H 1.73, N 15.07. Found: C 38.83, H 1.82, N 15.11.

[Ir(F_2-PPy-CN)$_2$(F_3C-PTZ -Me)]$^+$[PF_6]$^-$ ^{1}H-NMR (Acetone-*d*^{6}, 400 MHz). δ (ppm) = 8.92 – 8-91 (m, 1H), 8.81 – 8.78 (m, 1H), 8.64 (s_{br},1H), 8.43 – 8.37 (m, 3H), 7.52 – 7.49 (m, 1H), 6.96 – 6.83 (m, 3H), 6.76 – 6.02 (m, 1H), 5.90 – 5.88 (m, 1H), 4.59 (s, 3H). **^{13}C-NMR** (Acetone-*d*^{6}, 100 MHz). δ (ppm) = 165.92, 163.80, 156.90, 153.24, 152.22, 151.96, 148.40, 148.36, 139.07, 126.76, 126.18, 125.74, 124.07, 123.68, 123.54, 116.43, 115.75, 115.60, 115.01, 114.83, 100.35, 99.81, 99.64, 99.38, 99.11, 42.53. **ESI-MS** (*m/z*, CH_3CN): [M^+] = 852; [M^-] = 145. Y = 0.098 g (65 %). Anal. Calcd. For $C_{32}H_{16}N_9F_{13}P_1Ir_1$ (996.7) C 38.56, H 1.62, N 12.56. Found: C 37.92, H 1.64, N 12.06.

OLED device fabrication. OLEDs were fabricated by growing a sequence of thin layers on clean glass substrates pre-coated with a 120 nm-thick layer of indium tin oxide (ITO) with a sheet resistance of 20 Ω per square. A 40 nm thick hole injecting layer of poly(3,4-ethylene dioxythiophene) polystyrene sulfonate (PEDOT:PSS, Clevios P VP AI 4083) was spin-coated (4000 rpm) and then the substrates were placed in an oven at 140 °C for 10 min. After the ITO/PEDOT:PSS substrates were cooled down, a 40 nm-thick film of emitting layer composed of 8 wt% of **[Ir(F_2-PPy-CN)$_2$(PTZ)]** and 92 wt% of 4,4',4''-tris(N-carbazolyl-triphenylamine (TCTA) was spin-coated (2000 rpm) in clean room environment from a 10 mg/mL dichloromethane solution. Electron transporting of 30 nm-thick 2,2′,2"-(1,3,5-benzinetriyl)-tris(1-phenyl-1-H-benzimidazole) TPBi and cathode electrode of 0.5 nm-thick LiF with cap of 100 nm-thick Al were deposited in succession by thermal evaporation under vacuum of ~ 10-6 hPa. The current-voltage characteristics were measured with a Keithley Source-Measure unit, model 236, under continuous operation mode, while the light output power was measured with an EG&G power meter and electroluminescence spectra by StellarNet spectroradiometer. All measurements were carried out at room temperature under argon atmosphere and were reproduced for many runs, excluding any irreversible chemical and morphological changes in the devices.

X-ray crystallography. Crystal data and collection details for **[Ir(PPy-CN)$_2$(F_3C-PTZ)]·*solv*** are reported in Table S1. The diffraction experiments were carried out on a Bruker APEX II diffractometer equipped with a PHOTON2 detector and using Mo-Kα radiation. Data were corrected for Lorentz polarization and absorption effects (empirical absorption correction SADABS).[21] Structures were solved by direct methods and refined by full-matrix least-squares based on all data using F^2.[22] H-atoms were placed in calculated positions and refined isotropically using a riding model. All non-hydrogen atoms were refined with anisotropic displacement parameters. The unit cell contains an additional total potential solvent-accessible void of 1059 Å^3, corresponding to 1-2 solvent molecule per unit formula. These solvent molecules are highly disordered and, therefore, these voids have been treated using the SQUEEZE routine of PLATON.[23 a,b] An alert of level A is present in the check-cif. This is due to high values for the residual

electron density. This maximum is located close to the Ir atom, in a position which is not realistic for any atom. This is a series termination error, as often found in structures containing heavy atoms.

DFT Calculations. All the simulations reported in this work have been performed with Gaussian 16 using the Stuttgart-Dresden (SDD) effective core potential for Ir(III) and the 6-311G** basis set for all other atoms.[24] The long-range corrected hybrid functional (CAM-B3LYP) was also used for the exchange and correlation part.[25] The effect of the solvent was mimicked utilizing the self-consistent reaction field model (SCRF) with parameters suitable for acetonitrile.[26] The geometry of all complexes was relaxed with "tight" optimization criteria and the vibrational frequencies were computed to verify that there were no imaginary frequencies and the minimum energy state was reached. The relaxed structures were then used to perform TD-DFT calculations to compute the absorption spectra. To obtain values HOMO-LUMO gap consistent with the electrochemical measurements we mimicked the experiments by adding and removing one electron from the complex. The structures were further relaxed in the implicit solvent to model the fact that electrochemistry experiments have much longer time scales than photochemical measurement and therefore the molecular geometry as ample time to relax to its new minimum energy configuration. The HOMO-LUMO gap was then computed as:

$$\Delta E_{gap} = EA - IP$$

Where *EA* and *IP* are the electron affinity and the ionization potential, respectively. The electron affinity was computed as the energy of the reduced state minus the energy of the initial state and it is assumed to correspond to the energy of the LUMO. The ionization potential was computed as the energy of the oxidized state minus the energy of the initial state and it was assumed to correspond to the negative of the HOMO energy. It has also been shown that DFT typical underestimates the energy gap due to error in the exchange and correlation functionals, but the long-range corrected functionals, such as the one used here, are among the best performers.[27]

2.6 References

[1] C. Caporale, M. Massi, *Coord. Chem. Rev.*, **2018**, 363, 71–91.

[2] a) D. A. Nicewicz, D. W. C. MacMillan, *Science*, **2008** ,*322*, 77 – 80. b) M. A. Ischay, M. E. Anzovino, J. Du, T. P. Yoon. *J. Am. Chem. Soc.*, **2008**, *130*, 12886 – 12887. c) M. R. Narayanam, J. W. Tucker, C. R. J. Stephenson. *J. Am.Chem. Soc.*, **2009**, *131*, 8756 – 8757.

[3] A. R. B. M. Yusoff, A. J. Huckaba, M. K. Nazeeruddin, (**2017**) Phosphorescent Neutral Iridium (III) Complexes for Organic Light-Emitting Diodes. In: N. Armaroli, H. Bolink (eds) Photoluminescent Materials and Electroluminescent Devices. Topics in Current Chemistry Collections. Springer, Cham.

[4] D. Ma, T. Tsuboi, Y. Qiu, L. Duan, *Adv. Mater.* **2017**, *29*, 1603253.

[5] L. Flamigni, A. Barbieri, C. Sabatini, B. Ventura, F. Barigelletti, *Top. Curr. Chem.*, **2007**, *281*, 143–203.

[6] a) J. C. Deaton, F. N. Castellano, Archetypal Iridium(III) Compounds for Optoelectronic and Photonic Applications: Photophysical Properties and Synthetic Methods. In Iridium(III) in Optoelectronic and Photonics Applications; E. Zysman-Colman, Ed. Wiley-VHC:Weinheim, Germany, **2017**, 1−70 and references cited herein. b) J. Frey, B. F. E. Curchod, R. Scopellitti, I. Tavernelli, U. Rothlisberger, M. K. Nazeeruddin, E. Baranoff, *Dalton. Trans.*, **2014**, *43*, 5667.

[7] a) S. Stagni, E. Orselli, A. Palazzi, L. De Cola, S. Zacchini, C. Femoni, M. Marcaccio, F. Paolucci, S. Zanarini, *Inorg. Chem.*, **2007**, *46*, 9126-9138. b) S. Stagni, A. Palazzi, S. Zacchini, B. Ballarin, C. Bruno. M. Marcaccio, F. Paolucci, M. Monari, M. Carano, A. J. Bard, *Inorg. Chem.*, **2006**, *45*, 695-709.

[8] a) M. V. Werrett, S. Muzzioli, P. J. Wright, A. Palazzi, P. Raiteri, S. Zacchini, M. Massi, S. Stagni, *Inorg. Chem.*, **2014**, *53*, 229-243. b) M. V. Werrett, G. S. Huff, S. Muzzioli, V. Fiorini, S. Zacchini, B. Skeleton, A. Maggiore, J. M. Malicka, M. Cocchi, K. C. Gordon, S. Stagni, M. Massi, *Dalton. Trans.*, **2015**,

44, 8379. c) V. Fiorini, A. M. Ranieri, S. Muzzioli, K. D. M. Magee, S. Zacchini, N. Akabar, A. Stefan, M. I. Ogden, M. Massi, S. Stagni, *Dalton. Trans*., **2015**, *44*, 20597.

[9] S. Stagni, S. Colella, A. Palazzi, G. Valenti, S. Zacchini, F. Paolucci, M. Marcaccio, R. Q. Albuquerque, L. De Cola, *Inorg. Chem*., **2008**, *47*, 10509–10521.

[10] a) V. Fiorini, A. D'Ignazio, K. D. M. Magee, M. I. Ogden, M. Massi, S. Stagni, **2016**, *45*, 3256 – 3259. b) V. Fiorini, S. Zacchini, P. Raiteri, R. Mazzoni, V. Zanotti, M. Massi, S. Stagni, *Dalton. Trans.*, **2016**, *45*, 12884-12896. c) V. Fiorini, I. Zanoni, S. Zacchini, A. L. Costa, A. Hochkoeppler, V. Zanotti, A. M. Ranieri, M. Massi, A. Stefan, S. Stagni, *Dalton. Trans.*, **2017**, *46*, 12328-12338.

[11] N. Miyaura, A. Suzuki, *J. Chem. Soc., Chem. Commun.*, **1979**, *0*, 866-867.

[12] M. Nonoyama, *Bull. Chem. Soc. Jpn*., **1974**, *47*, 767.

[13] K. Nakamura, *Bull. Chem. Soc. Jpn*., **1982**, *55*, 2697–2705.

[14] C. M. Cardona, W. Li, A. E. Kaifer, D. Stockdale, G. C. Bazan, *Adv. Mater*., **2011**, *23*:2367–2371.

[15] E. Longhi, L. De Cola, Iridium(III) Complexes for OLED Appication. In Iridium(III) in Optoelectronic and Photonics Applications; E. Zysman-Colman, Ed. Wiley-VHC:Weinheim, Germany, **2017**, 205−274 and references cited herein.

[16] G. A. Crosby and J. N. Demas, *J. Phys. Chem*., **1971**, *75*, 991-1024.

[17] D. F. Eaton, *Pure Appl. Chem*., **1988**, *60*, 1107-1114.

[18] K. Nakamura, *Bull. Chem. Soc. Jpn*., 1982, **55**, 2697–2705.

[19] R. N. Butler, Tetrazoles. In "Comprehensive Heterocyclic Chemistry II"; Storr, R. C., Ed. Pergamon Press: Oxford, U.K., **1996**; Vol. *4*, 621-678, and references cited therein.

[20] K. Koguro, T. Oga, S. Mitsui and R. Orita, *Synthesis*, **1998**, 910-914.

[21] G. M. Sheldrick, *SADABS-2008/1 - Bruker AXS Area Detector Scaling and Absorption Correction*, Bruker AXS: Madison, Wisconsin, USA, 2008.

[22] G. M. Sheldrick, *Acta Crystallogr. C*, **2015**, *71*, 3.

[23] a) A. L. Spek, *J. Appl. Cryst.*, **2003**, *36*, 7-13; b) A. L. Spek, *Acta Cryst.*, **2009**, D65, 148-155.

[24] Gaussian 16, Revision C.01. M. J. Frisch, G. W. Trucks, H. B. Schlegel, G. E. Scuseria, M. A. Robb, J. R. Cheeseman, G. Scalmani, V. Barone, G. A. Petersson, H. Nakatsuji, X. Li, M. Caricato, A. V. Marenich, J. Bloino, B. G. Janesko, R. Gomperts, B. Mennucci, H. P. Hratchian, J. V. Ortiz, A. F. Izmaylov, J. L. Sonnenberg, D. Williams-Young, F. Ding, F. Lipparini, F. Egidi, J. Goings, B. Peng, A. Petrone, T. Henderson, D. Ranasinghe, V. G. Zakrzewski, J. Gao, N. Rega, G. Zheng, W. Liang, M. Hada, M. Ehara, K. Toyota, R. Fukuda, J. Hasegawa, M. Ishida, T. Nakajima, Y. Honda, O. Kitao, H. Nakai, T. Vreven, K. Throssell, J. A. Montgomery, Jr., J. E. Peralta, F. Ogliaro, M. J. Bearpark, J. J. Heyd, E. N. Brothers, K. N. Kudin, V. N. Staroverov, T. A. Keith, R. Kobayashi, J. Normand, K. Raghavachari, A. P. Rendell, J. C. Burant, S. S. Iyengar, J. Tomasi, M. Cossi, J. M. Millam, M. Klene, C. Adamo, R. Cammi, J. W. Ochterski, R. L. Martin, K. Morokuma, O. Farkas, J. B. Foresman, D. J. Fox, Gaussian, Inc., Wallingford CT, 2019.

[25] T. Yanai, D. P. Tew, N. C. Handy, *Chem. Phys. Lett.*, **2004**, *393*, 51–57.

[26] G. Scalmani, M. J. Frisch, *J. Chem. Phys.*, **2010**, *132*, 114110.

[27] T. Tsuneda, J -W. Song, S. Suzuki, K. Hirao, *J. Chem. Phys.*, **2010**, *133*, 174101.

Chapter 3 Antibacterial activity of a new class of tris homoleptic Ru(II)-complexes with alkyl-tetrazoles as diimine-type ligands*

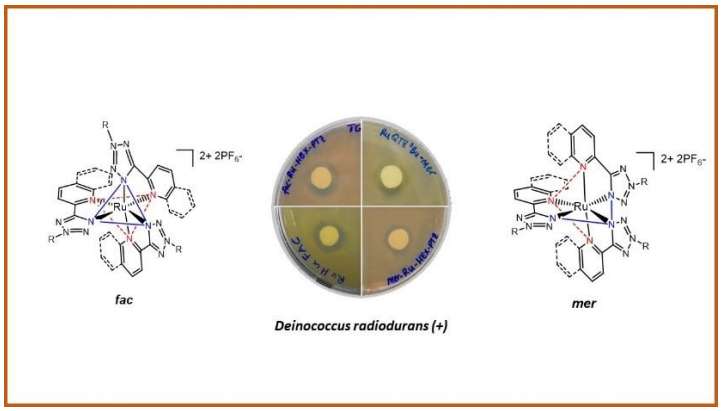

*This chapter is part of: *Appl. Organomet. Chem*., **2020**, 34:e5806.

3.1 Abstract

Herein, we describe a new family of tris chelate homoleptic Ru(II) complexes, **[Ru(N^N)$_3$]$^{2+}$**, where the diimine-type ligands (N^N) are represented by 2-pyridyl (PTZ) or 2-quinolyl tetrazole (QTZ) derivatives decorated with different alkyl substituents at the N-2 position of the tetrazole ring. The new Ru(II) complexes with the general formulae **[Ru(PTZ-R)$_3$]$^{2+}$** and **[Ru(QTZ-R)$_3$]$^{2+}$**, were obtained as statistical mixtures of facial (*fac*) and meridional (*mer*) isomers, as suggested by NMR (^{1}H, ^{13}C) experiments and confirmed in the case of ***mer*-[Ru(QTZ-Me)$_3$]$^{2+}$**, by X-ray crystallography. The photophysical behaviour of the tetrazole-based **[Ru(N^N)$_3$]$^{2+}$** type species was investigated by UV-vis absorption spectroscopy, providing trends typical of polypyridyl Ru(II) complexes. The new homoleptic complexes *fac/mer*-**[Ru(PTZ-R)$_3$]$^{2+}$** and *fac/mer*-**[Ru(QTZ-R)$_3$]$^{2+}$** have been assessed for any eventual antimicrobial activity towards two different bacteria such as Gram-negative *Escherichia coli* and Gram-positive *Deinococcus radiodurans*. Whereas being inactive toward *E. coli*, the response of agar disks diffusion tests suggested how some of the new *fac/mer* Ru(II) complexes could inhibit the growth of *D. radiodurans.*

This effect was further investigated by determining the growth kinetics in liquid medium of *D. radiodurans* exposed to the *fac/mer*-**[Ru(PTZ-R)$_3$]$^{2+}$** and *fac/mer*-**[Ru(QTZ-R)$_3$]$^{2+}$** complexes at different concentrations. The outcome of these experiments highlighted that the turn-on of the growth inhibitory effect took place as the linear hexyl chain was appended to the PTZ or QTZ scaffold, suggesting also how the inhibitory activity appeared more pronouncedly exerted by the facial isomers *fac*-**[Ru(PTZ-Hex)$_3$]$^{2+}$** and *fac*-**[Ru(QTZ-Hex)$_3$]$^{2+}$** (MIC = *ca.* 3.0 μg/mL) with respect to the corresponding meridional isomers (MIC = *ca.* 6.0 μg/mL).

3.2 Introduction

The presence of Ru(II) complexes is ubiquitous in studies focused on solar light harvesting, material sciences[1] and bio-imaging.[2] However, tris-homoleptic Ru(II) polypyridyl complexes with the general formula **$[Ru(N\hat{}N)_3]^{2+}$** have been recognized as potential antimicrobial agents for a long time.[3] In particular, even though the bactericidal properties of the archetypal complexes $[Ru(phen)_3]^{2+}$ and $[Ru(bpy)_3]^{2+}$ - where (phen) and (bpy) denote diimine chelators such as 1,10 phenanthroline and 2,2' bipyridine - were first described in the early 1950s by Dwyer and coworkers,[4a-b] the use of these substitution-inert mono and dinuclear Ru(II) polypyridyl complexes as viable alternatives to traditional organic drugs became effective a few decades later, when the ensuing and continued emergence of antibiotic-resistant bacteria prompted the search for new classes of antimicrobials. In this regard, chemical modifications of (phen) ligands set and/or the introduction of different ancillary ligands (L^L), has led to several homoleptic **$[Ru(N\hat{}N)_3]^{2+}$** or heteroleptic **$[Ru(N\hat{}N)_2(L\hat{}L)]^{2+}$** -type mononuclear complexes active towards Gram-positive bacteria such as *Staphylococcus aureus* and its methicillin-resistant variant MRSA. Furthering these promising results, Keene and coworkers have reported a family of dinuclear Ru(II) complexes – whose structure consists of two peripheral Ru(II) tris-diimine units tethered by alkyl chains with different lengths - as the most effective Ru(II)-based antimicrobial agents, which were active against both Gram-positive (*S. aureus* and MRSA, MIC = 1 μg/mL) and, importantly, Gram-negative bacteria (*i.e Escherichia coli*, MIC = 1 μg/mL).[5] Therefore, even though the antibacterial activity of metal complexes is likely governed by a delicate balance of sometimes contrasting factors (*i.e.* lipophilicity and global net charge), a consistent research effort has been addressed to extend these studies into other classes of octahedral metal complexes such as Ir(III)-cyclometalates,[6] and to the decoration of the Ru(II) ion with different types of diimine chelators. In these regards, Crowley and coworkers have recently investigated various 1,2,3 triazolyl pyridine containing various alkyl substituents as N^N ligands for a family of homoleptic Ru(II) complexes that showed an efficient antimicrobial activity towards Gram-positive bacteria such as MRSA.[7]

Within the general framework of our interests about the application of metal tetrazole complexes in life sciences,[8] we have recently shown that whereas neutrally charged Ir(III) tetrazolato complexes could be employed as luminescent labels for *in vivo* imaging of bacteria,[9] the corresponding series of cationic Ir(III)-tetrazole complexes - enlightening a behaviour very similar to that reported by Chao and coworkers for analogous cationic Ir(III) cyclometalates exposed to Gram-positive *Staphylococcus aureus* - [6a] exhibited remarkable antimicrobial activity towards Gram-positive *Deinococcus radiodurans*. [10] On these premises, and inspired by the work of Crowley and coworkers,[7] we put our effort in the design and preparation a new set of homoleptic "fully tetrazole" Ru(II) complexes with the general formula **[Ru(N^N)$_3$]$^{2+}$**, to be successively screened for their possible antimicrobial properties. In particular, the scaffold of the bis chelating diimine (N^N) is represented by 2-(tetrazol-5-yl)pyridine (**PTZ**) or 2-(tetrazol-5-yl)quinoline (**QTZ**), both kind of ligands being further decorated at the N-2 position of the tetrazole ring with alkyl chains with different length (**Scheme 1**). Following the approach that we have adopted in our recent works, the antimicrobial features of the resulting families of Ru(II) complexes, namely *fac/mer*-**[Ru(PTZ-R)$_3$]$^{2+}$** and *fac/mer*-**[Ru(QTZ-R)$_3$]$^{2+}$**, have been studied towards both Gram-negative *Escherichia coli* and Gram-positive *Deinococcus radiodurans*, a not pathogenic bacterium that is known as one of the toughest microorganisms, resistant to radiation, oxidative stress and DNA damage.[11]

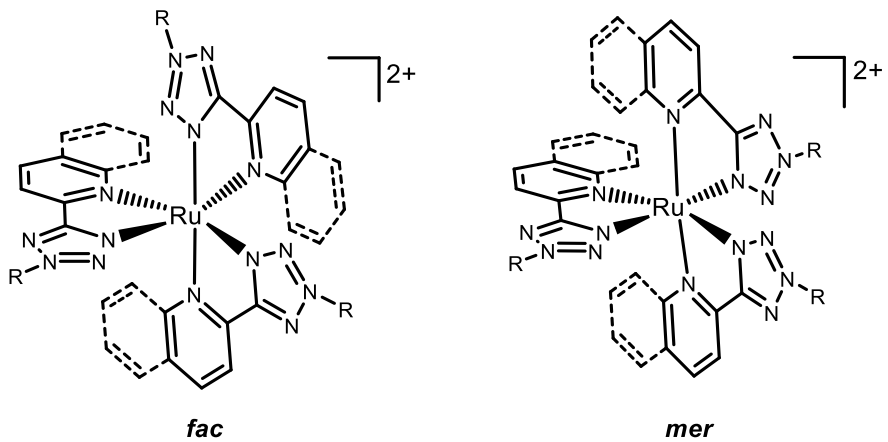

Scheme 1.3. Ru(II) complexes studied in this work.

3.3 Results and Discussion

The synthetic procedures followed in the preparation of the homoleptic Ru(II) complexes are outlined in **Scheme 2.3**.

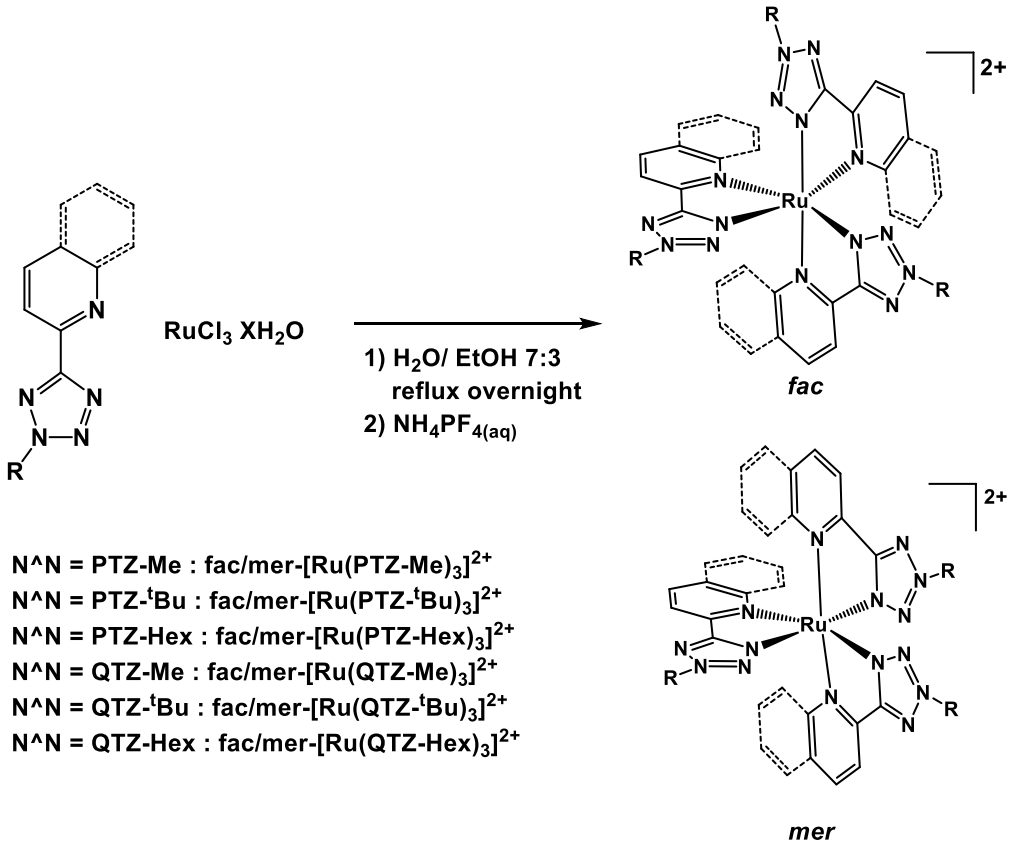

Scheme 2.3. Synthetic routes for the alkylated tetrazoles and the corresponding Ru(II) complexes with relative acronyms.

The N-2 alkylated tetrazoles employed in this work were prepared according to a two steps procedure involving the preliminary formation of the pyridyl and quinolyl tetrazoles,[12] followed by the addition of the desired alkyl moieties.[13 a-c] It has to be noted that the latter reaction usually produces a mixture of comparable amounts of two alkylated regioisomers[14] in which the alkyl residue can be bound either to the tetrazole N-1 or N-2 position. Aiming at using the N-2 alkylated tetrazoles as analogues of (bpy) or (phen)– type ligands, their purification from the N-1 isomers was accomplished through column chromatography.

Therefore, the corresponding homoleptic Ru(II) complexes were prepared by treating hydrate $RuCl_3$ with a slight molar excess of the appropriate N-2 alkyl tetrazole in a mixture of ethanol and water (7:3 v/v) at the reflux temperature. After a counterion exchange procedure aimed at replacing chlorides with two hexafluorophosphate anions, each of the resulting complexes was collected by filtration and washed with water and diethyl ether.

The formation of the new Ru(II) species was confirmed by ESI mass spectrometry, and the NMR (^{1}H, ^{13}C) studies suggested the occurrence of each Ru(II) complex as a statistical mixture of facial (*fac*) and meridional (*mer*) isomers. (**Figure 3.3**)

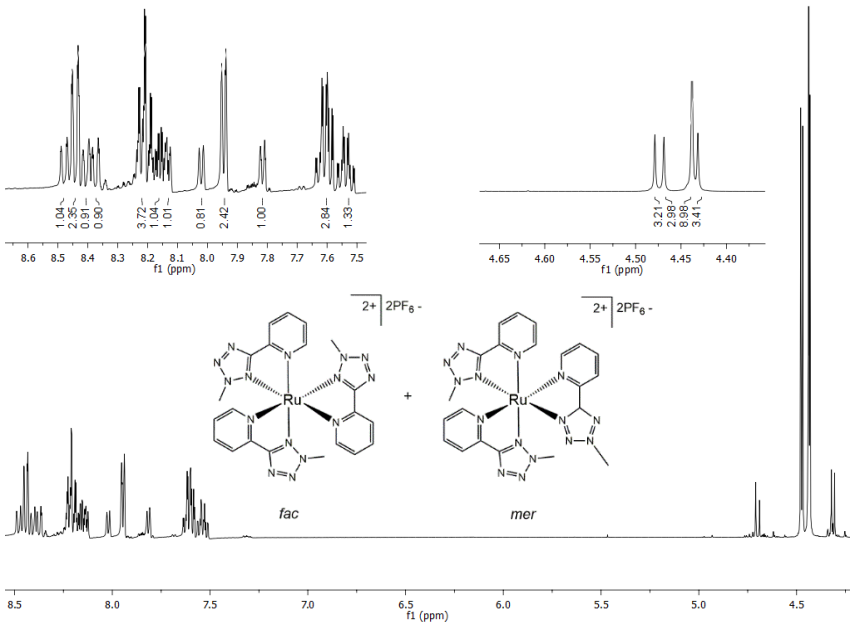

Figure 3.3. Selected NMR spectra of **$[Ru(PTZ\text{-}Me)_3]^{2+}$** as mixtures of *mer/fac* isomers before and after purification.

Focusing on the two diiminic nitrogens participating to the chelation of the metallic centre, and being N the nitrogen on the pyridyl or quinolyl ring and N' the N4 nitrogen of the pentatomic ring, it is possible to schematize the two different coordination isomers as illustrated in **Scheme 3.3**. In the facial (*fac*) isomer N (or N') type nitrogens occupy three vertexes describing a face of the octahedron, whereas in the meridional (*mer*) isomer the three vertexes describe a plane containing the metallic centre.

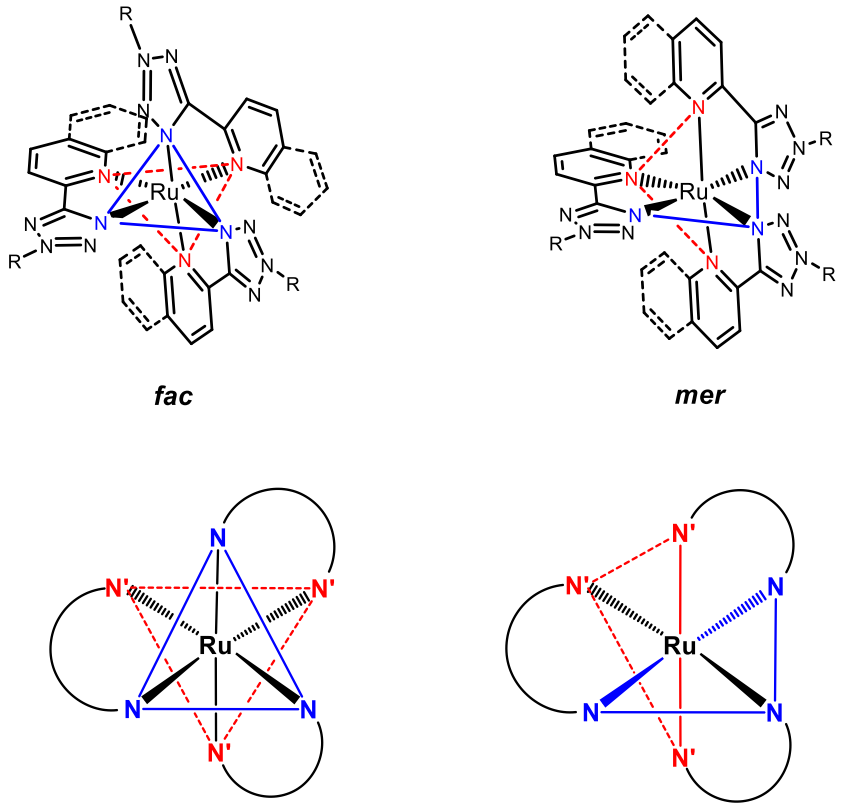

Scheme 3.3. Graphical representation of the two different coordination isomers for the prepared tris homoleptic Ru(II)-polypyridyl complexes.

For the *fac* isomer, the disposition adopted by the three chelating ligands around the metallic centre determines a C_3 symmetry axis passing for the metallic centre and perpendicular to the centre of the two face of the octahedron described by N or N' type nitrogens respectively (C_3 symmetry group). Based on such considerations, the three ligands in the *fac* isomer are magnetically equivalent, hence the $^{1}H/^{13}C$ NMR spectra of the reported *fac* complexes consist in a single pattern of signals corresponding to all of the coordinated ligands. (**Figure 4.3**) On the other hand, the coordination of the three ligands in a *mer* fashion does not originate any symmetry element, indeed the $^{1}H/^{13}C$ NMR spectra of the reported *mer* complexes report a pattern of signal for each of the three coordinated ligands (C_1 symmetry group). The separation of the *fac* and *mer* isomers was successful for all of the mixtures except for *fac*-**[Ru(QTZ-Hex)$_3$]$^{2+}$**, which was isolated in combination with the corresponding *mer*-isomer even after repeated attempts (*fac/mer* = 80:20 from ^{1}H-NMR data).

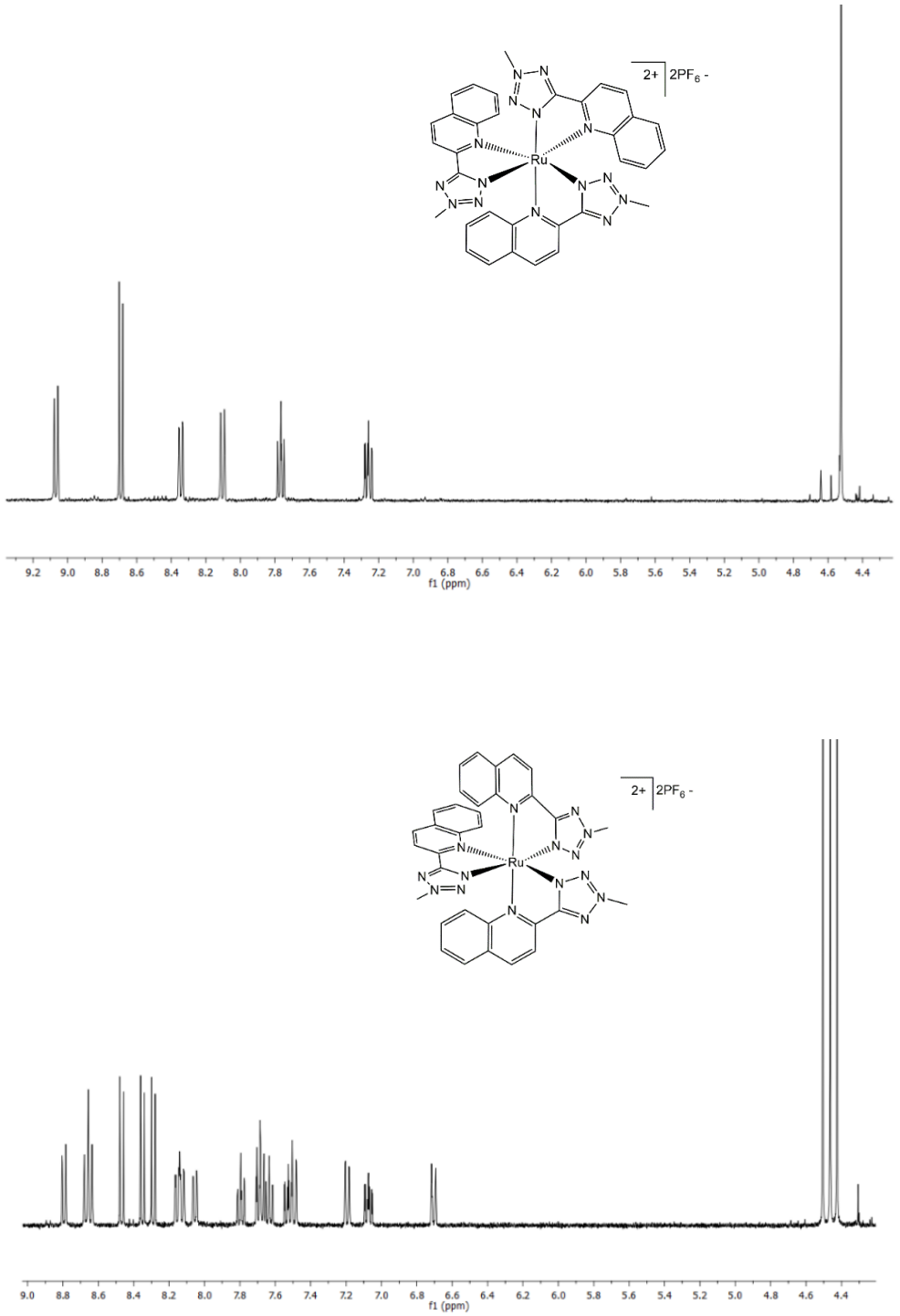

Figure 4.3. ^{1}H-NMR spectra of complexes *fac*-**[Ru(QTz-N2-Me)$_3$][PF$_6$]$_2$** (top) and *mer*-**[Ru(QTz-N2-Me)$_3$][PF$_6$]$_2$** (bottom); CD_3CN, 400 MHz.

3.3.1 *X-ray crystallography*

Among the series of the Ru(II) complexes, only the one that was suggested as *mer*-**[Ru(QTZ-Me)$_3$]$^{2+}$** afforded single crystals suitable for X-ray diffraction. (**Figure 5.3**)

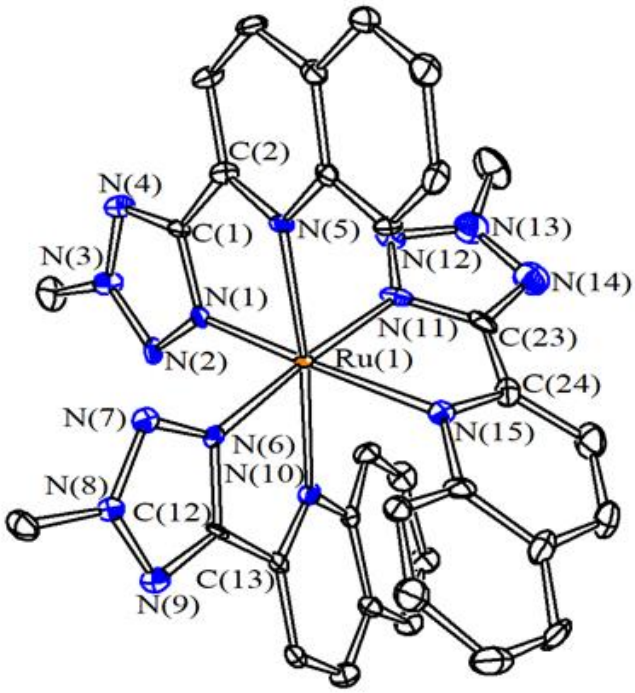

Figure 5.3. Molecular structure of the dication *mer*-**[Ru(QTZ-Me)$_3$]$^{2+}$** with key atoms labelled. Displacement ellipsoids are at the 50% probability level. H-atoms are omitted for clarity.

The analysis of its molecular structure provided results congruent with the occurrence of the expected octahedral complex in which the coordination sphere of the Ru(II) ion consisted of three bis chelate (QTZ-Me) ligands arranged in meridional (*mer*) geometry. As expected from tris chelate complexes, the unit cell of the crystal is represented by a racemic mixture of Δ and Λ enantiomers. In comparison to *mer* isomers of the homoleptic Ru(II) complexes reported by Crowley[7a] the molecular structure of *mer*-**[Ru(QTZ-Me)$_3$]$^{2+}$** evidenced a more pronounced distortion from the octahedral geometry. A closer inspection of the Ru-N bond distances revealed that the Ru-N (tetrazole) bonds in trans position to each other display almost identical distances [Ru(1)-N(6) = 2.044(4) Å, Ru(1)-N(11) = 2.043(5) Å], whereas the Ru-N(tetrazole) bond trans to Ru-N(quinolyl) is sensibly shorter [Ru(1)-N(1) = 2.010(4) Å]. Similarly,

the two Ru-N(quinolyl) bonds in relative trans position are identical within the experimental error [Ru(1)-N(5) = 2.130(4) Å, Ru(1)-N(10) = 2.135(4) Å], whereas the Ru-N(quinolyl) bond trans to the tetrazole ligand is significantly longer [Ru(1)-N(15) = 2.222(4) Å]. The three chelating (QTZ-Me) ligands are rather different concerning the coplanarity of the tetrazole and quinolyl ligands. Thus, the (QTZ-Me) ligand comprising N(1) to N(5) is almost coplanar [angle between the least-squares planes of the tetrazole and quinolyl rings = 6.3(3)°]. Conversely, the other two ligands comprising N(6) to N(10) [20.6(2)°] and N(11) to N(15) [20.9(3)°] are not coplanar. These deviations are likely to be due to the presence of the very rigid and bulk quinolyl condensed aromatic systems.

3.3.2 *Photophysical and electrochemical properties*

The absorption profiles obtained from dilute acetonitrile solutions at room temperature are representative of d^6 octahedral metal complexes,[15] with intense π-π* Ligand Centred (LC) transitions occurring in the UV region of the electromagnetic spectrum followed at lower energy by the metal-to-ligand charge transfer (MLCT) bands (**Figure 6.3**)

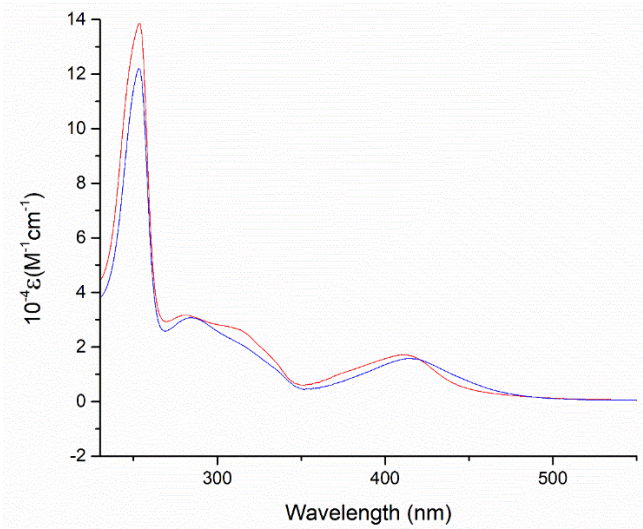

Figure 6.3. Absorption profiles of *fac*-**[Ru(QTZ-Me)$_3$]$^{2+}$** (red line) and *mer*-**[Ru(PTZ-Me)$_3$]$^{2+}$** (blue line), CH_3CN, 10^{-5}M, r.t.

If compared to $[Ru(bpy)_3]^{2+}$ as the reference compound for tris-chelate $[Ru(N\hat{}N)_3]^{2+}$-type species, all the Ru(II) tetrazole complexes described herein display blue-shifted absorption profiles, most likely in consideration of the reduced conjugation of the 5-aryl tetrazole ligands with respect to that of bpy. However, in close similitude with the isostructural Ru(II)-pyridyltriazole-based complexes reported by Crowley,[7a] the **PTZ**-based Ru(II) complexes described herein display MLCT maxima centred in between 380 and 390 nm. On passing to the 2-quinolyl analogues **QTZ**-based complexes, the position of the MLCT band is markedly shifted to lower energy (λ_{max} *ca.* 420 nm; **Figure 6**) an effect that is congruent with the more extended π-conjugation across the aromatic ligand. Relative to both series of complexes, only subtle differences were observed for the *fac* and *mer* pure isomers. Unlike $[Ru(bpy)_3]^{2+}$ and $[Ru(phen)_3]^{2+}$, all the Ru(II) complexes

described herein were not luminescent at room temperature. The lack of emission is most likely to be ascribed to the occurrence of thermally accessible metal-centred (MC) states causing the efficient depopulation of potentially emissive MLCT-type states.[11] The electrochemical properties of the Ru(II) complexes were investigated by cyclic voltammetry (CV) in acetonitrile solution at room temperature. In the region of positive potentials, each of the *fac/mer*-**[Ru(PTZ-R)$_3$]$^{2+}$** and *fac/mer*-**[Ru(QTZ-R)$_3$]$^{2+}$**-type complexes displayed one single and reversible Ru(II)/Ru(III)-based process, with no difference observed between each *fac* and *mer* isomer. Along the series of the PTZ-based complexes, *fac/mer*-**[Ru(PTZ-R)$_3$]$^{2+}$**, this process was found between *ca.* 1.63 V – as in the cases of *fac/mer*-**[Ru(PTZ-^{t}Bu)$_3$]$^{2+}$** - and 1.70 V, as for *fac/mer*-**[Ru(PTZ-Hex)$_3$]$^{2+}$**. The quinolyl analogues *fac/mer*-**[Ru(QTZ-R)$_3$]$^{2+}$** displayed the same metal-based process shifted to more positive potentials, being the corresponding potentials observed to span between ca. 1.72 V (for *fac/mer*-**[Ru(QTZ-^{t}Bu)$_3$]$^{2+}$**) and ca. 1.80 V, as in the cases of *fac/mer*-**[Ru(QTZ-Me)$_3$]$^{2+}$**. An analogous trend was observed in the region of the negative potentials, (see Supporting information, SI†, Table S2), in which the three ligand centred reductions that appeared in each voltammetric wave of the *fac/mer*-**[Ru(PTZ-R)$_3$]$^{2+}$** complexes were found to occur at more positive potentials than those displayed by the *fac/mer*-**[Ru(QTZ-R)$_3$]$^{2+}$** analogues. The analysis of these results suggested that the distinctive features that were observed from the comparison of *fac/mer*-**[Ru(PTZ-R)$_3$]$^{2+}$** and *fac/mer*-**[Ru(QTZ-R)$_3$]$^{2+}$**, were most likely due to the presence of the PTZ or the QTZ-type scaffolds, while no obvious correlations could be made in consideration of the occurrence of alkyl chains with different length and structure.

3.3.3 *Antimicrobial activity*

The antimicrobial activity of the *fac/mer*-**[Ru(QTZ-R)$_3$]$^{2+}$** and *fac/mer*-**[Ru(PTZ-R)$_3$]$^{2+}$**-type complexes was investigated against Gram-negative (*Escherichia coli*) and Gram-positive bacteria (*Deinococcus radiodurans*) by performing disk diffusion tests in agar plates followed, in case of positive response, by the broth dilution method to detect potential inhibition of bacterial growth. Given the moderate water solubility of the dicationic Ru(II)-complexes, the corresponding aqueous solutions containing DMSO up to 2% (v/v) were used for each testing. In all cases, the results of appropriate control experiments suggested the absence of any observable DMSO-related biological effect.

3.3.3.1 *Disk diffusion test in agar plates*

The antimicrobial activity exerted by the Ru(II) complexes was preliminarily assessed by disk diffusion tests in agar plates, in which the appearance of zones of growth inhibition around the paper disks impregnated with *fac/mer*-[Ru(N^N)$_3$]$^{2+}$ complexes was monitored and compared to the output of two further paper disks impregnated with ampicillin and DMSO as the positive and negative control, respectively. The growth of *E. coli* was not affected by any of the compounds tested since no visible inhibition haloes appeared, as reported in **Figure 7.3** for *fac/mer*-**[Ru(PTZ-Hex)$_3$]$^{2+}$**.

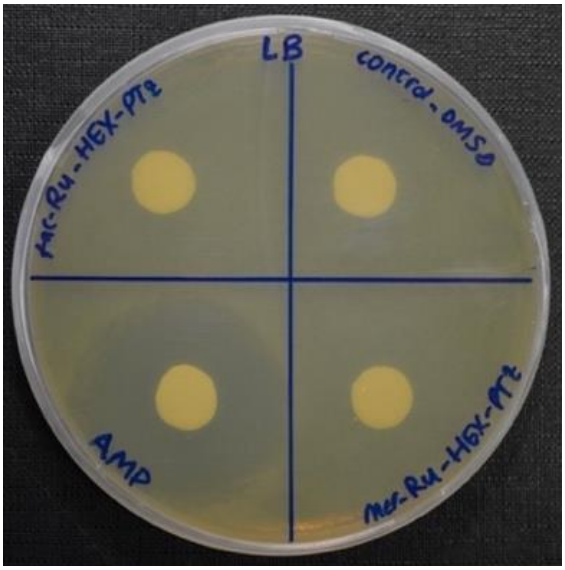

Figure 7.3. Disk diffusion test for *fac/mer*-**[Ru(PTZ-Hex)$_3$]$^{2+}$** against *E. coli*.

A completely different response was obtained when the same screening was performed with Gram-positive *D. radiodurans*. In particular, a clear growth inhibition zone did surround the paper disks imbued with *fac/mer*-**[Ru(PTZ-Hex)$_3$]$^{2+}$**, *fac/mer*-**[Ru(QTZ-Hex)$_3$]$^{2+}$** and *mer*-**[Ru(QTZ-^{t}Bu)$_3$]$^{2+}$** (Figure 5), while disks imbued with *fac*-**[Ru(QTZ-^{t}Bu)$_3$]$^{2+}$**, *fac/mer*-**[Ru(PTZ-^{t}Bu)$_3$]$^{2+}$**, *fac/mer*-**[Ru(PTZ-Me)$_3$]$^{2+}$**, and *fac/mer*-**[Ru(QTZ-Me)$_3$]$^{2+}$** did not inhibit bacterial growth.

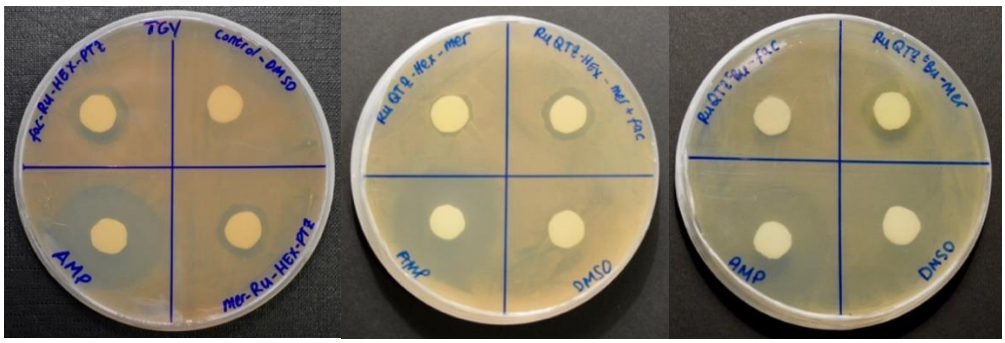

Figure 8.3. Disk diffusion test for *fac/mer*-**[Ru(PTZ-Hex)$_3$]$^{2+}$**, *fac/mer*-**[Ru(QTZ-Hex)$_3$]$^{2+}$** and *fac/mer*-**[Ru(QTZ-^{t}Bu)$_3$]$^{2+}$** against *D. radiodurans*.

3.3.3.2 *Kinetics of growth in a liquid medium*

In a successive stage, the antimicrobial properties of the Ru(II) complexes displaying a positive outcome in the disk diffusion tests against *D. radiodurans* were further investigated through analysis of the growth kinetics in a liquid medium. For the sake of comparison, also *fac*- and *mer*-**[Ru(QTZ-Me)$_3$]$^{2+}$** which resulted to be inactive toward *D. radiodurans* based on agar disks diffusion tests, were included in the series of Ru(II) complexes to be further screened. In the initial set of experiments, independent cultures containing the Ru(II) complexes at concentrations of 5 to 20 μM were prepared and their kinetics of growth were measured and compared to the control cultures. When *D. radiodurans* cultures were exposed to 20 μM solutions of *fac*- and *mer*-**[Ru(QTZ-Me)$_3$]$^{2+}$** (**Figure 9.3a**), a slight decrease of the rate of bacterial growth was observed. In excellent agreement with the outcome of the previous disk diffusion tests, these results suggest that no significant antibacterial activity could be traced back to neither the facial nor the meridional isomer of **[Ru(QTZ-Me)$_3$]$^{2+}$**. On the other hand, the replacement of the methyl group with a tert-butyl moiety produced a different result. Both *fac*- and *mer*-

[Ru(QTZ-^{t}Bu)$_3$]$^{2+}$ complexes were initially tested by treating individual *D. radiodurans* cultures with 20 μM of each isomer. (**Figure 9.3b**) Complete inhibition of the bacterial growth was observed in the presence of the *mer*-**[Ru(QTZ-^{t}Bu)$_3$]$^{2+}$** isomer, while the same concentration of *fac*-**[Ru(QTZ-^{t}Bu)$_3$]$^{2+}$** allowed a poor growth even though prolonged the lag phase (*i.e.* latent period). Conversely, at the lowest concentration limit (5 μM), both *fac* and *mer* **[Ru(QTZ-^{t}Bu)$_3$]$^{2+}$** reduced the rate of bacterial growth at a low extent, with a slightly more pronounced effect exerted by the *mer* isomer.

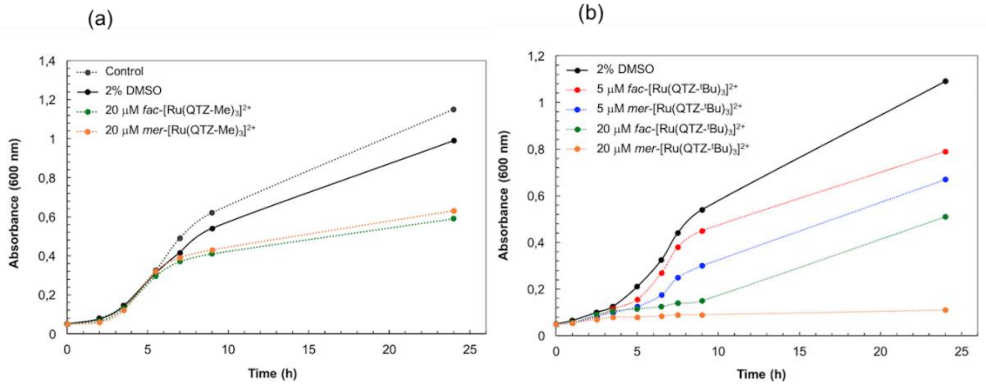

Figure 9.3. Kinetics of growth of *D. radiodurans* cultures incubated with *fac/mer*-**[Ru(QTZ-Me)$_3$]$^{2+}$** 20 μM (a) and *fac/mer*-**[Ru(QTZ-^{t}Bu)$_3$]$^{2+}$** 5 and 20 μM (b). Control cultures without any complex (black dots) and with 2% DMSO (black curve) were performed.

The influence played by the nature of the alkyl residue -**R** in determining the activity of the series of *fac/mer*-**[Ru(QTZ-R)$_3$]$^{2+}$** and *fac/mer*-**[Ru(PTZ-R)$_3$]$^{2+}$**-type complexes toward *D. radiodurans* became evident when the tetrazole rings were decorated with a linear hexyl chain (-**Hex**) to form the ligands abbreviated as **QTZ-Hex** and **PTZ-Hex**, respectively. In particular, *fac/mer*-**[Ru(QTZ-Hex)$_3$]$^{2+}$**, under the form of the pure *mer* isomer and as a mixture of *fac/mer* isomers - as mentioned earlier, samples of pure *fac*-**[Ru(QTZ-Hex)$_3$]$^{2+}$** could not be obtained even after several purification procedures - completely inhibited the growth of *D. radiodurans* both as 20 and 5 μM solutions (**Figure 10.3a**), suggesting the occurrence of a strong growth-inhibiting action even at their lower concentration limit. Successive experiments were performed to evaluate the lowest concentration values at which these latter complexes could exert a significant antibacterial activity.

To this extent, *D. radiodurans* cultures were exposed to pure *mer*-**[Ru(QTZ-Hex)$_3$]$^{2+}$** and to the mixture of isomers *fac/mer*-**[Ru(QTZ-Hex)$_3$]$^{2+}$** at the concentration values of 2.5 and 1.0 μM. Whereas pure *mer*-**[Ru(QTZ-Hex)$_3$]$^{2+}$** displayed the same poor antibacterial activity at both of the tested concentrations (Figure 7b, green and red lines), the mixture of isomers *fac/mer*-**[Ru(QTZ-Hex)$_3$]$^{2+}$** (**Figure 10.3b**, orange and blue lines) induced complete inhibition of the growth of *D. radiodurans* at the lowest concentration limit of 2.5 μM, highlighting a minimal inhibitory concentration (MIC) of 3.0 μg/mL. In further support of the importance of the hexyl substituent, it was observed that the 2-pyridyl tetrazole-based complexes *fac/mer*-**[Ru(PTZ-Hex)$_3$]$^{2+}$** displayed antimicrobial activity almost coincident to that determined for their quinolyl tetrazole analogues *fac/mer*-**[Ru(QTZ-Hex)$_3$]$^{2+}$**. Indeed, pure *fac*-**[Ru(PTZ-Hex)$_3$]$^{2+}$** (green and red lines, Figure 11.3, a) and *mer*-**[Ru(PTZ-Hex)$_3$]$^{2+}$** (orange and blue lines, **Figure 11.3a**) at a concentration of 20 and 5 μM, completely inhibited the growth of *D. radiodurans*.

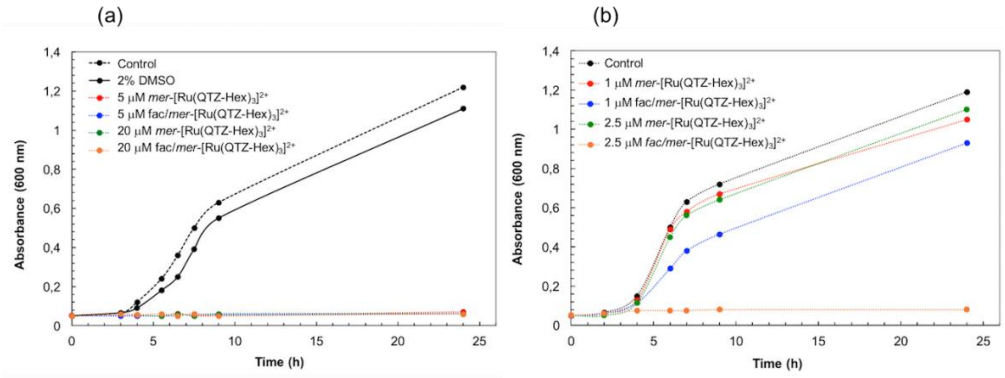

Figure 10.3. Kinetics of growth of *D. radiodurans* in the presence of *fac/mer*-**[Ru(QTZ-Hex)$_3$]$^{2+}$** at decreasing concentrations: 20 and 5 μM (a), 2.5 and 1 μM (b). Control cultures without any complex (black dots) were performed.

Also, when *fac* and *mer*-**[Ru(PTZ-Hex)$_3$]$^{2+}$** isomers were tested at lower concentrations (1 and 2.5 μM, **Figure 8b),** a significant inhibitory effect was detected only in the culture treated with the 2.5 μM solution of the pure isomer *fac*-**[Ru(PTZ-Hex)$_3$]$^{2+}$** (MIC = 3.0 μg/mL), while the growth rate of the remaining cultures – *i.e.* the ones containing 1 μM and 2.5 μM *mer*-**[Ru(PTZ-Hex)$_3$]$^{2+}$** and *fac*-**[Ru(PTZ-Hex)$_3$]$^{2+}$** at the concentration of 1 μM - was not affected (**Figure 11.3**).

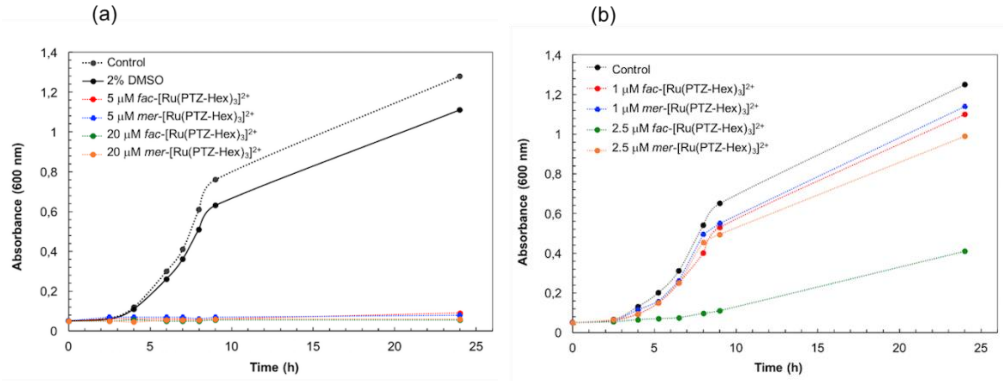

Figure 11.3. Kinetics of growth of *D. radiodurans* in the presence of *fac/mer*-**[Ru(PTZ-Hex)$_3$]$^{2+}$** at decreasing concentrations: 20 and 5 μM (a), 2.5 and 1 μM (b). Control cultures without any complex (black dots) were performed.

Taken together, these results suggest that whereas the choice of PTZ or QTZ-based scaffolds is, likely, not involved in inhibiting the growth of *D. radiodurans*; the proper turn-on of the growth inhibitory effect exerted by the corresponding Ru(II) complexes *fac/mer*-**[Ru(PTZ-R)$_3$]$^{2+}$** and *fac/mer*-**[Ru(QTZ-R)$_3$]$^{2+}$** takes place when the tetrazole ligands are decorated with a linear hexyl chain (-**Hex**). Also, investigation of the antimicrobial properties of *fac/mer*-**[Ru(PTZ-Hex)$_3$]$^{2+}$** and *fac/mer*-**[Ru(QTZ-Hex)$_3$]$^{2+}$** at concentrations below 5 μM suggested how the facial (*fac*) isomers apparently induced the inhibition of the growth of *D. radiodurans* (MIC ca. 3.0 μg/mL) to an extent higher than the one determined for corresponding meridional (*mer*) isomers (MIC ca. 6.0 μg/mL). It is worth noting how our findings concerning the antimicrobial activity of Ru(II)-tetrazoles derivatives *fac/mer*-**[Ru(PTZ-R)$_3$]$^{2+}$** and *fac/mer*-**[Ru(QTZ-R)$_3$]$^{2+}$** towards *D. radiodurans* share some important features with some previous reports dealing with effects deriving from the exposition of mononuclear Ru(II) polypyridyl complexes to different families of Gram-positive bacteria such as *B. subtilis* and, in particular, the pathogenic *S. aureus* and its methicillin-resistant variant MRSA.[3], [7a] First, the Ru(II)-tetrazole complexes described herein display the same selectivity to Gram-positive *versus* Gram-negative bacteria, the occurrence of which is probably related to the higher permeability of the cell wall of Gram-positive bacteria with respect to the Gram-negative ones. These latter microorganisms are indeed characterized by the presence of an outer membrane mainly composed of lipopolysaccharides (LPS), which

likely protects the Gram-negative bacteria from the Ru(II) bis cationic complexes.[3] Furthermore, in a manner identical as that reported by Crowley for Ru(II)pyridyl triazoles exposed to MRSA,[7a] the inhibitory activity towards *D. radiodurans* of our Ru(II) complexes *fac/mer*-**[Ru(PTZ-R)$_3$]$^{2+}$** and *fac/mer*-**[Ru(QTZ-R)$_3$]$^{2+}$** took place upon the introduction of a linear hexyl chain (R= Hex) in the backbone of the tetrazole based ligands. According to the explanations suggested by Crowley,[7a] this specific modification is most likely responsible for endowing the Ru(II) species of the appropriate level of lipophilicity for allowing these Ru(II) complexes to target the bacterial cytoplasmic membrane.

3.4 Conclusions

The introduction of one alkyl substituent at the N-2 position of the pentatomic ring of 2-pyridyl (PTZ) and 2-quinolyl tetrazole (QTZ) scaffolds led to a series of diimine-type chelators (N^N) that could be employed for the preparation of the new family of tris-homoleptic "fully tetrazole" $[Ru(N^N)_3]^{2+}$ complexes. The formation of the new Ru(II) species with the formula **$[Ru(PTZ\text{-}R)_3]^{2+}$** and **$[Ru(QTZ\text{-}R)_3]^{2+}$**, respectively, was confirmed by ESI mass spectrometry, and the NMR (^1H, ^{13}C) studies suggested the occurrence of each of the Ru(II) complexes as a statistical mixture of facial (*fac*) and meridional (*mer*) isomers. With the only exception of *fac*-**$[Ru(QTZ\text{-}Hex)_3]^{2+}$**), the *fac* and *mer* diastereomers were successfully separated by column chromatography, being the structure of one pure isomer, *mer*-**$[Ru(QTZ\text{-}Me)_3]^{2+}$**, confirmed by single-crystal X-ray diffraction. The investigation of the photophysical and electrochemical properties of the new Ru(II) complexes highlighted a behaviour that can be traced back to the family of tris-homoleptic Ru(II) polypyridyl complexes, and no significant difference between facial and meridional isomers of each complex was detected. The new families of bis cationic Ru(II) complexes, *fac/mer*-**$[Ru(PTZ\text{-}R)_3]^{2+}$** and *fac/mer*-**$[Ru(QTZ\text{-}R)_3]^{2+}$**, were therefore screened for any eventual antimicrobial activity *in vitro* against Gram-negative (*E. coli*) and Gram-positive (*D. radiodurans*) microorganisms. While all Ru(II) complexes were demonstrated as inactive toward *E. coli*, their growth inhibitory effect against *D. radiodurans* - a not pathogenic bacterium that is listed as one of the toughest microorganisms in light of its outstanding resistance to radiation, oxidative stress and DNA damage – appeared to be likely governed by specific structural features. In particular, it was observed the complete inhibition of the growth of *D. radiodurans* upon the introduction of a linear hexyl chain (**-Hex**) in the five-membered ring of the PTZ and QTZ ligands, also highlighting how the activity of the facial isomers, *fac*-**$[Ru(PTZ\text{-}Hex)_3]^{2+}$** and *fac*-**$[Ru(QTZ\text{-}Hex)_3]^{2+}$** (MIC = *ca.* 3.0 μg/mL) appeared more pronounced than the one displayed by the corresponding *mer* isomers (MIC = *ca.* 6.0 μg/mL). Therefore, our results on the antibacterial properties of these homoleptic "fully tetrazole" Ru(II) complexes, which are generally congruent with those relative to the closely related family of Ru(II)-pyrydyltriazole based species that have been previously reported

by the group of Crowley,[7a] support the possibility of getting useful insight for the determination of the structure to activity relationships that promote and, possibly, govern the antibacterial properties of tris homoleptic Ru(II) complexes. Even though our complexes have not been tested yet toward antibiotic-resistant bacteria such as *Staphylococcus aureus* MRSA, the consistency of our findings with respect to those described by Crowley might support the use of the non-pathogenic *Deinococcus radiodurans* as a useful model for Gram-positive bacteria in studies dealing with the search of new antimicrobials.

3.5 Experimental Section

General considerations. All the reagents and solvents were obtained commercially (Sigma Aldrich/Merck, Alfa Aesar, Strem Chemicals) and used as received without any further purification unless otherwise specified. All the reactions were carried out under an argon atmosphere following Schlenk protocols. The purification of the Ru(II) complexes was performed via column chromatography with the use of SiO_2 or Al_2O_3 as the stationary phase. ESI-mass spectra were recorded using a Waters ZQ-4000 instrument (ESI-MS, acetonitrile as the solvent). Nuclear magnetic resonance spectra (consisting of ^1H and ^{13}C) were always recorded using a Varian Mercury Plus 400 (^1H, 399.9; ^{13}C, 101.0 MHz). ^1H and ^{13}C chemical shifts were referenced to residual solvent resonances. Absorption spectra were recorded at 298K using an Agilent Cary 100 UV-vis spectrometer.

Cyclic Voltammetry

$TBAPF_6$ (tetrabutylammonium hexafluorophosphate, Sigma Aldrich) was used as received as the supporting electrolyte, CH_3CN was distilled over CaH_2 and thoroughly degassed under N_2 before each measurement. Electrochemical experiments were recorded with a Metrohm Autolab PGSTAT302N potentiostat-galvanostat using a Calomel electrode as reference (303/SCG/6 – Amel Electrochemistry) and a Platinum solid electrode (492/Pt/2 – Amel Electrochemistry) as working electrode.

Ligand synthesis

Tetrazole derivatives are used as components for explosive mixtures.[10] In this lab, the reactions described here were only run on a few grams scale and no problems were encountered. However, *great caution* should be exercised when handling or heating compounds of this type.

Following the general method reported by Koguro and co-workers,[8] tetrazole ligand [H-**PTZ**] and [H-**QTZ**] were obtained in quantitative yield.

[H-**PTZ**] ^{1}H-NMR (DMSO d^6, 400 MHz) δ (ppm) = 8.82 (m, 1H); 8.25 (m, 1H); 8.10 (m, 1H); 7.66 (m, 1H); [H-**QTZ**] **^{1}H-NMR**, (DMSO-d^6, 400 MHz) δ (ppm) = 8,65 (d,

1H, *J* = 8.79 Hz), 8,31 (d, 1H, *J* = 8.40 Hz), 8,17 (d, 1H, *J* = 8.40 Hz), 8,12 (d, 1H, *J* = 7.99 Hz), 7,90 (t, 1H), 7.74 (t, 1H);

Ligand functionalization

General procedure for the preparation of [PTZ-Me] and [QTZ-Me].[13a]

In a 100 mL two neck round-bottomed flask equipped with a stirring bar were added 1 eq of the desired tetrazole ligand (H-QTZ, H-PTZ), 2 eq. of CH_3I and 3 eq. of K_2CO_3 in 20 mL of CH_3CN. The mixture was heated at reflux for 24 h. The mixture was then allowed to cool down to room temperature (hereafter, r.t.) and the solvent removed by rotary evaporation. The crude was dissolved in 10 mL of CH_2Cl_2 and filtered over a glass frit filter to remove the insoluble fraction. The soluble fraction was then purified with column chromatography over SiO_2 (PTZ-Me: Toluene/Acetone 9:1; QTZ-Me: hexane/EtOAc 6:4) yielding the desired N2 methylated isomer as second fraction (PTZ-Me: Y = 20%, 0.69 mmol; QTZ-Me: Y = 39%, 0.79 mmol).

[PTZ-Me]: **^{1}H-NMR**, 400 MHz, $CDCl_3$ δ (ppm): 8.77 (ddd, J = 4.9, 1.8, 1.0 Hz, 1H), 8.23 (dt, J = 7.9, 1.1 Hz, 1H), 7.86 (td, J = 7.8, 1.8 Hz, 1H), 7.40 (ddd, J = 7.6, 4.8, 1.2 Hz, 1H), 4.44 (s, 3H) **^{13}C-NMR**, 100 MHz, $CDCl_3$ δ (ppm): 164.93 (C_t), 150.21, 146.82, 137.22, 124.87, 122.35, 39.68.

[QTZ-Me]: **^{1}H-NMR**, 400 MHz, $CDCl_3$ δ (ppm): 8.25 – 8.21 (m, 1H), 7.74 (d,1 H, J = 8.15 Hz), 7.70 – 7.66 (m, 1H), 7.50 – 7.46(m, 1H), 4.39 (s, 3H). **^{13}C-NMR**, 100 MHz, $CDCl_3$ δ (ppm): 164. 98 (C_t), 148.01, 146.49, 137.25, 130.01, 129.93, 128.32, 127.54, 127.42, 119.54, 39.71 (CH_3).

General procedure for the preparation of [PTZ-^{t}Bu] and [QTZ-^{t}Bu].[13b]

In a 50 mL two neck round bottomed flask equipped with a stirring bar was added the desired tetrazole ligand (H-QTZ, H-PTZ, 1eq.) to 15 mL of tert-butanol in the presence of 3.0 mL of trifluoroacetic acid and 3.0 mL of concentrated sulphuric acid. The mixture was left to stir at r.t. overnight, during which time the initial suspension turned to a yellowish solution. Then, the mixture was poured into ice–water and made alkaline (pH > 12) by the addition of KOH pellets. The resulting mixture was extracted with $CHCl_3$ (3 × 15 mL) and the organic layers were dried over $MgSO_4$. The solvent was then removed by rotary evaporation, providing the desired compound as an oily yellow residue (PTZ-^{t}Bu: Y = 77%, 2.53 mmol; QTZ-^{t}Bu: Y = 83% 1.27 mmol).

[PTZ-^{t}Bu]: **^{1}H-NMR**, 400 MHz, $CDCl_3$ δ (ppm): 8.80 (d, 1H, J = 4.18 Hz), 8.27 (d, 1H, J = 7.83 Hz), 7.86 (m, 1H), 7.39 (m, 1H), 1.83 (s, 9H).

[QTZ-^{t}Bu]: **^{1}H-NMR**, 400 MHz, $CDCl_3$ δ (ppm): 8.39 – 8.29 (m, 3H), 7.87 (ddd, J = 8.3, 1.6, 0.7 Hz, 1H), 7.77 (ddd, J = 8.5, 6.9, 1.5 Hz, 1H), 7.60 (ddd, J = 8.1, 6.9, 1.2 Hz, 1H), 1.87 (s, 9H).

General procedure for the preparation of [PTZ-Hex] and [QTZ-Hex].[13c]

In 100 mL two neck round bottomed flask equipped with a stirring bar was added the desired tetrazole ligand (H-QTZ, H-PTZ, 1eq.) to 30 mL of CH_3CN in the presence of 1-bromohexane (1.1 eq) and Et_3N (1.5 eq). The mixture was heated at reflux for 8h and then allowed to cool down to r.t. The crude product was then purified with column chromatography over SiO_2 (PTZ-Hex: Hexane/EtOAc 6:4; QTZ-Hex: Petroleum ether/EtOAc 9:1) yielding the desired N2-hexyl isomer as second fraction (PTZ-Hex: Y = 27 %, 0.92 mmol; QTZ-Hex: Y = 14%, 0.69 mmol).

[PTZ-Hex]: **^{1}H-NMR**, 400 MHz, $CDCl_3$ δ (ppm): 8.71-8.69 (m, 1H), 8.18-8.15 (m, 1H), 7.98-7.75 (m, 1H), 7.32-7.28 (m, 1H), 4.64-4.60 (m, 2H), 2.03-1.95 (m, 2H), 1.30-1.16 (m, 6H), 0.80-0.76 (m, 3H). **^{13}C-NMR**, 100 MHz, $CDCl_3$ δ (ppm): 164.60 (Ct), 150.20, 146.84, 137.04, 124.69, 122.28, 53.45, 30.93, 29.22, 25.92, 22.27, 13.81.

[QTZ-Hex]: **^{1}H-NMR**, 400 MHz, $CDCl_3$ δ (ppm): 8.38 – 8.27 (m, 3H), 7.85 (dd, J = 8.2, 1.4 Hz, 1H), 7.75 (ddd, J = 8.5, 6.9, 1.5 Hz, 1H), 7.58 (ddd, J = 8.1, 6.9, 1.1 Hz, 1H), 4.73 (t, J = 7.3 Hz, 2H), 2.11 (p, J = 7.4 Hz, 2H), 1.42 – 1.26 (m, 6H), 0.95 – 0.75 (m, 3H). **^{13}C-NMR**, 100 MHz, $CDCl_3$ δ (ppm): 164.83 (Ct), 148.09, 146.84, 137.38, 130.15, 128.44, 127.61, 127.51, 119.75, 53.61, 31.02, 29.38, 26.03, 22.36, 13.89.

General procedure for the synthesis of homoleptic fac-mer $[Ru(N\hat{}N)_3]^{2+}$-type complexes

To a 7:3 solution of EtOH/H_2O (30 mL) were added $RuCl_3$*xH_2O (100 mg, 1 eq) and 3.2 eq of the desired 5-Aryltetrazole. The solution was stirred at reflux temperature overnight. The solvent was removed by rotary-evaporation and water was added (10 mL). Anion exchange was carried out by adding an excess of NH_4PF_6 (5 eq) to the solution and stirring for 1 hour. The solid product was isolated via vacuum filtration then washed with H_2O and Et_2O.

***fac/mer* $[Ru(PTZ\text{-}Me)_3]^{2+}$** Y= 39 % (MW = 874.16 g/mol, 0.0680 g, 0.0778 mmol, Column chromatography over Al_2O_3 eluted with DCM/ACN 1:1).

fac: **^{1}H-NMR**, 400 MHz, CD_3CN δ (ppm): 8.48 -8.43 (m, 3H), 8.26 – 8.19 (m, 3H), 7.98 – 7.95 (m, 3H), 7.65 – 7.60 (m, 3H), 4.42 (s, 9H) **^{13}C-NMR**, 100 MHz, CD_3CN δ (ppm): 166.36 (C_t), 154.90, 147.40, 140.52, 129.84, 125.28, 42.97 (CH_3). **ESI-MS** (*m/z*): $[M]^{2+}$ = 292; $[M]^{2-}$ = 145 (PF_6^-). Anal. Calcd. For $C_{21}H_{21}N_{15}Ru_1P_2F_{12}$ (847.16) C 28.84, H 2.42, N 24.03. Found: C 27.54, H 2.42, N 21.90.

mer: **^{1}H-NMR**, 400 MHz, CD_3CN δ (ppm): 8.46 (ddd, J = 7.9, 1.5, 0.8 Hz, 1H), 8.39 (ddd, J = 7.9, 1.5, 0.8 Hz, 1H), 8.36 (ddd, J = 7.9, 1.5, 0.8 Hz, 1H), 8.23 – 8.08 (m, 4H), 8.00 (ddd, J = 5.6, 1.4, 0.8 Hz, 1H), 7.80 (ddd, J = 5.6, 1.4, 0.8 Hz, 1H), 7.60 (ddd, J = 7.8, 5.7, 1.5 Hz, 1H), 7.52 (tdd, J = 7.8, 5.6, 1.5 Hz, 2H), 4.46 (s, 3H), 4.45 (s, 3H), 4.41 (s, 3H). **^{13}C-NMR**, 100 MHz, CD_3CN δ (ppm): 166.55 (C_t), 166.46 (C_t), 166.38 (C_t), 155.37, 155.26, 147.58, 147.56, 147.35, 140.40, 140.37, 140.30, 129.69, 129.1), 128.96, 125.56 (s), 124.94, 124.74, 42.99 (CH_3), 42.92 (CH_3), 42.91 (CH_3). **ESI-MS** (*m/z*): $[M]^{2+}$

= 292; $[M]^{2-}$ = 145 (PF_6^-). Anal. Calcd. For $C_{21}H_{21}N_{15}Ru_1P_2F_{12}$ (847.16) C 28.84, H 2.42, N 24.03. Found: C 28.16, H 2.42, N 22.91.

***fac/mer* [Ru(PTZ-^{t}Bu)$_3$]$^{2+}$** Y = 26 % (MW= 1000.31 g/mol, 0.0937 g, 0.0937 mmol, Column chromatography over Al_2O_3 eluted with DCM/ACN 1:1).

fac: **^{1}H-NMR**, 400 MHz, CD_3CN δ (ppm): 8.43 - 8.37 (m, 3H), 8.25 - 8.18 (m, 3H), 8.03 – 7.97 (m, 3H), 7.72 – 7.52 (m, 3H), 1.71 (s, 27H, ^{t}Bu). **^{13}C-NMR**, 100 MHz, $(CD_3)_2O$ δ (ppm): 166.45 (C_t), 155.11, 148.06, 140.68, 130.10, 125.43, 69.50, 29.26 (CH_3). **ESI-MS** (*m/z*): $[M]^{2+}$ = 355; $[M]^{2-}$ = 145 (PF_6^-). Anal. Calcd. For $C_{30}H_{39}N_{15}Ru_1P_2F_{12}$ (1000.31) C 36.01, H 3.93, N 20.99. Found: C 36.89, H 4.06, N 21.51.

mer: **^{1}H-NMR**, 400 MHz, CD_3CN δ (ppm): 8.44 - 8.34 (m, 2H), 8.34 - 8.29 (m, 1H), 8.22 – 8.08 (m, 3H), 7.96 – 7.93 (m, 1H), 7.88 (dt, J = 5.4, 1.1 Hz, 1H), 7.85 (dt, J = 5.5, 1.2 Hz, 1H), 7.61 (ddd, J = 7.8, 5.6, 1.5 Hz, 1H), 7.56 - 7.46 (m, 2H), 1.75 (s, 9H), 1.73 (s, 9H), 1.71 (s, 9H). **^{13}C-NMR**, 100 MHz, CD_3CN δ (ppm): 166.33 (C_t), 166.23 (C_t), 166.06 (C_t), 155.29, 155.12, 155.00, 148.02, 147.93, 147.81, 140.33, 140.21, 140.18, 129.74, 128.89, 125.34, 124.77, 124.57, 29.22 (^{t}Bu), 29.18 (^{t}Bu), 29.15 (^{t}Bu). **ESI-MS** (*m/z*): $[M]^{2+}$ = 355; $[M]^{2-}$ = 145 (PF_6^-). Anal. Calcd. For $C_{30}H_{39}N_{15}Ru_1P_2F_{12}$ (1000.31) C 36.01, H 3.93, N 20.99. Found: C 34.3, H 3.81, N 19.35.

***fac/mer* [Ru(PTZ-Hex)$_3$]$^{2+}$** Y = 52 % (MW= 1084 g/mol, 0.216 g, 0.199 mmol, Column chromatography over Al_2O_3 eluted with EtOAc/Acetone 8:2).

fac: **^{1}H-NMR**, 400 MHz, CD_3CN δ (ppm): 8.75 – 8.73 (m, 3H), 8.19 – 8.16 (m, 3H), 7.96 – 7.94 (m, 3H), 7.51 – 7.43 (m, 3H), 4.75 – 4.69 (m, 6H), 2.06 – 1.98 (m, 6H) 1.36 – 1.27 (m, 18H), 0.90 – 0.87 (m, 9H). **^{13}C-NMR**, 100 MHz, CD_3CN δ (ppm): 165.43 (Ct), 154.07, 146.57, 139.59, 128.91, 124.35, 55.90, 30.45, 28.36, 25.24, 22.06, 13.19. **ESI-MS** (*m/z*): $[M]^{2+}$ = 397; $[M]^{2-}$ = 145 (PF_6^-). Anal. Calcd. For $C_{36}H_{51}N_{15}Ru_1P_2F_{12}$ (1084.07) C 39.86, H 4.74, N 19.37. Found: C 40.98, H 5.03, N 18.38.

mer: **^{1}H-NMR**, 400 MHz, CD_3CN δ (ppm): 8.47 – 8.44 (m, 1H), 8.41- 8.39 (m, 1H), 8.38 – 8-34 (m, 1H), 8.23 – 8.13 (m, 3H), 8.05 – 8.04 (m, 1H), 7.95 – 7.94 (m, 1H), 7.85 – 7.84 (m, 1H), 7.63 – 7.59 (m, 1H), 7.55 – 7.51 (m, 2H), 4.77 – 4.71 (m, 6H), 2.03 –

1.99 (m, 6H), 1.35 – 1.25 (m, 18H), 0.90 – 0.84 (m, 9H). **^{13}C-NMR**, 100 MHz, CD_3CN δ (ppm): 165.92 (Ct), 165.86 (Ct), 165.71 (Ct), 154.68, 154.53, 154.38, 147.07, 147.01, 146.88, 139.78, 139.73, 139.68, 129.07, 128.53, 128.30, 124.94, 124.35, 124.13, 56.35, 56.30, 56.09, 30.91, 30.82, 30.76, 28.75, 28.68, 28.52, 25.78, 25.71, 25.53, 22.37, 22.35, 22.31, 13.52, 13.50, 13.47. **ESI-MS** (*m/z*): $[M]^{2+}$ = 397; $[M]^{2-}$ = 145 (PF_6^-). Anal. Calcd. For $C_{36}H_{51}N_{15}Ru_1P_2F_{12}$ (1084.07) C 39.86, H 4.74, N 19.37. Found: C 40.43, H 4.89, N 18.86.

***fac/mer* [Ru(QTZ-Me)$_3$]$^{2+}$** Y = 49 % (MW = 1024.21 g/mol, 0.0923 g, 0.0895 mmol, Column chromatography over Al_2O_3 eluted with DCM/ACN 1:1). *fac:* **^{1}H-NMR**, 400 MHz, $(CD_3)_2CO$ δ (ppm): 9.07 (dd, J = 8.6, 0.8 Hz, 3H), 8.69 (d, J = 8.4 Hz, 3H), 8.34 (dd, J = 8.2, 1.5 Hz, 3H), 8.10 (dd, J = 8.9, 0.9 Hz, 3H), 7.76 (ddd, J = 8.1, 6.9, 1.0 Hz, 3H), 7.26 (ddd, J = 8.7, 7.0, 1.5 Hz, 3H), 4.52 (s, 9H, CH_3). **^{13}C-NMR**, 100 MHz, $(CD3)_2O$ δ (ppm):168.01 (C_t), 150.94, 148.90, 143.24, 134.01, 131.46, 131.42, 130.76, 130.76, 127.26, 120.82, 43.14 (CH_3). **ESI-MS** (*m/z*): $[M]^{2+}$ = 367; $[M]^{2-}$ = 145 (PF_6^-). Anal. Calcd. For $C_{33}H_{27}N_{15}Ru_1P_2F_{12}$ (1024.21) C 38.68, H 2.66, N 20.50. Found: C 39.45, H 2.84, N 21.03.

mer: **^{1}H-NMR**, 400 MHz, CD_3CN δ (ppm): 8.77 (dd, J = 8.5, 0.9 Hz, 1H), 8.67 - 8.59 (m, 2H), 8.45 (d, J = 8.5 Hz, 1H), 8.33 (d, J = 8.4 Hz, 1H), 8.27 (d, J = 8.4 Hz, 1H), 8.15 - 8.09 (m, 2H), 8.03 (dd, J = 8.2, 1.5 Hz, 1H), 7.77 (ddd, J = 8.1, 7.0, 1.1 Hz, 1H), 7.71 – 7.55 (m, 3H), 7.56 – 7.42 (m, 2H), 7.17 (dd, *J* = 8.9, 0.9 Hz, 1H), 7.05 (ddd, *J* = 8.8, 6.9, 1.5 Hz, 1H), 6.68 (dd, J = 8.9, 0.9 Hz, 1H), 4.49 (s, 3H), 4.44 (s, 3H), 4.40 (s, 3H). **^{13}C-NMR**, 100 MHz, $(CD_3)_2O$ δ (ppm): 167.65, 167.16, 166.58, 150.55, 150.44, 149.82, 149.05, 148.80, 148.10, 133.86, 133.32, 132.62, 130.51, 130.19, 130.04, 129.83, 129.74, 129.62, 129.55, 125.59 124.68, 124.11, 119.59, 119.45, 119.16, 42.33, 42.30, 42.27. **ESI-MS** (*m/z*): $[M]^{2+}$ = 367; $[M]^{2-}$ = 145 (PF_6^-). Anal. Calcd. For $C_{33}H_{27}N_{15}Ru_1P_2F_{12}$ (1024.21) C 38.68, H 2.66, N 20.50. Found: C 39.45, H 2.84, N 21.03.

***fac/mer* [Ru(QTZ-^{t}Bu)$_3$]$^{2+}$** Y = 47 % (MW = 1150 g/mol, 0.207 g, 0.180 mmol, Column chromatography over SiO_2 eluted with $CH_3CN/H_2O/KNO_{3(aq)}$ 20:1:0.1. Counterion

exchange was carried out by stirring overnight ***fac*** and ***mer*** **[Ru(QTZ-Hex)$_3$]$^{2+}$** in a saturated CH_2Cl_2/KPF_6 solution).

fac: **^{1}H-NMR**, 400 MHz, CD_3CN δ (ppm): 9.81 -9.79 (d, *J* = 7.9 Hz, 3H), 8.52 – 8.50 (d, *J* = 7.9 Hz, 3H), 8.30 – 8.28 (d, *J* = 7.9 Hz, 3H), 8.14 – 8.10 (m, 3H), 8.04 – 7.99 (m, 3H), 7.89 – 7.85 (m, 3H), 1.80 (s, 27H). **^{13}C-NMR**, 100 MHz, CD_3CN δ (ppm): 168.43 (Ct), 151.48, 149.95, 140.18, 130.33, 129.43, 128.30, 128.12, 127.04, 118.52, 68.02, 28.07. **ESI-MS** (*m/z*): $[M]^{2+}$ = 430; $[M]^{2-}$ = 145 (PF_6^-). Anal. Calcd. For $C_{42}H_{45}N_{15}Ru_1P_2F_{12}$ (1150) C 43.83, H 3.94, N 18.25. Found: C 43.16, H 4.05, N 17.97.

mer: **^{1}H-NMR**, 400 MHz, CD_3CN δ (ppm): 8.78 – 8.76 (d, *J* = 7.9 Hz, 1H), 8.56 – 8.62 (m, 2H), 8.45 – 8.43 (d, *J* = 7.9 Hz, 1H), 8.32 – 8.30 (d, *J* = 7.9 Hz, 1H), 8.22 – 8.20 (d, *J* = 7.9 Hz, 1H), 8.18 – 8.15 (m, 1H), 8.12 – 8.06 (m, 2H), 8.05 – 7.77 (m, 1H), 7.70 – 7.53 (m, 4H), 7.46 – 7.42 (m, 1H), 7.06 – 7.02 (m, 1H), 6.97 – 6.95 (m, 1H), 6.69 – 6.67 (m, 1H), 1.77 (s, 9H), 1.72 (s, 9H), 1.67 (s, 9H). **^{13}C-NMR**, 100 MHz, CD_3CN δ (ppm): 166.94, 166.61, 166.20, 150.65, 150.63, 150.26, 149.85, 149.60, 149.13, 148.51, 148.04, 141.80, 141.72, 141.49, 133.17, 132.81, 132.62, 132.33, 130.28, 130.06, 129.87, 129.75, 129.70, 128.02, 126.66, 125.99, 124.36, 119.87, 119.52 119.46, 69.32, 69.27, 68. 88, 28.36, 28.24, 28.19. **ESI-MS** (*m/z*): $[M]^{2+}$ = 430; $[M]^{2-}$ = 145 (PF_6^-). Anal. Calcd. For $C_{42}H_{45}N_{15}Ru_1P_2F_{12}$ (1150) C 43.83, H 3.94, N 18.25. Found: C 44.34, H 4.06, N 18.8.

fac/mer **[Ru(QTZ-Hex)$_3$]$^{2+}$** Y = 59 % (MW = 1234 g/mol, 0.279 g, 0.226 mmol, Column chromatography over SiO_2 eluted with $CH_3CN/H_2O/KNO_{3(aq)}$ 20:1:0.1. Counterion exchange was carried out by stirring overnight ***mer*** **[Ru(QTZ-Hex)$_3$]$^{2+}$** in a saturated CH_2Cl_2/KPF_6 solution).

fac: **^{1}H-NMR**, 400 MHz, CD_3CN δ (ppm): not isolated.

mer: **^{1}H-NMR**, 400 MHz, CD_3CN δ (ppm): 8.76 - 8.70 (m, 3H), 8.46 - 8.44 (m, 1H), 8.41 - 8.39 (m, 1H), 8.31 - 8.29 (m, 1H), 8.21 - 8.19 (m, 1H), 8.11 - 8.08 (m, 1H), 7.83 - 7.80 (m, 1H), 7.70 - 7.60 (m, 3H), 7.46 - 7.39 (m, 1H), 7.15 - 7.13 (m, 1H), 7.04 - 7.00 (m, 1H), 6.70 - 6.68 (m, 1H), 4.77 - 4.68 (m, 6H), 2.15 - 1.90 (m, 10H), 1.31 - 1.11 (m,

16H), 0.88 - 0.78 (m, 9H). **^{13}C-NMR**, 100 MHz, CD_3CN δ (ppm): 167.56, 167.07, 166.41, 150.85, 150.30, 150.17, 149.29, 148.84, 148.35, 141.90, 141.73, 141.65, 133.71, 133.09, 132.48, 130.61, 130.28, 130.19, 129.94, 129.88, 129.83, 129.61, 129.52, 125.39, 124.60, 124.35, 119.81, 119. 43, 119.33, 117.29, 56.47, 56.22, 56.07, 30.46, 30.44, 30.30, 28.46, 28.39, 28.32, 25.40, 25.31, 25.05, 22.06, 22.03, 22.1, 13.19, 13.17. 13.15. **ESI-MS** (*m/z*): $[M]^{2+}$ = 472; $[M]^{2-}$ = 145 (PF_6^-). Anal. Calcd. For $C_{48}H_{57}N_{15}Ru_1P_2F_{12}$ (1234) C 46.68, H 4.65, N 17.01. Found: C 47.06, H 4.74, N 17.56.

Disk diffusion test

The antimicrobial activity of *fac/mer* $[Ru(N\hat{}N)_3]^{2+}$ complexes was evaluated by using the disk diffusion test in agar plates. Single colonies of *Escherichia coli* TOP10 and *Deinococcus radiodurans* DSM 46620 were grown in LB (10 g/L tryptone, 5 g/L yeast extract, 10 g/L NaCl) and TGY (5 g/L tryptone, 3 g/L yeast extract, 1 g/L glucose) liquid medium at 37 or 30 °C, respectively. After overnight incubation, 0.1 mL of each bacterial suspension (approximately $1x10^7$ CFU) was spread onto LB-agar and YPD-agar plates (1.5% agar), respectively. Sterile paper disks (diameter: 1 cm, 4 disks per plate) impregnated individually with 20 μL of each ruthenium(II) compound (1 mg/1 mL DMSO) were placed on each plate. All plates included an ampicillin-disk as positive control (100 μg/mL) and a DMSO alone-disk (20 μL) as negative control. After incubation for 24 h at the proper temperature (30 °C for *D. radiodurans* and 37 °C for *E. coli*), the presence of inhibition zones of bacterial growth was evaluated.

Bacterial growth curves

Single colonies of *E. coli* were grown in LB medium (2 mL) at 37 °C under shaking for 15 h. The inoculum of *D. radiodurans* was prepared by growing a single colony in 5 mL of TGY broth at 30 °C for 24 h under shaking. Each pre-culture was diluted to 0.05 optical density at 600 nm (OD_{600nm}) into fresh LB and TGY medium (5 mL), respectively, and the kinetics of growth was measured at appropriate time intervals by reading the optical density at 600 nm using a plastic cuvette in a spectrophotometer (GeneQuant, Amersham Pharmacia). 5 μM and 20 μM of *fac/mer* $[Ru(N\hat{}N)_3]^{2+}$

complexes were separately added to *E. coli* or *D. radiodurans* cultures. Control cultures treated with DMSO alone (2%) were performed.

Determination of MIC

The minimal inhibitory concentration (MIC) was determined by the broth dilution method using different concentrations of *fac/mer*-**[Ru(PTZ-R)$_3$]$^{2+}$** and *fac/mer*-**[Ru(QTZ-R)$_3$]$^{2+}$** complexes. In detail, independent cultures of *D. radiodurans* (5 mL TGY), prepared as described before, were incubated with proper dilutions of *fac/mer*-**[Ru(PTZ-R)$_3$]$^{2+}$** and *fac/mer*-**[Ru(QTZ-R)$_3$]$^{2+}$**complexes to obtain final concentrations ranging from 0 to 5 μM. The dilutions of ruthenium(II) complexes were performed in DMSO. The MIC was determined as the lowest concentration of *fac/mer*-**[Ru(PTZ-R)$_3$]$^{2+}$** and *fac/mer*-**[Ru(QTZ-R)$_3$]$^{2+}$** complexes able to inhibit microbial growth. The rate of bacterial growth was evaluated by measuring the turbidity as described before. A control culture containing DMSO alone was also prepared.

X-ray crystallography

The diffraction experiments were carried out on a Bruker APEX II diffractometer equipped with a PHOTON100 detector and using Mo-K radiation. Data were corrected for Lorentz polarization and absorption effects (empirical absorption correction SADABS).[16] Structures were solved by direct methods and refined by full-matrix least-squares based on all data using F^2.[17] H-atoms were placed in calculated positions and refined isotropically using a riding model. All non-hydrogen atoms were refined with anisotropic displacement parameters.

3.6 References

[1] S. Campagna, F. Puntoriero, F. Nastasi G. Bergamini, and V. Balzani, *Top. Curr. Chem.*, **2007**, *280*, 117 – 214; b) M. D. K. Nazeeruddin, E. Baranoff, M. Grätzel, *Solar Energy*, **2011**, *85*, 1172-1178 and references cited herein.

[2] a) J. Shum, P. K.-K. Leung, and K. K.-W. Lo *Inorg. Chem.*, **2019**, *58*, 2231-2247, and references cited therein; b) Q. Zhao, C. Huang, F. Li, *Chem. Soc. Rev.*, **2011**, *40*, 2508-2524 and references cited therein.

[3] F. Li, J. G. Collins, F. R. Keene, *Chem. Soc. Rev.*, **2015**, *44*, 2529-2542 and references cited therein.

[4] a) F. Dwyer, E. C. Gyarfas, W. P. Rogers, J. H. Koch, *Nature*, **1952**, *170*, 190−1. b) F. Dwyer, I. K. Reid, A. Shulman, G. M. Laycock, S. Dixson, *Immunol. Cell Biol.*, **1969**, *47*, 203−18.

[5] F. Li, Y. Mulanya, M. Feterl, J. M. Warner, J. G. Collins, F. R. Keene, *Dalton Trans.*, **2011**, *40*, 5032-5038.

[6] a) L. Lu, L.–J. Liu, W.-C. Chao, H.-J. Zhong, M. Wang, X.–P. Chen, J.–J. Lu, R.-N Li, D.–L. Ma, C.–H. Leung, *Sci. Rep.*, **2015**, *5*, 14544; see also: b) J. A. Lemire, J. J. Harrison, R. J. Turner, *Nature Reviews Microbiology*, **2013**, *11*, 371–384.

[7] a) S. V. Kumar, S. Ø. Scottwell, E. Waugh, C. J. McAdam, L. R. Hanton, H. J. L. Brooks, J. D. Crowley, *Inorg. Chem.*, **2016**, *55*, 9767-9777; b) Q. V. C. van Hilst, R. A. S. Vasdev, D. Preston, J. A. Findlay, S. Ø. Scottwell, G. I. Giles, H. J. L. Brooks, J. D. Crowley, *Asian J. Org. Chem.*, **2019**, *8*, 496 –505.

[8] a) N. Akabar, V. Chaturvedi, G. E. Shillito, B. J. Schwehr, K. C. Gordon, G. S. Huff, J. J. Sutton, B. W. Skelton, A. N. Sobolev, S. Stagni, D. J. Nelson, M. Massi, *Dalton Trans.*, **2019**, *48*, 15613 – 15624; b) M. J. Stout, A. Stefan, B. W. Skelton, A. N. Sobolev, M. Massi, A. Hochkoeppler, S. Stagni, P. V. Simpson, *Eur. J. Inorg. Chem.*, **2020**, 292 – 298; c) A. Sorvina, C. A. Bader, J. R. T. Darby, M. C. Lock, J. Y. Soo, I. R. D. Johnson, C. Caporale, N. H. Voelcker, S. Stagni, M. Massi, J. L. Morrison, S. E. Plush, D. A. Brooks, *Sci. Rep.*, **2018**, *8*, 8191; d) V. Fiorini, L. Bergamini, N. Monti, S. Zacchini, S. E. Plush, M. Massi, A.

Hochkoeppler, A. Stefan, S. Stagni, *Dalton Trans.*, **2018**, *47*, 9400 - 9410; e) C. Caporale, C. A. Bader, A. Sorvina, K. D. M. MaGee, B. W. Skelton, T. A. Gillam, P. J. Wright, P. Raiteri, S. Stagni, J. L. Morrison, S. E. Plush, D. A. Brooks, M. Massi, *Chem. Eur. J.*, **2017**, *23*, 15666 – 15679, and references cited therein.

[9] A. M. Ranieri, C. Caporale, V. Fiorini, A. Hubbard, P. Rigby, S. Stagni, E. Watkin, M. I. Ogden, M. J. Hackett, M. Massi, *Chem. Eur. J.*, **2019**, *25*, 10566 – 10570.

[10] V. Fiorini, I. Zanoni, S. Zacchini, A. L. Costa, A. Hochkoeppler, V. Zanotti, A. M. Ranieri, M. Massi, A. Stefan, S. Stagni, *Dalton. Trans.*, **2017**, *46*, 12328-12338.

[11] (a) D. Slade and M. Radman, *Microbiol. Mol. Biol. Rev.*, 2011, **75**, 133–191; (b) L. Wei, M. Yun, X. Fangzhu, H. Shuya, *Adv. Nat. Sci.*, **2014**, *7*, 6–14.

[12] K. Koguro, T. Oga, S. Mitsui, R. Orita, *Synthesis*, **1998**, 910-914.

[13] a) R. A. Henry, *J. Am. Chem. Soc.*, 1951, **73**, 4470–4470. b) C. Femoni, S. Muzzioli, A. Palazzi, S. Stagni, S. Zacchini, F. Monti, G. Accorsi, M. Bolognesi, N. Armaroli, M. Massi, G. Valenti, M. Marcaccio, *Dalton. Trans.*, **2013**, *42*, 997; c) U. Sheridan, J. McGinley, J. F. Gallagher, A. Fleming, F. Kelleher, *Polyhedron*, **2013**, *59*, 8-16.

[14] R. N. Butler, Tetrazoles. In "Comprehensive Heterocyclic Chemistry II"; Storr, R. C., Ed.; Pergamon Press: Oxford, U.K., **1996;** Vol. 4, 621-678, and references cited therein.

[15] F. Puntoriero, F. Nastasi, M. Galletta, S. Campagna in "Photophysics and Photochemistry of Non-Carbonyl-Containing Coordination and Organometallic Compounds", Elsevier, **2013**, *8*, 255-337.

[16] G. M. Sheldrick, *SADABS-2008/1 - Bruker AXS Area Detector Scaling and Absorption Correction*, Bruker AXS: Madison, Wisconsin, USA, **2008**.

[17] G. M. Sheldrick, *Acta Crystallogr. C*, **2015**, *71*, 3.

Chapter 4 Alkyl tetrazoles as N^N diimine ligands for *fac*-[Re(N^N)(CO)$_3$(L)]-type complexes. Synthesis, characterization and preliminary studies of the interaction with Bovine Serum Albumin*

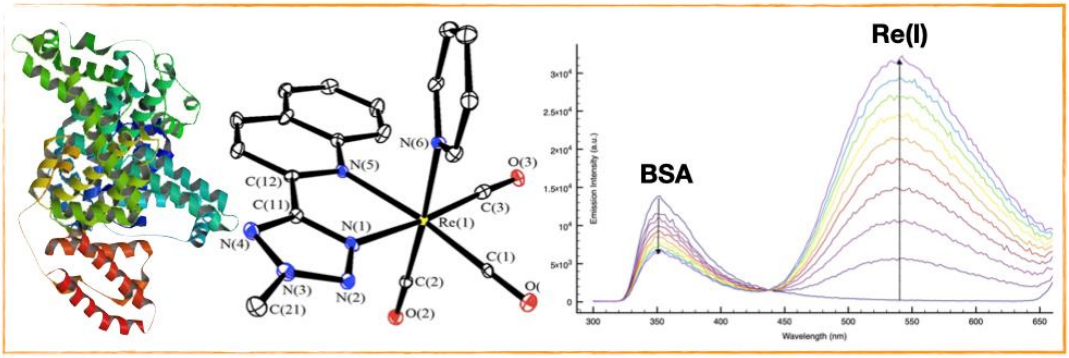

*This chapter is part of *Inorganica Chimica Acta*, **2021**, *518*, 1-11.

4.1 Abstract

Herein, we report a new family of luminescent Re(I) complexes with general formula *fac*-**[Re(diim)(CO)$_3$L]$^{0/+}$** in which the role of the diimine-type chelating ligand (**diim**) is played by alkylated tetrazoles. In particular, the design of the new complexes involved the choice of molecular scaffolds based on 2-pyridyl tetrazole (PTZ) and 2-quinolyl tetrazole (QTZ) which were decorated with various alkyl residues at the N-2 position of the pentatomic ring, thereby endowing the resulting alkyl tetrazoles **PTZ-R** and **QTZ-R** with the proper "bpy-like" coordination attitude. As the "third" ligand (L), pyridine (**pyr**) or the 5-phenyl tetrazolato anion (**Tph**)$^-$ were selected, leading to cationic species such as *fac*-**[Re(CO)$_3$(PTZ-R)(pyr)]$^+$**, *fac*-**[Re(CO)$_3$(QTZ-R)(pyr)]$^+$** and the neutrally charged "fully tetrazole" complex *fac*-**[Re(CO)$_3$(QTZ-Me)(Tph)]**. All the new complexes were identified by ESI-MS spectrometry and fully characterized by IR, ^{1}H and ^{13}C-NMR spectroscopy. The findings that were suggested from the interpretation of the spectroscopic data were further confirmed by X-ray crystallography, with the analysis of the molecular structures of the cationic complexes *fac*-**[Re(CO)$_3$(PTZ-Me)(pyr)][PF$_6$]** and *fac*-**[Re(CO)$_3$(PTZ-Me)(pyr)][PF$_6$]**.

Following the in-depth investigation of their photophysical properties, the new luminescent Re(I) tetrazole -based complexes were studied for any possible interaction with Bovine Serum Albumin (BSA). The results obtained from this preliminary screening highlighted that, along the series of the Re(I) tetrazole complexes, the compound bearing a **QTZ-R** residue, thus *fac*-**[Re(CO)$_3$(QTZ-Me)(pyr)]$^+$**, *fac*-**[Re(CO)$_3$(QTZ-^{t}Bu)(pyr)]$^+$** and the "fully tetrazole" complex *fac*-**[Re(CO)$_3$(QTZ-Me)(Tph)]**, displayed the highest affinity to BSA.

4.2 Introduction

An "archetypal" structure like *fac*-**[Re(CO)$_3$(diim)(L)]$^{0/+}$**, where (diim) represents a bidentate aromatic diimine and (L) is a monodentate ancillary ligand, is commonly used to depict Re(I)tricarbonyl diimines, which are known as one of the most important classes of phosphorescent d^6-metal complexes that have been – and continue to be - at the centre of intense investigation in many areas of science and technology.[1] In particular, Re(I) tricarbonyl diimines have been extensively studied in the context of life science, as witnessed by the numerous reports dealing with their use as luminescent imaging for live cells and tissues and intra- or extracellular sensing agents for a wide range of analytes.[2-4]

The reasons that have driven this family of Re(I) complexes to such a biology-oriented applicative scenario are explained by their use as model compounds for the technetium-99 congeners and to their displaying a peculiar environmental sensitivity of the emission stemming from metal-to-ligand charge transfer (MLCT) excited states.[5] In particular, the structure-to-properties approach that is commonly adopted for the design of *fac*-**[Re(CO)$_3$(diim)L]$^{0/+}$** type species for bioimaging purposes relies upon the modulation of their luminescent outputs by performing chemical modifications onto the chelate diimine ligand (diim), while the biological targeting is pursued with the choice of an appropriate "third" monodentate ligand (L).[6]

The factors that govern the cellular uptake and the intracellular localization of luminescent metal complexes are yet far from being fully understood. Nevertheless, the adoption of a similar design strategy - which also included the decoration of *fac*-**[Re(CO)$_3$(diim)L]$^{0/+}$** type complexes with pendant biologically active molecules – has led to an impressively high number of reports dealing with the use of such kind of Re(I) complexes as luminescent imaging reagents, among which the mitochondria specific Re(I) cationic complex reported by Coogan and co-workers in 2012 represents one of the most successful examples.[7] In this specific context, we have dedicated intense research efforts to the design of luminescent markers for cellular imaging based on neutrally charged Re(I) complexes with general formula *fac*-**[Re(CO)$_3$(diim)(L)]$^{0/+}$**, in which the third ligand (L) was represented by variably substituted 5-aryl tetrazolato anion [R-CN$_4^-$].

The results obtained so far have highlighted how the nature of the residue/substituent R represented a key factor for determining any eventual localization of the corresponding Re(I) complexes, which could be directed toward lipid droplets (as in the case of 4-benzonitrile substituted tetrazolato anion) or to the endoplasmic reticulum, as was observed when the residue R was represented by the 3-pyridyl ring.[8]

Aiming at getting further insights about the importance of tetrazole ligands for this class of Re(I)-based luminescent markers, we now extend our studies to the design and the preparation of series of new *fac*-**[Re(CO)$_3$(diim)(L)]$^{0/+}$** type complexes in which alkylated tetrazoles play the role of the chelating "diimine like" (diim) ligands. For this specific purpose, the 2-pyridyl (PTZ) and 2-quinolyl tetrazole (QTZ) molecular scaffolds were modified with the introduction one methyl (**PTZ-Me** and **QTZ-Me**) or one tert-butyl (**PTZ-^{t}Bu** and **QTZ-^{t}Bu**) substituent group in the pentatomic ring, to afford the precursor species *fac*-**[Re(CO)$_3$(PTZ-R)(Br)]** and *fac*-**[Re(CO)$_3$(QTZ-R)(Br)]**, respectively.

In the successive stage, their molecular architecture was modified either by introducing pyridine as the (L) ligand, leading to the series of cationic complexes with general formula *fac*-**[Re(CO)$_3$(PTZ-R)(pyr)]$^+$** and *fac*-**[Re(CO)$_3$(QTZ-R)(pyr)]$^+$**, (Figure 1) or with the replacement of the bromide ion with one phenyl tetrazolato anion, thereby causing the formation of "fully tetrazole" neutrally charged complex *fac*-**[Re(CO)$_3$(QTZ-Me)(Tph)]**. (**Scheme 1.4**)

Herein, the synthesis and the spectroscopic and structural characterization of the new complexes are described, along with an in-depth analysis of their photophysical properties. Moreover, continuing our recent studies dealing with the use of Re(I) tetrazole complexes as luminescent staining agents for proteins,[9] the preliminary results about the investigation of any possible interaction of the new Re(I) complexes with a model protein such as bovine serum albumin (BSA) are reported.

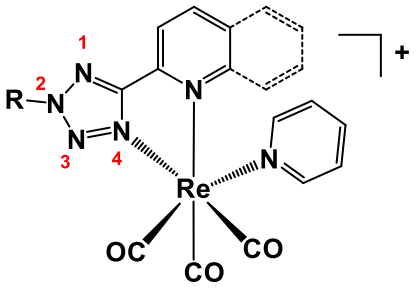

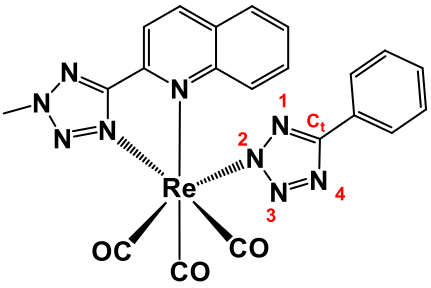

—— = PTZ; R = Me, ^{t}Bu

***fac*-[Re(CO)$_3$(PTZ-Me)(pyr)]$^+$**

***fac*-[Re(CO)$_3$(PTZ-^{t}Bu)(pyr)]$^+$**

------ = QTZ; R = Me, ^{t}Bu

***fac*-[Re(CO)$_3$(QTZ-Me)(pyr)]$^+$**

***fac*-[Re(CO)$_3$(QTZ-^{t}Bu)(pyr)]$^+$**

fac-[Re(CO)$_3$(QTZ-Me)(Tph)]

Scheme 1.4. Re(I) tricarbonyl complexes presented in this chapter and atom numbering of the tetrazole ring.

4.3 Result and Discussions

Since tetrazoles are commonly considered the nitrogen analogues of the corresponding carboxylic acids, the use of the pyridyl-(PTZ) and quinolyl-tetrazole (QTZ) molecular scaffold as neutral diimine type chelate ligands required the replacement of the fairly acidic hydrogen of the -CN_4H moiety with an alkyl residue, leading to the alkylated tetrazoles abbreviated as **PTZ-R** and **QTZ-R**, respectively, in which the -R group was introduced at the N-2 position of the tetrazole moiety. In doing this, the peculiar reactivity that tetrazoles display toward the addition of electrophiles had to be taken into account. Indeed, the alkylation reaction of tetrazoles usually leads to the recovery of the alkylated products as a mixture of regioisomers depending whether the electrophilic addition takes place at the N-1 or the N-2 position of the pentatomic ring.[10] (**Scheme 2.4**)

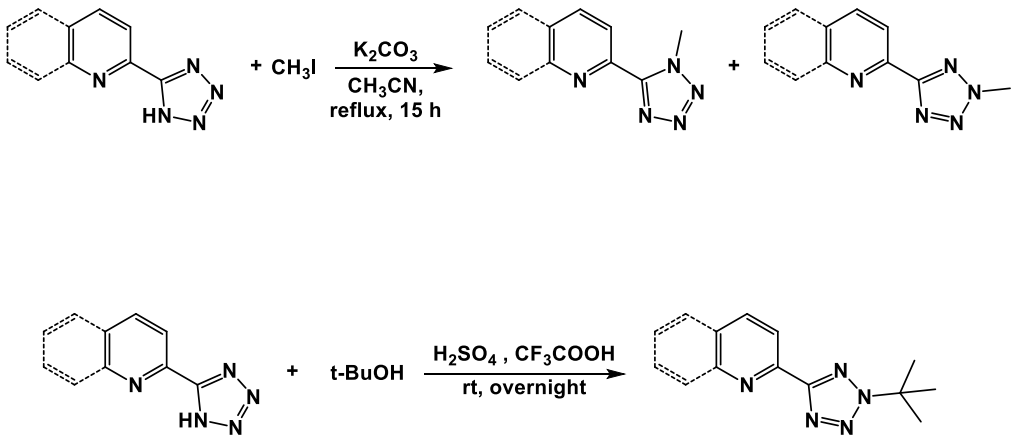

Scheme 2.4. Functionalization of tetrazole ligands PTZ-H and QTZ-H.

As the steric hindrance of the -R group is the most important factor for determining any eventual regiospecificity of the alkylation reactions, the addition of the bulky tert-butyl (^{t}Bu) residue to 2-pyridyl tetrazole (**PTZ-H**) and 2-quinolyl tetrazole (**QTZ-H**) led to the exclusive formation of the desired N-2 tert-butylated derivatives (**PTZ-^{t}Bu**) and (**QTZ-^{t}Bu**). On the other hand, the methylation reaction performed onto the same tetrazole substrates provided the methylated compounds (**PTZ-Me**) and (**QTZ-Me**) as mixtures of both regioisomers, from which the N-2 substituted isomers were isolated via

column chromatography. In particular, the clear distinction of the two substitution isomers could be made from the analysis of the corresponding ^{13}C NMR spectra. Whereas the resonance of the tetrazole carbon (C_t) of N-1 isomers is typically found in the chemical shifts range comprised between 151 and 155 ppm, the isolation of **PTZ-Me** and **QTZ-Me** as the N-2 alkylated regioisomers was confirmed by the significant downfield shifting of the corresponding C_t signals to chemical shift values ranging from 164 -168 ppm.[10] (**Figure 1.4**)

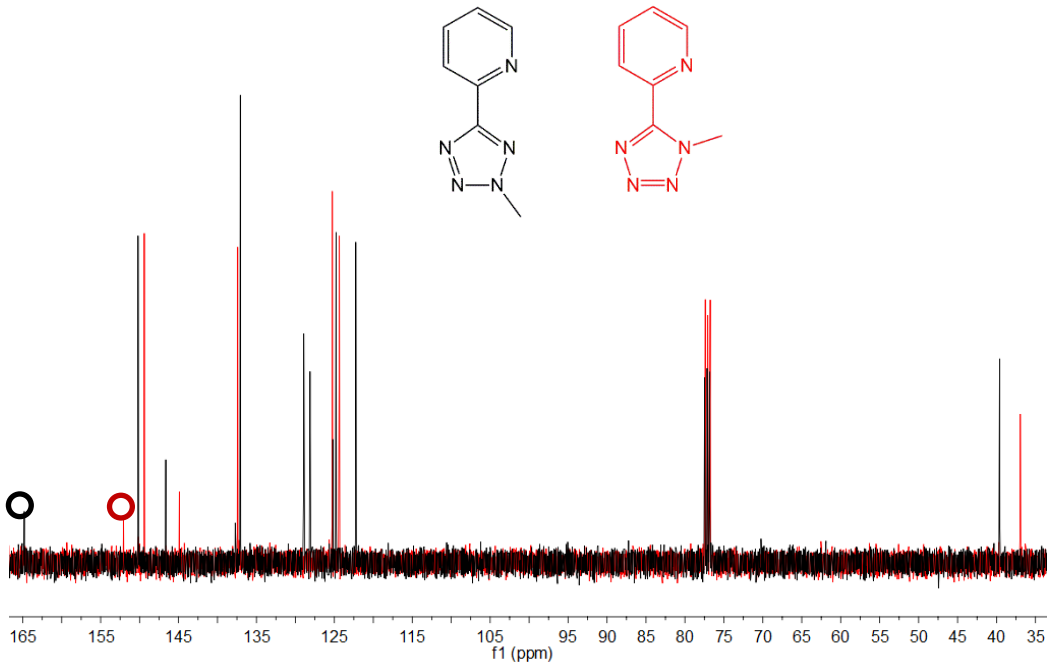

Figure 1.4. ^{13}C-NMR spectra superimposition of the two different alkylation isomers for **PTZ-Me**: **PTZ**-N1-**Me** (red trace) and **PTz**-N2-**Me** (black trace), $CDCl_3$ 400 MHz.

The reaction of $Re(CO)_5Br$ with a slight molar excess (1:1.2) of the N-2 substituted tetrazole **PTZ-R** or **QTZ-R** in toluene at the reflux temperature led, in all cases, to the isolation of one single and neutrally charged product (**Scheme 3.4**), as suggested by electrospray ionization mass spectrometry (ESI-MS) experiments.

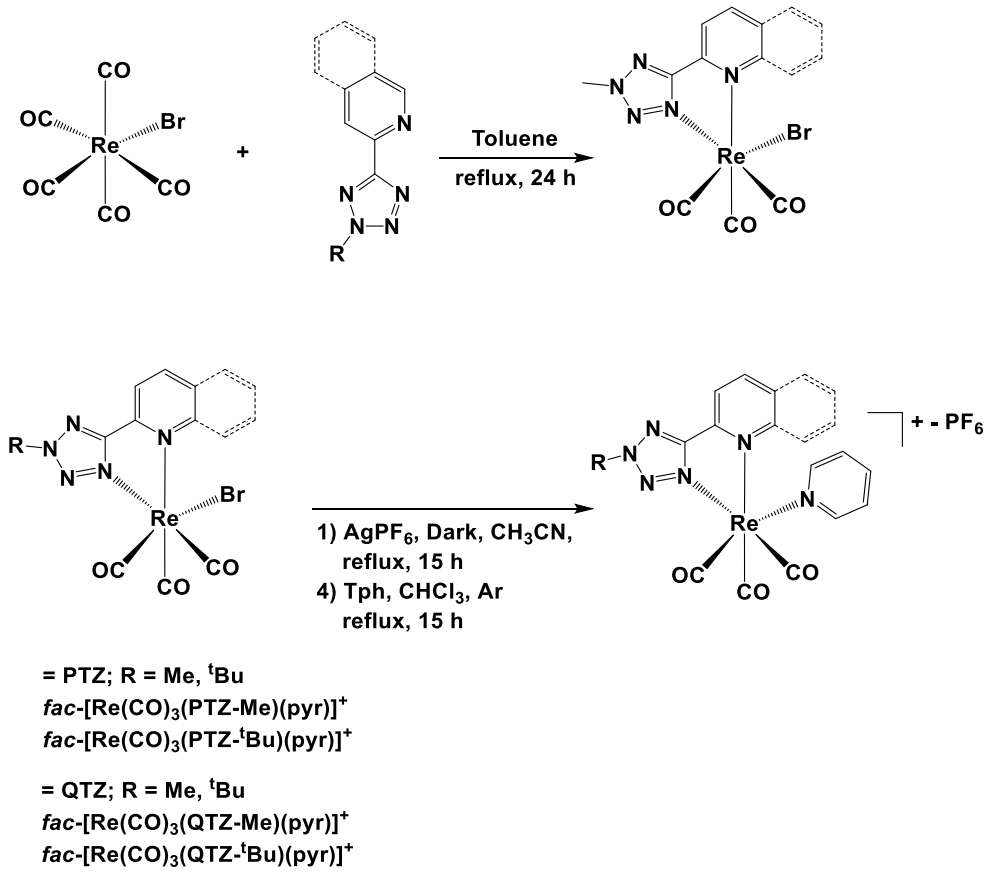

Scheme 3.4. The synthetic procedure used for the preparation of *fac*-$[Re(CO)_3(N\hat{}N)(pyr)]^+$ -type complexes.

For all of the new Re(I) complexes, the facial (*fac*) configuration of the three CO ligands was suggested by their displaying solid-state infrared (IR) spectra consisting of one sharp band at *ca.* 2031 cm^{-1}, that is assigned to the completely symmetric in- phase stretching A′(1), followed by two broader bands at *ca.* 1906 and 1930 cm^{-1}, which results from the of the completely symmetric out-of-phase stretching A′(2) and the asymmetric stretching A″.[11]

The presence of **PTZ-R** or **QTZ-R** ligands in the structure of the Re(I) complexes and, in particular, their adopting the desired chelate coordination to the Re(I) centre, was suggested by the comparison of the ^{1}H-NMR spectra of *fac*-**[Re(CO)$_3$(PTZ-R)(Br)]** and *fac*-**[Re(CO)$_3$(QTZ-R)(Br)]** with those of the free ligands **PTZ-R** and **QTZ-R**, respectively.

For instance, in the exemplar case described in **Figure 2.4**, it is possible to observe how in complex *fac*-**[Re(CO)$_3$(QTZ-^{t}Bu)(Br)]** the chelation of **QTZ-^{t}Bu** onto the metallic centre led to the appearance of a different and much better-resolved pattern of aromatic signals than the one recorded from **QTZ-^{t}Bu** as a "free" ligand, in which the mutual rotation of the tetrazole and the quinolyl ring is not prevented.

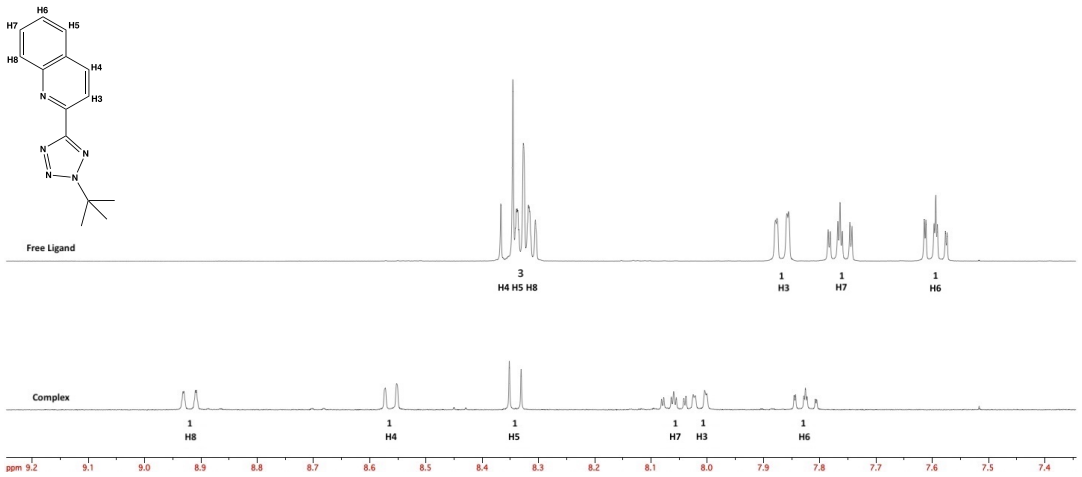

Figure 2.4. ^{1}H-NMR of (**QTZ-^{t}Bu**) (top) and ***fac*-[Re(CO)$_3$(QTZ-^{t}Bu)(Br)]** (bottom) 400 MHz, $CDCl_3$; Inset: aromatic region from 9 to 7.5 ppm. "1" and "3" are referred to the integral value of the resonance above.

In the successive stage, the obtained complexes *fac*-**[Re(CO)$_3$(PTZ-R)(Br)]** and *fac*-**[Re(CO)$_3$(QTZ-R)(Br)]** were used as starting materials for reactions aimed at the replacement of the coordinated bromide ion either with a neutrally charged ligand such as pyridine (**pyr**) or with the phenyl tetrazolato anion (**Tph**)$^-$. As the preliminary step, both procedures involved the Ag(I)-assisted halide extraction on *fac*-**[Re(CO)$_3$(PTZ-R)(Br)]** and *fac*-**[Re(CO)$_3$(QTZ-R)(Br)]** precursor. The resulting cationic intermediates *fac*-**[Re(CO)$_3$(PTZ-R)(NCCH$_3$)][PF$_6$]** and *fac*-**[Re(CO)$_3$(QTZ-R)(NCCH$_3$)][PF$_6$]** were successively treated with an excess of pyridine (**pyr**) in $CHCl_3$, leading to the formation the target cationic complexes *fac*-**[Re(CO)$_3$(PTZ-R)(pyr)][PF$_6$]** and *fac*-**[Re(CO)$_3$(QTZ-R)(pyr)][PF$_6$]**, respectively. Along with ESI-MS, these reactions were monitored by IR spectroscopy, enlightening how the transformation of the neutrally charged starting compounds into the cationic products was witnessed by the expected shift to higher wavenumbers of the CO stretchings, whose

number and relative intensities were again congruent with the facial arrangement of the CO ligands. Following a closer inspection of the IR profiles (**Figure 3.4**), it was possible to notice that, as sometimes reported for the family of *fac*-**[Re(N^N)(CO)$_3$(L)]** -type complexes,[12,13] the cationic species *fac*-**[Re(CO)$_3$(PTZ-R)(NCCH$_3$)][PF$_6$]**, *fac*-**[Re(CO)$_3$(QTZ-R)(NCCH$_3$)][PF$_6$]**, *fac*-**[Re(CO)$_3$(PTZ-R)(pyr)][PF$_6$]** and *fac*-**[Re(CO)$_3$(QTZ-R)(pyr)][PF$_6$]**, displayed the superimposition of the A′(2) and A'' stretching modes into a single broad band. In addition, from the comparison of the IR profiles of ***fac*-[Re(CO)$_3$(PTZ-R)(pyr)][PF$_6$]** and *fac*-**[Re(CO)$_3$(QTZ-R)(pyr)][PF$_6$]** with respect to the cationic intermediates *fac*-**[Re(CO)$_3$(PTZ-R)(NCCH$_3$)][PF$_6$]** and *fac*-**[Re(CO)$_3$(QTZ-R)(NCCH$_3$)][PF$_6$]**, it was observed that the substitution of coordinated acetonitrile molecule in favour of pyridine (**pyr**) caused the shift towards lower wavenumbers of the pattern relative to the CO stretchings (*ca.* 2030, 1930 and 1905 cm^{-1}), the occurrence of which effect is most likely to ascribe due to the reduced π-acidity of pyridine concerning that of acetonitrile. (**Figure 3.4)**

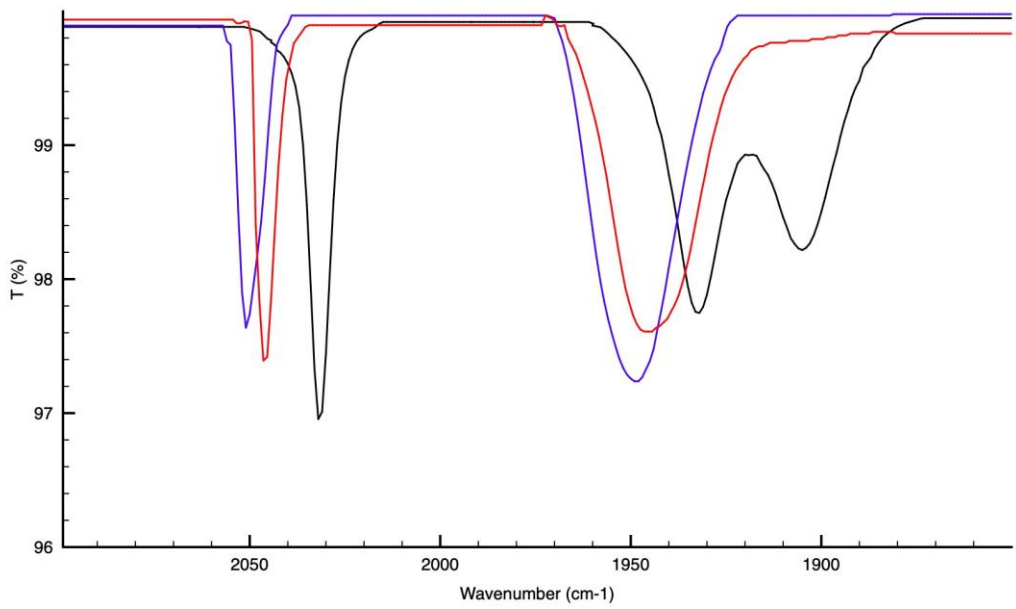

Figure 3.4. IR spectra of *fac*-**[Re(CO)$_3$(PTZ-^{t}Bu)(Br)]**(black trace), *fac*-**[Re(CO)$_3$(PTZ-^{t}Bu)(CH$_3$CN)][PF$_6$]** (blue trace) and *fac*-**[Re(CO)$_3$(PTZ-^{t}Bu)(pyr)][PF$_6$]** (red trace), FTIR-ATR.

As reported in **Figure 4.4**, the successful introduction of the pyridine ligand within the first coordination sphere of the Re(I) centre was also confirmed by the appearance of the characteristic pattern of signals in the aromatic region in both the ^{1}H and ^{13}C NMR spectra of the corresponding *fac*-**[Re(CO)$_3$(PTZ-R)(pyr)][PF$_6$]** and *fac*-**[Re(CO)$_3$(QTZ-R)(pyr)][PF$_6$]** type species.

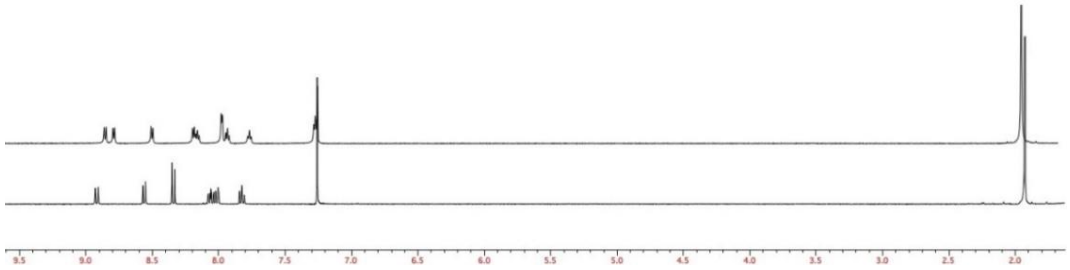

Figure 4.4. ^{1}H-NMR spectra of ***fac*-[Re(CO)$_3$(QTZ-^{t}Bu)(Br)][PF$_6$]** (bottom) and ***fac*-[Re(CO)$_3$(QTZ-^{t}Bu)(pyr)][PF$_6$]** (top), 400 MHz, $CDCl_3$.

In a different instance, the intermediate species *fac*-**[Re(CO)$_3$(QTZ-Me)(CH$_3$CN)][PF$_6$]** was treated with a slight excess of the 5-(phenyl)tetrazolato anion, abbreviated as **Tph** (**Scheme 4.4**). The ESI-MS, IR and NMR spectroscopic characterization of the resulting product confirmed the occurrence of the expected neutrally charged and "fully-tetrazole" complex *fac*-**[Re(CO)$_3$(QTZ-Me)(Tph)]**, as witnessed by the shift to lower wavenumbers of the *fac*-type CO stretchings pattern and the concomitant appearance of two distinct tetrazole carbon (Ct) resonances in the chemical shift region comprised between 164 and 168 ppm.

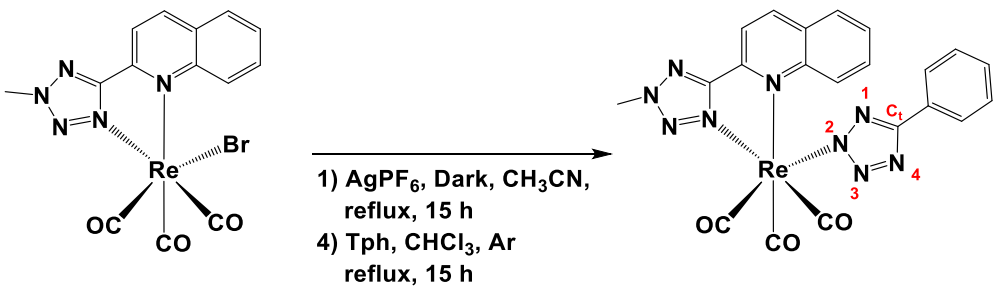

Scheme 4.4. The synthetic procedure used for the preparation of ***fac*-[Re(CO)$_3$(QTZ-Me)(Tph)]**.

4.3.1 *X-ray crystallography*

Along the series of the new Re(I)-tetrazole complexes, two cationic species – namely, those suggested as ***fac*-[Re(CO)$_3$(QTZ-Me)(pyr)][PF$_6$]** and ***fac*-[Re(CO)$_3$(PTZ-Me)(pyr)][PF$_6$]** – afforded crystals suitable for X-ray diffraction. For both complexes, the analysis of their molecular structure (**Figure 5.4**) provided results congruent with the occurrence of the expected octahedral complexes in which the coordination environment of Re (I) ion consisted of three CO ligands arranged in a facial (*fac*) geometry, the pyridyl (PTZ-Me) or quinolyl tetrazole (QTZ-Me) ligands exerting bis-chelate coordination, and was completed by pyridine as the "third" monodentate ligand. The two complexes show very similar geometries and bonding parameters. The Re-N distances are in the expected range for Re-N(sp^2) interactions.[9,12,14,20] Re(1)-N(1) distances (2.132(8) and 2.029(6) Å for *fac*-**[Re(CO)$_3$(QTZ-Me)(pyr)][PF$_6$]** and *fac*-**[Re(CO)$_3$(PTZ-Me)(pyr)][PF$_6$]**, respectively), involving the five-member tetrazolato ring, are slightly shorter than Re(1)-N(5) (2.276(7) and 2.245(7) Å), involving a condensed six-member ring. The Re(1)-N(6) interactions (2.201(7) and 2.210(4) Å) are in the middle, given the monodentate nature of the pyridine ring.

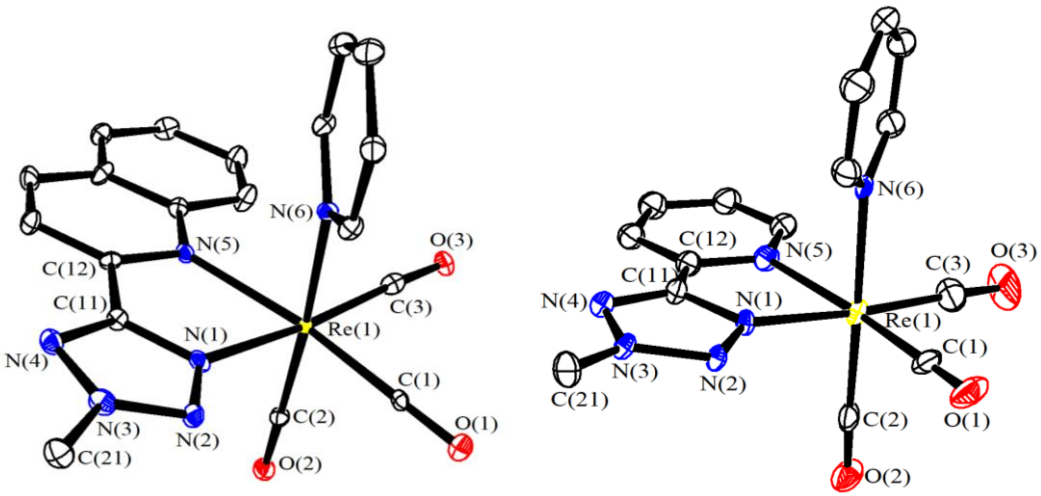

Figure 5.4. Molecular structure of ***fac*-[Re(CO)$_3$(QTZ-Me)(pyr)][PF$_6$]** (left) and ***fac*-[Re(CO)$_3$(PTZ-Me)(pyr)][PF$_6$]** (right) with key atoms labelled. Displacement ellipsoids are presented at the 30% probability level, the H-atoms and counterion are omitted for clarity.

4.3.2 *Photophysical properties*

The relevant photophysical data of the target cationic and neutrally charged Re(I) complexes described herein are summarized in **Table 1.4**.

Table 1.4. Relevant Absorption and Emission data of all the target Re(I) complexes described in this chapter; CH_2Cl_2 solutions.

	Absorption	**Emission 298 K**					**Emission 77 K**	
Complex CH_2Cl_2 as solvent	λ_{abs} (nm) ($10^{-4}\varepsilon$) ($M^{-1}cm^{-1}$)	λ_{em} (nm)	τ_{air} (ns)[a]	τ_{Ar} (ns)[a]	φ_{air} (%)[b]	φ_{Ar} (%)[b]	λ_{em} (nm)[c]	τ (ns)[c]
***fac*-[Re(CO)$_3$(PTZ-Me)(pyr)]$^+$**	271 (4.82), 362 (0.93)	578	154	494	2.1	7.6	518	5997
***fac*-[Re(CO)$_3$(PTZ-^{t}Bu)(pyr)]$^+$**	262 (5.41), 337 (1.34)	514	465	2059	2.4	6.4	482	4063
***fac*-[Re(CO)$_3$(QTZ-Me)(pyr)]$^+$**	256 (7.96), 328 (1.38), 373 (0.92)	604	1025	3226	3.0	18.0	532, 566	12000
***fac*-[Re(CO)$_3$(QTZ-^{t}Bu)(pyr)]$^+$**	256 (7.49), 328 (1.32), 373 (0.88)	604	876	4040	3.0	19.0	538, 568	10000
***fac*-[Re(CO)$_3$(QTZ-Me)(Tph)]**	253 (9.68), 324 (1.43), 368 (0.90)	632	407	721	1.5	9.0	536, 574	10500

[a]: "Air" means air equilibrated solutions, "Ar" means deoxygenated solutions under argon atmosphere; [b]: $[Ru(bpy)_3]Cl_2/H_2O$ was used as a reference for quantum yield determinations (Φ_r = 0.028)[37]; [c]: in frozen CH_2Cl_2.

As commonly observed for octahedral d^6 metal complexes,[1] the absorption profiles of the Re(I) complexes – which were obtained from the corresponding dilute (10^{-5}M) dichloromethane solutions - displayed the UV region dominated by intense ligand-centred (LC) transitions (250–270 nm), followed by metal-to-ligand charge transfer (MLCT) processes (300–410 nm) tailing off in the visible region. (**Table 1.4**, **Figure 6.4**)

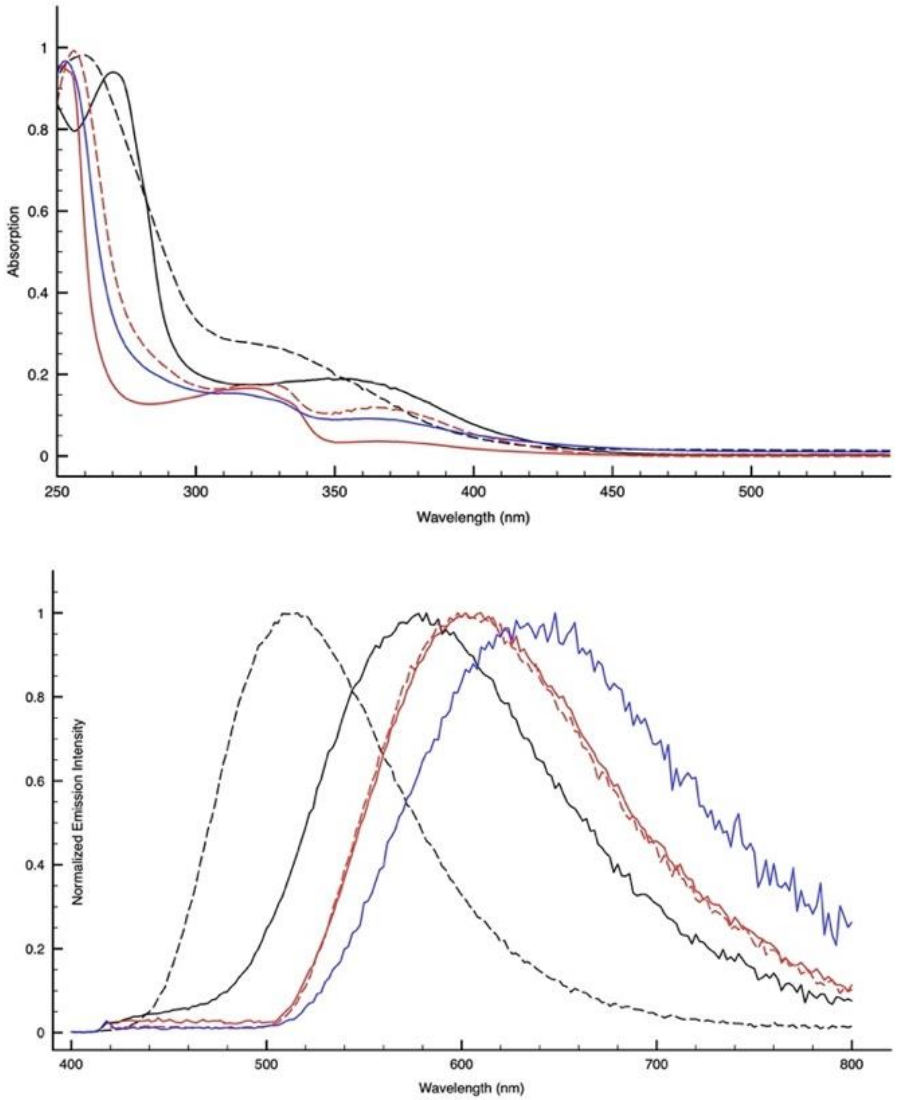

Figure 6.4. Normalized emission(top) and absorption profiles (bottom) of ***fac*-[Re(CO)$_3$(PTZ-Me)(pyr)]$^+$** (black solid line), ***fac*-[Re(CO)$_3$(PTZ-^{t}Bu)(pyr)]$^+$** (black dotted line), ***fac*-[Re(CO)$_3$(QTZ-Me)(pyr)]$^+$** (red solid line), ***fac*-[Re(CO)$_3$(QTZ-^{t}Bu)(pyr)]$^+$** (red dotted line) and ***fac*-[Re(CO)$_3$(QTZ-Me)(Tph)]** (blue solid line), 298K, CH_2Cl_2.

Upon excitation of the corresponding MLCT features (λ = 370 nm), the cationic *fac*-**[Re(CO)$_3$(PTZ-R)(pyr)]$^+$** and *fac*-**[Re(CO)$_3$(QTZ-R)(pyr)]$^+$** type species and the neutral complex *fac*-**[Re(CO)$_3$(QTZ-Me)(Tph)]** displayed bright luminescence that, in line with the behaviour typical of the family of fac-Re(I) tricarbonyl diimine complexes, was represented by broad and structureless emission profiles centred between *ca.* 510 nm and 630 nm. In particular, if the emissions originating from the **PTZ-R**- based complexes *fac*-**[Re(CO)$_3$(PTZ-R)(pyr)]$^+$** were found to span from λ_{max} = 514 nm to λ_{max} = 578 nm, those observed from the series of **QTZ-R** -based cationic derivatives *fac*-**[Re(CO)$_3$(QTZ-R)(pyr)]$^+$** were quite expectedly found to peak at lower energy, as in the cases of for *fac*-**[Re(CO)$_3$(QTZ-Me)(pyr)]$^+$** and *fac*-**[Re(CO)$_3$(QTZ-^{t}Bu)(pyr)]$^+$**, whose emissions being both centred at 604 nm.

The further redshift of the emission maxima (λ_{max} = 632 nm) was observed for the neutrally charged "fully tetrazole" complex *fac*-**[Re(CO)$_3$(QTZ-Me)(Tph)]**. However, in all cases, the emission can be confidently described as phosphorescence originating from charge-transfer states of triplet multiplicity, ^{3}CT, in a manner analogous to what we have reported previously for neutral and ionic Re(I) tetrazolato complexes.[8,9,12,13] Indeed, the excited state lifetime (τ) and quantum yield (Φ) are sensitive to the presence of dissolved dioxygen (**Table 1.4**). Further in support of the MLCT nature of the emissive excited states was the significant blue shift of the emissions – the so-called *rigidochromism* - that was observed on passing from 298 K to 77 K,[15] highlighting an effect that can be ascribed to the ensuing reduction, or almost complete removal, of vibrational and collisional quenching phenomena (**Table 1.4**).

It is worth noting that under all the different the experimental conditions in which the measurements were carried out (**Table 2.4**), the *fac*-**[Re(CO)$_3$(QTZ-R)(L)]$^{0/+}$** type complexes displayed photoluminescence performances superior to those displayed by the parent *fac*-**[Re(CO)$_3$(PTZ-R)(pyr)]$^+$** derivatives, in terms both of higher quantum yields (Φ_{Ar}) and longer emission lifetimes (τ). This trend did become even more evident on passing from air equilibrated to O_2-free solutions, and was quite unexpected in consideration of the energy gap law, since the emission maxima of all the **QTZ-R** based complexes did peak at significantly lower energies than what observed for the **PTZ-R** analogous species. Whereas the more extended π-conjugation across the **QTZ** backbone

reasonably accounts for the red-shifted emission of the **QTZ-R** based complexes, their displaying higher quantum yields and longer emission lifetimes might be explained by assuming a likely higher rigidity of the *fac*-**[Re(CO)$_3$(diim)(pyr)]$^+$** structure that is possibly brought by the benzofused **QTZ** scaffold with respect to what happens in the presence of the **PTZ**-based diimine ligand. d

4.3.3 *Interaction with BSA – Bovine Serum Albumin*

Within the general framework of our extensive studies concerning the use of Re(I)-tetrazolato complexes in life science,[8,16-22] we have recently reported the very first examples of Re(I)-based luminescent markers for proteins purified by SDS-PAGE (Sodium Dodecyl Sulphate - Polyacrylamide Gel Electrophoresis).[9] (Chapter 5) In the first stage of those studies, the new Re(I) complexes - designed with the general formula *fac*-[Re(CO)$_3$(diim)(L)]$^{0/-}$, where diim could be either bathophenanthroline (BP) or bathophenanthroline disulfonate (BPS) and L was represented by the 5-(phenyl)tetrazolato anion [Tph$^-$] - were successfully screened toward the luminescent detection of bovine serum albumin (BSA), which is considered as a model protein due to its structural similarities with HSA (human serum albumin).

Relying on these premises we have endeavoured to preliminarily investigate the occurrence of any possible interaction involving BSA and the new complexes *fac*-**[Re(CO)$_3$(diim)(L)]$^{0/+}$** presented herein, namely the cationic species *fac*-**[Re(CO)$_3$(PTZ-R)(pyr)]$^+$** and *fac*-**[Re(CO)$_3$(QTZ-R)(pyr)]$^+$** (R is -Me or -^{t}Bu) and the neutral complex *fac*-**[Re(CO)$_3$(QTZ-Me)(Tph)]**. To this end, both absorption and emission titration experiments were performed by adding 20 x 5μL (DMSO as the solvent, 2.1*10^{-3} M) to 2 mL of BSA as 1*10^{-5} M solution in aqueous PBS buffer. As reported in the literature,[23] the absorption profile of BSA consists of an intense transition centred at 220 nm followed by a weaker band peaking at 280 nm, which are usually assigned to the secondary structure of the protein and the aromatic residues of amino acids, respectively.

Table 2.4. BSA-Re(I) binding experiments data, 298K.

Complex PBS/DMSO 95:5, 298K	λ_{em} (nm)	$\tau_{0\ BSA}$[a] (ns)	τ_{BSA}[a] (ns)	τ_0/τ_{BSA}[a]	K_D[b] (M^{-1})	K_q[b] ($M^{-1}s^{-1}$)	K_b[c] (M^{-1})	n[c]
***fac*-[Re(CO)$_3$(PTZ-Me)(pyr)]$^+$**	586	6.7	6.1	1.1	$9.8*10^2$	$1.46*10^{11}$	$8.8*10^5$	1.3
***fac*-[Re(CO)$_3$(PTZ-^{t}Bu)(pyr)]$^+$**	538	6.7	6.2	1.1	$8.4*10^2$	$1.25*10^{11}$	$1.6*10^5$	1.2
***fac*-[Re(CO)$_3$(QTZ-Me)(pyr)]$^+$**	580	6.7	5.1	1.3	$3.3*10^3$	$4.92*10^{11}$	$2.8*10^6$	1.0
***fac*-[Re(CO)$_3$(QTZ-Me)(Tph)]**	614	6.7	4.5	1.5	$5.0*10^3$	$1.49*10^{11}$	$1.5*10^6$	1.3
***fac*-[Re(CO)$_3$(QTZ-^{t}Bu)(pyr)]$^+$**	604	6.7	4.5	1.5	$4.8*10^3$	$7.10*10^{11}$	$6.8*10^6$	1.5

[a]: ±8%, ±16%.[b]: $\tau_0/\tau = 1+K_D[Q]$. [c]: Derived from Log (I_0-I/I) = Log K + n Log[Q].

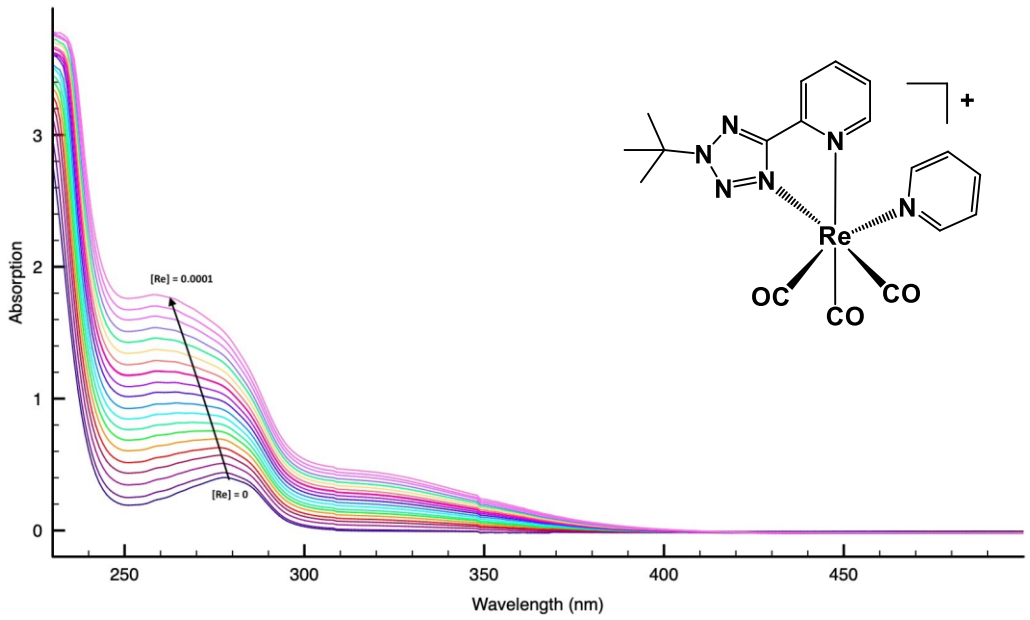

Figure 7.4. Absorption Titration of BSA 10^{-5} M/PBS buffer 0.05 M vs ***fac*-[Re(CO)$_3$(PTZ-^{t}Bu)(pyr)]$^+$**, 20x5µL $2.1*10^{-3}$M, PBS/DMSO 95:5, 298K.

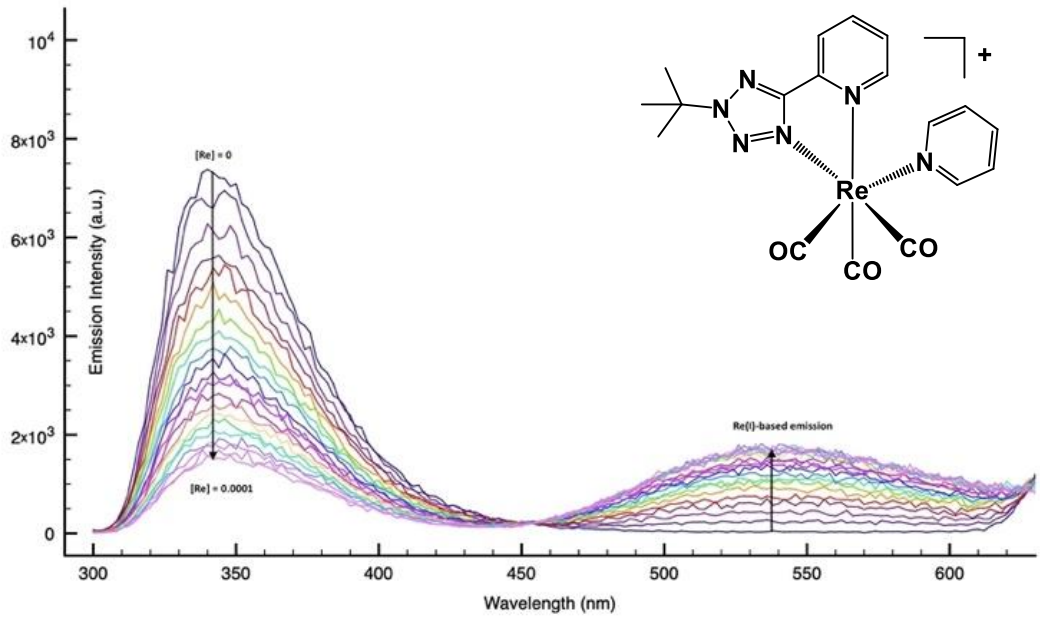

Figure 8.4. Emission Titration of BSA 10^{-5} M/PBS buffer 0.05 M vs ***fac*-[Re(CO)$_3$(PTZ-^{t}Bu)(pyr)]$^+$**, 20x5µL 2.1*10^{-3}M, PBS/DMSO 95:5, 298K. λ_{emi} = 538 nm. λ_{emi} BSA = 346 nm. λ_{exc} = 280 nm.

Accordingly, whereas the perturbations of the secondary structure of BSA usually lead to an intensity decrease of the transition centred at 220 nm, the alterations in the surroundings of aromatic amino-acid residues are associated to changes in the process found at 280 nm. Upon incremental additions of 2.1*10^{-3} M solutions of Re(I) -tetrazole based species to 2mL of a 10^{-5}M BSA solution, the resulting absorption profiles presented an ever-growing process at 220 nm, while at higher wavelengths (250 -300 nm), overlapped processes from both BSA and Re(I) quenchers were observed, (**Figure 7.4** for ***fac*-[Re(CO)$_3$(PTZ-^{t}Bu)(pyr)]$^+$**), making it impossible to discern the static or dynamic nature of the quenching mechanism.

The intrinsic fluorescence of BSA is often referred to the presence of two tryptophan residues, whose accessibility is strictly correlated to the intensity of such emission, as well as the polarity of the solvent.[24] Modifications in the emission intensity of BSA upon the addition of successive aliquots of a quencher (*i.e.* Re(I) complexes) might be indicative for an alteration of the environment surrounding the protein, thus suggesting the occurrence of binding interactions between BSA and the quencher. For all the Re(I) complexes reported herein, a decrease in the emission intensity of BSA was observed as a result of the increased concentration of quencher (0-10^{-4}M). Instead, only in the case

of the cationic complex *fac*-**[Re(CO)$_3$(PTZ-^{t}Bu)(pyr)]$^+$** (**Figure 8.4**) and the neutrally charged species *fac*-**[Re(CO)$_3$(QTZ-Me)(Tph)]** (**Figure 9.4**), an appreciable increase of the Re(I)-based emission intensity was observed.

To get more insights on the quenching mechanism occurring between BSA and the different Re(I)-based quenchers, Stern-Volmer analyses were carried out (**Figure 9.4, 10.4).** In all cases, experimental results exhibited a non-linear behaviour of the I_0/I vs [Q] plot (I_0 and I are the emission intensities of BSA with and without quencher, respectively; [Q] is the concentration of the Re(I)-quencher considered), while the decay time of BSA decreased with increasing concentration of quencher (**Table 2.4**). Usually, upward curvature of Stern−Volmer plot may be due to (i) static as well as dynamic quenching mechanisms that occur simultaneously and/or (ii) high extent of quenching at higher concentration region of quencher.[25,26,27] Thus, a modified Stern-Volmer equation[28] which accounts for the positive curvature observed was used

$$\frac{\boldsymbol{I_0}}{\boldsymbol{I}} = (\mathbf{1} + \boldsymbol{K_D}[\boldsymbol{Q}])(\mathbf{1} + \boldsymbol{K_S}[\boldsymbol{Q}])$$

Attempts to obtain K_D and K_S values (dynamic and static quenching constants, respectively) using the latter relation were unsuccessful because the resulting quadratic equations were in all cases unsolvable.[29] This may be due to the poor contribution of dynamic quenching in the overall process, that was found to range from 10^2 to 10^3 M^{-1} from lifetime data (K_D, Table 2.4). Moreover, as the resulting bimolecular quenching constants (kq, Table 2.4) are higher than the maximum scatter collision-quenching constant of diverse kinds of quenchers for biopolymers fluorescence ($2*10^{10}$ $M^{-1}s^{-1}$),[30,31] the static quenching mechanism seems to be prevalent in the interaction between BSA and the presented Re(I) complexes. On these basis, the affinity (binding constant, k_b) and the number of binding sites (n) of BSA towards our Re(I) complexes were determined according to the Scatchard equation.[32,33,34] The obtained values (**Table 3.4**) denote an efficient interaction between our Re(I) complexes – in particular, the ones

containing the QTZ-based diimine ligands - and BSA, as the optimum range for K_b to be indicative for an efficient process is considered to be 10^4- 10^6 L mol^{-1}.[35]

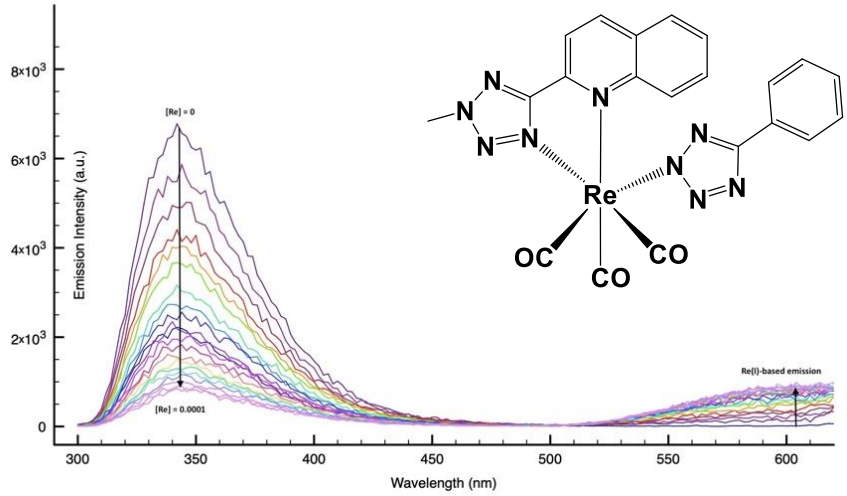

Figure 9.4. Emission Titration of BSA 10^{-5} M/PBS buffer 0.05 M vs ***fac*-[Re(CO)$_3$(QTZ-Me)(Tph)]**, 20x5µL 2.1*10^{-3}M, PBS/DMSO 95:5, 298K. λ_{emi} = 614 nm. λ_{emi} BSA = 346 nm. λ_{exc} = 280 nm.

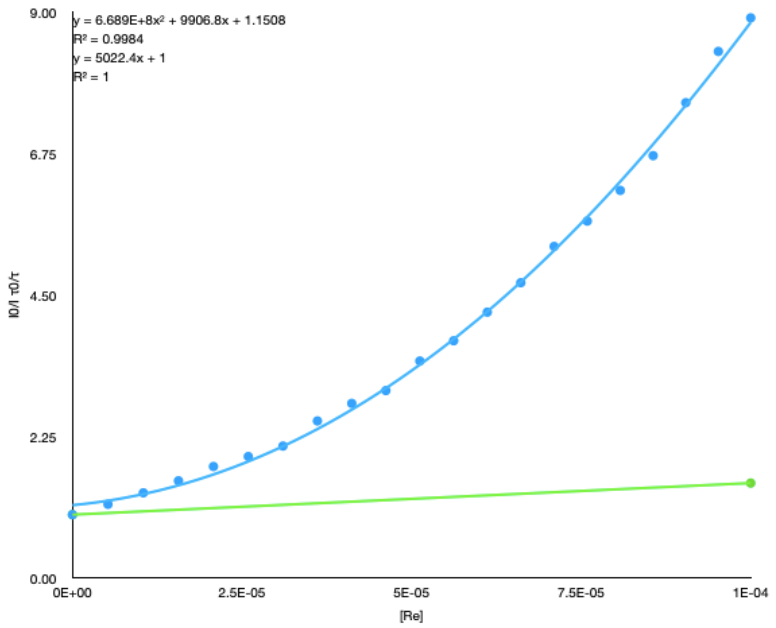

Figure 10.4. Stern Volmer plot of the emission titration reported in **Figure 9.4**.

4.4 Conclusions

N-alkylated tetrazoles such as those based of the 2-pyridyl (PTZ) and 2-quynolyl molecular scaffolds, can actually play the role of diimine "diim" ligands for tricarbonyl Re(I) complexes with general formula ***fac*-[Re(CO)$_3$(diim)(L)]$^{0/+}$**. In particular, the analysis of the photophysical behaviour of the new Re (I) complexes, both in the form of cationic species complexes ***fac*-[Re(CO)$_3$(PTZ-R)(pyr)]$^+$**, ***fac*-[Re(CO)$_3$(QTZ-R)(pyr)]$^+$**, where pyr is pyridine, and of the neutrally charged "fully tetrazole" derivative ***fac*-[Re(CO)$_3$(QTZ-Me)(Tph)]** displayed results in excellent agreement with those usually described for the family of *fac*-Re(I) tricarbonyl diimines. Among the new Re(I) complexes, in particular, unexpectedly efficient emissive performances were exhibited by the whole series of the ***fac*-[Re(CO)$_3$(QTZ-R)(L)]$^{0/+}$** type complexes, enlightening an effect that we have preliminarily ascribed to the likely more rigid environment that is brought by the QTZ-based diimine ligands in the corresponding complexes. Another suggestion for the influence played by the **QTZ-R** scaffolds in determining the extent of the various properties of the Re(I) complexes was provided by the results obtained from the preliminary studies about the interaction of the new Re(I) complexes with Bovine Serum Albumin (BSA), as the K_b values for ***fac*-[Re(CO)$_3$(QTZ-R)(L)]$^{0/+}$** type complexes were found to be higher than those relative to ***fac*-[Re(CO)$_3$(PTZ-R)(pyr)]$^+$** series. It is also worth noting that in the cases of ***fac*-[Re(CO)$_3$(PTZ-^{t}Bu)(pyr)]$^+$** and ***fac*-[Re(CO)$_3$(QTZ-Me)(Tph)]**, beyond to the BSA quenching, an appreciable Re(I)- based emission was still observed. Taken together, these preliminary results pave the way for the further development of our Re(I) tetrazole complexes by investigating their interaction toward a wider range of protein targets and by exploring their possible use as luminescent markers for proteins.

4.5 Experimental Section

General considerations. All the reagents and solvents were obtained commercially (Sigma Aldrich/Merck, Alfa Aesar, Strem Chemicals) and used as received without any further purification unless otherwise specified. When required, the reactions were carried out under an argon atmosphere following Schlenk protocols and the purification of the Re(I) complexes was performed via column chromatography with the use of SiO_2 as the stationary phase. ESI-mass spectra were recorded using a Waters ZQ-4000 instrument (ESI-MS, acetonitrile as the solvent). Nuclear magnetic resonance spectra (consisting of ^{1}H and ^{13}C) were always recorded using a Varian Mercury Plus 400 (^{1}H, 399.9; ^{13}C, 101.0 MHz). ^{1}H and ^{13}C chemical shifts were referenced to residual solvent resonances.

Photophysics. Absorption spectra were recorded at room temperature using a Perkin Elmer Lambda 35 UV/vis spectrometer. Uncorrected steady-state emission and excitation spectra were recorded on an Edinburgh FLSP920 spectrometer equipped with a 450 W xenon arc lamp, double excitation and single emission monochromators, and a Peltier-cooled Hamamatsu R928P photomultiplier tube (185−850 nm). Emission and excitation spectra were acquired with a cut-off filter (395 nm) and corrected for source intensity (lamp and grating) and emission spectral response (detector and grating) by a calibration curve supplied with the instrument. The wavelengths for the emission and excitation spectra were determined using the absorption maxima of the MLCT transition bands (emission spectra) and at the maxima of the emission bands (excitation spectra). Quantum yields (Φ) were determined using the optically dilute method by Crosby and Demas[36] at excitation wavelength obtained from absorption spectra on a wavelength scale [nm] and compared to the reference emitter by the following equation:[37]

$$\phi_s = \phi_r \left[\frac{A_r(\lambda_r)}{A_s(\lambda_s)}\right]\left[\frac{I_r(\lambda_r)}{I_s(\lambda_s)}\right]\left[\frac{n_s^2}{n_r^2}\right]\left[\frac{D_s}{D_r}\right]$$

where A is the absorbance at the excitation wavelength (λ), I is the intensity of the excitation light at the excitation wavelength (λ), n is the refractive index of the solvent,

D is the integrated intensity of the luminescence, and Φ is the quantum yield. The subscripts r and s refer to the reference and the sample, respectively. A stock solution with an absorbance > 0.1 was prepared, then two dilutions were obtained with dilution factors of 20 and 10, resulting in absorbances of about 0.02 and 0.08 respectively. The Lambert-Beer law was assumed to remain linear at the concentrations of the solutions. The degassed measurements were obtained after the solutions were bubbled for 10 minutes under Ar atmosphere, using a septa-sealed quartz cell. Air-equilibrated $[Ru(bpy)_3]Cl_2/H_2O$ solution ($\Phi = 0.028$)[38] was used as reference. The quantum yield determinations were performed at identical excitation wavelengths for the sample and the reference, therefore deleting the $I(\lambda r)/I(\lambda s)$ term in the equation. Emission lifetimes (τ) were determined with the single-photon counting technique (TCSPC) with the same Edinburgh FLSP920 spectrometer using pulsed picosecond LED (EPLED 360, FWHM < 800ps) as the excitation source, with repetition rates between 1 kHz and 1 MHz, and the above-mentioned R928P PMT as the detector. The goodness of fit was assessed by minimizing the reduced $\chi 2$ function and by visual inspection of the weighted residuals. To record the 77 K luminescence spectra, the samples were put in quartz tubes (2 mm diameter) and inserted in a special quartz Dewar filled with liquid nitrogen. The solvent used in the preparation of the solutions for the photophysical investigations was of spectrometric grade. Experimental uncertainties are estimated to be ±8% for lifetime determinations, ±20% for quantum yields, and ±2 nm and ±5 nm for absorption and emission peaks, respectively.

Ligand synthesis. Tetrazole derivatives are used as components for explosive mixtures.[10] In this lab, the reactions described here were only run on a few grams scale and no problems were encountered. However, *great caution* should be exercised when handling or heating compounds of this type. Following the general method reported by Koguro and co-workers,[39] tetrazole ligands [H-**Tph**], [H-**QTZ**] and [H-**PTZ**] were obtained in almost quantitative yield.

[H-**Tph**] **^{1}H-NMR** (DMSO d^6, 400 MHz) δ (ppm) = 8.06 - 8.03 (m, 2H), 7.62 -7.60 (m, 3H); [H-**PTZ**] **^{1}H-NMR**, (DMSO-d^6, 400 MHz) δ (ppm): 8.79-8.77 (m, 1H), 8.22-8.20 (m, 1H), 8.08-8.04 (m, 1H), 7.63-7.60 (m,1H); [H-**QTZ**] **^{1}H-NMR**, (DMSO-d^6, 400

MHz) δ (ppm) = 8.65 (d, 1H, J = 8.79 Hz), 8.31 (d, 1H, J = 8.40 Hz), 8.17 (d, 1H, J = 8.40 Hz), 8.12 (d, 1H, J = 7.99 Hz), 7.90 (t, 1H), 7.74 (t, 1H).

Ligand Functionalization The ligands **PTZ-Me** (N-3), **QTZ-Me** (N-3) and **PTZ-^{t}Bu**, **QTZ-^{t}Bu** were obtained according to previously reported literature procedures.[40]

PTZ-Me (N-3) **^{1}H-NMR**, ($CDCl_3$, 400 MHz) δ (ppm): 8.67-8.65 (m,1H), 8.13-8.10 (m, 1H), 7.77-7.73 (m, 1H), 7.30-7.26 (m, 1H), 4.34 (s, 3H). **^{13}C-NMR**, ($CDCl_3$, 100 MHz) δ (ppm): 164.78 (C_{tet}), 150.18, 146.60, 137.00, 124.73, 122.20, 39.59.

QTZ-Me (N-3) **^{1}H-NMR**, ($CDCl_3$, 400 MHz) δ (ppm): 8.38-8.36 (m, 3H), 7.91-7.88 (m, 1H), 7.82-7.76 (m, 1H), 7.65-7.61 (m, 1H), 4.52 (s, 3H). **^{13}C-NMR**, ($CDCl_3$, 100 MHz) δ (ppm): 164. 98 (Ct), 148.01, 146.49, 137.25, 130.01, 129.93, 128.32, 127.54, 127.42, 119.54, 39.71 (CH_3).

PTZ-^{t}Bu ^{1}H-NMR, ($CDCl_3$, 400 MHz) δ (ppm): 8.81-8.80 (d, 1H, J = 4.00 Hz), 8.28-8.26 (d, 1H, J = 7.60 Hz), 7.88-7.84 (m, 1H), 7.40-7.37 (m, 1H), 1.84 (s, 9H). **^{13}C-NMR**, ($CDCl_3$, 100 MHz) δ (ppm): 164.1 (C_t), 155.2, 149.4, 137.2, 124.2, 123.7, 73.1 (C-$(CH_3)_3$), 28.3 ((CH_3)$_3$).

QTZ-^{t}Bu ^{1}H-NMR, ($CDCl_3$, 400 MHz) δ (ppm): 8.38 – 8.30 (m, 3H), 7.87 (m, 1H), 7.77 (m, 1H), 7.60 (m, 1H), 1.87 (s, 9H). **^{13}C-NMR**, ($CDCl_3$, 100 MHz) δ (ppm): 163.5 (C_t), 157.4, 144.2, 137.3, 129.8, 128.3, 127.1, 125.3, 121.0, 119.5, 72.9 (C-$(CH_3)_3$), 28.6 ((CH_3)$_3$).

General Procedure for the Preparation of fac-[Re(CO)$_3$(N^N)-(pyr)]$^+$ and fac-[Re(CO)$_3$(QTZ-Me)-(Tph)] -type complexes

The preparation of ***fac*-[Re(CO)$_3$(N^N)-(pyr)]$^+$** -type complexes was accomplished by following a multistep procedure which involved at first the formation of the neutral *fac*-[Re(CO)$_3$(N^N)(Br)] by refluxing Re(CO)$_5$Br (1 eq) with the appropriate (N^N) ligand (1.1 eq) in 20 mL of toluene for 24h. The crude was allowed to cool to room temperature and the addition of Et_2O induced the precipitation of bright yellow to orange solids collected by filtration, air-dried and used for the successive steps without any further purification. In a two neck round-bottomed flask protected from light, 1 eq of the desired neutral *fac*-[Re(CO)$_3$(N^N)(Br)] and 1.5 eq. of $AgPF_6$ were combined in 20 mL of CH_3CN and refluxed for 3 hrs. The crude was cooled to room temperature, filtered over a celite pad to remove AgBr and successively combined with pyridine (5 eq.) in $CHCl_3$ (20 mL) . The solutions were heated over reflux (70°C) under an argon atmosphere for 15 hrs, after which the pale to bright yellow precipitates formed were collected by filtration and washed with Et_2O. In the case of ***fac*-[Re(CO)$_3$(QTZ-Me)(Tph)]**, 1.2 eq. of H-Tph were added to the reaction mixture instead of pyridine after the halide extraction step. The crude was then purified by column chromatography over SiO_2 eluted with a CH_2Cl_2/Acetone 9:1 mixture. The product was obtained as the first fraction.

***fac*-[Re(CO)$_3$(QTZ-Me)(Br)] ^{1}H-NMR**, (Acetone-d^6, 400 MHz) δ (ppm): 9.01-8.99 (d, 1H, J = 8.80 Hz), 8.87-8.85 (d, 1H, J = 8.80 Hz), 8.53-8.51 (d, 1H, J = 8.40 Hz), 8.34-8.32 (d, 1H, J = 8.00 Hz), 8.24-8.20 (t, 1H, J =16.00 Hz, J = 8.40 Hz, J = 7.60 Hz), 8.00-7.96 (t, 1H, J = 15.20 Hz, J = 8.00 Hz, J = 7.20 Hz), 4.83 (s, 3H). **ESI-MS** : $[M+Na]^+$ = 584 m/z. **IR-ATR** ν (cm^{-1}) : 2031 (CO), 1931 (CO), 1910 (CO). Y = 73% (MW= 561 g/mol, 0.51 mmol).

***fac*-[Re(CO)$_3$(QTZ-^{t}Bu)(Br)] ^{1}H-NMR**, ($CDCl_3$, 400 MHz) δ (ppm): 8.93-8.91 (d, 1H, J = 8.00 Hz), 8.58-8.56 (d, 1H, J = 8.0 Hz), 8.35-8.33 (d, 1H, J = 8.40 Hz), 8.10-8.01 (m, 2H), 7.90-7.81 (m, 1H), 1.93 (s, 9H). **ESI-MS** (m/z) : $[M+Na]^+$= 626, $[M+K]^+$= 642. **IR-ATR** ν (cm^{-1}): 2031 (CO), 1930 (CO), 1907 (CO). Y= 73% (MW= 553 g/mol, 0.60 mmol). Y = 41% (MW= 603 g/mol, 0.14 mmol).

***fac*-[Re(CO)$_3$(PTZ-Me)(Br)] ^{1}H-NMR**, ($CDCl_3$, 400 MHz) δ (ppm): 9.11-9.09 (m, 1H), 8.28-8.25 (m, 1H), 8.16-8.11 (m, 1H), 7.65-7.62 (m, 1H), 4.59 (s, 3H). **ESI-MS** (m/z): $[M+Na]^+$ = 534, $[M+K]^+$ = 550. **IR-ATR** ν (cm^{-1}): 2033 (CO), 1934 (CO), 1907 (CO). Y = 69% (MW= 511 g/mol, 0.35 mmol).

***fac*-[Re(CO)$_3$(PTZ-^{t}Bu)(Br)] ^{1}H-NMR**, ($CDCl_3$, 400 MHz) δ (ppm): 9.10-9.08 (m, 1H), 8.30-8.26 (m, 1H), 8.14-8.10 (m, 1H), 7.63-7.59 (m, 1H), 1.88 (s, 9H). **ESI-MS** (m/z): $[M+Na]^+$ = 575. **IR-ATR** ν (cm^{-1}): 2032 (CO), 1933 (CO), 1905 (CO). Y = 19% (MW= 698 g/mol; 0.05 mmol).

***fac*-[Re(CO)$_3$(PTZ-Me)-(Pyr)]$^+$** Y =75% (MW= 655 g/mol; 0.303 mmol).

***fac*-[Re(CO)$_3$(PTZ-^{t}Bu)-(Pyr)]$^+$** Y =19% (MW= 698 g/mol; 0.05 mmol). **^{1}H-NMR**, ($CDCl_3$, 400 MHz) δ (ppm): 9.17-9.16 (d, 1H, J = 5.60 Hz, PTZ-^{t}Bu), 8.44-8.42(d, 1H, J = 7.20 Hz, pyr), 8.34-8.30 (m, 1H, PTZ-^{t}Bu), 8.26-8.24 (d, 2H, J = 5.20 Hz, PTZ-^{t}Bu), 7.91-7.81 (m, 2H, pyr), 7.43-7.40 (m, 2H, pyr), 1.92 (s, 9H, -^{t}Bu). **ESI-MS** (m/z): $[M]^+$= 553; $[M]^-$= 145 (PF_6). **IR-ATR** ν (cm^{-1}): 2045 (CO), 1940 (CO). **^{13}C-NMR**, (Acetone-*d*^{6}, 100 MHz) δ (ppm): 166.98 (C_t), 155.22 (C_{ipso}), 152.61 (PTZ-^{t}Bu), 144.93 (pyr), 142.37 (PTZ-^{t}Bu), 140.20 (pyr), 130.32 (PTZ-^{t}Bu), 127.06 (PTZ-^{t}Bu), 124.84 (pyr), 69.36 (C^{t}Bu), 40.55 (-^{t}Bu). Y =19% (MW= 698 g/mol; 0.05 mmol). Anal. Calcd. For $C_{18}H_{18}N_6O_3P_1F_6Re_1$ (697.55) C 30.99, H 2.60, N 12.05. Found: C 29.43, H 2.45, N 11.94.

***fac*-[Re(CO)$_3$(QTZ-Me)-(Pyr)]$^+$** Y= 34% (MW= 705 g/mol; 0.088 mmol). **^{1}H-NMR**, (CD_3CN, 400 MHz) δ (ppm): 8.95-8.88 (m, 1H, QTZ-Me), 8.49-8.47 (d, 1H, J = 8.0 Hz, QTZ-Me), 8.31-8.27 (m, 2H, QTZ-Me, pyr), 8.17-8.15 (m, 1H, QTZ-Me), 8.03-8.00 (m, 2H, pyr), 7.86-7.80 (m, 2H, pyr), 7.70-7.66 (m, 1H, QTZ-Me), 7.23-7.20 (m, 1H, QTZ-Me), 4.46 (s, 3H, CH_3). **ESI-MS** (m/z): $[M]^+$= 561; $[M]^-$=145 (PF_6). **IR-ATR** ν (cm^{-1}): 2045 (CO), 1940 (CO). **^{13}C-NMR**, (CD_3CN, 100 MHz) δ (ppm): 166.78 (C_t), 152.53 (C_{ipso}), 147.44 (QTZ-Me), 143.73 (pyr), 139.94 (pyr), 138.34 (QTZ-Me), 134.84 (QTZ-Me), 131.02 (QTZ-Me), 130.81 (QTZ-Me), 130.44 (QTZ-Me), 130.31 (QTZ-Me), 129.40 (QTZ-Me), 128.94 (QTZ-Me), 128.76 (QTZ-Me), 128.18 (QTZ-Me), 126.93 (pyr), 119.99 (QTZ-Me), 42.39 (CH_3). Y= 34% (MW= 705 g/mol; 0.088 mmol). Anal.

Calcd. For $C_{19}H_{14}N_6O_3P_1F_6Re_1$ (705.53) C 32.35, H 2.00, N 11.91. Found: C 30.39, H 2.04, N 10.63.

***fac*-[Re(CO)$_3$(QTZ-^{t}Bu)-(Pyr)]$^+$** Y = 12% (MW= 748 g/mol; 0.016 mmol). **^{1}H-NMR**, ($CDCl_3$, 400 MHz) δ (ppm): 8.87-8.85 (d, 1H, J = 8.80 Hz, QTZ-^{t}Bu), 8.80-8.78 (d, 1H, J = 8.40 Hz, QTZ-^{t}Bu), 8.53-8.51 (d, 1H, J = 8.40 Hz, QTZ-^{t}Bu), 8.20-8.14 (m, 2H, pyr), 8.00-7.98 (d, 2H, J = 5.20 Hz, QTZ-^{t}Bu), 7.96-7.92 (m, 1H, QTZ-^{t}Bu), 7.79-7.76 (t, 1H, J = 15.60 Hz, J = 8.00 Hz, J =7.60 Hz, pyr), 7.30-7.26 (m, 2H, pyr), 1.96 (s, 9H, -^{t}Bu). **ESI-MS** (m/z) : $[M]^+$= 603, $[M]^-$ = 145 (PF_6). **IR-ATR** ν (cm^{-1}): 2030 (CO), 1926 (CO), 1940 (CO). **^{13}C-NMR** ($CDCl_3$, 100 MHz) δ (ppm): 167.60 (C_t), 151.73 (C_{ipso}), 147.18 (QTZ-^{t}Bu), 143.42 (pyr), 140.21 (pyr), 134.33 (QTZ-^{t}Bu), 130.83 (QTZ-^{t}Bu), 130.50 (QTZ-^{t}Bu), 130.15 (QTZ-^{t}Bu), 128.55 (QTZ-^{t}Bu), 127.26 (QTZ-^{t}Bu), 121.08 (pyr), 105.01 (QTZ-^{t}Bu), 70.01 (^{t}Bu), 29.63 (^{t}Bu). Y = 12% (MW= 748 g/mol; 0.016 mmol). Anal. Calcd. For $C_{22}H_{20}N_6O_3P_1F_6Re_1$ (747.61) C 35.35, H 2.70, N 11.24. Found: C 36.27, H 2.91, N 11.03.

***fac*-[Re(CO)$_3$(QTZ-Me)(Tph)]** Y= 48 % (MW=627 g/mol; 0.12 mol). **^{1}H-NMR**, ($CDCl_3$, 400 MHz) δ (ppm): 8.99-8.97 (d, 1H, J = 8.80 Hz, QTZ-Me), 8.59-8.57 (d, 1H, J = 8.40 Hz, QTZ-Me), 8.33-8.31 (d, 1H, J = 8.40 Hz, QTZ-Me), 8.07-8.03 (m, 1H, QTZ-Me), 8.00-7.98 (m, 1H, QTZ-Me), 7.86-7.84 (m, 2H, Tph), 7.82-7.78 (m,1H, QTZ-Me), 7.31-7.24 (m, 3H, Tph), 4.64 (s, 3H, CH_3). **ESI-MS** (m/z): [M+H] = 628 m/z. **IR-ATR** ν (cm^{-1}): 2036 (CO), 1932 (CO). **^{13}C-NMR**, (Acetone-d^6, 100 MHz) δ (ppm): 197.34 (CO), 194.13 (CO), 193.09 (CO), 168.91 (C_t, QTZ-Me), 162.65 (C_t, Tph), 148.08 (C_{ipso}), 147.57 (C_{ipso}), 133.54 (QTZ-Me), 130.22 (QTZ-Me), 130.17 (QTZ-Me), 129.77 (QTZ-Me), 129.74 (QTZ-Me), 129.56 (Tph), 128.41 (Tph), 128.30 (QTZ-Me), 128.14 (QTZ-Me), 125.81 (Tph), 119.46 (QTZ-Me), 41.69 (CH_3). Y= 48 % (MW=627 g/mol; 0.12 mol). Anal. Calcd. For $C_{21}H_{14}N_9O_3Re_1$ (626.6) C 40.25, H 2.25, N 20.12. Found: C 37.14, H 2.27, N 17.72.

Absorption and Emission Titration Experiments

PBS buffer (1 L) was prepared by dissolving Na_2HPO_4 (1.44 g), KH_2PO_4 (0.245 g), NaCl (8g) and KCl (0.2g) in 0.8 L of H_2O. After complete mixing, the solution was topped up to volume. Final pH = 7.4. Then, a 100 mL $4.4*10^{-4}$ M BSA (Sigma Aldrich, MW = 66463 g/mol) solution was prepared by dissolving 2.9 g of BSA in 100 mL of PBS buffer. The final concentration of BSA used in the absorption and emission titration was $1*10^{-5}$M (45.45 μL of $4.4*10^{-4}$ M BSA to V_{tot} = 2mL). The Re(I)-complexes solutions were prepared by dissolving 1.2-1.4 mg of complex in 1mL of DMSO, resulting in concentrations of $2.1*10^{-3}$ M. 2 mL of the BSA/PBS solution were placed in a quartz cuvette and successive aliquots of Re(I) complexes solutions in DMSO were added with a micropipette (20x5μL). For absorption titration, absorption spectra were collected from 230 to 800 nm after each addition. For emission titration, emission spectra were collected from 300 to 800 nm by monitoring the 346 nm maxima (BSA emission) upon 280 nm excitation.

X-ray crystallography

Crystal data and collection details for ***fac*-[Re(PTZ-Me)(CO)$_3$(pyr)][PF$_6$]·CH$_2$Cl$_2$** and ***fac*-[Re(QTZ-Me)(CO)$_3$(pyr)][PF$_6$]·CHCl$_3$** are reported in ESI†, Table S2. Data were recorded on a Bruker APEX II diffractometer equipped with a PHOTON2 (***fac*-[Re(QTZ-Me)(CO)$_3$(pyr)][PF$_6$]·CHCl$_3$**) or CCD (***fac*-[Re(PTZ-Me)(CO)$_3$(pyr)][PF$_6$]·CH$_2$Cl$_2$**) detector using Mo–Kα radiation. Data were corrected for Lorentz polarization and absorption effects (empirical absorption correction SADABS).[41] The structures were solved by direct methods and refined by full-matrix least-squares based on all data using F^2.[42] Hydrogen atoms were fixed at calculated positions and refined by a riding model. All non-hydrogen atoms were refined with anisotropic displacement parameters. The PTZ-Me ligand and $[PF_6]^-$ anion of ***fac*-[Re(PTZ-Me)(CO)$_3$(pyr)][PF$_6$]·CH$_2$Cl$_2$** are disordered. They have been split into two positions and refined using one occupancy factor per disordered group. CCDC 2044691 and 2044692 contains the supplementary crystallographic data for ***fac*-[Re(PTZ-Me)(CO)$_3$(pyr)][PF$_6$]·CH$_2$Cl$_2$** and ***fac*-[Re(QTZ-Me)(CO)$_3$(pyr)][PF$_6$]·CHCl$_3$**.

4.6 References

[1] R. A. Kirgan, B. P. Sullivan and D-P. Rillema, Photochemistry and Photophysics of Coordination Compounds: Rhenium. In: V. Balzani, S. Campagna (eds) "Photochemistry and Photophysics of Coordination Compounds II", *Top. Curr. Chem.*, **2007**, *281*, 45-100.

[2] a) K. Y. Zhang and K. K.-W. Lo, "Chemosensing and Diagnostics", in Coordination and Organometallic Chemistry of Comprehensive Inorganic Chemistry II, ed. V. W.-W. Yam, Elsevier, Amsterdam, **2013**, *8*, 657–732, and references cited therein.

[3] S. Hostachy, C. Policar and N. Delsuc, *Coord. Chem. Rev.*, **2017**, *351*, 172-188.

[4] K. K.-W Lo, *Acc. Chem. Res.*, **2015**, *12*, 2985-2995.

[5] L. C.-C. Lee, K.-K. Leung and K. K.-W. Lo, *Dalton Trans.*, **2017**, *46*, 16357 – 16380.

[6] V. Fernandez-Moreira, F. L. Thorp-Greenwood and M. P. Coogan, Chem. Commun. **2010**, *46*, 186–202.

[7] F. L. Thorp-Greenwood, M. P. Coogan, L. Mishra, N. Kumari, G. Raic and S. Saripellad, *New J. Chem.*, **2012**, *36*, 64-72.

[8] C. A. Bader, R. D. Brooks, Y. S. Ng, A. Sorvina, M. V. Werrett, P. J. Wright, A. G. Anwer, D. A. Brooks, S. Stagni, S. Muzzioli, M. Silberstein, B. W. Skelton, E. M. Goldys, S. E. Plush, T. Shandala and M. Massi, *RSC Adv.*, **2014**, *4*, 16345-16351.

[9] V. Fiorini, L. Bergamini, N. Monti, S. Zacchini, S. E. Plush, M. Massi, A. Hochkoeppler, A. Stefan and S. Stagni, *Dalton. Trans.*, **2018**, *47*, 9400-9410.

[10] R. N. Butler "Tetrazoles" In "Comprehensive Heterocyclic Chemistry II"; Storr, R. C., Ed.; Pergamon Press: Oxford, U.K., 1996; Vol. **4**, 621-678, and references cited therein.

[11] S. Sato, T. Morimoto and O. Ishitani, Inorg. Chem., **2007**, *46*, 9051-9053.

[12] M. V. Werrett, D. Chartrand, J. D. Gale, G. S. Hanan, J. G. MacLellan, M. Massi, S. Muzzioli, P Raiteri, B. W. Skelton, M. Silberstein and S. Stagni, *Inorg. Chem.*, **2011**, *50*, 1229-1241.

[13] M.V. Werrett, S. Muzzioli, P. J. Wright, A. Palazzi, P. Raiteri, S. Zacchini, M. Massi, S. Stagni, *Inorg. Chem.*, **2014**, *53*, 229-243.

[14] M. V. Werrett, G. S. Huff, S. Muzzioli, V. Fiorini, S. Zacchini, B. W. Skelton, A. Maggiore, J. M. Malicka, M. Cocchi, K. C. Gordon, S. Stagni and M. Massi, *Dalton. Trans.*, **2015**, *44*, 8379-8393.

[15] L. Flamigni, A. Barbieri, C. Sabatini, B. Ventura and F. Barigelletti, Photochemistry and Photophysics of Coordination Compounds: Iridium. In: V. Balzani, S. Campagna (eds) "Photochemistry and Photophysics of Coordination Compounds II", *Top. Curr. Chem.*, **2007**, *281*, 143-203.

[16] N. Akabar, V. Chaturvedi, G. E. Shillito, B. J. Schwehr, K. C. Gordon, G. S. Huff, J. J. Sutton, B. W. Skelton, A. N. Sobolev, S. Stagni, D. J. Nelson and M. Massi, *Dalton Trans.*, **2019**, *48*, 15613-15624.

[17] J. L. Wedding, H. H. Harris, C. A. Bader, S. E. Plush, R. Mak, M. Massi, D. A. Brooks, B. Lai, S. Vogt, M. V. Werrett, P. V. Simpson, B. W. Skelton and S. Stagni, *Metallomics*, **2017**, *9*, 382-390.

[18] C. A. Bader, A. Sorvina, P. V. Simpson, P. J. Wright, S. Stagni, S. E. Plush, M. Massi and D. A. Brooks, *FEBS Letters*, **2016**, *590*, 3051-3060.

[19] C. A. Bader, E. A. Carter, A. Safitri, P. V. Simpson, P. J. Wright, S. Stagni, M. Massi, P. A. Lay, D. A. Brooks and S. E. Plush, Mol. BioSyst., **2016**, *12*, 2064-2068.

[20] C. A. Bader, T. Shandala, E. A. Carter, A. Ivask, T. Guinan, S. M. Hickey, M. V. Werrett, P. J. Wright, P. V. Simpson, S. Stagni, N. H. Voelcker, P. A. Lay, M. Massi, S. E. Plush and D. A. Brooks, *PLoS ONE*, **2016**, *11*, e0161557.

[21] V. Fiorini, A. M. Ranieri, S. Muzzioli, K. D. M. Magee, S. Zacchini, N. Akabar, A. Stefan, M. I. Ogden, M. Massi and S. Stagni, *Dalton Trans.*, **2015**, *44*, 20597-20608.

[22] M. V. Werrett, P. J. Wright, P. V. Simpson, P. Raiteri, B W. Skelton, S. Stagni, A. G. Buckley, P. J. Rigby and M. Massi, *Dalton Trans.*, **2015**, *44*, 20636-20647.

[23] T. Topala, A. Bodoki, L. Oprean and R. Oprean *Clujul Medical*, **2014**, *87*, 215-219.

[24] T. Peters "Serum Albumin", *Adv. Protein Chem.*, **1985**, *37*, 161-245.

[25] D. Peak, T. C. Werner, R. M. Dennin and J. K. Baird, *J. Chem. Phys.*, **1983**, *79*, 3328

[26] H. Boaz and G. K. Rollefson, *J. Am. Chem. Soc.*, **1950**, *72*, 3435–3443

[27] J. Keizer, *J. Am. Chem. Soc.*, **1983**, *105*, 1494–1498

[28] J. R. Lakowicz, 3rd ed." *Plenum: New York*, **2006**.

[29] K. M. Danielsen, Y-P. Chin, J. S. Buterbaugh, T. L. Gustafson and S. J. Traina, *Environ. Sci. Technol.*, **1995**, *29*, 2162-2165.

[30] W. R. Ware, *J. Phys. Chem.*, **1962**, *66*, 455.

[31] C-Y. Gao, X. Qiao, Z-Y. Ma, Z-G. Wang, J. Lu, J-L. Tian, J-Y. Xu and S-P. Yan, *Dalton Trans.*, **2012**, *41*, 12220–12232.

[32] G. Scatchard, *Ann. N.Y. Acad. Sci.*, **1949**, *51*, 660.

[33] N. Ghosh, R. Mondal and S. Mukherjee, *Langmuir*, **2015**, 29, 8074–8080

[34] M. van de Weert, L. Stella, *J. Mol. Struct.*, **2011**, *998*, 144-150.

[35] V. Rajendiran, R. Karthik, M. Palaniandavar, H. Stoeckli-Evans, V. S. Periasamy, M. A. Akbarsha, B. S. Srinag and H. Krishnamurthy, *Inorg. Chem.* **2007**, *46*, 8208–8221.

[36] G. A. Crosby and J. N. Demas, *J. Phys. Chem.*, 1971, **75**, 991-1024.

[37] F. Eaton “Reference materials for luminescence measurements”, *Pure Appl. Chem*., 1988, **60**, 1107-1114.

[38] K. Nakamaru, *Bull. Chem. Soc. Jpn*., **1982**, *55*, 2697–2705.

[39] K. Koguro, T. Oga, S. Mitsui and R. Orita, *Synthesis*, **1998**, 910-914.

[40] N. Monti, S. Zacchini, M. Massi, A. Hochkoeppler, L. Giorgini, V. Fiorini, A. Stefan and S. Stagni, *Appl. Organomet. Chem*., **2020**, 34:e5806.

[41] G. M. Sheldrick “*SADABS-2008/1 - Bruker AXS Area Detector Scaling and Absorption Correction*” Bruker AXS: Madison, Wisconsin, USA, **2008**.

[42] G. M. Sheldrick, “Crystal structure refinement with SHELXL – IUCr”, *Acta Crystallogr. C*, **2015**, *71*, 3.

Chapter 5 Luminescent Protein Staining with Re(I) Tetrazolato Complexes*

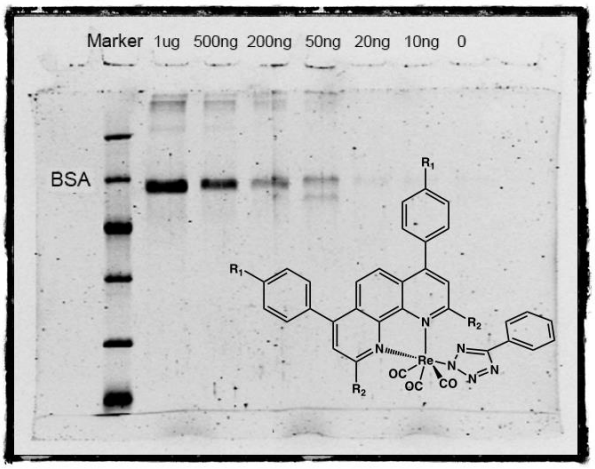

*This chapter is part of *Dalton. Trans.,* **2018**, *47,* 9400-9410.

5.1 Abstract

Within the general framework of our past and current studies dealing with the investigation of the photophysical properties and the biological behaviour of the family of tetrazolato and tetrazole Re(I) complexes, we have endeavoured to investigate their potential in the luminescent staining of proteins purified by acrylamide gel electrophoresis. To provide the first examples of luminescent Re(I) complexes to be exploited for this specific purpose, we have designed and prepared four new Re(I)-based species with the general formula *fac*-**[Re(CO)$_3$(N^N)(Tph)]$^{2-/0}$**, where **Tph** is the 5-(phenyl)tetrazolato anion and **N^N** is in turn represented by bathophenanthroline disulfonate (**BPS**), bathocuproine disulfonate (**BCS**) or by the SO_3^- free bathocuproine (**BC**). In this latter case, the neutral complex *fac*-**[Re(CO)$_3$(BC)(Tph)]** served as a model species for the characterization of the former disulfonate complexes. Its cationic analogue *fac*-**[Re(CO)$_3$(BC)(Tph-Me)]$^+$** was also prepared by a straightforward methylation reaction. All complexes displayed bright phosphorescence in organic media and, relative to their water solubility, the dianionic species *fac*-**[Re(CO)$_3$(BPS)(Tph)]$^{2-}$** and *fac*-**[Re(CO)$_3$(BCS)(Tph)]$^{2-}$** were also highly emissive in aqueous solution. The sulfonate groups played a key role in promoting and significantly enhancing the

luminescent staining performances of both the Re(I) complexes *fac*-**[Re(CO)$_3$(BPS)(Tph)]$^{2-}$** and *fac*-**[Re(CO)$_3$(BCS)(Tph)]$^{2-}$** for proteins. Highlighting a response superior to that of Coomassie Blue and comparable to the one obtained by the well-known silver staining method, these dianionic Re(I)-complexes could efficiently detect up to 50 ng of pure Bovine Serum Albumin (BSA), as well as all proteins found in a Standard Protein Marker mix and from a total protein extract. A lower but still good response for luminescent protein staining was surprisingly obtained by employing the -SO_3^- free neutral and cationic complexes *fac*-**[Re(CO)$_3$(BC)(Tph)]** and *fac*-**[Re(CO)$_3$(BC)(Tph-Me)]$^+$**, respectively. These preliminary results open up new possibilities for the further widening of the use of Re(I)-based complexes as luminescent protein staining agents.

5.2 Introduction

The development of luminescent sensors aimed at targeting biologically relevant molecules has been central to the research interests of many groups worldwide. Further to the well-established protocols that are centred on organic fluorophores, a great deal of attention has been dedicated to the use of the most popular classes of luminescent metal complexes, such as those based on Ru(II), Ir(III), Re(I) and Pt(II) for the extra and intracellular luminescent detection of bio-molecules.[1] Among the various targets, proteins are one of the most important, and intense research efforts have been dedicated to their sensing by taking advantage of the different interactions (*i.e.* covalent, not covalent) that can occur between proteins and luminescent metal complexes. In addition to providing critical information into the involvement of key proteins in biological processes,[2] these studies have had a significant impact on proteomic analysis. For example, a series of Ru(II)-based compounds, such as ruthenium(II) *tris*(bathophenanthroline disulfonate), abbreviated as RuBPS,[3] and SYPRO Ruby® (whose structure is yet undisclosed),[4a-b] have been indeed commercialized as luminescent agents for the staining of the discrete protein bands that are obtained from Sodium Dodecyl Sulphate - PolyAcrylamide Gel Electrophoresis (SDS-PAGE). The strategy underpinning the use of RuBPS relies upon the water solubility that is conferred by the sulfonate moieties and, importantly, by the occurrence of electrostatic interactions between the peripheral $–SO_3^-$ groups of the BPS ligands and the $-NH_2$ groups of the proteins.[3,4] The structure of RuBPS has inspired the successive development of BPS-based Ir(III) cyclometalated complexes with the general formula $[Ir(C\hat{}N)_2(BPS)]$, in which the peculiar and intense luminescent output of this class of metal complexes was combined with the "usual" protein recognition properties displayed by the sulfonate groups.[5] In these regards, it is worth noting that a recent report by Zhou and coworkers showed that also cationic and neutrally charged Ir(III) cyclometalated complexes devoid of any $–SO_3^-$ moieties could also be used as protein staining agents, pointing to the importance of other factors aside of electrostatic interactions in determining the performances of protein stains.[6]

To the best of our knowledge, no examples of *fac*-tricarbonyl Re(I) diimines, one of the most extensively studied classes of luminescent d^6 metal complexes, have been considered for the specific purpose of protein staining. To this end, we have prepared a library of Re(I)-tetrazolato complexes with the general formula ***fac*-[Re(CO)$_3$(N^N)(Tph)]$^{0/+/2-}$** where **Tph** denotes the 5-(phenyl)tetrazolato, to be exploited as new luminescent protein staining agents for SDS PAGE. In particular, our design strategy for the **N^N** ligand involves the use of disulfonate ligands; either bathophenanthroline disulfonate (**BPS**) or bathocuproine disulfonate (**BCS**, see Scheme 1). We also prepared the neutral SO_3^- free bathocuproine (**BC**) complex ***fac*-[Re(CO)$_3$(BC)(Tph)]** and its cationic methylated analogue ***fac*-[Re(CO)$_3$(BC)(Tph-Me)]$^+$** (see Schemes 1 and 3) by taking advantage of the reactivity that the tetrazolate ligand displays toward electrophiles. Our results highlight how Re(I) disulfonate complexes can be regarded as very sensitive staining agents for proteins in SDS-PAGE while the non-sulfonate neutral and cationic derivatives, in addition to being useful model complexes, also display a promising potential for the detection of proteins.

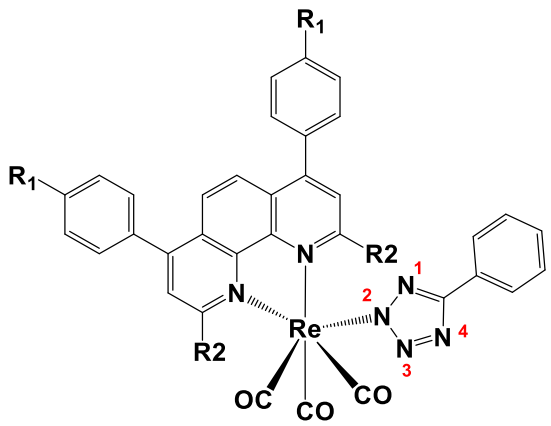

$R_1 = SO_3^-$, $R_2 = CH_3$; *fac*-[Re(CO)$_3$(BCS)(Tph)]$^{2-}$
$R_1 = SO_3^-$, $R_2 = H$; *fac*-[Re(CO)$_3$(BPS)(Tph)]$^{2-}$
$R_1 = H$, $R_2 = H$; *fac*-[Re(CO)$_3$(BC)(Tph)]

Scheme 1.5. Structures, acronyms of the complexes and numbering for 5-(phenyl)tetrazolato (**Tph**) reported in this work.

Results and Discussion

The 5-(phenyl)tetrazolato anion **Tph** was chosen due to its strong binding to the Re(I) centre which results in a substitution inert complex. This is important to ensure that any interactions between the complexes and proteins can be confidently ascribed to the disulfonate **N^N** ligands **BPS** or **BCS**. To this end, as depicted in **Scheme 2.5**, the preparation of the corresponding Re(I)-tetrazolato complexes *fac*-**[Re(CO)$_3$(BPS)(Tph)]$^{2-}$** and *fac*-**[Re(CO)$_3$(BCS)(Tph)]$^{2-}$** was pursued by a multistep procedure that required the preliminary counterion exchange of the sodium salts of the ligands **BPS** and **BCS.** This lead to the corresponding tetrabutylammonium $[Bu_4N]^+$ analogues which were found to be more soluble in organic solvents.[7] Following this modification, the Re(I) complexes were obtained by our standard route[8a-b] which involved the initial formation of the bromide precursors *fac*-**[Re(CO)$_3$(BPS)(Br)]$^{2-}$** and *fac*-**[Re(CO)$_3$(BCS)(Br)]$^{2-}$**, followed by the Ag(I)-mediated bromide extraction and, finally, the coordination of the 5-(phenyl)tetrazolato anion to the Re(I) ion. (**Scheme 2.5**)

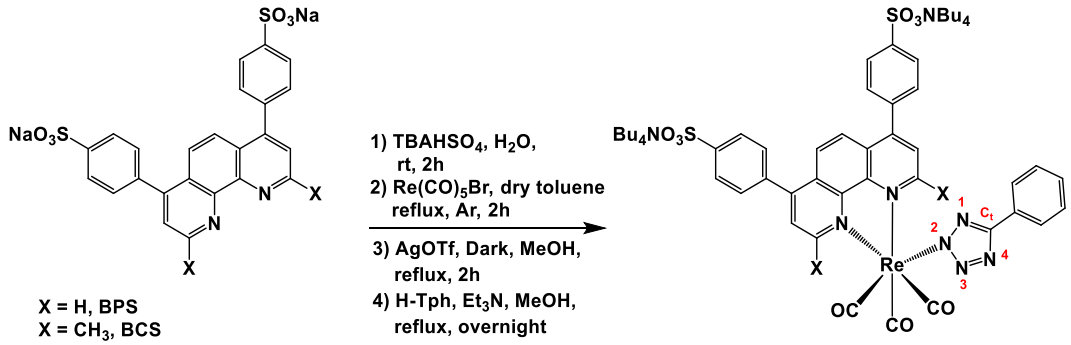

Scheme 2.5. The synthetic procedure used for the preparation of Re(I) disulfonate compounds described in this work (C_t means tetrazolic carbon).

After column chromatography, the target dianionic complexes *fac*-**[Re(CO)$_3$(BPS)(Tph)]$^{2-}$** and *fac*-**[Re(CO)$_3$(BCS)(Tph)]$^{2-}$** were characterized by performing Electro-Spray Ionisation Mass Spectrometry (ESI-MS) and Infrared (IR) spectroscopy.

The collected data supports their formation as tetrabutylammonium salts and with the facial arrangement of the three CO ligands (ESI). The analysis of the NMR (^{1}H and ^{13}C) data for the disulfonate Re(I)-complexes required direct comparisons to the well-resolved ^{1}H and ^{13}C NMR spectra of the neutral sulfonate-free model complex *fac*-**[Re(CO)$_3$(BC)(Tph)]**. This is due to the occurrence of the commercial **BPS** and **BCS** as mixtures of regioisomers,[6,9] which complicated the peak assignment. The pattern of signals of the neutral sulfonate-free model complex *fac*-**[Re(CO)$_3$(BC)(Tph)]** were consistent with the presence of one *cis*-chelate bathocuproine (**BC**) as the diimine (N^N) ligand and one axially coordinated 5-(phenyl)tetrazolato anion were clearly displayed (ESI). Also, the direct comparison of the ^{13}C-NMR spectra of *fac*-**[Re(CO)$_3$(BC)(Tph)]** with those relative to *fac*-**[Re(CO)$_3$(BPS)(Tph)]$^{2-}$** and *fac*-**[Re(CO)$_3$(BPS)(Tph)]^{2}** revealed how, in all complexes, the tetrazolic carbon (Ct) was found to resonate at values of chemical shifts that, according to our previous work, is characteristic of the regioselective coordination of the tetrazolate ligand to the Re(I) ion through the N-2 atom of the pentatomic ring. (**Schemes 2.5** and **3.5** for atom numbering)

5.2.1 *X-ray crystallography*

This evidence was further corroborated by the analysis of the molecular structure obtained by X-ray diffraction of *fac*-**[Re(CO)$_3$(BC)(Tph)]**, (**Figure 1.5**) which shows bonding parameters in excellent agreement with those reported earlier for related and isostructural Re(I) tetrazolato complexes.[8a-b]

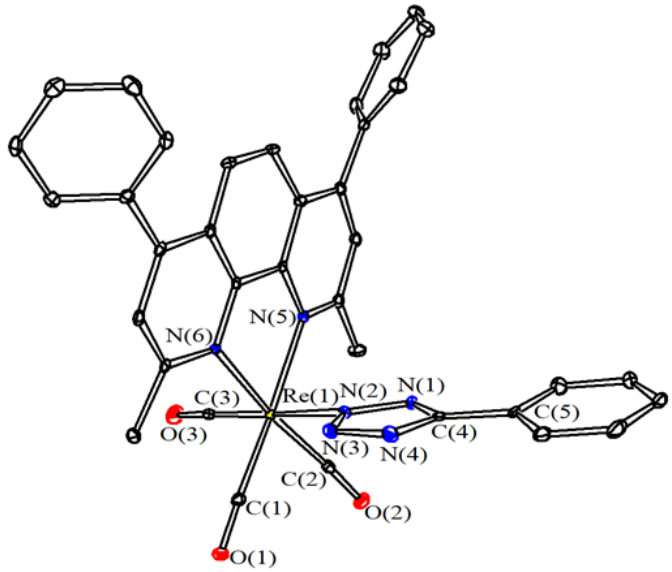

Figure 1.5. Molecular structure of ***fac*-[Re(CO)$_3$(BC)(Tph)]** with key atoms labelled. Displacement ellipsoids are at the 30% probability level. Hydrogen atoms have been omitted for clarity.

Over the past decade, we have extensively exploited the reactivity of luminescent Ru(II),[10a-b] Ir(III)[11a-b] and Re(I)-tetrazolato complexes toward electrophiles such as H^+,[12] CH_3^+ and divalent metal cations.[8a-b] These studies highlight how such a relatively simple and straightforward chemical modulation of the tetrazolato ancillary ligand of the corresponding Ru(II) and, particularly, Ir(III) and Re(I)-tetrazolato complexes could be regarded as a viable strategy to modify their luminescence outputs and to impart alternative biological behaviour in terms of cellular incubation, localisation,[13a-c] cytotoxicity,[14] and antibacterial properties.[15] On such basis, aiming to investigate the effect of the variation of the global charge of the SO_3^- free Re(I) tetrazolato complexes on their eventual luminescent protein staining properties, the neutral complex *fac*-**[Re(CO)$_3$(BC)(Tph)]** was converted into the corresponding cationic analogue *fac*-**[Re(CO)$_3$(BC)(Tph-Me)]$^+$** by methylation reaction. (**Scheme 3.5**)

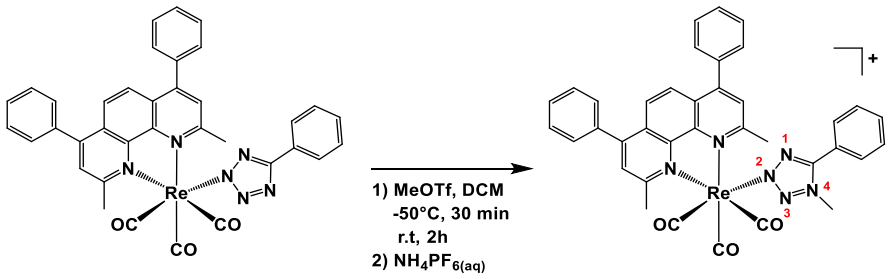

Scheme 3.5. The synthetic procedure used for the preparation of ***fac*-[Re(CO)$_3$(BC)(Tph-Me)]$^+$**.

The analysis of the NMR features of the methylated complex *fac*-**[Re(CO)$_3$(BC)(Tph-Me)]$^+$** suggests its occurrence as a mixture of two structural isomers. In detail, the signals relative to *fac*-**[Re(CO)$_3$(BC)(Tph-Me)]$^+$** appeared split into two distinct patterns of resonances, both in the case of the ^{1}H and ^{13}C-NMR spectrum. While analysis of the ^{1}H-NMR spectrum suggests that the two isomers coexist in a 0.47:1 ratio, the ^{13}C-NMR shows two different tetrazolic carbon resonances, both of which are centred below 160 ppm, highlighting the presence of two linkage isomers where methylation occurred regioselectively at the position N-4 of the tetrazole, while the Re(I) fragment was bound to either position N-2 or N-1 of the same pentatomic ring (see **Schemes 1.5**, **2.5** and **3.5** for atom numbering). This is consistent with our previous reports.[8a]

5.2.2 *Photophysical Properties*

The relevant photophysical data of all the Re(I) complexes described herein are summarized in **Table 1.5**. While both the dianionic disulfonate complexes *fac*-**[Re(CO)$_3$(BPS)(Tph)]$^{2-}$** and *fac*-**[Re(CO)$_3$(BCS)(Tph)]$^{2-}$** were found to be water-soluble as expected, they were also soluble in organic media (DCM for *fac*-**[Re(CO)$_3$(BPS)(Tph)]$^{2-}$** and MeOH in the case of *fac*-**[Re(CO)$_3$(BCS)(Tph)]$^{2-}$**). Contrarily, the absorption and emission spectra of the -SO_3^- free neutral and cationic species *fac*-**[Re(CO)$_3$(BC)(Tph)]** and *fac*-**[Re(CO)$_3$(BC)(Tph-Me)]$^+$**, respectively, could only be obtained from the corresponding dichloromethane solutions. However, as a general feature and irrespective of the nature of the solvent, the absorption profiles of the Re(I) complexes all display a UV region dominated by intense ligand-centred (LC) transitions (250-310 nm), followed by metal-to-ligand charge transfer (MLCT) processes (320-400 nm) tailing off in the visible region. (**Figure 2.5** and **3.5**)

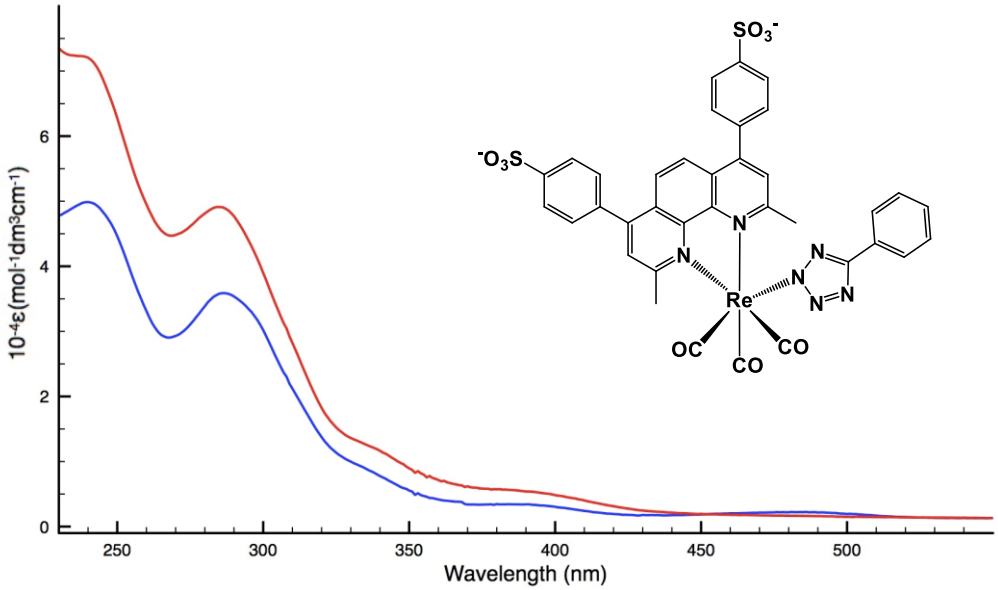

Figure 2.5. Absorption profile of ***fac*-[Re(CO)$_3$(BCS)(Tph)]$^{2-}$**, in CH_3OH (red trace) and H_2O (blue trace). (Bottom)

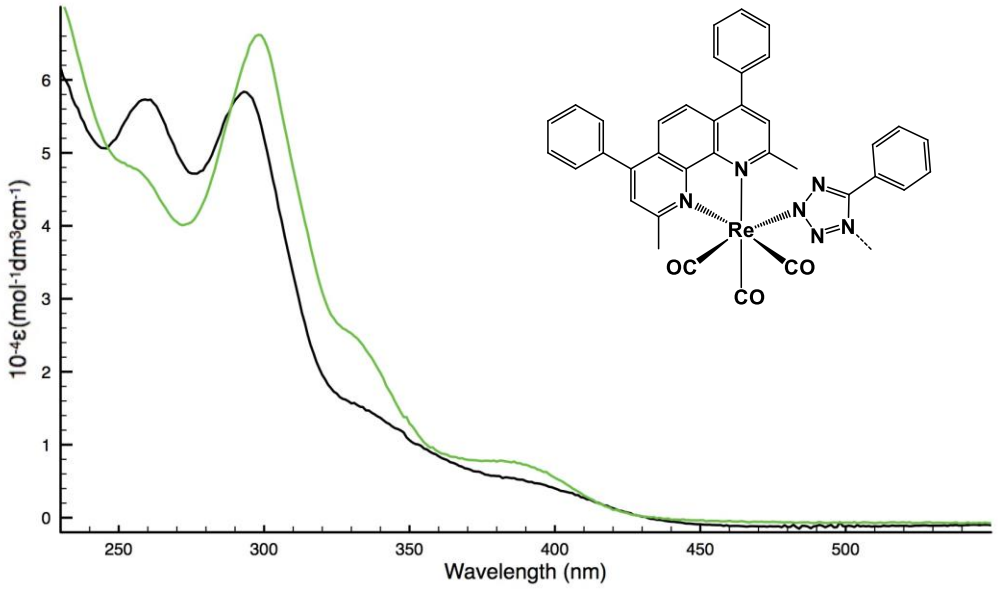

Figure 3.5. Absorption profile of ***fac*-[Re(CO)$_3$(BC)(Tph)]** (black trace), and ***fac*-[Re(CO)$_3$(BC)(Tph-Me)]$^+$** (green trace), CH_2Cl_2, 298K.

Table 1.5. Relevant photophysical data for the Re(I) complexes presented in this work.

		Absorption	Emission 298 K					Emission 77 K[c]	
Complex	Solv.	λ_{abs} (nm) ($10^{-4}\varepsilon$) ($M^{-1}cm^{-1}$)	λ_{em} (nm)	τ_{air} (μs)[a]	τ_{Ar} (μs)[a]	φ_{air} (%)[b]	φ_{Ar} (%)[b]	λ_{em} (nm)	τ (μs)
***fac*-[Re(CO)$_3$(BC)(Tph)]**	*DCM*	256(5.72), 293(5.84), 343(1.29), 392(0.49)	592	0.33	0.87	1.97	6.35	534	2.41
***fac*-[Re(CO)$_3$(BC)(Tph-Me)]$^+$**	*DCM*	257(4.75), 298(6.62), 331(2.49), 390(0.73)	546	1.36	12.1	2.96	15.01	514	39
***fac*-[Re(CO)$_3$(BPS)(Tph)]$^{2-}$**	*DCM*	288 (3.62), 392 (0.70)	600	0.58	1.54	4.08	4.26	550	1.54
***fac*-[Re(CO)$_3$(BCS)(Tph)]$^{2-}$**	*MeOH*	285 (4.98), 383 (0.57)	602	0.24	0.82	0.66	2.40	542	4.98
***fac*-[Re(CO)$_3$(BCS)(Tph)]$^{2-}$**	*H_2O*	240 (4.15), 286 (3.58), 389 (0.34)	452 592	0.007 0.25	0.58	2.7	3.80	/*	/*
***fac*-[Re(CO)$_3$(BPS)(Tph)]$^{2-}$**	*H_2O*	289 (4.45), 387 (0.77)	604	0.492	0.66	2.2	3.30	/*	/*

[a]: "Air" means air equilibrated solutions, "Ar" means deoxygenated solutions under argon atmosphere; [b]: $[Ru(bpy)_3]Cl_2/H_2O$ was used as a reference for quantum yield determinations ($\Phi_r = 0.028$)[22]; [c]: in a frozen solvent matrix; *: not determined.

While the absorption profiles of the dianionic complexes did not significantly differ from each other, a subtle but evident *hypsochromic* shift of the MLCT features was observed when the neutral complex *fac*-**[Re(CO)$_3$(BC)(Tph)]** was converted into its cationic analogue *fac*-**[Re(CO)$_3$(BC)(Tph-Me)]$^+$**. In agreement with our previous studies,[8a,12] this trend is consistent with the variation of the global net charge that occurs upon the addition of a CH_3^+ moiety and the concomitant reduction of electron density on the tetrazole ring.

In dilute dichloromethane (or as in the case of *fac*-**[Re(CO)$_3$(BCS)(Tph)]$^{2-}$** as a methanol solution) at room temperature, upon excitation of the corresponding MLCT features (typically, λ_{exc} = 350-370 nm) all the Re(I) complexes are luminescent and, in line with the typical behaviour of this family of *fac*-Re(I) tricarbonyl diimine complexes,[16] display broad and structureless bands centred between *ca.* 540 and 600 nm (**Table 1.5**). In all cases, the emission can be confidently ascribed to phosphorescence originating from charge-transfer states of triplet multiplicity, ^{3}CT,

similarly to the previously reported for neutral and ionic Re(I) tetrazolato complexes. In fact, the excited state lifetime τ and quantum yield Φ are sensitive to the presence of dissolved O_2 (**Table 1.5**). At 77 K, the emission profiles appear blue-shifted as a consequence of rigidochromism (ESI) and the values of τ and Φ increase due to the lack of vibrational and collisional quenching.[17a-b]

As we have previously documented for the methylation of similar Re(I) tetrazolato complexes,[8a] the methylated and cationic complex *fac*-**[Re(CO)$_3$(BC)(Tph-Me)]$^+$** displays phosphorescent emission which is significantly more intense, longer-lived and blueshifted ($\Delta\lambda_{max}$ = 1433 cm^{-1}) with respect to that exhibited by its neutral precursor *fac*-**[Re(CO)$_3$(BC)(Tph)]** (**Figure 6.5**). In particular, the photophysical properties of the N-3 and N-4 linkage isomers that represent the complex *fac*-**[Re(CO)$_3$(BC)(Tph-Me)]$^+$** appear identical, as witnessed by their displaying one single band in the emission profile and by the satisfactorily monoexponential fitting of the excited state decay.

It is worth noting that the water-soluble sulfonated complexes *fac*-**[Re(CO)$_3$(BCS)(Tph)]$^{2-}$** and *fac*-**[Re(CO)$_3$(BPS)(Tph)]$^{2-}$** basically retained their phosphorescent properties on passing from organic media to aqueous solutions, as witnessed by their displaying almost unaltered broad and unstructured emission profiles centred at ca. 600 nm upon excitation of the corresponding MLCT manifold (**Figure 4.5**). The only exception was observed in the emission spectrum recorded from an air-equilibrated solution of the complex *fac*-**[Re(CO)$_3$(BCS)(Tph)]$^{2-}$**, where an additional fluorescent feature (τ = 7 ns, **Table 1.5**) centred at λ = 452 nm, whose intensity increased upon exciting the sample at wavelengths shorter than 370 nm (ESI), appeared further to the phosphorescent emission peaking at 592 nm. The triplet spin multiplicity of the emissive excited states was further suggested by their different response to the removal of dissolved O_2. Upon degassing, only the phosphorescent process centred at λmax = 592 nm experienced both elongation of the corresponding excited-state lifetime and, in particular, a significant enhancement of the emission intensity, making the fluorescent emission peak at *ca*. 452 nm almost undetectable (ESI). However, we suspect that the occurrence of a similar behaviour might be explained by considering the possibility of the replacement of the tetrazolate anion (Tph$^-$) with one water molecule in the coordination sphere of *fac*-**[Re(CO)$_3$(BCS)(Tph)]$^{2-}$**. Indeed, the coexistence of

fluorescent and phosphorescent emissions originating from ^{1}IL (intra-ligand) and ^{3}MLCT (metal−to-ligand charge transfer) type excited states, respectively, has been previously described by Wolcan and co-workers for aqueous solutions of the parent Re(I) complex *fac*-$[Re(CO)_3(BCS)Cl]^{2-}$,[18] where the insurgence of a fluorescent emission centred at *ca.* 450 nm was rationalized as the result of the partial hydrolysis of the chloride complex *fac*-$[Re(CO)_3(BCS)Cl]^{2-}$.

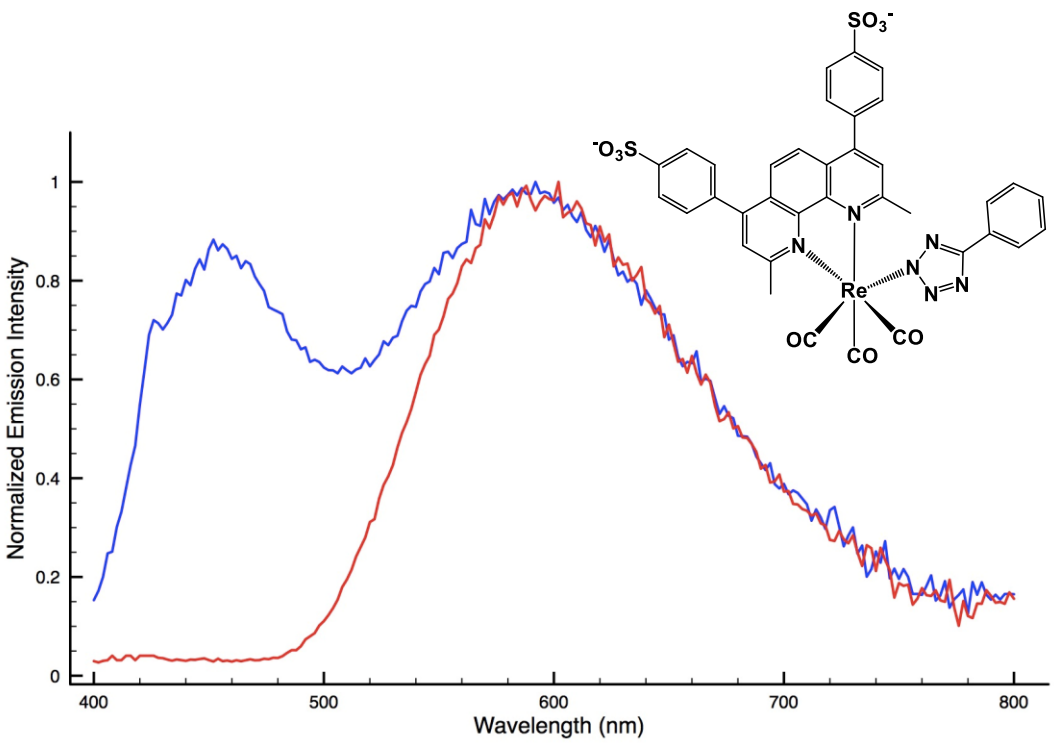

Figure 4.5. Normalized emission profile of ***fac*-[Re(CO)$_3$(BCS)-(Tph)]$^{2-}$**, in CH_3OH (red trace) and H_2O (blue trace).

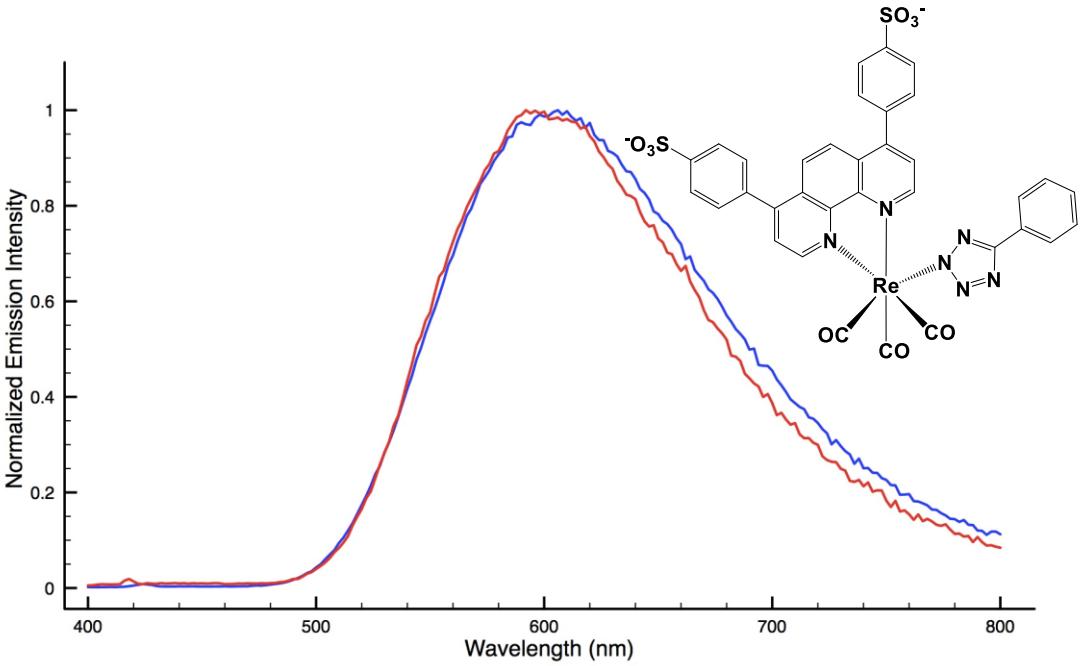

Figure 5.5. Normalized emission profile of ***fac*-[Re(CO)$_3$(BPS)(Tph)]$^{2-}$**, in CH_2Cl_2 (red trace) and H_2O (blue trace).

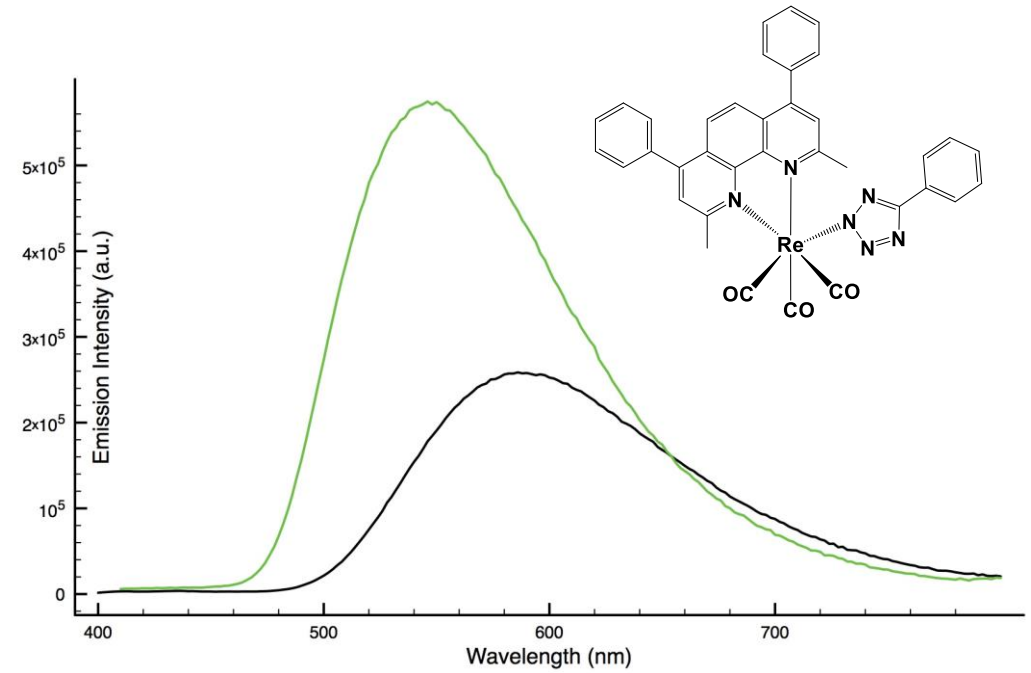

Figure 6.5. Emission profile of ***fac*-[Re(CO)$_3$(BC)(Tph)]** (black trace), and ***fac*-[Re(CO)$_3$(BC)(Tph-Me)]$^+$** (green trace), CH_2Cl_2, 298K.

5.2.3 *Luminescent staining of proteins*

We then investigated the ability of the Re(I) tetrazolato complexes, either those containing disulfonated diimine ligands and SO_3-free bathocuproine ligands, to behave as luminescent probes for the visualization of proteins that are separated upon performing SDS-PAGE. In a preliminary assessment, the disulfonate Re(I)-based complexes *fac*-**[Re(CO)$_3$(BCS)(Tph)]$^{2-}$** and *fac*-**[Re(CO)$_3$(BPS)(Tph)]$^{2-}$**, were tested as protein staining agents toward pure BSA (Bovine Serum Albumin, 66.2 kDa), which was selected as a target protein to be determined in polyacrylamide gels. Specifically, different dilutions of BSA (stock solution 1 mg/mL), ranging from 50 ng to 1 μg, were separated by SDS-PAGE. Gels were first fixed (30% ethanol, 10% acetic acid) then stained for a period of 15 hours with a 1 μM solution in 20% ethanol of *fac*-**[Re(CO)$_3$(BCS)(Tph)]$^{2-}$** and *fac*-**[Re(CO)$_3$(BPS)(Tph)]$^{2-}$**, respectively. Thereafter, protein bands were readily visualised by using a UV trans-illuminator (λ_{exc} = 302 nm).

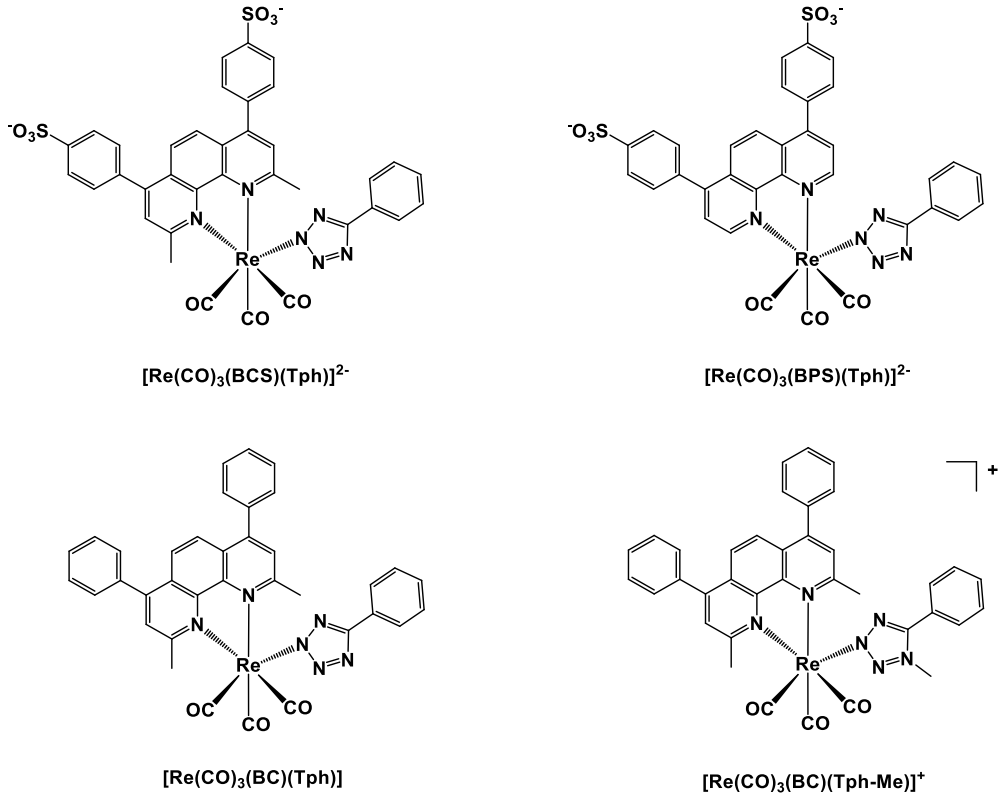

[Re(CO)$_3$(BCS)(Tph)]$^{2-}$ **[Re(CO)$_3$(BPS)(Tph)]$^{2-}$**

[Re(CO)$_3$(BC)(Tph)] **[Re(CO)$_3$(BC)(Tph-Me)]$^{+}$**

Scheme 6.5. Re(I)-tetrazole complexes used as luminescent dyes in protein staining.

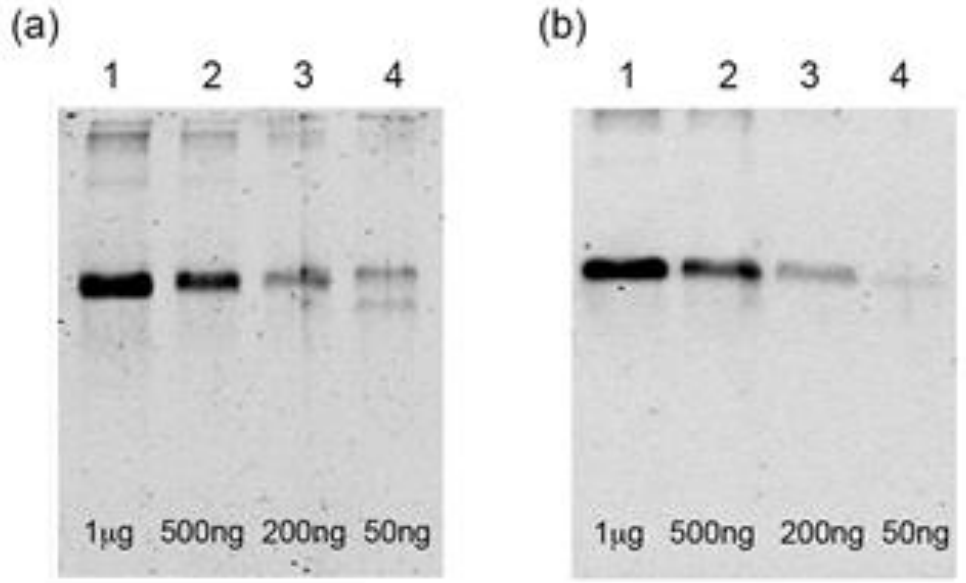

Figure 7.5. SDS-PAGE of different amounts of BSA. Lane 1 to 4: 1, 0.5, 0.2 and 0.05 µg BSA, respectively. (a) Staining with ***fac*-[Re(CO)$_3$(BCS)(Tph)]$^{2-}$**and (b) staining with ***fac*-[Re(CO)$_3$(BPS)(Tph)]$^{2-}$**.

Both Re(I)-based stains (**Figure 7.5**) featured high sensitivity; concentrations of pure BSA down to 50 ng were detected. These charged dyes most likely interact with proteins in a non-covalent manner through a mechanism comparable to that of Coomassie staining, which is assumed to involve electrostatic interaction between sulfonate groups and basic amino acids.

To better investigate their staining capability, both *fac*-**[Re(CO)$_3$(BCS)(Tph)]$^{2-}$** and *fac*-**[Re(CO)$_3$(BPS)(Tph)]$^{2-}$** were then tested against a standard Protein Molecular Weight Marker (Thermo Scientific™ Pierce), a mixture of seven known proteins such as Beta-galactosidase (116 kDa), Bovine serum albumin (66.2 kDa), Ovalbumin (45.0 kDa), Lactate dehydrogenase (35.0 kDa), REase Bsp98I (25.0 kDa), Beta-lactoglobulin (18.4 kDa) and Lysozyme (14.4 kDa). The Protein Marker was diluted sequentially from the stock solution (0.1-0.2 mg/mL of each protein), and run in a gel using decreasing concentrations from lane 1 to 4 (Figure 6 a and b). Both *fac*-**[Re(CO)$_3$(BCS)(Tph)]$^{2-}$** (**Figure 8.5a**) and *fac*-**[Re(CO)$_3$(BPS)(Tph)]$^{2-}$** (**Figure 8.5b**) produced very clear and sharp bands, being able to detect, with a similar intensity, each loaded protein (down to

0.5 μL, corresponding to about 50-100 ng of protein/band). Interestingly both *fac*-**[Re(CO)$_3$(BCS)(Tph)]$^{2-}$** and *fac*-**[Re(CO)$_3$(BPS)(Tph)]$^{2-}$** had a similar response to protein, suggesting that the sulfonate residues in the **BCS** and **BPS** diimine ligands play a key role in the Re(I) complex-protein interaction.

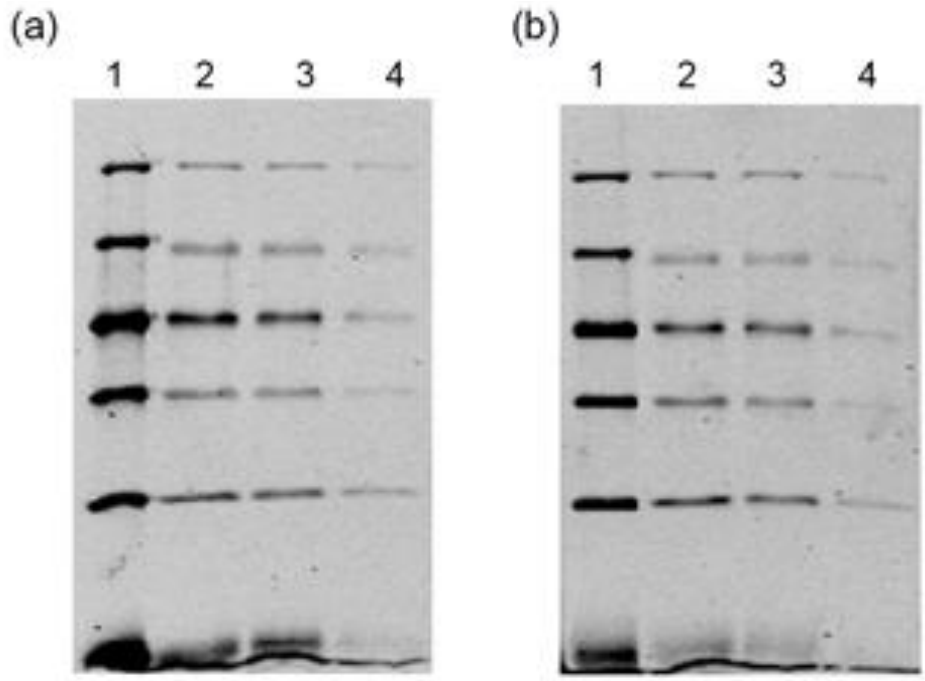

Figure 8.5. SDS-PAGE of different dilutions of the Protein Molecular Weight Marker. Lane 1 to 4: 6, 3, 1.5 and 0.5 μL, respectively; (a) staining with ***fac*-[Re(CO)$_3$(BCS)(Tph)]$^{2-}$** and, (b) staining with ***fac*-[Re(CO)$_3$(BPS)(Tph)]$^{2-}$**.

To ensure that the Re(I)-based staining agents can also be used for the recognition of proteins from more complex mixtures, total protein extracts from *Escherichia coli* cells were loaded on polyacrylamide gels and then stained as previously indicated. As depicted in **Figure 9.5**, a total protein profile was identified independently of the characteristics of the protein mixture. Both *fac*-**[Re(CO)$_3$(BCS)(Tph)]$^{2-}$**and *fac*-**[Re(CO)$_3$(BPS)(Tph)]$^{2-}$** featured comparable efficacy to recognize unknown proteins, being able to detect down to a few micrograms/lane.

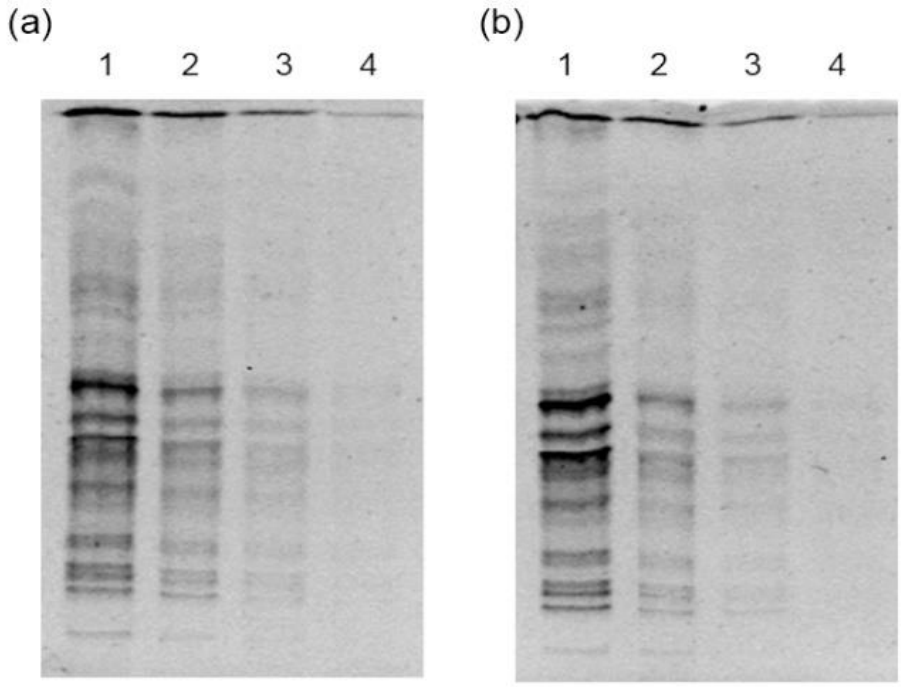

Figure 9.5. SDS-PAGE of total protein extracts. Lane 1 to 4: 5, 2, 1 and 0.5 μg, respectively; (a) staining with ***fac*-[Re(CO)$_3$(BCS)(Tph)]$^{2-}$** and (b) staining with ***fac*-[Re(CO)$_3$(BPS)(Tph)]$^{2-}$**.

5.2.3.1 *Comparison with colourimetric staining*

Once the efficacy of *fac*-**[Re(CO)$_3$(BCS)(Tph)]$^{2-}$** and *fac*-**[Re(CO)$_3$(BPS)(Tph)]$^{2-}$** as staining agents to detect proteins in gels was verified, a comparison with two classical colourimetric stains, Coomassie Blue R250 and Silver staining, was carried out. To achieve this, three identical gels containing an equal amount of each standard protein were prepared (same dilutions as those shown in **Figure 8.5**). Gels were treated separately with different staining protocols,[19] then the intensity of the bands were compared, revealing how the fluorescent method based on *fac*-**[Re(CO)$_3$(BCS)(Tph)]$^{2-}$** and *fac*-**[Re(CO)$_3$(BPS)(Tph)]$^{2-}$** features comparable sensitivity, if not superior, to the traditional silver staining. (**Figure 10.5**) In particular, both Re(I) based stains were easily able to detect up to the last dilution of the protein marker (gels a and c, lane 1-4, **Figure 10.5**). In contrast, Coomassie Blue staining (gel b, **Figure 10.5**) exhibited a lower level of sensitivity with lanes containing less than 3μg/L being visually difficult to distinguish

from the background. Beyond the high quality of detection, a conventional ethanol-acetic acid destaining, required for the Coomassie procedure, is not necessary when the luminescent Re(I)-compounds are used as stains instead a simple washing with water can efficiently reduce background staining. Interestingly, gels stained with Re(I)-based dyes can be re-stained with Coomassie Brilliant Blue without altering its sensitivity, and vice-versa.

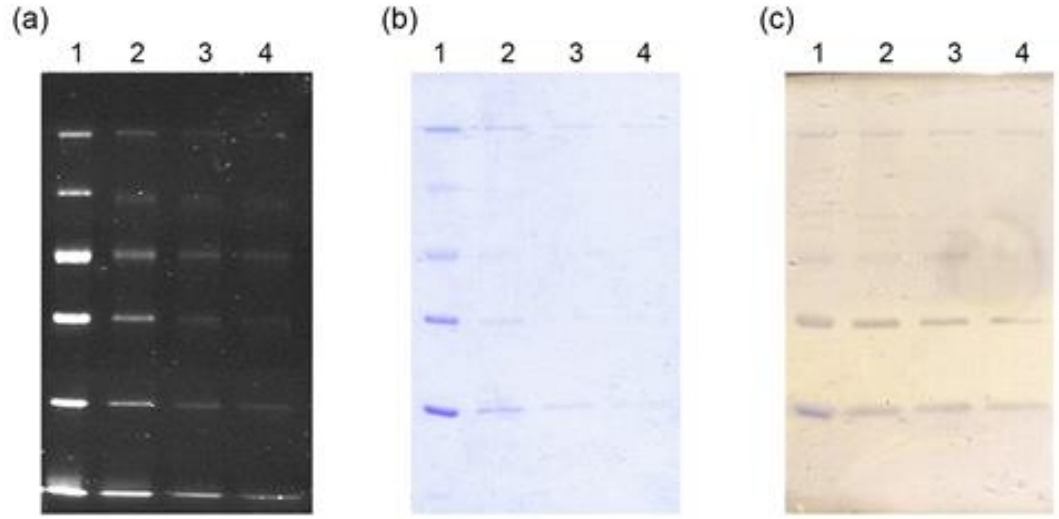

Figure 10.5. Comparison of three staining methods for the detection of different dilutions of the Protein Molecular Weight Marker in SDS-polyacrylamide gels. Lane 1 to 4: 6, 3, 1.5 and 0.5 μL of protein marker, respectively. (a) ***fac*-[Re(CO)$_3$(BCS)(Tph)]$^{2-}$** staining, (b) Coomassie Blue staining and (c) Silver staining.

5.2.3.2 *Staining of gels with non-sulfonate complexes*

To further investigate the importance of the SO_3^- groups for the luminescent staining of proteins, the two non-sulfonated neutral and cationic Re(I) tetrazolate complexes, namely *fac*-**[Re(CO)$_3$(BC)(Tph)]** and *fac*-**[Re(CO)$_3$(BC)(Tph-Me)]$^+$**, were tested as well. As described before, different dilutions of the protein molecular marker were run on SDS-PAGE, then gels were stained with a solution 1 μM solution of either neutral *fac*-**[Re(CO)$_3$(BC)(Tph)]** or the cationic *fac*-**[Re(CO)$_3$(BC)(Tph-Me)]$^+$** in 20% ethanol. Interestingly, protein staining was easily observed for both non-sulfonated

complexes (**Figure 11.5a** and **b**), albeit the sensitivity was somewhat reduced compared with the disulfonated complexes (**Figure 10.5**). Recently, an analogous behaviour has been reported relative to neutral and cationic brightly emissive Ir(III) complexes containing non-sulfonated ligands.[6] In these cases, the performance of the protein stains was attributed to the extended π-conjugation across either the cyclometalated or the ancillary ligand. Therefore, we suspect that a similar effect arising from the **BC** ligand may account for the luminescent protein staining performances displayed by the neutral and cationic SO_3^- free Re(I)-complexes *fac*-**[Re(CO)$_3$(BC)(Tph)]** and *fac*-**[Re(CO)$_3$(BC)(Tph-Me)]$^+$**, respectively. Interestingly, when the same gels were subjected to Coomassie staining, a comparable intensity of each protein band was obtained (**Figure 11.5c** and **d**).

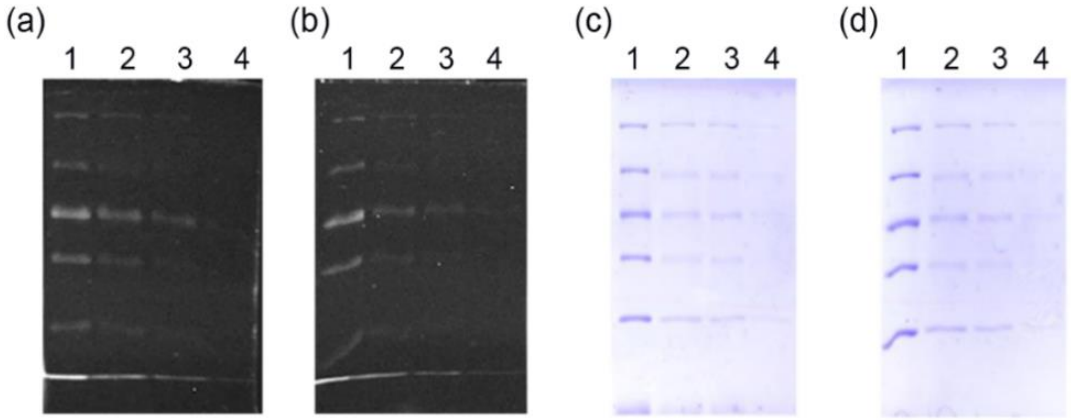

Figure 11.5. SDS-PAGE of different dilutions of the Protein Molecular Marker (lane 1, 2, 3, 4): staining with ***fac*-[Re(CO)$_3$(BC)(Tph)]** (a) and ***fac*-[Re(CO)$_3$(BC)(Tph-Me)]$^+$** (b); (c) and (d): subsequent Coomassie staining of gels (a) and (b).

These results highlight the relevance of the design of the ligands beyond their "simple" decoration with -SO_3^- groups in the preparation of luminescent complexes as protein staining agents. Moreover, it is worth mentioning that the time-saving synthesis that is required for the non-sulfonated complexes can open promising perspectives for the use of SO_3^- - free Re(I) complexes in protein staining.

5.3 Conclusions

In summary, we have demonstrated how Re(I) tetrazolato complexes with the general formula *fac*-**[Re(CO)$_3$(N^N)(Tph)]$^{0/+/2-}$**, where Tph means the 5-phenyl tetrazolato anion, do interact with proteins and, particularly, display a promising potential for the luminescent staining of SDS gels. These results pave the way for the exploitation of this general class of luminescent Re(I) complexes as protein staining agents. In this specific context, we could observe that the decoration of the diimine ligand (N^N) with sulfonate (-SO_3^-) end groups appears as a favourable requisite for the enhancement of their protein staining performances. This is in line with the design strategy that has been pursued for the isoelectronic Ru(II)-polypyridyls and Ir(III)-cyclometalates and also for this family of substitution inert fac-[Re(CO)$_3$(N^N)L] type complexes.

Our findings suggest that the sulfonated and dianionic Re(I) complexes herein described, namely *fac*-**[Re(CO)$_3$(BCS)(Tph)]$^{2-}$** and *fac*-**[Re(CO)$_3$(BPS)(Tph)]$^{2-}$**, where BPS and BCS denote bathophenanthroline disulfonate and bathocuproine disulfonate respectively, can detect a variety of protein targets that span from pure BSA to a standard mixture of proteins of known molecular weights and, interestingly, to crude protein extracts. This is achieved with very good sensitivity and by displaying a response superior to the traditional colourimetric method based on Coomassie Blue R250 and was comparable to the well-established Silver staining method.

Interestingly, both -SO_3^- free derivatives that are represented by the neutral model complex *fac*-**[Re(CO)$_3$(BC)(Tph)]** and the corresponding cationic methylated analogue *fac*-**[Re(CO)$_3$(BC)(Tph-Me)]$^+$** were found to detect proteins subjected to SDS-PAGE in a response that was comparable to that of Coomassie Blue under the same experimental conditions. This is in contrast to what may be expected based on a structure-activity relationship, which from the literature would have suggested that the -SO_3^- free derivatives would possess only limited staining capability. In addition, to report for the first time that tricarbonyl Re(I) diimine complexes can be used for this application, these latter findings are very encouraging since they may open up new possibilities for furthering the studies dealing with the use of the synthetically more easily accessible Re(I) complexes as luminescent protein staining agents. Nevertheless, future experiments will be focused on testing if our staining protocol could be shortened

(e.g. by reducing the incubation time), and if it is compatible with mass spectrometry (MS) for proteomic analysis.

5.4 Experimental Section

General considerations. All the reagents and solvents were obtained commercially (Sigma Aldrich/Merck, Alfa Aesar, Strem Chemicals) and used as received without any further purification unless otherwise specified. All the reactions were carried out under an argon atmosphere following Schlenk protocols. Where required, the purification of the Re(I) complexes was performed via column chromatography with the use of SiO_2 as the stationary phase. ESI-mass spectra were recorded using a Waters ZQ-4000 instrument (ESI-MS, acetonitrile as the solvent). Nuclear magnetic resonance spectra (consisting of ^{1}H and ^{13}C) were always recorded using a Varian Mercury Plus 400 (^{1}H, 399.9; ^{13}C, 101.0 MHz). ^{1}H and ^{13}C chemical shifts were referenced to residual solvent resonances.

Photophysics. Absorption spectra were recorded at room temperature using a Perkin Elmer Lambda 35 UV/vis spectrometer. Uncorrected steady-state emission and excitation spectra were recorded on an Edinburgh FLSP920 spectrometer equipped with a 450 W xenon arc lamp, double excitation and single emission monochromators, and a Peltier-cooled Hamamatsu R928P photomultiplier tube (185−850 nm). Emission and excitation spectra were acquired with a cut-off filter (395 nm) and corrected for source intensity (lamp and grating) and emission spectral response (detector and grating) by a calibration curve supplied with the instrument. The wavelengths for the emission and excitation spectra were determined using the absorption maxima of the MLCT transition bands (emission spectra) and at the maxima of the emission bands (excitation spectra). Quantum yields (Φ) were determined using the optically dilute method by Crosby and Demas[20] at excitation wavelength obtained from absorption spectra on a wavelength scale [nm] and compared to the reference emitter by the following equation:[21]

$$\phi_s = \phi_r \left[\frac{A_r(\lambda_r)}{A_s(\lambda_s)}\right]\left[\frac{I_r(\lambda_r)}{I_s(\lambda_s)}\right]\left[\frac{n_s^2}{n_r^2}\right]\left[\frac{D_s}{D_r}\right]$$

where A is the absorbance at the excitation wavelength (λ), I is the intensity of the excitation light at the excitation wavelength (λ), n is the refractive index of the solvent,

D is the integrated intensity of the luminescence, and Φ is the quantum yield. The subscripts r and s refer to the reference and the sample, respectively. A stock solution with an absorbance > 0.1 was prepared, then two dilutions were obtained with dilution factors of 20 and 10, resulting in absorbances of about 0.02 and 0.08 respectively. The Lambert-Beer law was assumed to remain linear at the concentrations of the solutions. The degassed measurements were obtained after the solutions were bubbled for 10 minutes under Ar atmosphere, using a septa-sealed quartz cell. Air-equilibrated $[Ru(bpy)_3]Cl_2/H_2O$ solution ($\Phi = 0.028$)[22] was used as reference. The quantum yield determinations were performed at identical excitation wavelengths for the sample and the reference, therefore deleting the $I(\lambda r)/I(\lambda s)$ term in the equation. Emission lifetimes (τ) were determined with the single-photon counting technique (TCSPC) with the same Edinburgh FLSP920 spectrometer using pulsed picosecond LED (EPLED 360, FWHM < 800ps) as the excitation source, with repetition rates between 1 kHz and 1 MHz, and the above-mentioned R928P PMT as the detector. The goodness of fit was assessed by minimizing the reduced $\chi 2$ function and by visual inspection of the weighted residuals. To record the 77 K luminescence spectra, the samples were put in quartz tubes (2 mm diameter) and inserted in a special quartz Dewar filled with liquid nitrogen. The solvent used in the preparation of the solutions for the photophysical investigations was of spectrometric grade. Experimental uncertainties are estimated to be ±8% for lifetime determinations, ±20% for quantum yields, and ±2 nm and ±5 nm for absorption and emission peaks, respectively.

Ligand synthesis

Warning! Tetrazole derivatives are used as components for explosive mixtures.[23] In this lab, the reactions described here were only run on a few grams scale and no problems were encountered. However, great caution should be exercised when handling or heating compounds of this type.

Following the general method reported by Koguro and co-workers,[24] tetrazole ligand [H-**Tph**] was obtained in quantitative yield. [H-**Tph**] ^{1}H-NMR (DMSO d^6, 400 MHz) δ (ppm) = 8.06 - 8.03 (m, 2H), 7.62 -7.60 (m, 3H).

General Procedure for the Preparation of fac-[Re(CO)$_3$(N^N)-(Tph)]$^{2-}$ -type complexes

To an aqueous solution (5 mL) of $TBAHSO_4$ (tetrabutylammonium hydrogensulphate) (0.140 g, 0.42 mmol) was added the desired diimine ligand BCS or BPS as sodium salt (0.102 g, 0.18 mmol). The resulting solution was stirred for 2h at r.t. and then extracted with CH_2Cl_2 (3 x 3 mL). The organic phase was then dried with $MgSO_4$ and the removal of the solvent afforded the targeted [Bu_4N] salt of BCS or BPS in almost quantitative yield. To a suspension of $Re(CO)_5Br$ (46 mg, 0.11 mmol) in dry toluene (5 mL) was added either [Bu_4N][BCS] or [Bu_4N][BPS] (0.11 mmol). The mixture was heated for 2h at reflux under argon atmosphere to afford an orange gel. The solvent was decanted, removed and the gel formed was washed several times with hexane until it became solid, then dried to give *fac*-[Re(CO)$_3$(N^N)Br]$^{2-}$. To a solution of *fac*-[Re(CO)$_3$(N^N)Br]$^{2-}$ in CH_3OH (0.11 mmol, 10 mL) repaired from light was added AgOTf (0.11 mmol). The mixture was heated at reflux for 2h. The resulting solution was filtered over a celite pad to remove AgBr and reduced in volume (to about 10 mL). To the latter one was added dropwise a CH_3OH + Et_3N mixture of [H-Tph] (2 mL + 0.23 μL) and heated at reflux, overnight. The resulting yellow solution was evaporated to dryness and purified over SiO_2 column chromatography (CH_2Cl_2/CH_3OH 3:1) to give *fac*-[Re(CO)$_3$(N^N)-(Tph)]$^{2-}$ as second fraction (N^N = BCS: 0.055 g, 0.038 mmol, Y = 35%; N^N = BPS: 0.076 g, 0.055 mmol, 50%).

***fac*-[Re(CO)$_3$(BPS)(Tph)]$^{2-}$ ESI-MS** [M]$^{2-}$ = 452 *m/z* (CH_3OH); **IR ν** (cm^{-1}) = 2026.4 (CO), 1918.7 (CO), (CH_2Cl_2); Given the uncertainty about the effective position of the SO_3^- groups on the commercial **BPS** ligand (*i.e* the presence of structural isomers in the starting material),[5, 8] it was not possible to confidently attribute the various signals in both ^{1}H and ^{13}C NMR of ***fac*-[Re(CO)$_3$(BPS)(Tph)]$^{2-}$**. **^{1}H-NMR** (CD_3OD, 400 MHz) δ (ppm) = 7.34-7.25 (m, 2H), 7.46-7.39 (m, 1H), 7.63-7.55 (m, 1H), 7.82-7.67 (m, 5H), 8.21-8.00 (m, 9H), 9.68-9.62 (m, 1H). **^{13}C-NMR** (CD_3OD, 100 MHz) δ (ppm) = 197.72, 194.43, 166.26, 155.25, 155.12, 152.34, 150.12, 149.31, 149.22, 148.05, 147.76, 147.70,

141.64, 138.66, 137.09, 132.58, 131.02, 130.39, 129.93, 128.34, 128.27, 128.21, 127.87, 127.77, 127.62, 126.80, 123.39, 120.22, 59.51, 59.48, 59.46, 58.85, 51.29, 49.63, 49.42, 49.21, 49.00, 48.78, 48.57, 48.36, 47.92, 24.93, 24.76, 24.60, 20.68, 20.67, 20.66, 20.49, 13.92, 13.73. Anal. Calcd. For $C_{66}H_{91}N_8O_9Re_1S_2$ (1390.84) C 57.00, H 6.59, N 8.06. Found: C 57.08, H 6.66, N 8.00.

***fac*-[Re(CO)$_3$(BCS)-(Tph)]$^{2-}$ ESI-MS** $[M]^{2-}$= 467 m/z, $[M+Na]^{2-}$ = 957 *m/z*, $[M]^-$ = 1176 *m/z* (CH_3OH); **IR ν** (cm^{-1}) = 2029.0 (CO), 2015.5 (CO), 1914.3 (CO) (CH_2Cl_2); Given the uncertainty about the effective position of the SO_3^- groups on the commercial **BCS** ligand (*i.e* the presence of structural isomers in the starting material),[5, 8] it was not possible to confidently attribute the various signals in both ^1H and ^{13}C NMR of ***fac*-[Re(CO)$_3$(BCS)(Tph)]$^{2-}$**; **^{1}H-NMR** (CD_3OD, 400 MHz) δ (ppm) = 3.50 (s, 6H), 7.26-7.33 (m, 3H), 7.35-7.41 (m, 2H), 7.43-7.49 (m, 3H), 7.52-7.57 (m, 2H), 7.61-7.69 (m, 6H), 7.79-7.85 (m, 1H), 8.01-8.04 (m, 9H). **^{13}C-NMR** (CD_3OD, 100MHz) δ (ppm) = 164.77, 162.72, 160.93, 158.78, 150.53, 148.65, 148.38, 145.81, 145.42, 145.04, 137.86, 135.94, 131.17, 129.41, 129.28, 128.88, 128.68, 128.59, 128.55, 128.34, 128.28, 128.23, 126.72, 126.33, 126.26, 125.81, 125.73, 125.70, 124.41, 124.14, 124.00, 122.73, 58.10, 30.15, 23.35, 19.20, 12.51. Anal. Calcd. For $C_{68}H_{95}N_8O_9Re_1S_2$ (1418.89) C 57.75, H 6.75, N 7.90. Found: C 57.85, H 6.64, N 7.98.

General Procedure for the Preparation of fac-[Re(CO)$_3$(BC)(Tph)] and fac-*[Re(CO)$_3$(BC)(Tph-Me)]$^+$ complexes*

***fac*-[Re(CO)$_3$(BC)(Tph)].** A 0.100 g aliquot of *fac*-[Re(BC)(CO)$_3$Br] (0.140 mmol) was dissolved in 20 mL of an ethanol/water mixture (3:1 v/v) under an Ar atmosphere. A 5.0 mL portion of an ethanol/water (3:1 v/v) solution containing 0.033 g (0.22 mmol) of Tph^- was added drop wise. Once the addition was completed, the resulting suspension was stirred at the reflux temperature for 24 h. After this time, the mixture was cooled to r.t. and filtered through a glass frit, affording the desired complex as a yellow microcrystalline powder, requiring any further purification process (Y = 0.056 g, 0.072 mmol, 51%). **ESI-MS** $[M+H]^+$ = 777 *m/z*; **IR** ν (cm^{-1}) = 2022.71 (CO), 1918.04 (CO),

1898.22 (CO) (CH_2Cl_2); **^{1}H NMR** (Acetone-d^6, 400 MHz) δ (ppm) = 3.57 (s, 6H, CH_3 BC), 7.23-7.29 (m, 3H), 7.60-7.65 (m, 10H), 7.72-7.95 (m, 2H), 7.97 (m, 2H), 8.09 (m, 2H). **^{13}C-NMR** (Acetone-d^6, 100 MHz) δ (ppm) = 197.72(CO), 194.38(CO), 164.91(Ct), 163.65, 152.16, 149.74, 136.88, 131.31, 130.57, 130.48, 129.91, 129.18, 128.98, 128.05, 127.76, 126.73, 125.24, 31.56 (CH_3-BC). Anal. Calcd. For $C_{36}H_{25}N_6O_3Re_1$ (775.84) C 55.73, H 3.25, N 10.83. Found: C 55.65, H 3.18, N 10.91.

***fac*-[Re(CO)$_3$(BC)(Tph-Me)]$^+$**. 0.100 g of *fac*-[Re(CO)$_3$(BC)-(Tph)] was dissolved in 20 mL of CH_2Cl_2 and the mixture was allowed to cool down by immersion into an ethanol/liquid nitrogen cold bath. Then, methyl trifluoromethanesulfonate (1.2 equiv., solution in dichloromethane 0.179 M) was added. The reaction was stirred under nitrogen for 30 minutes while being kept in the cold bath, and then allowed to warm up to room temperature and stirred for 3 hours. Anion exchange was carried out by adding an excess of NH_4PF_6 in water to the solution and stirring for 20 minutes. The product was then extracted using dichloromethane (3×10 mL) and the organic components were combined and dried over anhydrous $MgSO_4$. Subsequent purification by column chromatography on alumina (gradient: CH_2Cl_2/acetone 8:2, second fraction) yielded *fac*-[Re(CO)$_3$(BC)(Tph-Me)]$^+$[PF_6]$^-$

(Y = 0.059 g, 0.063 mmol, 49%). **ESI-MS** [M]$^+$ = 791 *m/z*: , [M]$^-$ = 145 *m/z* (PF_6); **IR** ν (cm^{-1}) = 2037 (CO), 1934 (CO, br), (CH_2Cl_2);The ratio of system *a : b* is 1 : 0.47. **^{1}H NMR** (Acetone-d^6, 400 MHz) δ (ppm) = 3.23 (s, 6H, -CH_3 BC, a), 3.54 (s, 3H, -CH_3 BC, b), 3.73 (s, 3 H, -CH_3 Tph, a), 4.18 (s, 1.71 H, -CH_3 Tph, b), 7.34-7.27 (m, 2.60 H), 7.59-7.54 (m, 3.84 H), 7.75-7.63 (m, 15 H, aromatic system BC a, b), 8.05-8.03 (m, 3.96 H, Tph, a), 8.08 (m, 1.19 H, Tph, b), 8.19 (m, 1.31 H, Tph, b). **^{13}C-NMR** (Acetone-d^6, 100 MHz) δ (ppm) = 164.62, 164.44, 157.23, 156.59, 151.96, 151.81, 148.75, 148.21, 135.61, 135.57, 132.52, 132.27, 129.86, 129.83, 129.29, 129.26, 129.16, 129.11, 128.79, 128.68, 127.55, 127.36, 127.33, 127.19, 124.80, 124.71, 121.69, 120.71, 36.20, 34.89, 30.78, 30.58. Anal. Calcd. For $C_{37}H_{28}N_6O_3Re_1P_1F_6$ (935.84) C 47.49, H 3.02, N 8.98. Found: C 47.53, H 3.11, N 9.10.

Gel electrophoresis

12.5 % SDS-PAGE gels were used for the proteins separation in a Mini-PROTEAN® Bio-Rad electrophoresis system. The unstained Protein Molecular Marker (Thermo Scientific™ Pierce) contained a mixture of seven proteins (0.1 to 0.2 mg/mL of each) with a known molecular weight: beta-galactosidase (116 kDa), bovine serum albumin (66.2 kDa), ovalbumin (45.0 kDa), lactate dehydrogenase (35.0 kDa), REase Bsp98I (25.0 kDa), beta-lactoglobulin (18.4 kDa), lysozyme (14.4 kDa). Before loading onto the gel, the marker solution was boiled for 5 minutes. A stock solution 1 mg/mL of bovine serum albumin (BSA) in water was used as the protein standard.

All protein samples (in a 20 µL volume) were prepared by adding 5 µL of sample buffer 5x (250 mM Tris·HCl pH 6.8, 10% SDS, 40% (v/v) glycerol, 5% (v/v) β-mercaptoethanol, 0.1% (w/v) Bromophenol Blue). Samples were boiled for 5 minutes then loaded on the gel. Electrophoresis was carried out at 120 V for 2 h in Tris/glycine running buffer (25 mM Tris pH 8.3, 192 mM glycine, 0.1 % SDS).

Total protein extracts

Escherichia coli TOP10 cells (Invitrogen, Carlsbad, CA, USA) were grown in 50 mL of liquid medium LB (10 g/L tryptone, 5 g/L yeast extract, 10 g/L NaCl) at 37 °C for 15 h under shaking (180 rpm). Cells were harvested by centrifugation (4500g for 20 minutes at 4 °C) then lysed by sonication in 50 mM Tris-HCl pH 8, 150 mM NaCl, 1 mM EDTA (3 cycles on ice, 15 sec on/off at 15 w). Protein quantification was performed according to the Bradford assay.[25]

Gel staining and imaging

Later after electrophoresis, polyacrylamide gels were stained. When the Coomassie Brilliant Blue (CBB) protein staining was used, gels were briefly rinsed in distilled water, then incubated with gentle shaking at room temperature for 2-3 h in 50 mL of CBB solution (30% v/v ethanol, 10% v/v acetic acid, 0.1% w/v Coomassie brilliant blue R-250). Gels were destained in a solution of 30% ethanol and 10% acetic acid until the protein bands appeared. Alternatively, when the silver nitrate staining was used, gels

were washed with distilled water for 5 minutes and fixed for 30 minutes in 30% ethanol, 10% acetic acid solution. Gels were rinsed twice in 10% ethanol for 5 min, then in distilled water (2 x 5 minutes). The following Sensitizer, Stain and Developer working solutions were prepared and used according to the Pierce Silver Stain Kit (Thermo Scientific™ Pierce). When the protein bands were visible, 20 mL of Stop solution (5% acetic acid) were added. For the fluorescent staining, gels were firstly fixed in a solution of 30% ethanol, 10% acetic acid for 2 h at room temperature. After three rinsings in 20% ethanol (10 minutes each), gels were incubated with 30 mL of the stain solution (1 μM of each Re-complex in 20% ethanol) on a small plastic box covered with an aluminium foil to protect the dye from light. The staining was carried out overnight with gentle shaking at room temperature. Gels were destained in water (2 x 10 minutes) before the imaging using the Gel Doc™ XR System (BioRad) equipped with UV light illuminators (excitation 302 nm).

X-ray crystallography

Crystal data and collection details for ***fac*-[Re(CO)$_3$(BC)(Tph)]** are reported in ESI (Table S2†). The diffraction experiments were carried out on a Bruker APEX II diffractometer equipped with a PHOTON100 detector and using Mo-K□ radiation. Data were corrected for Lorentz polarization and absorption effects (empirical absorption correction SADABS).[26] Structures were solved by direct methods and refined by full-matrix least-squares based on all data using F^2.[27] H-atoms were placed in calculated positions and refined isotropically using a riding model. All non-hydrogen atoms were refined with anisotropic displacement parameters. CCDC 1843521 for ***fac*-[Re(CO)$_3$(BC)(Tph)]** contain the supplementary crystallographic data for this paper.

5.5 References

[1] a) K. Y. Zhang and K. K.-W. Lo, Chemosensing and Diagnostics, in *Coordination and Organometallic Chemistry of Comprehensive Inorganic Chemistry II*, ed. V. W.-W. Yam, Elsevier, Amsterdam, vol. 8, 2013, pp. 657–732and references cited therein; see also: b) D.-L. Ma, W.-L. Wong, W.-H. Chung, F.-Y. Chan, P.-K. So, T.-S. Lai, Z.-Y. Zhou, Y.-C. Leung and K.-Y. Wong *Angew. Chem.*, **2008**, 120, 3795-3799; c) C.-Y. Wong, L.-H. Chung, S. Lin, D. S.-H. Chan, C.-H. Leung and D.-L. Ma *Sci. Rep.* 2014, 4, 7136

[2] a) D.-L. Ma, M. Wang, C. Liu, X. Miao, T.-S. Kang and C.-H Leung *Coord. Chem. Rev.*, **2016**, 324, 90-105; see also: b) D.-L. Ma, G. Wu, C. Li and C.-H Leung *J. Anal. Test.*, **2018**, 2, 77-89.

[3] T. Rabilloud, J-M. Strub, S. Luche, A. van Dorsselaer and J. Lunardi, *Proteomics,* **2001**, 1, 699–704.

[4] a) K. Berggren, E. Chernokalskaya, T. H. Steinberg, C. Kemper, M. F. Lopez, Z. Diwu, R. P. Haugland and W. F. Patton, *Electrophoresis*, 2000, **21**, 2509-2521; b) T. H. Steinberg, E. Chernokalskaya, K. Berggren, M. F. Lopez, Z. Diwu, R. P. Haugland and W. F. Patton, *Electrophoresis*, **2000**, 21, 486-496.

[5] J. Jia, H. Fei and M. Zhou, *Electrophoresis*, **2012**, 33, 1397–1401.

[6] Y. Zhou, J. Jia, X. Wang, W. Guo, Z. Wu, and N. Xu, *Chem. Eur. J.*, **2016**, 22, 16796 – 16800.

[7] A. J. Amoroso, M. P. Coogan, J. E. Dunne, V. Fernandez-Moreira, J. B. Hess, A. J. Hayes, D. Lloyd, C. Millet, S. J. A. Pope and C. Williams, *Chem. Commun.*, **2007**, 3066–3068.

[8] a) M. V. Werrett, G. S. Huff, S. Muzzioli, V. Fiorini, S. Zacchini, B. W. Skelton, A. Maggiore, J. M. Malicka, M. Cocchi, K. C. Gordon, S. Stagni and M. Massi, *Dalton Trans.*, **2015**, 44, 8379; b) V. Fiorini, A. M. Ranieri, S. Muzzioli, K. D. M. Magee, S. Zacchini, N. Akabar, A. Stefan, M. I. Ogden, M. Massi and S. Stagni, *Dalton Trans.*, **2015**, 44, 20597-20608.

[9] C. Liu, L. Yu, Y. Liu, F. Li and M. Zhou, *Magn. Reson. Chem*., **2011**, 49, 816–823.

[10] a) S. Stagni, A. Palazzi, S. Zacchini, B. Ballarin, C. Bruno, M. Marcaccio, F. Paolucci, M. Monari, M. Carano and A. J. Bard, *Inorg. Chem*. **2006**, 45, 695−709; b) S. Stagni, E. Orselli, A. Palazzi, L. De Cola, S. Zacchini, C. Femoni, M. Marcaccio, F. Paolucci and S. Zanarini, *Inorg. Chem.,* **2007**, 46, 9126−9138.

[11] a) Stagni, S. Colella, A. Palazzi, G. Valenti, S. Zacchini, F. Paolucci, M. Marcaccio, R. Q. Albuquerque and L. De Cola, *Inorg. Chem.* **2008**, 47, 10509-10521; b) V. Fiorini, S. Zacchini, P. Raiteri, R. Mazzoni, V. Zanotti, M. Massi and S. Stagni, *Dalton Tran*s., **2016**, 45, 12884-12896.

[12] M. V. Werrett, S. Muzzioli, P. J. Wright, A. Palazzi, P. Raiteri, S. Zacchini, M. Massi and S. Stagni, *Inorg. Chem.*, **2014**, 53, 229−243.

[13] a) C. A. Bader, R. D. Brooks, Y. S. Ng, A. Sorvina, M. V. Werrett, P. J. Wright, A. G. Anwer, D. A. Brooks, S. Stagni, S. Muzzioli, M. Silberstein, B. W. Skelton, E. M. Goldys, S. E. Plush, T. Shandala and M. Massi, *RSC Adv.*, **2014**, 4, 16345 - 16351; b) C. A. Bader, E. A. Carter, A. Safitri, P. V. Simpson, P. Wright, S. Stagni, M. Massi, P. A. Lay, D. A. Brooks and S. E. Plush, *Mol. BioSyst*., **2016**, 12, 2064 - 2068; c) C. A. Bader, T. Shandala, E. A. Carter, A. Ivask, T. Guinan, S. M. Hickey, M. V. Werrett, P. J. Wright, P. V. Simpson, S. Stagni, N. H. Voelcker, P. A. Lay, M. Massi, Sally E. Plush and D. A. Brooks, PLoS ONE 11(8): e0161557.

[14] C. Caporale, C. A. Bader, A. Sorvina, K. D. M. MaGee, B. W. Skelton, T. A. Gillam, P. J. Wright, P. Raiteri, S. Stagni, J. L. Morrison, S. E. Plush, D. A. Brooks and M. Massi, *Chem. Eur. J.*, **2017**, 23, 15666 – 15679.

[15] V. Fiorini, I. Zanoni, S. Zacchini, A. L. Costa, A. Hochkoeppler, V. Zanotti, A. M. Ranieri, M. Massi, A. Stefan and S. Stagni, *Dalton Trans*., **2017**, 46, 12328 - 12338.

[16] R. A. Kirgan, B. P. Sullivan and D. P. Rillema, *Top. Curr. Chem.*, **2007**, 281, 45–100.

[17] a) A. Kumar, S. –S. Sun, A. Lees, *Photophysics and Photochemistry of Organometallic Rhenium Diimine Complexes*, In Photophysics of Organometallics, Ed.; Springer: Berlin and Heidelberg, Germany, **2010**; Vol. 29, 37−71; b) L. Flamigni, A. Barbieri, C. Sabatini, B. Ventura and F. Barigelletti, *Top. Curr. Chem.,* **2007**, 281, 143-203.

[18] H. H. Martinez Saavedra, F. Ragone, G. T. Ruiz, P. M. D. Gara and E. Wolcan, *J. Phys. Chem. A*, **2014**, 118, 9661−9674.

[19] J. Sasse and S. R. Gallagher, *Curr. Protoc. Mol. Biol.*, **2009**, 10.6.1-10.6.27

[20] G. A. Crosby and J. N. Demas, *J. Phys. Chem*., **1971**, 75, 991-1024.

[21] D. F. Eaton, *Pure Appl. Chem*., **1988**, 60, 1107-1114.

[22] K. Nakamura, *Bull. Chem. Soc. Jpn*., **1982**, 55, 2697–2705.

[23] R. N. Butler, Tetrazoles. In "Comprehensive Heterocyclic Chemistry II"; Storr, R. C., Ed.; Pergamon Press: Oxford, U.K., **1996**; Vol. 4, 621-678, and references cited therein.

[24] K. Koguro, T. Oga, S. Mitsui and R. Orita, *Synthesis*, **1998**, 910-914.

[25] M. M. Bradford, *Anal. Biochem.*, **1976**, b, 248-254.

[26] G. M. Sheldrick, SADABS-2008/1 - Bruker AXS Area Detector Scaling and Absorption Correction, Bruker AXS: Madison, Wisconsin, USA, 2008.

[27] G. M. Sheldrick, *Acta Crystallogr. C*, **2015**, 71, 3.

Chapter 6 New luminescent Ir(III)-tetrazolate complexes as potential redox-active probes for intra- and extracellular sensing of hypoxia in bioimaging

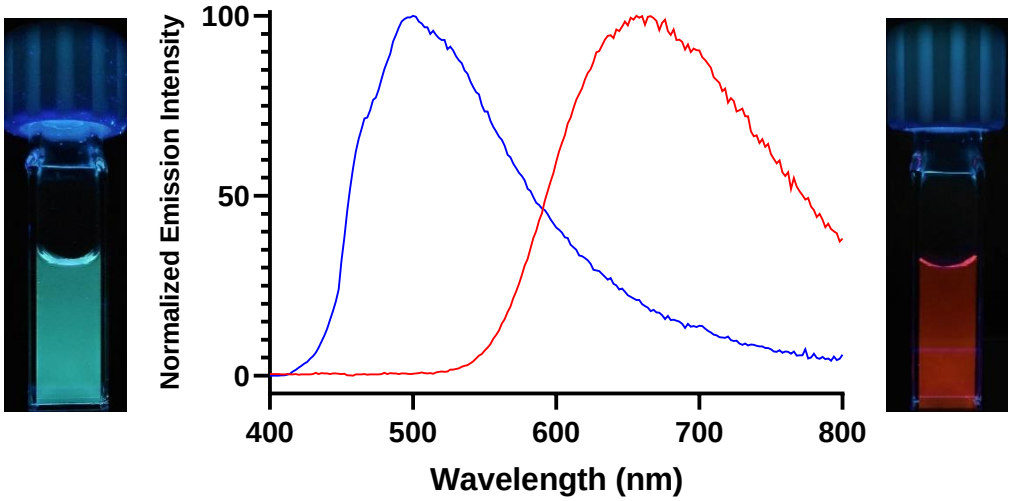

6.1 Abstract

In the context of our studies centred on the application of metal-tetrazolato complexes in life science, we are currently engaged in the design and preparation of new Ir(III)-tetrazolates with the general formula **[Ir(NO_2-C^N)$_2$-(Tz)]$^{-1/0/+1}$** as luminescent probes for bioimaging. In particular, the reduction of the scarcely emissive nitro containing complexes **[Ir(O_2N-C^N)$_2$-(Tz)]$^{-1/0/+1}$** into the corresponding and brightly luminescent amino derivatives **[Ir(H_2N-C^N)$_2$-(Tz)]$^{-1/0/+1}$**, in combination with the good solubility that both kinds of species display in an aqueous medium, can be exploited for the luminescent sensing of extra- and intracellular sensing of hypoxia. Also, the peculiar emission behaviour displayed by the complexes **[Ir(O_2N-C^N)$_2$-(Tz)]$^{-1/0/+1}$**, which appear to be strictly correlated with the presence of the -NO_2 group in the scaffold of the C^N ligands, will be discussed.

6.2 Introduction

In the last part of my PhD, I have been focusing on a research project started in collaboration with Associate Professor Max Massi, who hosted me in his research group at Curtin University, Perth - Western Australia, from January 2019 to September 2019. Aiming at broadening the application of Ir(III)-tetrazolate complexes in the field of life science, we decided to prepare a new family of Ir(III)-NO_2 tetrazole complexes in which a substantial modification of their luminescent output can be accomplished upon reduction of the pending nitro group on the cyclometalated (C^N) ligands to the corresponding amino moiety. Such behaviour, in combination with specific biological conditions, suggests their possible application as luminescent probes for intracellular and extracellular sensing of hypoxic environments in bioimaging.[1]

Molecular oxygen is essential for the majority of living organisms. It is consumed in cellular respiration during phosphorylation of adenosine diphosphate (ADP) to produce adenosine triphosphate (ATP) in mitochondria. Oxygen concentration is a very useful indicator of pathological conditions such as inflammatory diseases[2] and solid tumours[3] are often associated to a decrease in the local concentration of oxygen; such phenomenon is named hypoxia.

In tissues and air, oxygen occurs in its triplet state ($^3O_2$), whereas the majority of other molecules are in a singlet state. Considering that interactions are allowed only between molecules with same spin multiplicity, triplet oxygen $^3O_2$ is relatively inert in biological systems; whereas, on the same considerations, singlet oxygen $^1O_2$ will readily react with an available substrate.

In bioinorganic applications of luminescent metal complexes, the triplet (T_1) character of the luminescent MLCT excited state has been exploited due to its ability to interact with oxygen in its triplet state ($^3O_2$). One example is photodynamic therapy, in which a compound named photosensitiser in a triplet excited state, such as a transition metal complex, is responsible for the production of cytotoxic singlet oxygen $^1O_2$ and other reactive oxygen species (ROS) by interaction with triplet oxygen $^3O_2$.

Beside therapeutic purposes, diagnostic applications of transition metal complexes based on such interaction have been proposed. In 2017, Huang et al. reported several examples

of luminescent Ir(III) complexes in which the phosphorescent output of the luminophore can be tuned by varying the oxygen concentration in the solution,[4] making such system able to detect hypoxic, normoxic and hyperoxic conditions.

More recently, New et al. reported a hypoxia-responsive fluorescent probe in which the switch-on of the luminesce is achieved upon reduction of the nitro group localized in the main scaffold of the molecule in physiological condition.[1] It is known how nitroaromatic moieties in physiological conditions undergo an enzyme-mediated reduction catalysed by ubiquitous nitroreductase enzymes, leading to an intermediate species that can be re-oxidized by molecular oxygen. Although, in a hypoxic environment such intermediate can be furtherly reduced to the corresponding amino-aromatic substrate. (**Scheme 1.6**).

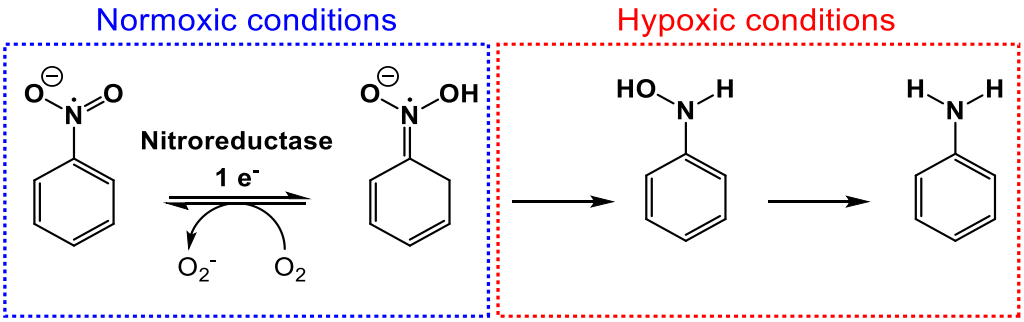

Scheme 1.6 Enzyme-mediated reduction of nitroaromatic moieties in cells.

This peculiar behaviour of nitroaromatic compounds was exploited by New's group in the design of a 1,8-naphthalimidic probe possessing a pending nitro group on the main scaffold that eventually led to a fluorescent probe in which the turn-on of the luminescent is achieved uniquely in hypoxic conditions.[1]

On these premises, aiming at the preparation of metalorganic phosphorescent probes based on such reactivity, a new family of Ir(III)-tetrazole complexes with the general formula **[Ir((C^N)-NO$_2$)$_2$(N^N')]$^{-1/0/+1}$** was prepared, where N^N' represents a chelating 5-aryltetrazole ancillary ligand or its N2-alkylated derivatives, and C^N is the fluorinated or non-fluorinated cyclometalating ligand displaying one **NO$_2$** group at the *para* position of the pyridyl ring (**PPy-NO$_2$** and **F$_2$-PPy-NO$_2$**) or at the *para* position (with respect to the cyclometalated carbon) of the phenyl ring (**O$_2$N-PPy**). (**Scheme 2.6**).

In light of the effect of the neat charge of such systems on their cellular internalization and localization, differently charged Ir(III)-tetrazole complexes were prepared. Neutral and positively charged Ir(III) complexes were obtained by reaction of the corresponding Ir(III)-NO_2 dimer precursors with tetrazolato (**PTZ**$^-$) or N-2 alkyl tetrazoles (**PTZ-Me**, **PTZ-^{t}Bu**), respectively. A further series of anionic Ir(III) complexes with the general formula **[Ir((C^N)-NO_2)$_2$(1,2-BTB)][Et_3NH]**, was obtained with the introduction of the bis tetrazolato (**1,2-BTB**$^{2-}$) which represents the deprotonated form of 1,2-bistetrazolyzbenzene (**1,2-BTB-H_2**) and consists of two tetrazole groups tethered by a phenyl ring. Interestingly, emission measurement in DCM of complexes possessing a **NO_2** group at the para position of the pyridyl ring of the (**C^N**) ligands, in some cases displayed an unusual emissive behavior that will be discussed herein.

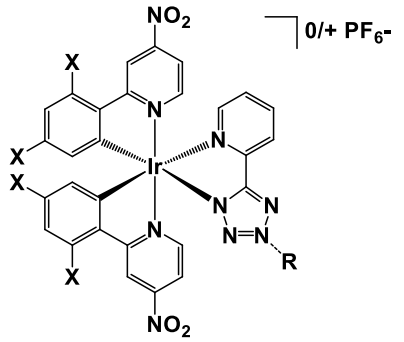

X = H, R not present; [Ir(PPy-NO_2)$_2$(PTZ)]
X = H, R = Me; [Ir(PPy-NO_2)$_2$(PTZ-Me)][PF_6]
X = H, R = ^{t}Bu; [Ir(F_2-PPy-NO_2)$_2$(PTZ-^{t}Bu)][PF_6]
X = F; [Ir(F_2-PPy-NO_2)$_2$(PTZ)]
X = F, R = Me; [Ir(F_2-PPy-NO_2)$_2$(PTZ-Me)][PF_6]
X = F, R = ^{t}Bu; [Ir(F_2-PPy-NO_2)$_2$(PTZ-^{t}Bu)][PF_6]

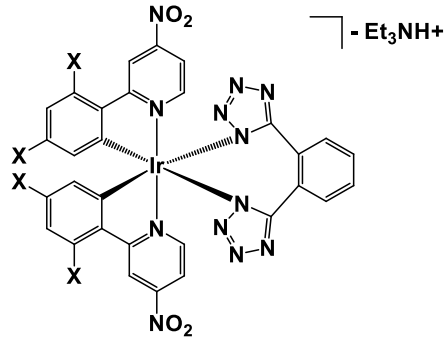

X = H; [Ir(PPy-NO_2)$_2$(1,2-BTB)][Et_3NH]
X = F; [Ir(F_2-PPy-NO_2)$_2$(1,2-BTB)][Et_3NH]

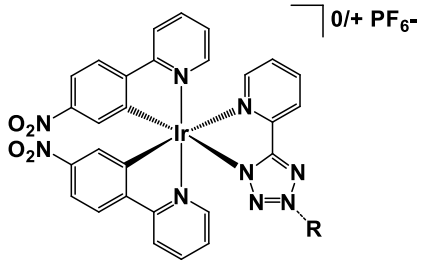

R not present; [Ir(O_2N-PPy)$_2$(PTZ)]
R = Me; [Ir(O_2N-PPy)$_2$(PTZ-Me)][PF_6]
R = ^{t}Bu; [Ir(O_2N-PPy)$_2$(PTZ-^{t}Bu)][PF_6]

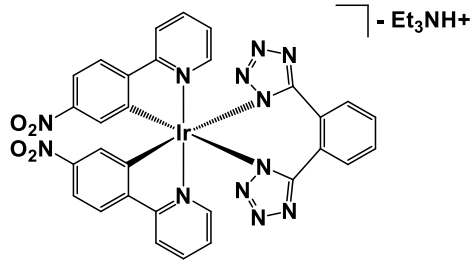

[Ir(O_2N-PPy)$_2$(1,2-BTB)][Et_3NH]

Scheme 2.6. Ir(III)-NO_2 complexes presented herein and relative acronyms.

6.3 Results and Discussion

6.3.1 *Synthesis of the ligands and corresponding Ir(III) complexes.*

To obtain Ir(III) complexes possessing nitro functional groups NO_2, a set of *2-phenylpyridine* type ligands **PPy-NO_2**, **F_2-PPy-NO_2** and **O_2N-PPy** was synthesised with almost quantitative yield via Suzuki-Miyaura coupling.[5] (**Scheme 3.6**) The combination of conveniently substituted 2-bromopyridines and phenylboronic acids allowed us to obtain three **(C^N)-NO_2** ligands each bearing a nitro group on the phenyl ring or the pyridyl ring respectively. At this point, by reaction of Ir(III) chloride and 2.5 eq of cyclometalating ligand **(C^N)-NO_2** three new dichloro-bridged Ir(III) dimers **[Ir(PPy-NO_2)$_2$Cl]$_2$**, **[Ir(F_2-PPy-NO_2)$_2$Cl]$_2$**, and **[Ir(O_2N-PPy)$_2$Cl]$_2$** were obtained in good yield.[6]

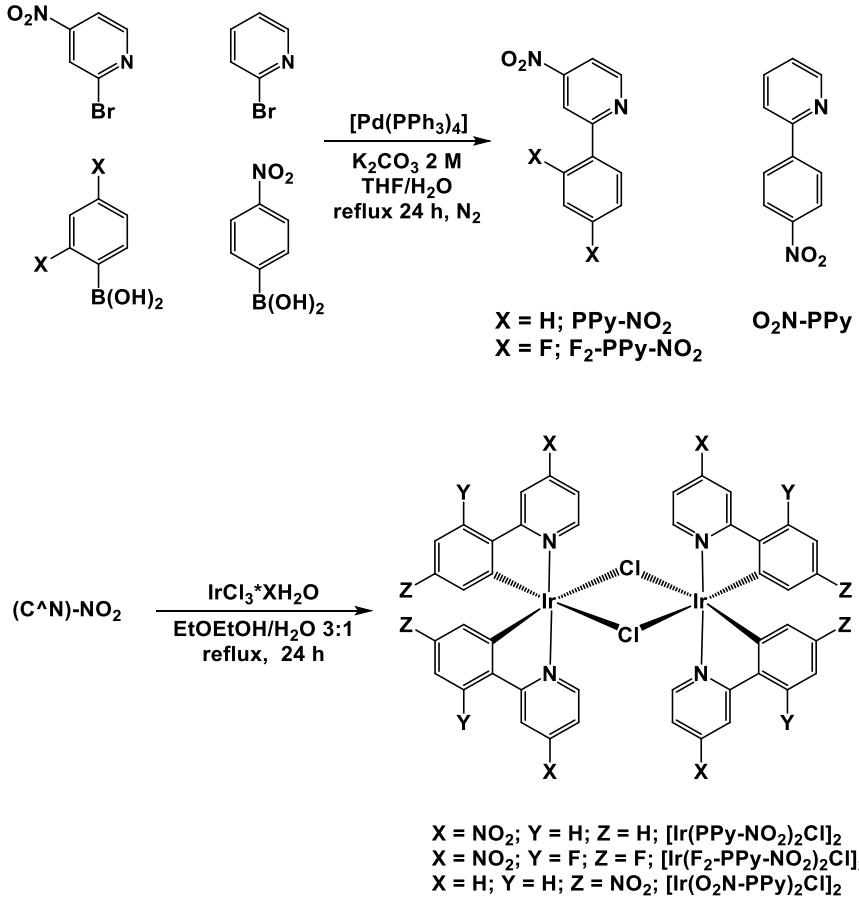

Scheme 3.6. Synthetic procedures for the preparation of the **(C^N)-NO_2** ligands **PPy-NO_2**, **F_2-PPy-NO_2** and **O_2N-PPy** and of the corresponding dichloro-bridged Ir(III) dimers.

As confirmed by ^{1}H-NMR spectroscopy, the cyclometalated iridium dimers were obtained as statistic mixtures of homochiral *rac* (ΛΛ/ΔΔ; D_2 symmetry) and hetorochiral *meso* (ΛΔ/ΔΛ; C_{2h} symmetry) diasteroisomer. (**Scheme 4.6**)

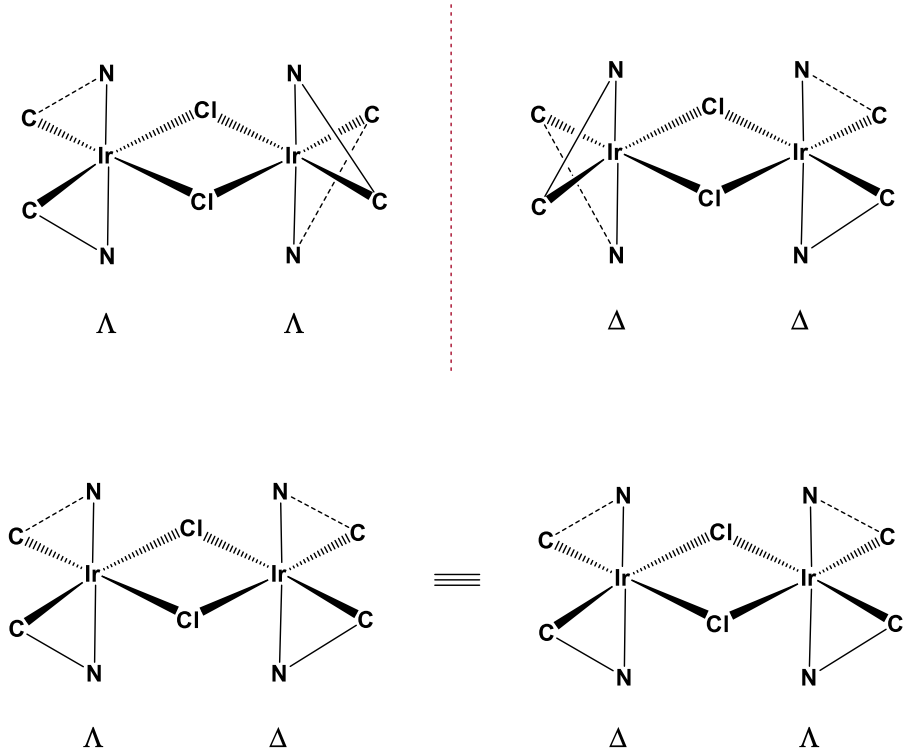

Scheme 4.6. Graphical representation of the homochiral (top) and heterochilar (bottom) Ir(III) dimers.

In **Figure 1.6** is reported the ^{1}H-NMR spectra of the dichloro-bridged Ir(III) dimer **[Ir(PPy-NO_2)$_2$Cl]$_2$**. From its analysis, it is possible to notice the presence of two distinct pattern of signals differing only for the relative positions of the resonances. Taking a closer look to the spatial conformation of such species, it is possible to notice how both homo and heterochiral dimers display a C_2 axis passing through both Ir centres, hence the two ligands coordinating a given Ir centre will be equivalent. Based on such premises, and considering the presence of three different species (a racemic mixture and a meso form), this would lead to the presence of four patterns of signals.

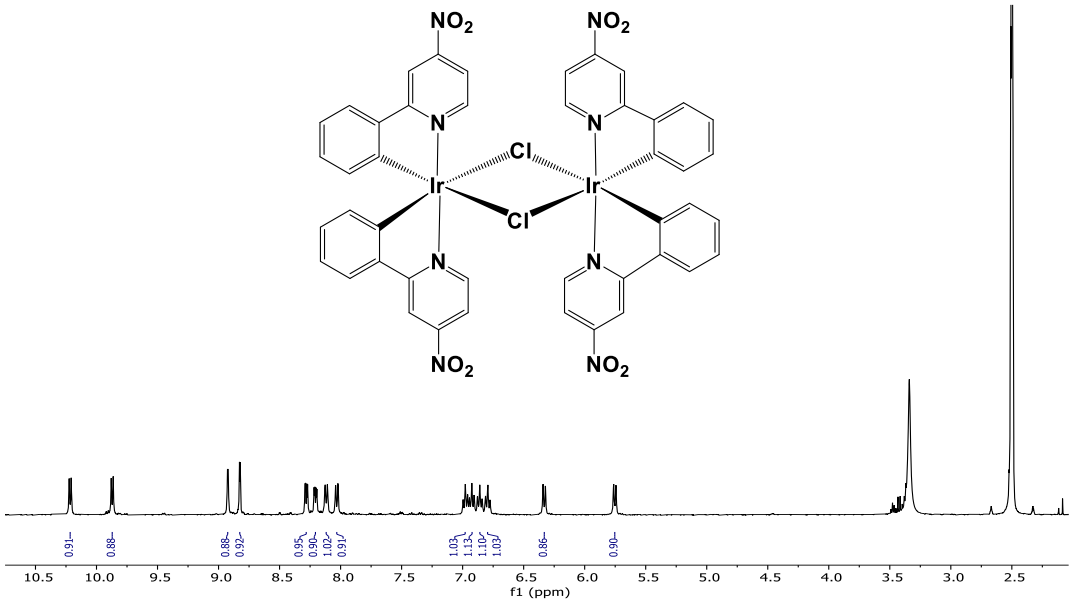

Figure 1.6. ^{1}H-NMR spectrum of biscyclometalated Ir(III) dimer $[Ir(PPy\text{-}NO_2)_2Cl]_2$; 400 MHz, d_6-DMSO. The reported structure would correspond to the heterochiral meso forms of such dimer.

Furtherly analysing the symmetry elements of such dimers, for the homochiral dimers one may notice the presence of two additional C_2 axis, one passing through both chloride atoms and another one passing through the centre of the dimer and perpendicular to the plane described by the two Ir centre and the two chlorine atoms (Ir_2Cl_2 plane). The first axis makes both Ir centres equivalent, whereas the second one interconverts the two Ir centres and their ligands, thus resulting in a single pattern of signal for the racemic mixture ΛΛ/ΔΔ.

Regarding the heterochiral dimer, a single pattern of signals corresponding to all the four C^N ligands can be explained in light of the presence of a mirror plane containing the two chlorine atoms and perpendicular to the Ir_2Cl_2 plane which interconverts the two Ir centres and their ligands. To summarize, the ^{1}H-NMR spectra of dichlorobridge Ir(III) dimers consists in a pattern of signals corresponding to the homochiral dimers along with another pattern of signals relative to the heterochiral meso compound.Further evidence verifying the equivalence of the two C^N ligands can be found by preparing a trischelate iridium complex using a symmetric “third” ligand.

In complex **[Ir(F$_2$-PPy-NO$_2$)$_2$(acac)]**, reported as an example, the coordination sphere of the **[Ir(C^N)$_2$]$^+$** fragment is completed with a symmetric chelating ligand, namely acetylacetonate (**acac**, the deprotonated form of 2,4-butanedione). Once again, the presence of a C_2 axis passing through the metal centre results in the magnetic equivalency of the two C^N ligands. In **Figure 2.6** the ^{1}H-NMR spectra of the complex reports a single pattern of signals associable to both the cyclometalated ligands, in agreement with the integration of the signals at 1.80 ppm associable to the methyl group of acac.

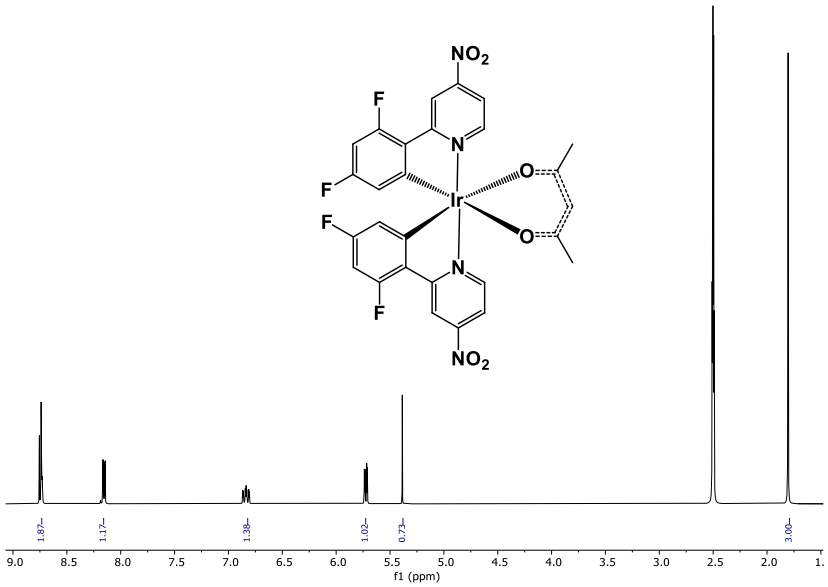

Figure 2.6. ^{1}H-NMR spectrum of complex **[Ir(F$_2$-PPy-NO$_2$)$_2$(acac)]**; 400 MHz, d_6-DMSO.

In the end, a new family of differently charged Ir(III)-tetrazole complexes with the general formula **[Ir((C^N)-NO$_2$)$_2$(N^N')]$^{-1/0/+1}$** (where N^N' represents a chelating 5-aryltetrazole species) was prepared (**Scheme 5.6**). Neutral and positively charged Ir(III) complexes were obtained by reaction of the aforementioned Ir(III) precursors with a set of tetrazolato and N-2 alkyl tetrazoles differing for the substitution on the pentatomic ring (**PTZ-H**, **PTZ-Me**, **PTZ-^{t}Bu**). Besides, one further bis tetrazole based ligand, namely 1,2-bistetrazolyzbenzene abbreviated as **1,2-BTB-H$_2$**, which consists of two tetrazole groups tethered by a phenyl ring, has been used to obtain a series of negatively charged Ir(III) complexes with the general formula **[Ir((C^N)-NO$_2$)$_2$(1,2-BTB)][Et$_3$NH]**.

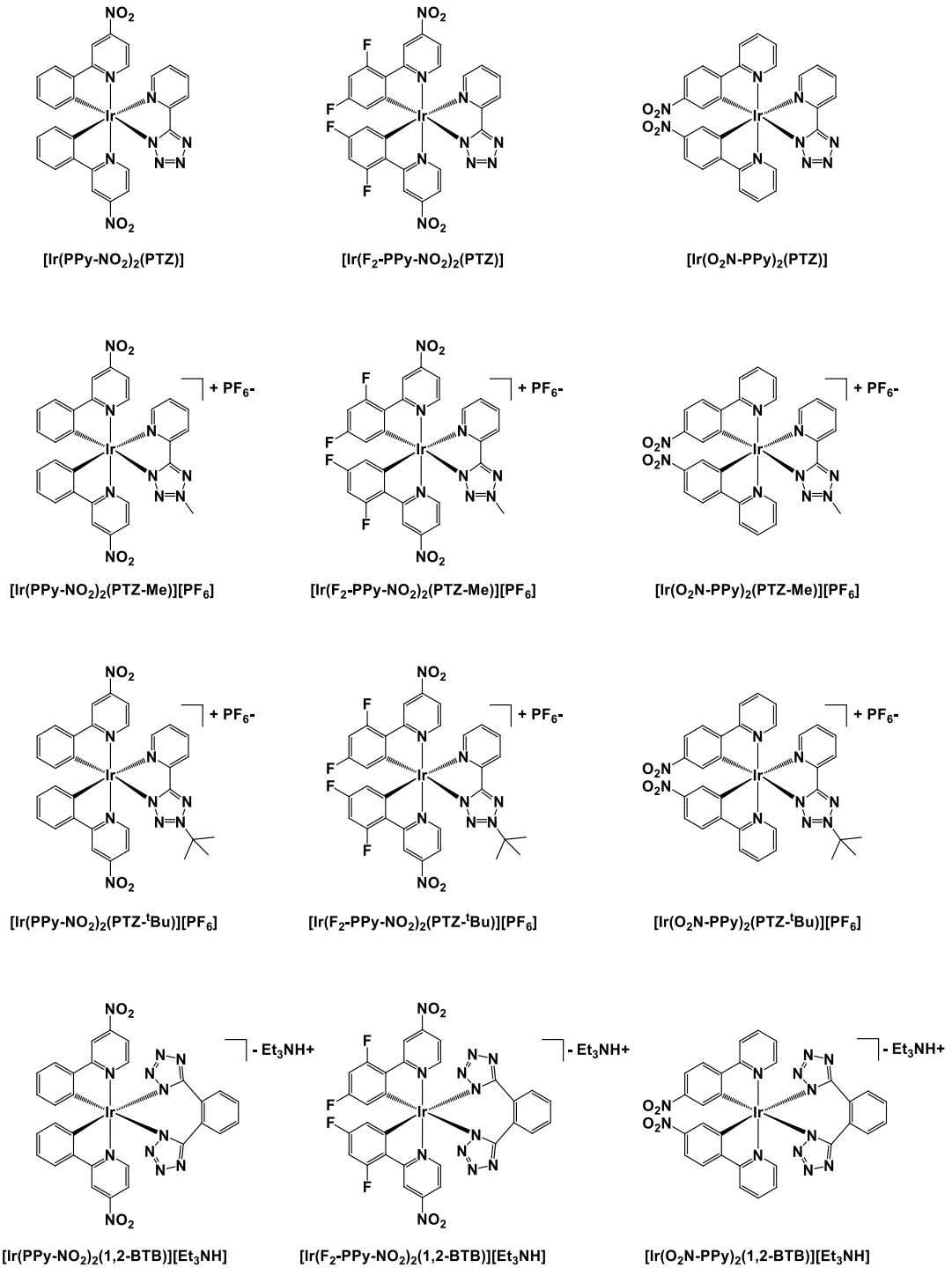

Scheme 5.6. Representation of the prepared **[Ir((C^N)-NO$_2$)$_2$(N^N')]$^{-1/0/+1}$** complexes. **Row 1**: neutral **[Ir((C^N)-NO$_2$)$_2$(PTZ)]** type complexes. **Row 2-3**: cationic **[Ir((C^N)-NO$_2$)$_2$(PTZ-R)][PF$_6$]** type complexes. **Row 4**: anionic **[Ir((C^N)-NO$_2$)$_2$(1,2-BTB)][Et$_3$NH]** type complexes.

The followed synthetic pathway is reported in **Scheme 6.6** and represents an adaptation of the general procedures for the preparation of Ir(III)-tetrazole complexes we utilised so far.[7,8] To cope with the poor solubility of the dichloro-bridged Ir(III) precursors, a preliminary chloride extraction with $AgPF_6$ was performed in refluxing 1:1 v/v DCM/MeOH to give an intermediate Ir(III)-solvato complex that in all cases was straightforwardly reacted with a slight excess of ligand **L1**/**L2**/**L3**/**L4** to give the corresponding Ir(III)-tetrazole complex.

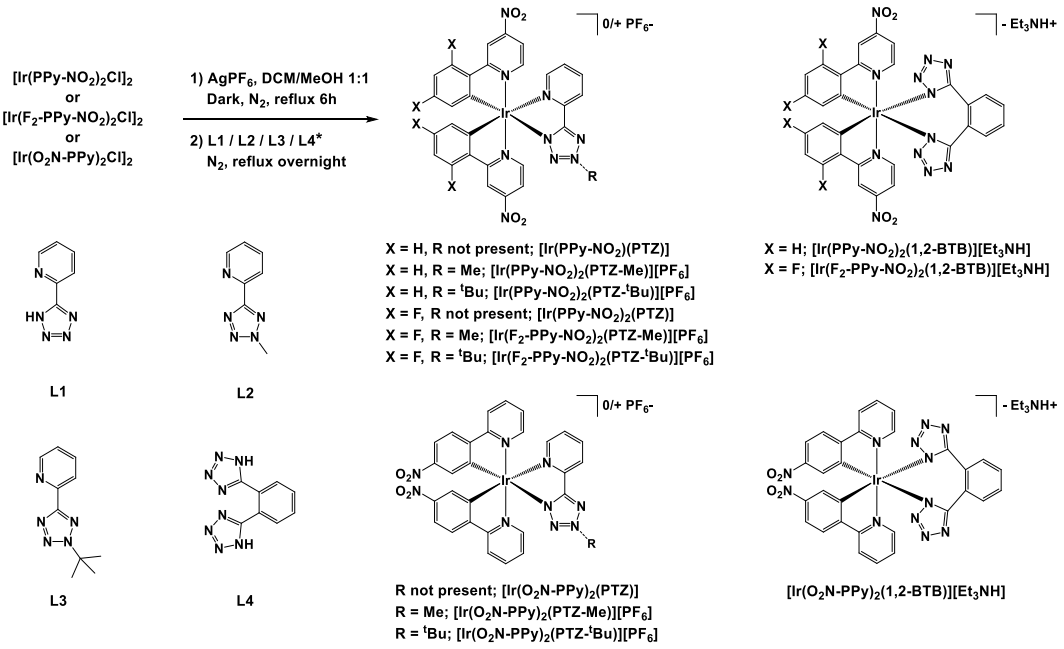

Scheme 6.6. Synthetic procedure for the preparation of **[Ir((C^N)-NO$_2$)$_2$(N^N')]$^{-1/0/+1}$** type complexes. (See experimental for ligands synthesis). (*) In reactions involving L4 as the (N^N) ligand, 2.5 eq of Et_3N were added to deprotonate the tetrazolic ligand with simultaneous formation of the counter-ion Et_3NH^+

After purification via Al_2O_3 column chromatography, each of the prepared complexes was characterized through Electron Spray Ionization Mass Spectrometry (ESI-MS), ^1H and ^{13}C-NMR spectroscopy. The obtained ESI-MS spectra confirmed the actual charge of the Ir(III)-tetrazole complexes showing in the ESI+ scan the peak corresponding to the **[Ir+Na]$^+$** or **[Ir]$^+$** cation for neutral and cationic complexes respectively. On the contrary, the negative peak relative to the **[Ir]$^-$** anion was observed for all negatively charged complexes. The ionic nature of the cationic and anionic complexes was further

corroborated by the presence of the corresponding counterion, represented in turn by **$[PF_6]^-$** or **$[Et_3NH]^+$**. (**Figure 3.6**) Alongside ESI-MS data, the analysis of all the collected ^1H and ^{13}C NMR spectra verified the expected structures, with each complex displaying resonances in agreement with tris-chelate C_s-symmetric Ir(III) complexes. (**Figure 4.6-9.6**) Analogously to some previously reported of anionic Ir(III)-tetrazolate displaying **1,2-BTB^{2-}** as the bis chelating ancillary ligand,[8] well-resolved ^1H and ^{13}C NMR spectra could only be obtained via VT-NMR experiments. (**Figure 4.6-6.6**) Such behaviour was explained in consideration of the not coplanar arrangement adopted by the coordinated (**1,2 BTB^{2-}**) ligand. The likely reason that might account for such a fluxional behaviour could be attributed to the exchange through a ring inversion of the strained seven membered ring (–IrNC4N–) that is described by the coordinated bis-tetrazolate ligand and the Ir(III) center. The occurrence of a similar mechanism has been described in previous reports dealing with heterocyclic analogues of benzocycloheptene.

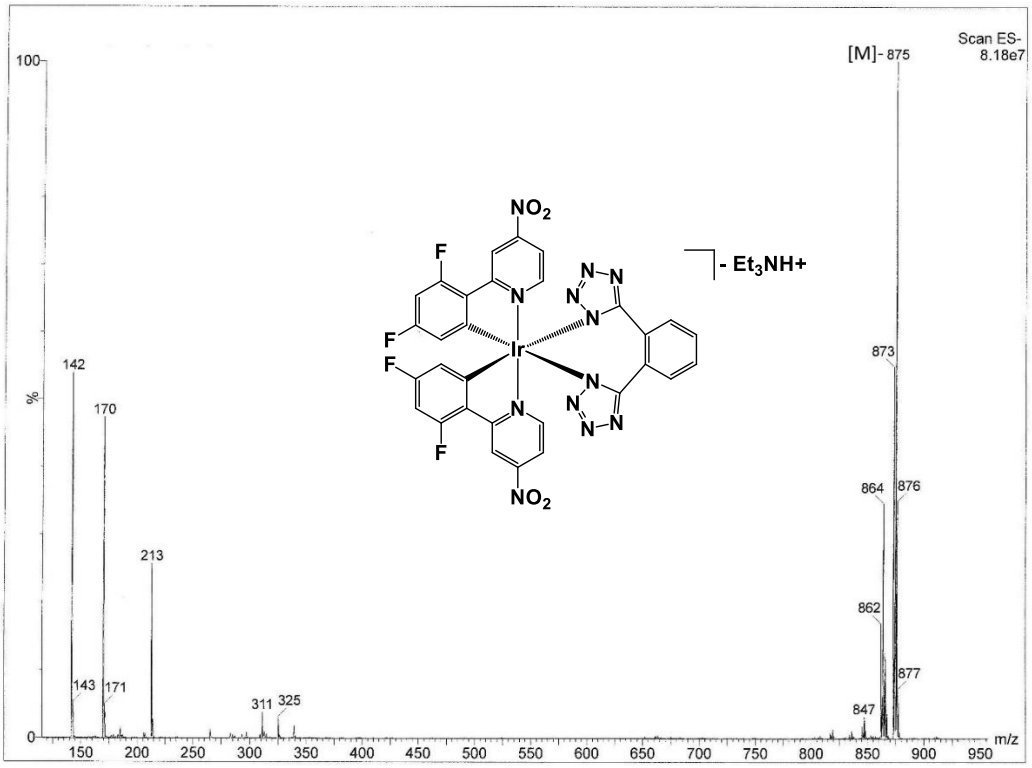

Figure 3.6. ESI-MS spectrum of **$[Ir(PPy\text{-}NO_2)_2(1,2\text{-}BTB)[Et_3NH]$**, (negative ions region) [M]- = 875.

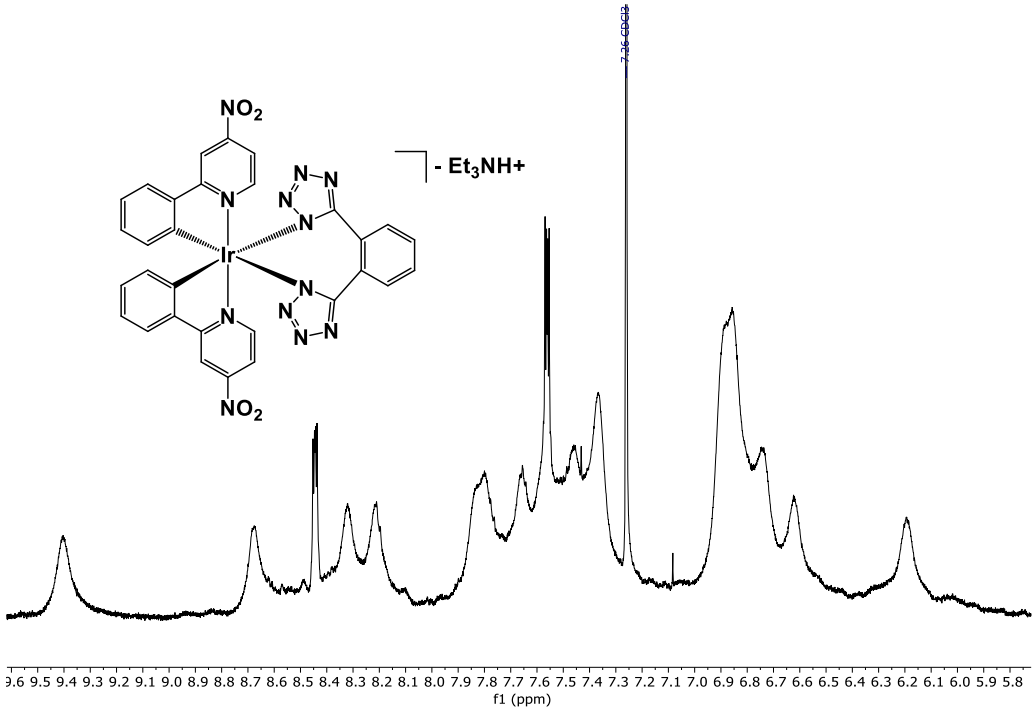

Figure 4.6. ^{1}H-NMR spectrum of **[Ir(PPy-NO$_2$)$_2$(1,2-BTB)[Et$_3$NH]**, $CDCl_3$, 600 MHz, 298K.

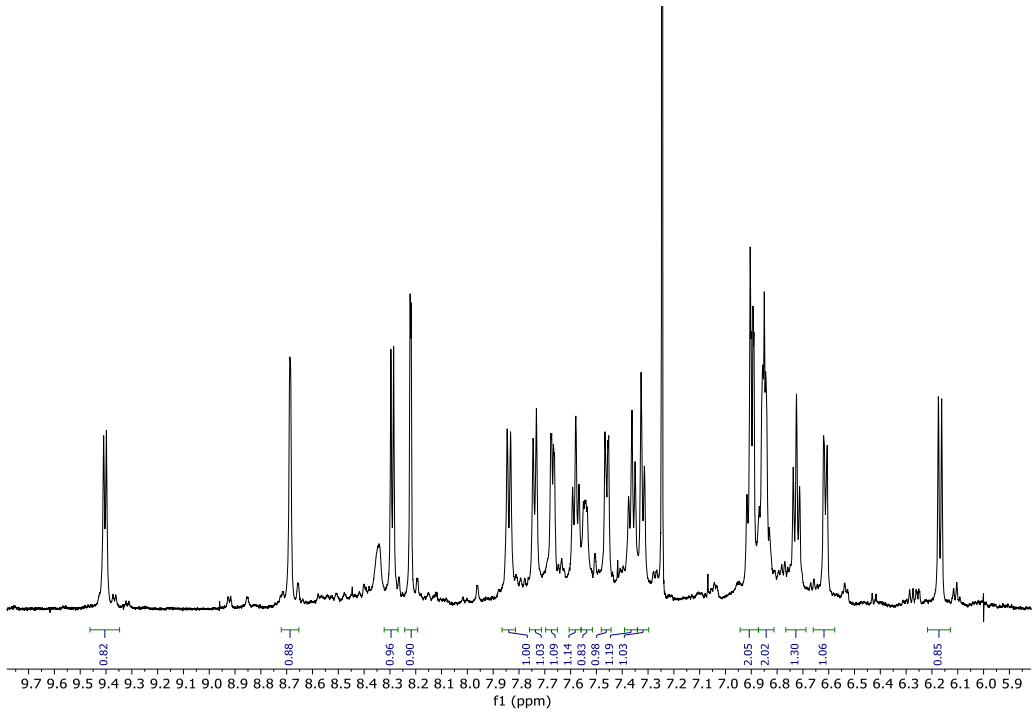

Figure 5.6. ^{1}H-NMR spectrum of **[Ir(PPy-NO$_2$)$_2$(1,2-BTB)[Et$_3$NH]**, $CDCl_3$, 600 MHz, 253K.

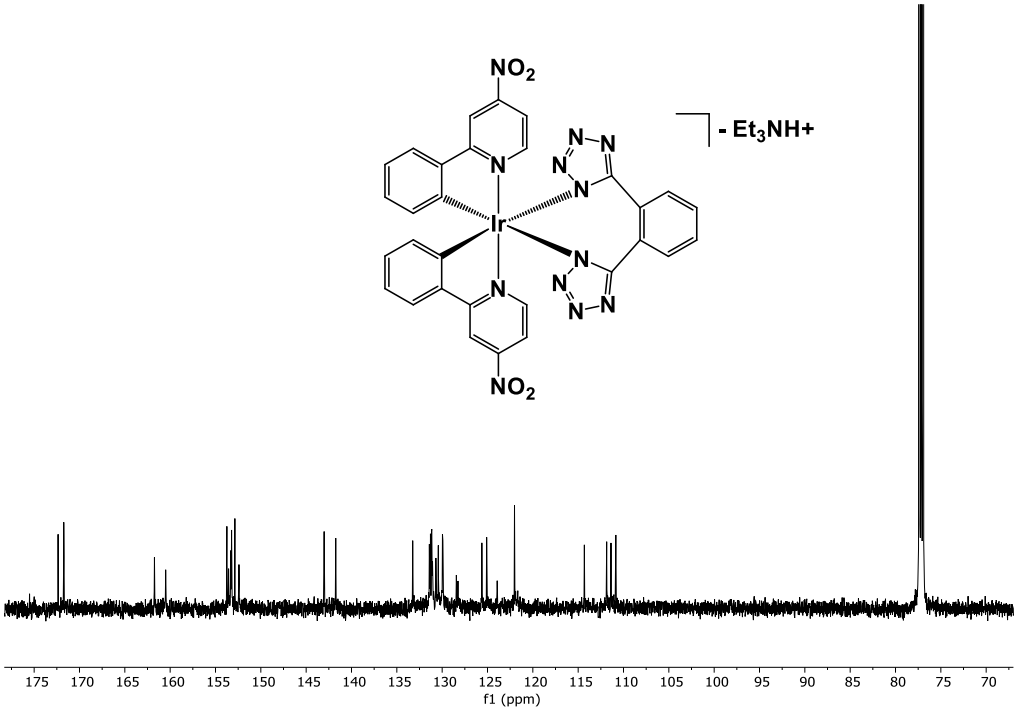

Figure 6.6. ^{13}C-NMR spectrum of **[Ir(PPy-NO_2)$_2$(1,2-BTB)[Et_3NH]**, $CDCl_3$, 150 MHz, 253K.

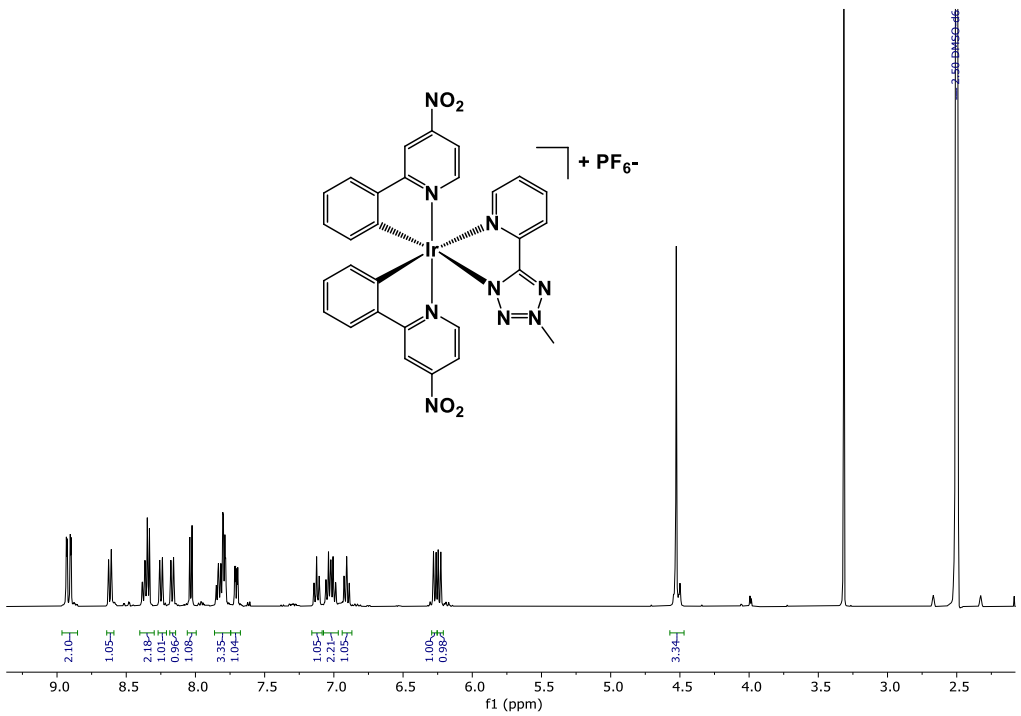

Figure 7.6. ^{1}H-NMR spectrum of **[Ir(PPy-NO_2)$_2$-(PTZ-Me)][PF_6]**, DMSO-d_6, 400 MHz, 298K.

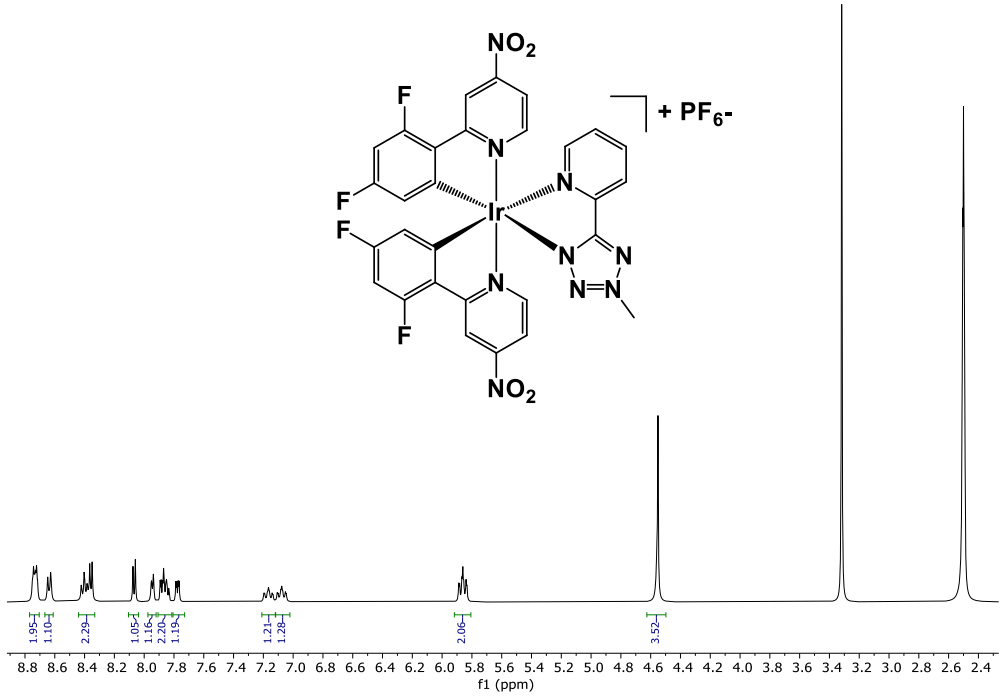

Figure 8.6. ^{1}H-NMR spectrum of **[Ir(F$_2$-PPy-NO$_2$)$_2$-(PTZ-Me)][PF$_6$]**, DMSO-d$_6$, 400 MHz, 298K.

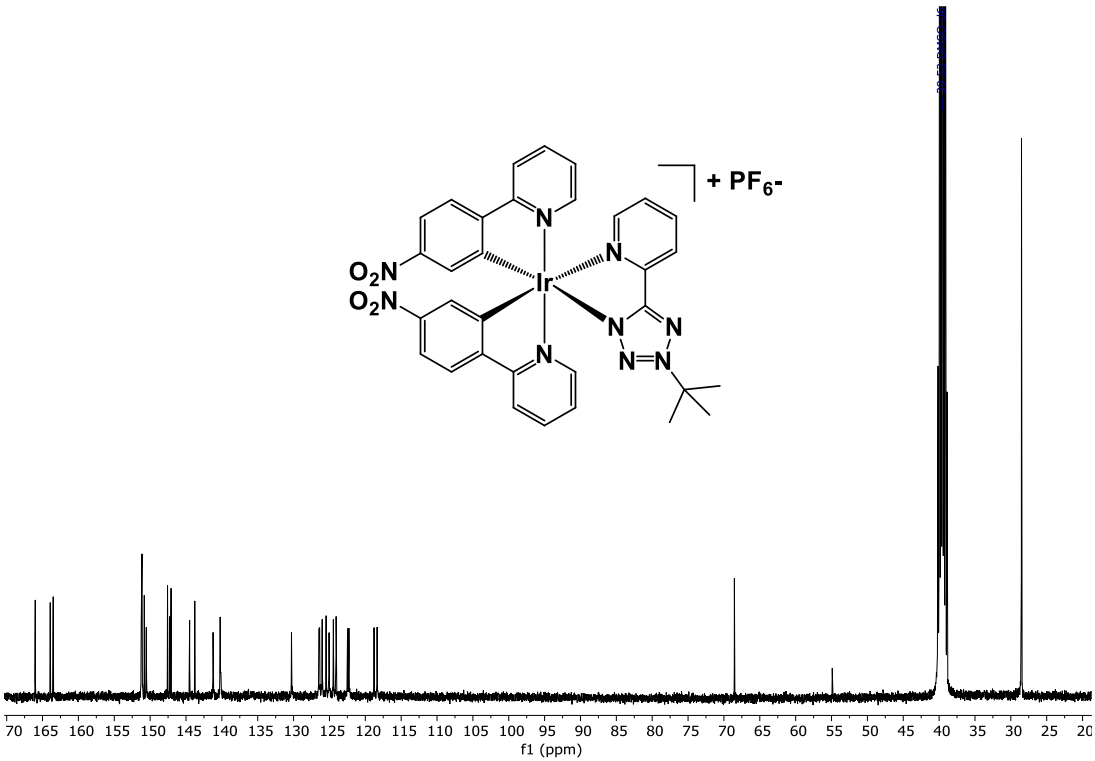

Figure 9.6. ^{13}C-NMR spectrum of **[Ir(O$_2$N-PPy)$_2$-(PTZ-^{t}Bu)][PF$_6$]**, DMSO-d$_6$, 100 MHz, 298K.

6.3.2 *X-ray crystallography*

The evidence deduced from $^{1}H/^{13}C$ NMR experiments were further confirmed from the X-ray diffraction of **[Ir((C^N)-NO$_2$)$_2$(N^N')]$^{-1/0/+1}$**. Their molecular structure is similar to that of previously reported [Ir(C^N)$_2$(N^N)] complexes.[7,8]

Along the series of the new Ir-tetrazole complexes, one neutral complex, namely **[Ir(F$_2$-PPy-NO$_2$)$_2$(PTZ)]**, three cationic species – namely, **[Ir(F$_2$-PPy-NO$_2$)$_2$(PTZ-^{t}Bu)][PF$_6$]**, , **[Ir(O$_2$N-PPy)$_2$(PTZ-Me)][PF$_6$]** and **[Ir(O$_2$N-PPy)$_2$(PTZ-^{t}Bu)][PF$_6$]**, and two negatively charged complexes – namely **[Ir(F$_2$-PPy-NO$_2$)$_2$(1,2-BTB)][Et$_3$NH]**, **[Ir(O$_2$N-PPy)$_2$(1,2-BTB)][Et$_3$NH]** – afforded crystals suitable for X-ray diffraction. For the reported complexes, the analysis of their molecular structure (**Figure 10.6, 11.6, 12.6**) provided results congruent with the occurrence of the expected octahedral complexes in which the coordination environment of the distorted Ir(III) centre consists in two *cis*-metalated carbons, two *trans*-phenylpyridyl nitrogen atoms, and two diiminic nitrogens from the tetrazolic ligand.

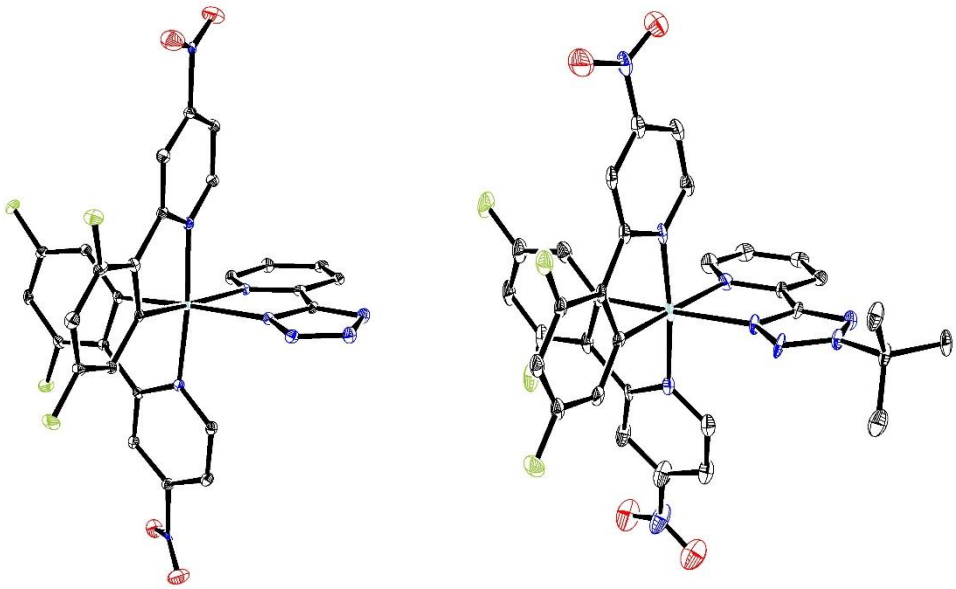

Figure 10.6. Molecular structure of **[Ir(F$_2$-PPy-NO$_2$)$_2$(PTZ)]** (left) and **[Ir(F$_2$-PPy-NO$_2$)$_2$(PTZ-^{t}Bu)]$^{+}$** (right). Displacement ellipsoids are at the 30% probability level. Hydrogen atoms and the PF_6^- counterion have been omitted for clarity.

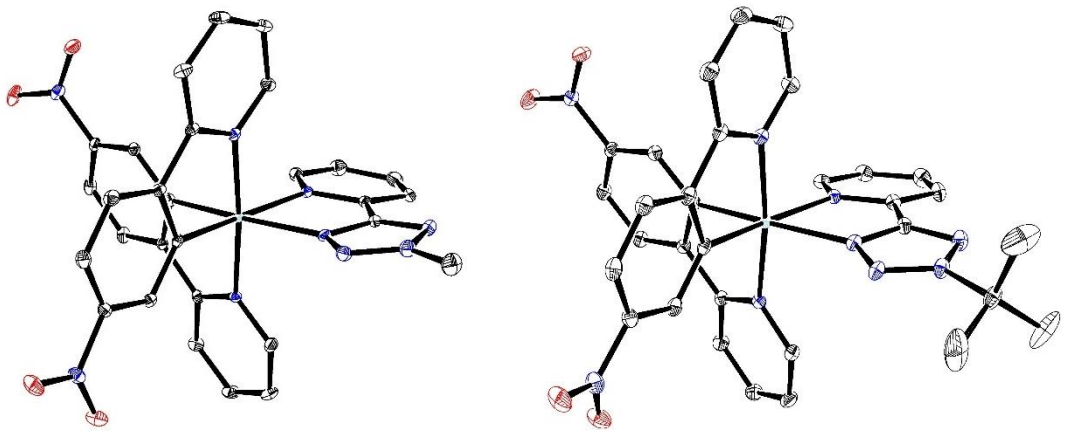

Figure 11.6. Molecular structure of **[Ir(O_2N-PPy)$_2$(PTZ-Me)]**$^+$ (left) and **[Ir(O_2N-PPy)$_2$(PTZ-^{t}Bu)]**$^+$ (right). Displacement ellipsoids are at the 30% probability level. Hydrogen atoms and the PF_6^- counterion have been omitted for clarity.

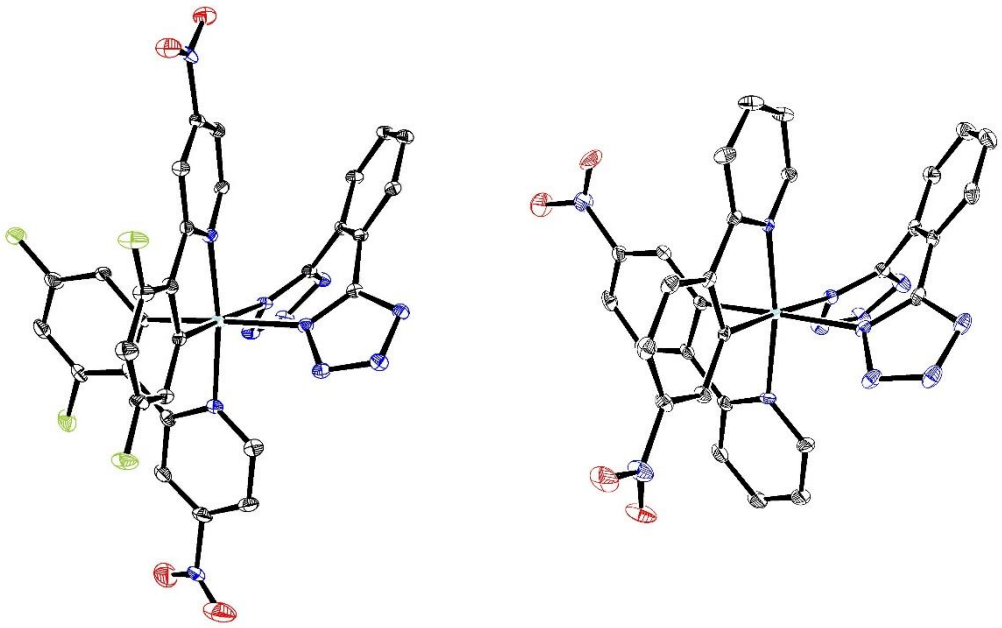

Figure 12.6. Molecular structure of **[Ir(F_2-PPy-NO_2)$_2$(1,2-BTB)]**$^-$ (left) and **[Ir(O_2N-PPy)$_2$(1,2-BTB)]**$^+$. Displacement ellipsoids are at the 30% probability level. Hydrogen atoms and the Et_3NH^+ counterion have been omitted for clarity.

6.3.3 *Photophysical properties*

Absorption spectroscopy

Absorption behaviour of complexes **C1-C12** was initially studied at room temperature in DCM solution and the resulting photophysical data is summarized in **Table 1.6**. The collected absorption spectra are reported in **Figure 13.6 , 14.6, 15.6** and all profiles are characterized by intense absorption bands at higher energy (230 – 370 nm) associable to ^{1}LC (Ligand Centred) $^1(\pi\rightarrow\pi^*)$ transitions,[7,8] followed by weaker and less-energetic transitions (430 - 550 nm), relatable to both spin-allowed and spin-forbidden ^{1}MLCT (*Metal to Ligand Charge Transfer*) phenomena. Although for each set of complexes the global shape of the absorption profiles seems to be mainly determined by the **(C^N)-NO$_2$** ligands, it is worth noticing how for all profiles a hypsochromic shift occurs with the increasing neat charge of the complexes. Such behaviour can be rationalized in consideration of the widening of the HOMO-LUMO gap of the complex as a consequence of the decreasing σ-donating (or increasing π-accepting) ability of the ancillary ligand when the tetrazolic ring is substituted.[9] The same effect is observable by sorting the complexes according to the tetrazolic ligand: a hypsochromic shift of the absorption profile takes place with the increasing electron-withdrawing ability of the substituents on the phenyl ring of the **(C^N)- NO$_2$** ligands passing from **PPy-NO$_2$** to **F$_2$-PPy-NO$_2$** to **O$_2$N-PPy**.

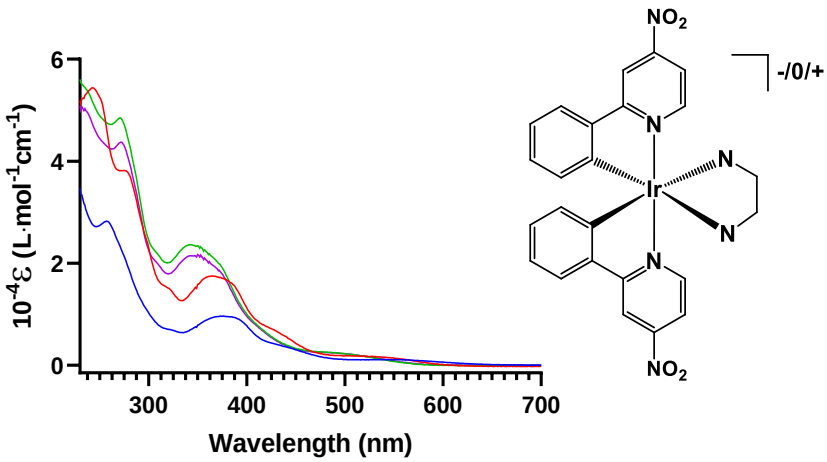

Figure 13.6. Absorption spectra of complexes **[Ir(PPy-NO$_2$)$_2$(PTZ)]** (red line), **[Ir(PPy-NO$_2$)$_2$(PTZ-Me)]$^+$** (green line**), [Ir(PPy-NO$_2$)$_2$(PTZ-^{t}Bu)]$^+$** (purple line), **[Ir(PPy-NO$_2$)$_2$(1,2-BTB)]$^-$** (blue line), obtained from 10^{-5} M solution in DCM at 298K.

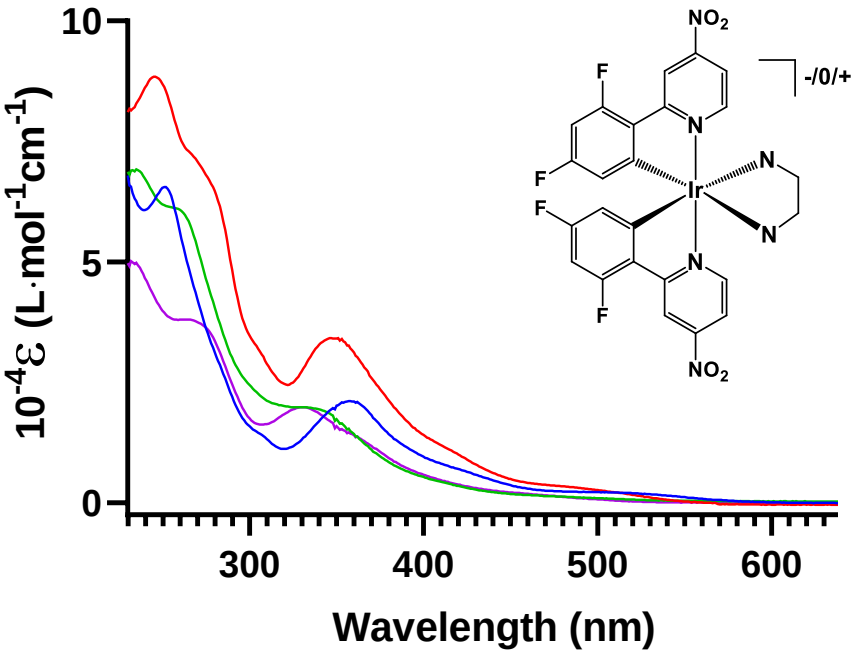

Figure 14.6. Absorption spectra of complexes **[Ir(F$_2$-PPy-NO$_2$)$_2$(PTZ)]** (red line), **[Ir(F$_2$-PPy-NO$_2$)$_2$(PTZ-Me)]$^+$** (green line), **[Ir(F$_2$-PPy-NO$_2$)$_2$(PTZ-^{t}Bu)]$^+$** (purple line), **[Ir(F$_2$-PPy-NO$_2$)$_2$(1,2-BTB)]$^-$** (blue line), obtained from 10^{-5} M solution in DCM at 298K.

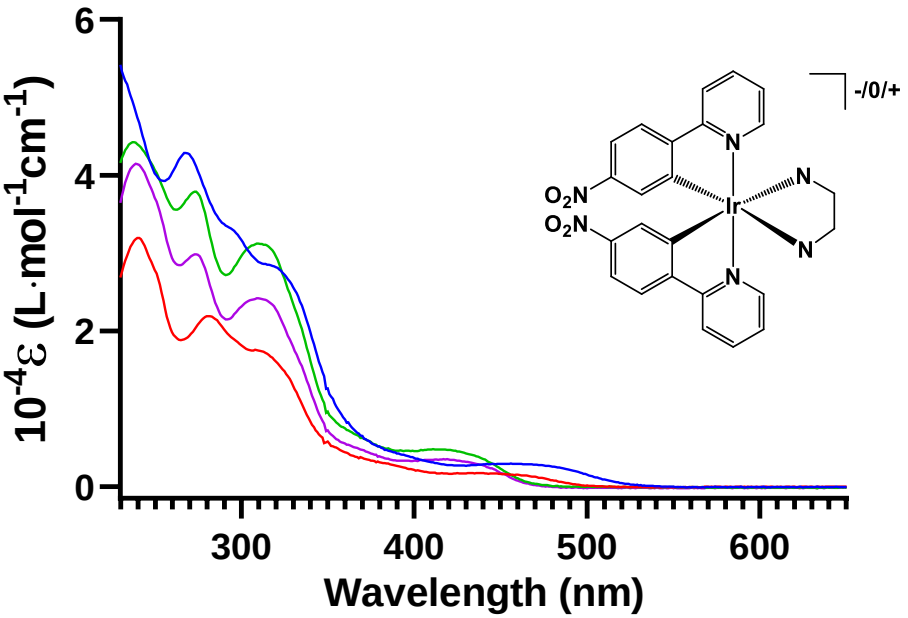

Figure 15.6. Absorption spectra of complexes **[Ir(O$_2$N-PPy)$_2$(PTZ)] (red line), [Ir(O$_2$N-PPy)$_2$(PTZ-Me)]$^+$** (green line), **[Ir(O$_2$N-PPy)$_2$(PTZ-^{t}Bu)]$^+$** (purple line), **[Ir(O$_2$N-PPy)$_2$(1,2-BTB)]$^-$** (blue line), obtained from 10^{-5} M solution in DCM at 298K.

Table 1.6. Photophysical data for neutral, cationic and anionic Ir(III) complexes reported in this work; DCM solutions.

Complex	**Absorption**	**Emission 298 K**			**Emission 77 K**	
10^{-5} M solution in CH_2Cl_2	λ(nm) 10^{-4}ε ($cm^{-1}M^{-1}$)	λ_{em} (nm)	τ_{ox} (μs)	τ_{deox} (μs)	λ_{em} (nm)	τ (μs)
[Ir(PPy-NO_2)$_2$(PTZ)]	243 (5.44), 277 (3.80), 320 (1.47), 366 (1.75), 440_{sh} (0.60) 520 (0.17)	492 518	0.15 -	0.780 -	-	-
[Ir(PPy-NO_2)$_2$(PTZ-Me)]$^+$	237_{sh} (5.38), 271 (4.85), 307_{sh} (2.22), 341 (2.36), 480 (0.25)	480 510	- -	- 0.198	472 506 638	0.725 0.487 0.487
[Ir(PPy-NO_2)$_2$(PTZ-^{t}Bu)]$^+$	235 (5.02), 272 (4.37), 310_{sh} (1.97), 343 (2.15), 375_{sh} (1.79), 415 (0.69), 490 (0.24)	480 510	- -	0.10 0.08	472 506 645	0.45 0.45 0.38
[Ir(PPy-NO_2)$_2$(1,2-BTB)]$^-$	257 (2.82), 320 (0.70), 376 (0.97), 450_{sh} (0.31), 540 (0.11)	500	-	-		-
[Ir(F_2-PPy-NO_2)$_2$(PTZ)]	246 (8.84), 278_{sh} (6.62), 307_{sh} (3.02), 348 (3.41)	462 492 730	- - -	0.08 - -	454 486 605	- - 2.9
[Ir(F_2-PPy-NO_2)$_2$(PTZ-Me)]$^+$	235 (6.92), 258_{sh} (6.11), 331 (1.99)	460 490 650	- - -	- 0.07 -	450 480 580	- - 2.0
[Ir(F_2-PPy-NO_2)$_2$(PTZ-^{t}Bu)]$^+$	233 (4.98), 263 (3.80), 331 (1.98), 360_{sh} (1.40)	456 486 630	- - 0.02	- - 0.02	472 506 645	0.45 0.45 0.38
[Ir(F_2-PPy-NO_2)$_2$(1,2-BTB)]$^-$	251 (6.55), 308 (1.38), 358 (2.11), 430 (0.58), 500 (0.22)	470 498	- -	- -	460 470 650	- - 0.47
[Ir(O_2N-PPy)$_2$(PTZ)]	241 (3.19), 250_{sh} (2.78), 281 (2.19), 308 (1.76), 432 (0.175)	635	-	-	508 580 618	0.25 2.50 2.50
[Ir(O_2N-PPy)$_2$(PTZ-Me)]$^+$	237 (4.42), 273 (3.79), 310 (3.12), 416 (0.48)	580	0.98	1.80	560 600	4.80 4.80
[Ir(O_2N-PPy)$_2$(PTZ-^{t}Bu)]$^+$	239 (4.14), 251_{sh} (3.65), 274 (2.98), 309 (2.42), 370_{sh} (0.47), 417 (0.35)	580	0.96	2.2	560 600	4.04 4.78
[Ir(O_2N-PPy)$_2$(1,2-BTB)]$^-$	268 (4.29), 297_{sh} (3.25), 320_{sh} (2.81), 390_{sh} (0.42), 453 (0.30)	660	-	-	614 655	- 0.57

6.3.4 *Emission spectroscopy*

The emission behaviour of the prepare complexes was studied in several solvents such as DCM, DMSO, Toluene, H_2O and H_2O/DMSO mixtures. (**Table 1.6, 2.6, 3.6, 4.6)**

Emission behaviour DCM

By excitation at 310 nm, solutions of the prepared complexes in polar solvents exhibited modest luminescent output, most likely in reason of the presence of NO_2 groups, which notoriously contribute to the deactivation of excited states via non-radiative decay pathways.[10] The photophysical data collected from 10^{-5} M solutions of the prepared **Ir(III)-NO_2** complexes in DCM and DMSO reflects the presence of an EWG on the main scaffold of the molecule. Analogously to the aforementioned **Ir(III)-CN** complexes, a blue-shift of the emission profile occurred once the neutral species were converted into their corresponding cationic derivatives. (**Figure 16.6**)

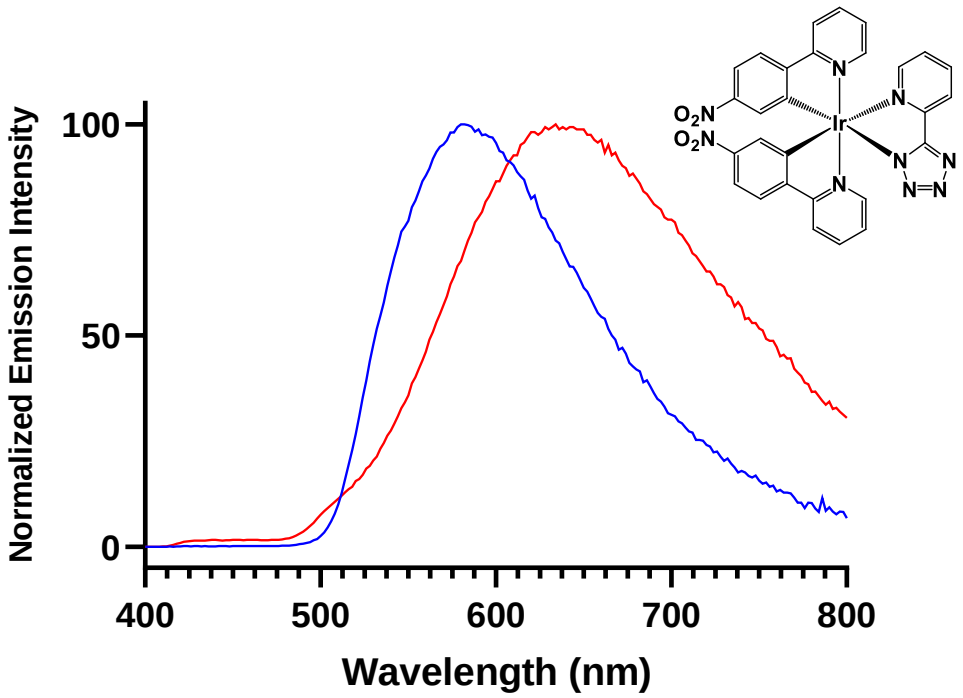

Figure 16.6. Normalized emission spectra of complexes **[Ir(O_2N-PPy)$_2$(PTZ)]** (red trace) and **[Ir(O_2N-PPy)$_2$(PTZ-Me)]**$^+$ (blue trace); obtained from 10^{-5} M solutions in DCM at 298K.

Interestingly, emission measurement in DCM of complexes possessing a NO_2 group at the para position of the pyridyl ring of the (**C^N**) ligands, in some cases revealed the participation of multiple processes in the determination of the total emission profile of the complex. For example, in the emission spectra of complex **[Ir(F_2-PPy-NO_2)$_2$(PTZ)]** reported in **Figure 17.6** one can notice a featured emission centred at about 480 nm and a red-shifted structureless emission down to about 730 nm. Whereas, the emission profile of complex **[Ir(F_2-PPy-NO_2)$_2$(PTZ)]** in DMSO presents uniquely a featured emission centred at about 480 nm. (**Figure 18.6**)

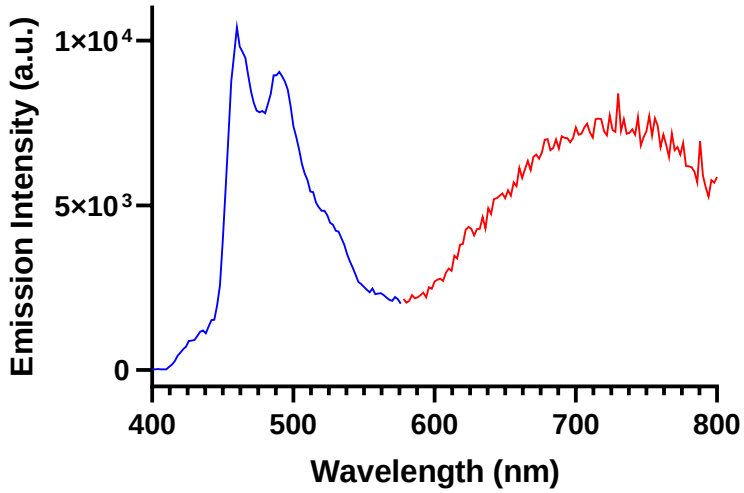

Figure 17.6. Emission profile of complex **[Ir(F_2-PPy-NO_2)$_2$(PTZ)]** obtained from 10^{-5} M solutions in DCM at 298K.

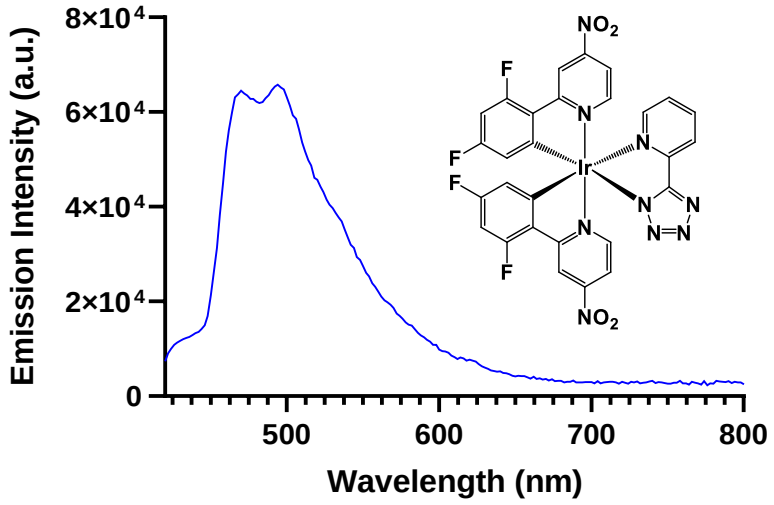

Figure 18.6. Emission profile of complex **[Ir(F_2-PPy-NO_2)$_2$(PTZ)]** obtained from 10^{-5} M solutions in DMSO at 298K.

Such behaviour has been previously observed for square planar Pt(II)-complexes, which are notoriously correlated to aggregation phenomena in light of the presence free d orbitals perpendicular to the molecule plane which are responsible for Pt-Pt π-π stacking interactions.[11]

Aggregation is sometimes considered an unfavourable phenomenon for satisfying luminescent properties of transition metal complexes. Formation of molecular aggregates may lead to aggregation-induced quenching (AIQ), implying dramatic decreases in luminescence properties such as emission intensity and photoluminescence quantum yield. Otherwise, in some cases aggregation can give rise to enhanced luminescence properties, due to antipodal phenomena such as aggregation-induced emission or aggregation-induced emission enhancement (AIEE).[12] This could result in a switch-on in the emission or in the appearance of a different emission feature. This second process is generally located at a lower energy in comparison to the lowest excited state of the monomer, resulting in a red-shifted emission originating from the macrostructure excited state.[13]

Since it is clear how aggregation phenomena must be concentration-dependent, the presence of aggregation-induced emission (AIE) can be verified, for example, by monitoring the emission profile of a luminophore in different solubility conditions. Solvents with high solvation capacity towards the compound of interest, such as DMSO in the case of metal complexes, will decrease the tendency to form aggregates thus the emission of the isolated complex will be displayed. On the other hand, if aggregation phenomena can take place, decreasing the complex solubility by increasing the concentration of a non-solvent, H_2O for example, or using a solvent with intermediate solvation capacity likewise DCM for complex **[Ir(F$_2$-PPy-NO$_2$)$_2$(PTZ)]**, could lead to modification on the overall emission profile. [14,15]

Emission studies in different solvents

To assess whether or not the red-shifted process in the emission spectrum of complex **[Ir(F$_2$-PPy-NO$_2$)$_2$(PTZ)]** in DCM (10^{-5} M solution) could be due to AIE, its emission behaviour was studied in DMSO/H_2O mixtures. The reported spectra (**Figure 19.6**),

acquired from 10^{-5} M solutions of complex **[Ir(F_2-PPy-NO_2)$_2$(PTZ)]**, show how the blue featured emission observable from a solution of the complex in pure DMSO is gradually replaced by a red structureless emission by increasing the H_2O/DMSO ratio and so the non-solvent concentration.

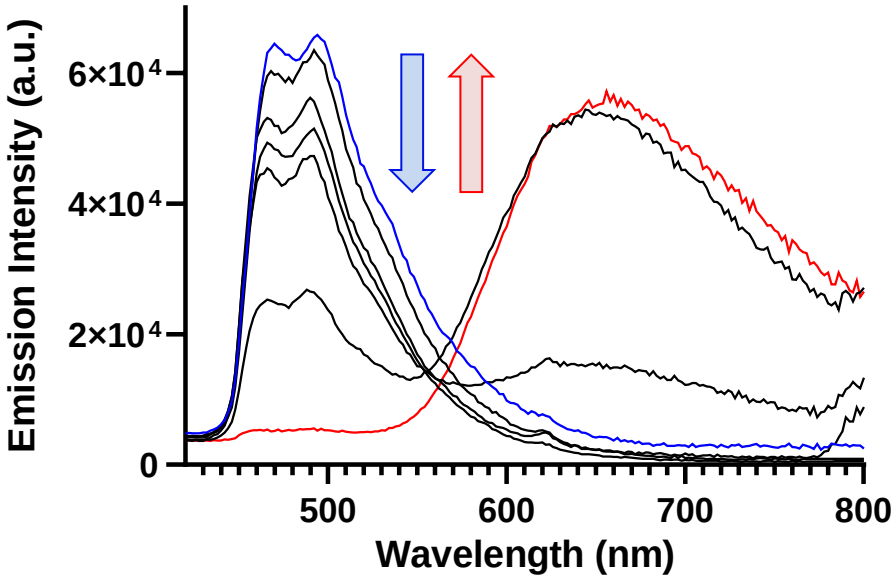

Figure 19.6. Emission profiles obtained from 10^{-5}M solutions of complex **[Ir(F_2-PPy-NO_2)$_2$(PTZ)]** in H_2O/DMSO mixtures. Blue profile: 100% DMSO; Red Profile: 1% DMSO / 99% H_2O.

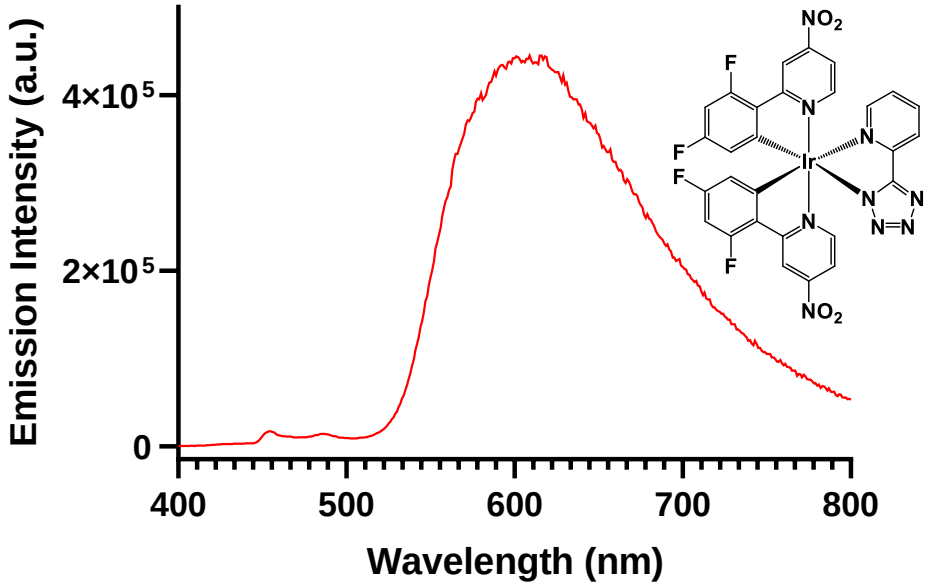

Figure 20.6. Emission profile of complex **[Ir(F_2-PPy-NO_2)$_2$-(PTz)]**, 10^{-5} M solution in DCM, 77K.

Additional evidence supporting the possible presence of aggregation phenomena is found in the emission spectra of complex **[Ir(F_2-PPy-NO_2)$_2$(PTZ)]** collected at 77K.(**Figure 20.6**) The solubility of the complex is dramatically decreased by freezing the solvent system down to 77K. This is reflected by the total replacement of the previous featured emission centred at 480 nm with a broad emission at 660 nm.

To furtherly study the relationship between the complex luminescence behaviour and its solubility in the designated solvent we decide to investigate its emission behaviour in a solvent displaying minimum solvation capacity, eventually choosing toluene. As expected, as a consequence of a solubility decrease, the emission spectra of a 10^{-5} M solution of complex **[Ir(F_2-PPy-NO_2)$_2$(PTZ)]** consists uniquely in a broad emission band centred at 610 nm. (**Figure 21.6**) The 50 nm blue shift in comparison to the emission maxima of the complex in water is probably due to the lower polarity of toluene causing a less significant stabilization of the polar emissive excited state, thus suggesting the CT nature of the transition associated to the aggregate system.

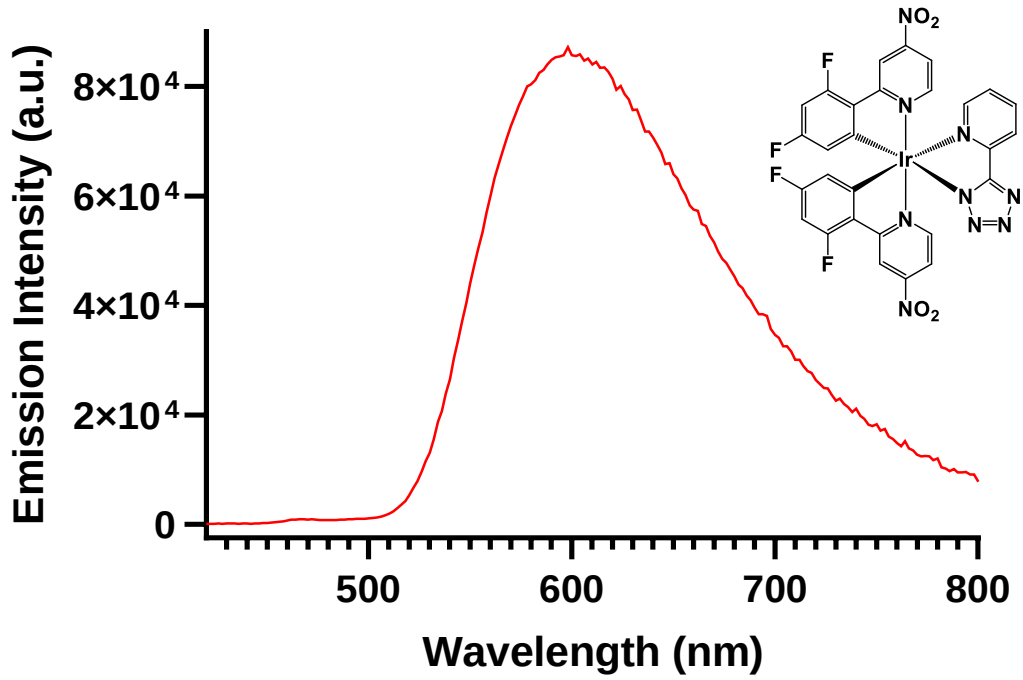

Figure 21.6 Emission profile of complex **[Ir(F_2-PPy-NO_2)$_2$-(PTz)]**, air-equilibrated (red line) and deoxygenated (blue line), 10^{-5} M solution in Toluene, 298K.

The contribution of the nitro group, and its relative position, in the phenomena responsible for the red-shifted emission may be suggested by comparison between emission spectra of complex **[Ir(O_2N-PPy)$_2$(PTZ)]** in H_2O (1% DMSO) and pure DMSO. (**Figure 22.6**) In this case, when the nitro groups are located on the phenyl ring of the C^N ligands, the only effect produced by switching solvent is a slight shift of the emission profile associable to their different stabilization effects on the emissive excited state. In addition, for complex **[Ir(O_2N-PPy)$_2$(PTZ)]**, the emission spectrum collected at 77K exhibits the occurrence of a structured profile that might account for the interplay of ^{3}LC/^{3}MLCT type emissive excited states.[16] (**Figure 23.6**)

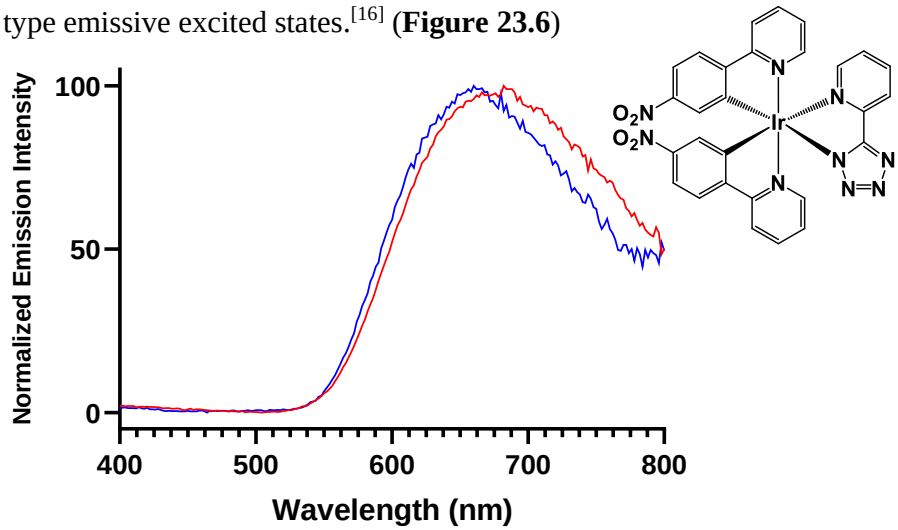

Figure 22.6. Normalized emission profile of complex **[Ir(O_2N-PPy)$_2$(PTZ)]** obtained from DMSO (red trace) and H_2O - 1%DMSO (blue trace) 10^{-5} M solution.

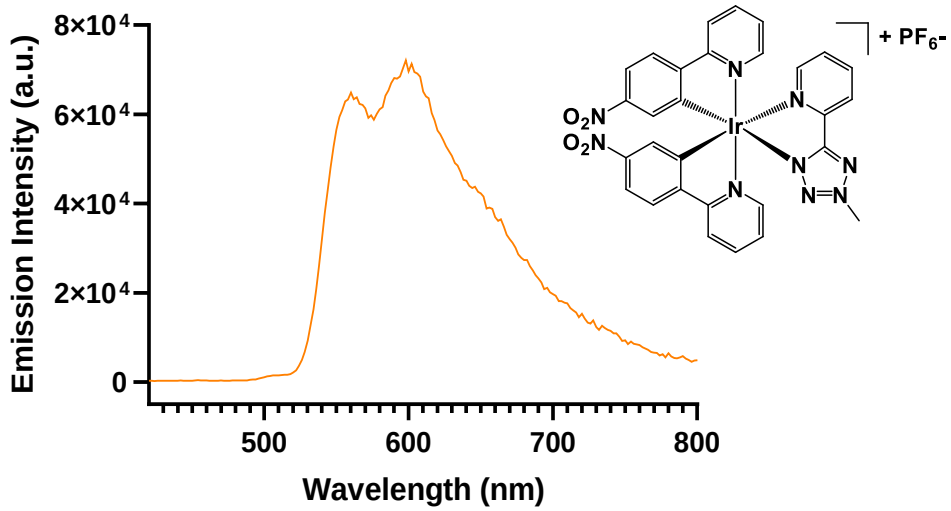

Figure 23.6. Emission spectra of complexes **[Ir(O_2N-PPy)$_2$(PTZ-Me)]**; 10^{-5} M DCM frozen matrix, 77K.

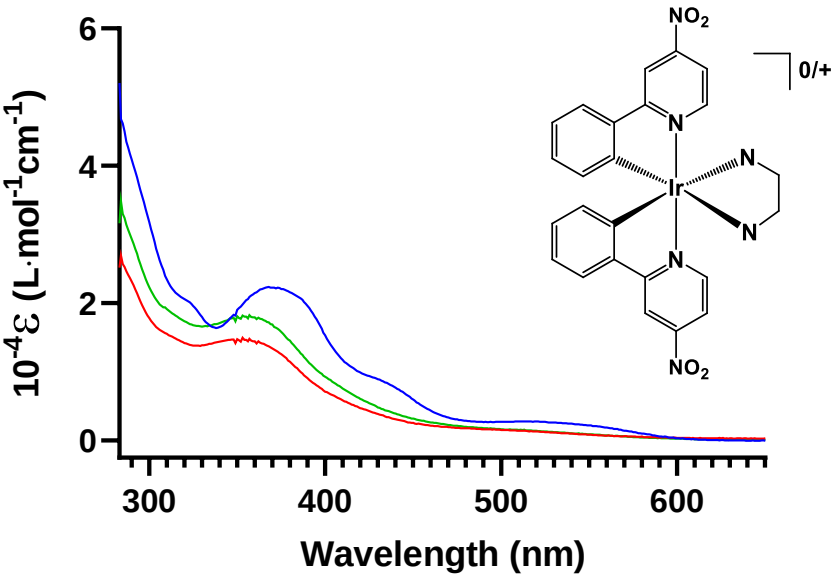

Figure 24.6. Absorption spectra of complexes **[Ir(PPy-NO_2)$_2$(PTZ)]** (blue line), **[Ir(PPy-NO_2)$_2$(PTZ-Me)]$^+$** (red line**), [Ir(PPy-NO_2)$_2$(PTZ-^{t}Bu)]$^+$** (green line), obtained from 10^{-5} M solution in Toluene at 298K.

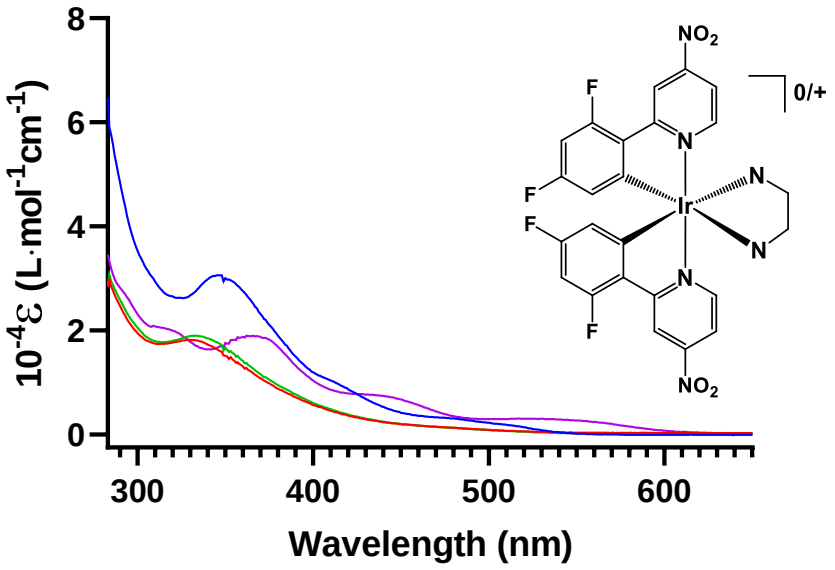

Figure 25.6. Absorption spectra of complexes **[Ir(F_2-PPy-NO_2)$_2$(PTZ)]** (blue line), **[Ir(F_2-PPy-NO_2)$_2$(PTZ-Me)]$^+$** (red line), **[Ir(F_2-PPy-NO_2)$_2$(PTZ-^{t}Bu)]$^+$** (green line) and **[Ir(F_2-PPy-NO_2)$_2$(acac)]** (purple line) obtained from 10^{-5} M solution in Toluene at 298K.

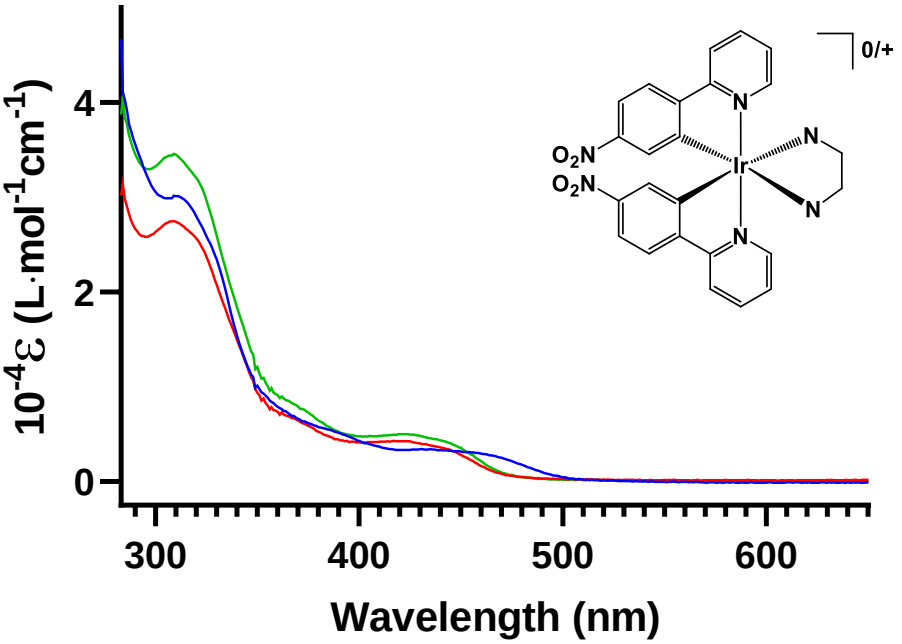

Figure 26.6. Absorption spectra of complexes **[Ir(O$_2$N-PPy)$_2$(PTZ)]** (blue line), **[Ir(O$_2$N-PPy)$_2$(PTZ-Me)]$^+$** (red line), **[Ir(O$_2$N-PPy)$_2$(PTZ-^{t}Bu)]$^+$** (green line), obtained from 10^{-5} M solution in Toluene at 298K.

Table 2.6. Photophysical data for neutral and cationic Ir(III)-NO$_2$ complexes reported in this work; toluene solutions.

Complex	**Absorption**	**Emission 298 K**		
10^{-5} M solution in Toluene	λ(nm) 10^{-4}ε ($cm^{-1}M^{-1}$)	λ_{em} (nm)	τ_{ox} (ns)	τ_{deox} (ns)
[Ir(PPy-NO$_2$)$_2$(PTZ)]	322 (2.02), 368 (2.24), 436$_{sh}$ (0.83), 520 (0.27)	680	-	-
[Ir(PPy-NO$_2$)$_2$(PTZ-Me)]$^+$	290$_{sh}$ (2.32), 350 (1.48), 500 (0.15)	700	-	-
[Ir(PPy-NO$_2$)$_2$(PTZ-^{t}Bu)]$^+$	357 (1,82)	710	-	-
[Ir(F$_2$-PPy-NO$_2$)$_2$(PTZ)]	308$_{sh}$ (2.99), 347 (3.01), 415$_{sh}$ (0.96)	600	120.44	118.43
[Ir(F$_2$-PPy-NO$_2$)$_2$(PTZ-Me)]$^+$	329 (1.82)	608	56.55	44.74
[Ir(F$_2$-PPy-NO$_2$)$_2$(PTZ-^{t}Bu)]$^+$	332 (1.90)	608	-	70.94
[Ir(O$_2$N-PPy)$_2$(PTZ)]	309 (3.00), 390$_{sh}$ (0.51), 430 (0.34)	598	207.29	441.39
[Ir(O$_2$N-PPy)$_2$(PTZ-Me)]$^+$	309 (2.75), 417 (0.43)	540 574	457.81 457.78	942.44 942.81
[Ir(O$_2$N-PPy)$_2$(PTZ-^{t}Bu)]$^+$	309 (3.46), 421 (0.50)	540 574	455.09 448.34	1057.16 1019.00

Table 3.6. Photophysical data for neutral, cationic and anionic Ir(III) complexes reported in this work; DMSO solutions.

Complex	Absorption	Emission 298 K			Emission 77 K	
10^{-5} M solution in DMSO	λ(nm) 10^{-4}ε ($cm^{-1}M^{-1}$)	λ_{em} (nm)	τ_{ox} (ns)	τ_{deox} (ns)	λ_{em} (nm)	τ (μs)
[Ir(PPy-NO_2)$_2$(PTZ)]	270 (7.36), 320 (2.88), 367 (3.229), 430 (1.25), 520 (0.35)	502 520	254 275	1002 1042	458 478 512 560_{sh}	- 2.479 2.466 1.122
[Ir(PPy-NO_2)$_2$(PTZ-Me)]$^+$	270 (6.76), 356 (2.96), 420 (0.93), 500 (0.25)	488 514	281 221	927 932	472 506 550_{sh}	3.668 3.917 1.829
[Ir(PPy-NO_2)$_2$(PTZ-^{t}Bu)]$^+$	271 (11.5), 310 (4.37), 354 (3.95), 420 (1.27), 500 (0.37)	488 514	155 151	251 248	454 472 508 550_{sh}	- 3.678 3.594 1.906
[Ir(PPy-NO_2)$_2$(1,2-BTB)]$^-$	280 (5.79), 325 (2.12), 384 (2.73), 450 (1.03), 550 (0.36)	512	-	1084	-	-
[Ir(F_2-PPy-NO_2)$_2$(PTZ)]	280 (5.94), 310 (2.86), 346 (3.42), 415 (1.02), 485 (0.28)	470 494	228 221	871 802	452 486 596	- 2.218 1.806
[Ir(F_2-PPy-NO_2)$_2$(PTZ-Me)]$^+$	275 (7.12), 334 (3.62), 360 (2.83), 410 (1.01), 470 (0.32)	460 488 528_{sh}	232 303 -	656 640 -	432 450 482 564	- 3.553 3.457 1.515
[Ir(F_2-PPy-NO_2)$_2$(PTZ-^{t}Bu)]$^+$	280 (7.03), 334 (4.03), 360 (3.04), 406 (1.12), 465 (0.29)	460 488	159 92		450 484 586	- - 1.224
[Ir(F_2-PPy-NO_2)$_2$(1,2-BTB)]$^-$	288 (3.79), 358 (2.93), 420 (1.06), 501 (0.31)	480 502	- -	753	456 488 624	- - -
[Ir(O_2N-PPy)$_2$(PTZ)]	280 (8.11), 325 (4.94), 390 (0.88), 441 (0.51)	676	168	181	580 616	1.977 1.739
[Ir(O_2N-PPy)$_2$(PTZ-Me)]$^+$	277 (7.11), 314 (5.60), 380 (1.18), 428 (0.76)	626	550	904	564 598 660_{sh}	3.921 3.836 2.605
[Ir(O_2N-PPy)$_2$(PTZ-^{t}Bu)]$^+$	276 (8.13), 314 (6.51), 380 (1.32), 428 (0.82)	628	501	912	564 600 660_{sh}	3.854 3.544 2.841
[Ir(O_2N-PPy)$_2$(1,2-BTB)]$^-$	271 (6.70), 300 (4.82), 328 (3.87), 450 (0.39)	-	-	-	-	-

6.3.5 *Reduction tests with sodium dithionite ($Na_2S_2O_4$).*

To assess whether or not the prepared Ir(III)-NO2 complexes could be utilised as redox-active probes for sensing hypoxic environment upon reduction of the pending nitro groups, their redox behaviour was studied performing reduction tests with sodium dithionite as the reducing agent. The collected data is reported in **Table 4.6**.

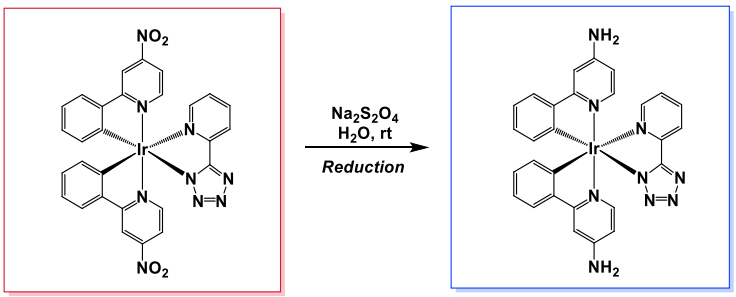

Scheme 7.6. Reduction or the reported Ir-NO_2 complexes with sodium dithionite in aqueous solution (1% DMSO). Complex **[Ir(PPy-NO_2)$_2$(PTZ)]** is reported as an example.

Table 4.6. Photophysical data for Ir-NO_2 and Ir-NH_2 type complexes reported in this work

Complex	Absorption	Emission
H_2O (1% DMSO) 20 μM Solutions	λ^{abs} (nm)	λ^{emi} (nm)
[Ir(PPy-NO_2)-(PTZ)]	255_{sh}, 368, 440_{sh}, 550	515
RED	233, 270_{sh}, 362	55
[Ir(PPy-NO_2)-(PTZ-Me)]$^+$	280, 350, 420, 510	480_{sh}, 502
RED	-	584
[Ir(PPy-NO_2)-(PTZ-tBu)]$^+$	270sh, 348, 420, 520	507, 650
RED	233, 260_{sh}, 350	580
[Ir(PPy-NO_2)-(1,2-BTB)]$^-$	270_{sh}, 366, 430, 530	516, 494
RED	540	508
[Ir(F_2-PPy-NO_2)-(PTZ)]	233, 270, 415_{sh}, 500	660
RED	540	500, 465(sh)
[Ir(F_2-PPy-NO_2)-(PTZ-Me)]$^+$	237, 260_{sh}, 334, 475	630, 480, 453
RED	270_{sh}, 314	500
[Ir(F_2-PPy-NO_2)-(PTZ-tBu)]$^+$	265_{sh}, 337	630
RED	232, 350	550
[Ir(F_2-PPy-NO_2)-(1,2-BTB)]$^-$	348_{sh}, 500	464, 492
RED	233, 285_{sh}, 353	478
[Ir(O_2N-PPy)-(PTZ)]	231, 250, 277, 325_{sh}, 470	660
RED	314, 470	482, 514
[Ir(O_2N-PPy)-(PTZ-Me)]$^+$	260_{sh}, 273, 316, 440	650
RED	233, 275, 315, 380	516
[Ir(O_2N-PPy)-(PTZ-tBu)]$^+$	237, 274, 315, 430	630
RED	/	/
[Ir(O_2N-PPy)-(1,2-BTB)]$^-$	265, 322, 470	680
RED	275, 320, 400	482, 514

The addition of solid $Na_2S_2O_4$ to a 20 μM aqueous solution (1% DMSO) of **Ir-NO_2** complex led to a dramatic modification of their luminescent output in terms of intensity and colour of the luminescence. In the majority of the cases, the addition of $Na_2S_2O_4$ led to a large increase in their luminescence intensity, along with a marked shift of the emission profile with respect to the corresponding unreduced complex. (**Figure 24.6, 25.6, 26.6**). Overall, the occurrence of a similar behaviour is likely to be ascribed to the transformation of the **Ir-NO_2** complexes into the corresponding Ir(III)-NH_2 derivatives. For the reported complex **[Ir(F_2-PPy-NO_2)$_2$(PTZ)]**, upon addition of $Na_2S_2O_4$ the broad red emission centred at 660 nm is replaced by an intense blue emission centred at 500 nm associated to the reduced form of the complex. (**Table 4.6**). It is possible to observe how the emission profile of the starting compound is profoundly modified upon reduction of the NO_2 moiety, highlighting substantial variations in emission colour, intensity, and in the nature of the emissive excited states: such behaviour, along with the displayed solubility in acqueous media, suggests how the newly prepared **Ir-NO_2** complexes represent good candidates as luminescent hypoxia-responsive probes.

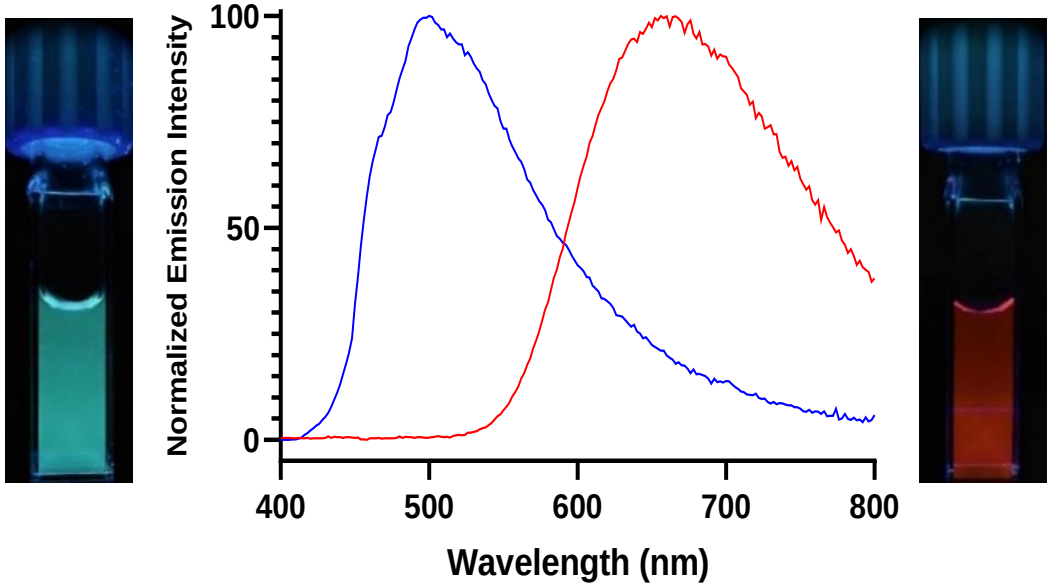

Figure 24.6. Normalized emission profiles obtained from complex **[Ir(F_2-PPy-NO_2)$_2$(PTZ)]** before (right, red) and after (left, blue) the addition of $Na_2S_2O_4$; 298K, air equilibrated, 20 μM H_2O (DMSO 1%) solution.

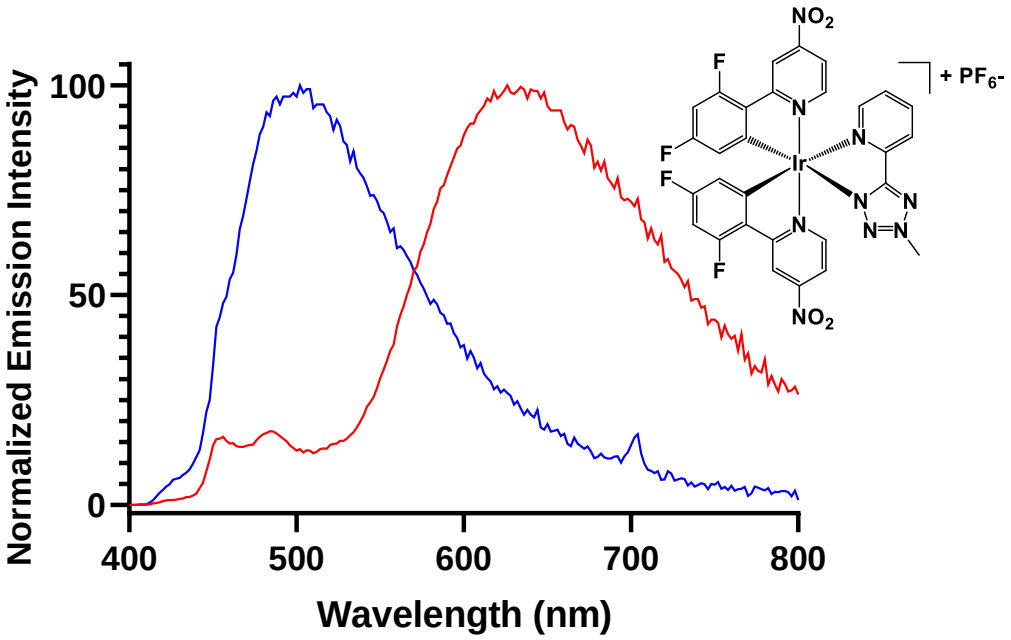

Figure 25.6. Normalized emission profiles obtained from complex **[Ir(F$_2$-PPy-NO$_2$)$_2$(PTZ-Me)]$^+$** before (right, red) and after (left, blue) the addition of $Na_2S_2O_4$; 298K, air equilibrated, 20 μM H_2O (DMSO 1%) solution.

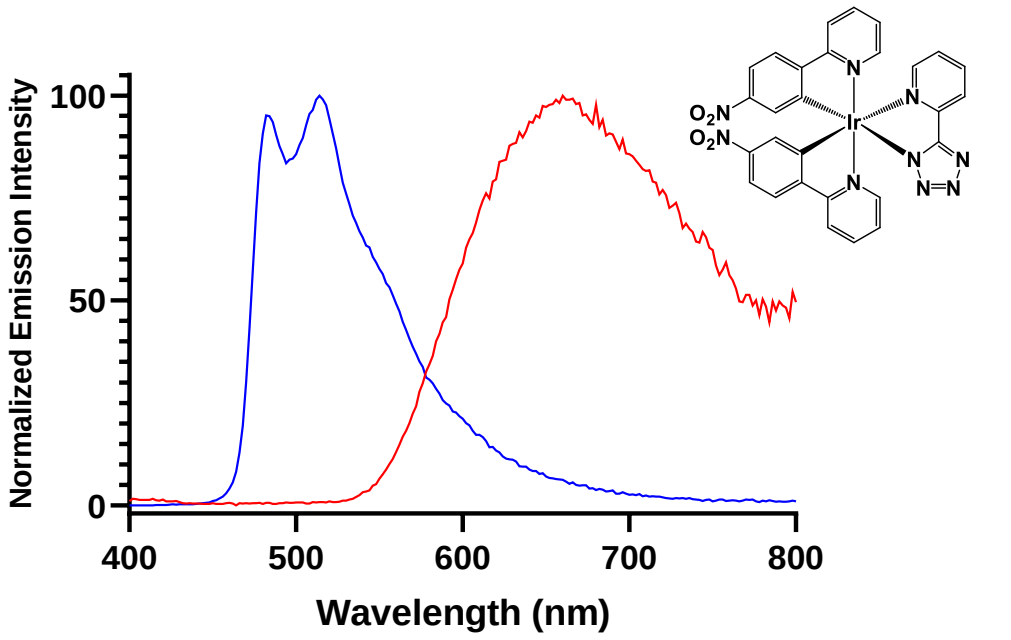

Figure 26.6. Normalized emission profiles obtained from complex **[Ir(O$_2$N-PPy)$_2$(PTZ)]** before (right, red) and after (left, blue) the addition of $Na_2S_2O_4$; 298K, air equilibrated, 20 μM H_2O (DMSO 1%) solution.

6.4 Conclusions

In this chapter, a new family of Ir(III)-tetrazole complexes with the general formula **[Ir((C^N)-NO_2)$_2$(N^N')]$^{-1/0/+1}$** is presented, where N^N' represents a chelating 5-aryltetrazole ancillary ligand or its N2-alkylated derivatives, and C^N is the fluorinated or non-fluorinated cyclometalating ligand displaying one NO_2 group at the *para* position of the pyridyl ring (**PPy-NO_2** and **F_2-PPy-NO_2**) or at the *para* position (with respect to the cyclometalated carbon) of the phenyl ring (**O_2N-PPy**). The introduction of a nitro group in the main scaffold of the complexes was aimed at the preparation of redox active probes, in which modification of the luminescent output can be achieved upon reduction of the pending functionality. Thus, a set of *2-phenylpyridine* type ligands **PPy-NO_2**, **F_2-PPy-NO_2** and **O_2N-PPy** was synthesised and by reaction of Ir(III) chloride and 2.5 eq of cyclometalating ligand (C^N)-NO_2 three new dichloro-bridged Ir(III) dimers **[Ir(PPy-NO_2)$_2$Cl]$_2$**, **[Ir(F_2-PPy-NO_2)$_2$Cl]$_2$**, and **[Ir(O_2N-PPy)$_2$Cl]$_2$** were obtained.

At this point, by reaction of the di-chloro-bridged precursors with a library of tetrazolate and tetrazole ligands, differently charged Ir(III)-tetrazole complexes were prepared. An intermediate Ag(I) halide extraction allowed us to overcome the poor solubility of the Ir(III) dimers in our standard conditions. Neutral and positively charged Ir(III) complexes were obtained by reaction of the corresponding Ir(III)-NO_2 dimer precursors with tetrazolato (**PTZ$^-$**) or N-2 alkyl tetrazoles (**PTZ-Me**, **PTZ-^{t}Bu**), respectively. The anionic Ir(III) complexes with the general formula **[Ir((C^N)-NO_2)$_2$(1,2-BTB)][Et_3NH]**, were obtained with the introduction of the bis tetrazolato **1,2-BTB^{2-}**. Photophysical measurements on solutions of the prepared complexes in polar solvents revealed a modest luminescent output, most likely in reason of the presence of NO_2 groups. Although, emission measurement in DCM of complexes possessing a NO_2 group at the para position of the pyridyl ring of the (C^N) ligands, in some cases revealed the participation of multiple processes in the determination of the total emission profile of the luminophores. Complex **[Ir(F_2-PPy-NO_2)$_2$(PTZ)]** was chosen as a model system in order to rationalize such phenomenon, and, studies of the variation of its the luminescent output in different solubility conditions suggested as how their emission behaviour could be related to aggregation phenomena involving the two aligned nitro groups.

Preliminary reduction tests on a 20 μM aqueous solution (1% DMSO) of Ir-NO2 complexes using sodium dithionite ($Na_2S_2O_4$) as the reducing agent, confirmed the possibility to achieve a consistent modification of the luminescent output of these complexes upon chemical modification of the pending nitro groups. Further studies will be carried out in order to bettere rationalize such behavior and the effective contribution of a nitro group to the photophysical propertis of luminescent Ir(III) complexes; anyhow these results represents an encouraging suggestion on how the prepared **Ir-NO_2** complexes could represent good candidates as luminescent hypoxia-responsive probes in bioimaging.

6.5 Experimental Section

General considerations. All reagents and solvents were obtained commercially (Sigma Aldrich/Merck, Alfa Aesar, Strem Chemicals) and used as received without any further purification unless otherwise specified. When required, reactions were carried out under an argon atmosphere following standard Schlenk protocols. The purification of the Ir(III) complexes was carried out via column chromatography using Al_2O_3 (Brockmann grade I or II) as the stationary phase. ESI-mass spectra were recorded using a Waters ZQ-4000 instrument (ESI-MS, acetonitrile or methanol solutions). ^{1}H, ^{13}C and ^{19}F Nuclear magnetic resonance spectra were recorded using a Varian Mercury Plus 400 (^{1}H 399.9 MHz; ^{13}C 101.0 MHz; ^{19}F 397 MHz) at room temperature unless specified otherwise. ^{1}H and ^{13}C chemical shifts were referenced to residual solvent resonances ($^{1}H/^{13}C$: DMSO-d^6 2.50/39.52 ppm; $CDCl_3$ 7.26/77.16 ppm).

Photophysics. Absorption spectra were recorded at room temperature using an Agilent Cary 100 UV-vis spectrometer. Uncorrected steady-state emission and excitation spectra and time-resolved measurements were recorded on an Edinburgh FLSP920 spectrometer equipped with a 450 W xenon arc lamp, double excitation and single emission monochromators, and a Peltier-cooled Hamamatsu R928P photomultiplier tube (185−850 nm). Emission and excitation spectra were acquired with cut-off filters (390 nm, 420 nm, 455 nm, 590 nm) and corrected for source intensity (lamp and grating) and emission spectral response (detector and grating) by a calibration curve supplied with the instrument. The wavelengths for the emission and excitation spectra were determined using the absorption maxima of the MLCT transition bands (emission spectra) and at the maxima of the emission bands (excitation spectra). The degassed measurements were obtained after the solutions were bubbled for 10 minutes under Ar atmosphere, using a septa-sealed quartz cell Emission lifetimes (τ) were determined by Time correlated single photon counting technique (TCSPC) using a pulsed picosecond LED (EPLED 360, FWHM < 800ps) as the excitation source.. The goodness of fit was assessed by minimizing the reduced $\chi 2$ function and by visual inspection of the weighted residuals. To record the 77 K luminescence spectra, samples were put in a 4 mm diameter quartz tube and inserted in a sample holder previously filled with liquid nitrogen. The solvent

used in the preparation of the solutions for the photophysical investigations was of spectrometric grade. Experimental uncertainties are estimated to be ±8% for lifetime determinations, and ±2 nm and ±5 nm for absorption and emission peaks, respectively.

Reduction experiments. Preliminary reduction tests were performed by adding an excess of $Na_2S_2O_4$ to 3 mL of 20 μM solutions of the prepared Ir-NO_2 type complexes. Aqueous solutions of the tested complexes were prepared by dilution of 30 μL of 2 mM DMSO stock solutions with water to a final volume of 3 mL to give aqueous solutions with 1% DMSO content. Absorption, emission and excitation spectra of the studied complexes were collected before and after the addition of $Na_2S_2O_4$.

Ligand synthesis. Tetrazole derivatives are used as components for explosive mixtures. The reactions described herein were run just on a few grams scale and no issues were encountered; nonetheless, great caution should be exercised when handling or heating such compounds.

[PTZ-H] ligand was obtained in almost quantitative yield following the general method reported by Koguro and co-workers,[17] **^{1}H-NMR**, 400 MHz, DMSO-d^6 δ (ppm): 8.82 (m, 1H), 8.25 (m, 1H), 8.10 (m, 1H), 7.66 (m, 1H). **^{13}C-NMR**, 100 MHz, DMSO-d^6 δ (ppm) = 155.3, 150.5, 144.1, 138.7, 126.6, 123.1

[1,2-BTB-H_2] was prepared according to Finnegan's protocol.[18] **^{1}H-NMR** (400 MHz, DMSO d6) δ (ppm) =7.91–7.89 (m, 2H), 7.81–7.78 (m, 2H). [H-TPYZ]

[PTZ-Me] and [PTZ-^{t}Bu] were prepared following previously reported procedures.[19]

[PTZ-Me]: **^{1}H-NMR**, 400 MHz, $CDCl_3$ δ (ppm): 8.79 (m, 1H), 8.26 (d, 1H, J = 7.83 Hz), 7.89 (s, 1H), 7.42 (s, 1H), 4.46 (s, 3H). **^{13}C-NMR**, 100 MHz, $CDCl_3$ δ (ppm): 164.93 (C_t), 150.21, 146.82, 137.22, 124.87, 122.35, 39.68 .**[PTZ-^{t}Bu]**: **^{1}H-NMR**, 400 MHz, $CDCl_3$ δ (ppm): 8.80 (d, 1H, J = 4.18 Hz), 8.27 (d, 1H, J = 7.83 Hz), 7.86 (m, 1H), 7.39 (m, 1H), 1.83 (s, 9H). **^{13}C-NMR**, 100 MHz, $CDCl_3$ δ (ppm): 164.1 (C_t), 155.2, 149.4, 137.2, 124.2, 123.7, 73.1 (C-$(CH_3)_3$), 28.3 ($(CH_3)_3$).

General procedure for the preparation of PPy-NO_2, F_2-PPy-NO_2 and O_2N-PPy. Cyclometalating ligands (**C^N**), **PPy-NO_2, F_2-PPy-NO_2** and **O_2N-PPy**, were synthesised by Suzuki-Miyaura coupling reaction[5]. The appropriate 2-bromopyridines (2.0 g, 1 eq) and phenylboronic acids (1 eq), [$Pd(PPh_3)_4$] (0.1 eq) and K_2CO_3 were combined in a 100 mL schlenk round bottom flask. The solid mixture was deoxygenated through repeated vacuum-nitrogen cycles then dissolved in a previously degassed 1:1 v/v THF/H_2O solution (40 mL). The reaction mixture was heated at reflux for 24 h under nitrogen. The crude was cooled then NaCl brine and EtOAc were added, the organic phase was separated and the aqueous phase extracted with EtOAc (3x15 ml). The organic layers were combined and dried over $MgSO_4$. The solvent was removed by rotary evaporation and the crude products were further purified via column chromatography (SiO_2; PS/EtOAc 9:1 v/v, second fraction) to provide the desired compounds as crystalline pale yellow solids.

(PPy-NO_2) ^{1}H-NMR, 400 MHz, CD3Cl δ (ppm): 8.97 (d, J = 5.3 Hz, 1H), 8.45 (d, J = 1.8 Hz, 1H), 8.14 – 8.00 (m, 2H), 7.94 (dd, J = 5.4, 2.1 Hz, 1H), 7.62 – 7.46 (m, 3H). **^{13}C-NMR**, 100 MHz, CD3Cl δ (ppm): 160.53, 154.91, 151.89, 137.37, 130.55, 129.26, 127.26, 114.41, 112.90.

(F_2-PPy-NO_2) ^{1}H-NMR, 400 MHz, CD_3Cl δ (ppm): 8.98 (d, J = 5.3 Hz, 1H), 8.59 – 8.41 (m, 1H), 8.12 (td, J = 8.9, 6.5 Hz, 1H), 7.97 (dd, J = 5.3, 2.0 Hz, 1H), 7.04 (dddd, J = 8.7, 7.7, 2.5, 1.0 Hz, 1H), 6.97 (ddd, J = 11.3, 8.6, 2.5 Hz, 1H). **^{13}C-NMR**, 100 MHz, CD_3Cl δ (ppm): 165.44 (d, J = 12.3 Hz), 162.92 (d, J = 12.3 Hz), 162.34 (d, J = 12.0 Hz), 159.81 (d, J = 12.2 Hz), 155.36 (d, J = 2.8 Hz), 154.50, 151.78, 132.39 (dd, J = 9.8, 3.9 Hz), 121.93 (dd, J = 10.8, 3.9 Hz), 116.60 (d, J = 12.1 Hz), 114.89, 112.50 (dd, J = 21.3, 3.7 Hz), 106.01 – 102.92 (m). **^{19}F-NMR**, 376 MHz, CD_3Cl δ (ppm): 106.44 (d, J_{F-F} = 9.5 Hz, 1F), -111.87 (d, J_{F-F} = 9.5 Hz, 1F).

(**O_2N-PPy) ^{1}H-NMR**, 400 MHz, CD_3Cl δ (ppm): 8.83 – 8.65 (m, 1H), 8.39 – 8.31 (m, 2H), 8.22 – 8.12 (m, 2 H), 7.88 – 7.74 (m, 2 H), 7.34 (ddd, J = 6.3, 4.8, 2.2 Hz, 1H).

General procedure for the synthesis of [Ir(C^N)$_2$Cl]$_2$ type dimers.[6] Hydrate $IrCl_3$ (350 mg) and 2.5 eq of **PPy-NO$_2$, F$_2$-PPy-NO$_2$** or **O$_2$N-PPy** were dissolved in 16 mL of a 3:1 v/v EtOEtOH/H_2O mixture in a 100 mL round-bottom flask. The mixture was refluxed for 24 h under inhert athmosphere. The crude was cooled down and water was added to induce the precipitation of the dichloro-bridged Ir(III) dimers **[Ir(PPy-NO$_2$)$_2$Cl]$_2$**, **[Ir(F$_2$-PPy-NO$_2$)$_2$Cl]$_2$** and **[Ir(O$_2$N-PPy)$_2$Cl]$_2$**. In the end, the desired products were isolated via vacuum filtration.

[Ir(PPy-NO$_2$)$_2$Cl]$_2$: Y = 87.43 % (MW = 1252.01 g/mol, 542.2 mg, 0.4327 mmol).

^{1}H-NMR, 400 MHz, d_6-DMSO δ (ppm): 10.21 (d, J = 6.5 Hz, 2H), 9.87 (d, J = 6.4 Hz, 2H), 8.92 (d, J = 2.2 Hz, 2H), 8.82 (d, J = 2.4 Hz, 2H), 8.28 (dd, J = 6.5, 2.4 Hz, 2H), 8.20 (dd, J = 6.5, 2.4 Hz, 2H), 8.14 – 8.06 (m, 2H), 8.03 (d, J = 7.7 Hz, 2H), 6.98 (t, J = 7.3 Hz, 2H), 6.92 (t, J = 7.5 Hz, 2H), 6.86 (t, J = 7.7 Hz, 2H), 6.79 (t, J = 7.3 Hz, 2H), 6.33 (d, J = 7.6 Hz, 2H), 5.75 (d, J = 7.6 Hz, 2H).

[Ir(F$_2$-PPy-NO$_2$)$_2$Cl]$_2$: Y = 82.96 % (MW = 1396.01 g/mol, 573.6 mg, 0.4108 mmol).

^{1}H-NMR, 400 MHz, d_6-DMSO δ (ppm): 10.17 (d, *J* = 6.6 Hz, 1H), 9.89 (d, *J* = 6.5 Hz, 1H), 8.80 – 8.63 (m, 2H), 8.37 (dd, *J* = 6.5, 2.5 Hz, 1H), 8.32 (dd, *J* = 6.6, 2.6 Hz, 1H), 7.05 – 6.91 (m, 2H), 5.95 (dd, *J* = 8.3, 2.3 Hz, 1H), 5.32 (dd, *J* = 8.5, 2.3 Hz, 1H).

General procedure for the synthesis of neutral [Ir((C^N)-NO_2)$_2$PTZ] and cationic [Ir((C^N)-NO_2)$_2$PTZ-R] complexes.

[Ir(PPy-NO_2)$_2$Cl]$_2$ or **[Ir(F_2-PPy-NO_2)$_2$Cl]$_2$** or **[Ir(O_2N-PPy)$_2$Cl]$_2$** respectively (100 mg, 1 eq) and $AgPF_6$ (2 eq) were combined in 30 mL of a 1:1 v/v DCM/EtOH solution in a 50 mL round-bottom flask protected from light. The reaction mixture was heated at reflux under nitrogen atmosphere for 6 hours. The solution was allowed to cool down to room temperature and filtered through a celite plug, then **PTZ-H**, **PTZ-Me** or **PTZ-^{t}Bu** (1.25 eq) was added. The reaction mixture was heated at reflux under nitrogen atmosphere overnight. The crude products were further purified via column chromatography (Al_2O_3; DCM/Acetone 9:1 or 40:1 DCM/MeOH).

[Ir(PPy-NO_2)$_2$(PTZ)]: Y = 60.9 % (MW = 736.73 g/mol, 71.6 mg, 0.0972 mmol).

^{1}H-NMR, 400 MHz, d_6-DMSO δ (ppm): 8.86 (d, J = 2.4 Hz, 2H), 8.39 (d, J = 7.7 Hz, 1H), 8.23 – 8.16 (m, 2H), 8.16 – 8.08 (m, 1H), 7.96 (d, J = 6.5 Hz, 1H), 7.89 (dd, J = 6.5, 2.5 Hz, 1H), 7.81 (d, J = 6.5 Hz, 1H), 7.75 (dd, J = 6.5, 2.5 Hz, 1H), 7.71 – 7.63 (m, 1H), 7.56 (ddd, J = 7.0, 5.5, 1.4 Hz, 1H), 7.08 (td, J = 7.7, 1.1 Hz, 1H), 7.03 – 6.94 (m, 2H), 6.88 (td, J = 7.5, 1.2 Hz, 1H), 6.39 – 6.31 (m, 1H), 6.30 – 6.24 (m, 1H). **^{13}C-NMR**, 100 MHz, d_6-DMSO δ (ppm): 170.01, 169.86, 163.57 (C_t), 154.59, 154.36, 151.99, 151.32, 151.08, 149.84, 147.90, 147.83, 142.91, 142.53, 140.51, 131.50, 131.33, 130.52, 127.22, 126.58, 126.10, 122.80, 122.71, 122.01, 117.23, 116.76, 112.71, 112.37. **ESI-MS** (*m/z*, CH_3CN): $[M+Na]^+$ = 760. Anal. Calcd. For $C_{28}H_{18}N_9O_4Ir_1$ (736.73) C 45.65, H 2.46, N 17.11, O 8.69. Found: C 46.12 H, N.

[Ir(O_2N-PPy)$_2$(PTZ)]: Y = 76.2 % (MW = 736.73 g/mol, 89.7 mg, 0.121 mmol).

^{1}H-NMR, 400 MHz, d_6-DMSO δ (ppm): 8.50 (dddd, J = 8.3, 2.5, 1.4, 0.7 Hz, 2H), 8.39 (ddd, J = 7.9, 1.4, 0.8 Hz, 1H), 8.26 – 8.17 (m, 3H), 8.11 (dddd, J = 8.2, 7.5, 2.3, 1.5 Hz, 3H), 7.87 (dd, J = 8.6, 2.4 Hz, 1H), 7.83 – 7.75 (m, 3H), 7.57 – 7.49 (m, 2H), 7.43 (ddd, J = 7.3, 5.8, 1.4 Hz, 1H), 7.37 (ddd, J = 7.3, 5.8, 1.4 Hz, 1H), 6.95 (d, J = 2.3 Hz, 1H), 6.86 (d, J = 2.4 Hz, 1H). **^{13}C-NMR**, 100 MHz, d_6-DMSO δ (ppm): 164.42, 164.37, 163.50, 151.92, 151.38, 151.13, 150.33, 149.66, 149.51, 147.74, 147.61, 147.57, 147.02,

140.54, 139.62, 139.33, 127.34, 126.17, 125.97, 125.77, 125.19, 124.56, 124.36, 122.80, 122.21, 121.93, 118.06, 117.43. **ESI-MS** (*m/z*, CH_3CN): $[M+Na]^+$ = 760.

[Ir(F_2-PPy-NO_2)$_2$(PTZ)]: Y = 80.3 % (MW = 808.69 g/mol, 93.0 mg, 0.114 mmol).

^{1}H-NMR, 400 MHz, d_6-DMSO δ (ppm): 8.72 (d, *J* = 2.7 Hz, 2H), 8.41 (d, *J* = 7.6 Hz, 1H), 8.24 (td, *J* = 7.8, 1.5 Hz, 1H), 8.02 – 7.94 (m, 2H), 7.86 – 7.75 (m, 3H), 7.65 – 7.58 (m, 1H), 7.14 – 6.97 (m, 2H), 5.95 (dd, *J* = 8.3, 2.3 Hz, 1H), 5.85 (dd, *J* = 8.5, 2.4 Hz, 1H). **^{13}C-NMR**, 100 MHz, d_6-DMSO δ (ppm): 165.29, 165.22, 164.38, 163.41, 162.66, 162.40, 161.83, 160.20, 160.07, 156.07, 154.70, 154.57, 151.71, 151.67, 150.47, 147.33, 145.96, 141.06, 127.78, 127.01, 126.81, 123.04, 117.90, 117.51, 115.47, 114.46, 99.48, 98.79, 54.90, 40.20, 40.15, 39.98, 39.94, 39.78, 39.73, 39.57, 39.52, 39.31, 39.10, 38.89. **ESI-MS** (*m/z*, CH_3CN): $[M+Na]^+$ = 832.

[Ir(PPy-NO_2)$_2$(PTZ-Me)][PF_6]: Y = 74.23 % (MW = 896.72 g/mol, 106.3 mg, 0.1185 mmol).

^{1}H-NMR, 400 MHz, d_6-DMSO δ (ppm): 8.92 (dd, J = 11.3, 2.5 Hz, 2 H), 8.62 (d, J = 7.9 Hz, 1 H), 8.41 – 8.31 (m, 2 H), 8.25 (d, J = 7.8 Hz, 1 H), 8.17 (d, J = 7.9 Hz, 1 H), 8.03 (d, J = 6.5 Hz, 1 H), 7.87 – 7.74 (m, 3 H), 7.71 (dd, J = 6.4, 2.5 Hz, 1 H), 7.12 (t, J = 7.5 Hz, 1 H), 7.08 – 6.94 (m, 2 H), 6.91 (td, J = 7.4, 1.2 Hz, 2H), 6.27 (d, J = 7.6 Hz, 1 H), 6.24 (d, J = 7.7 Hz, 1 H), 4.53 (s, 3 H). **^{13}C-NMR**, 100 MHz, d_6-DMSO δ (ppm): 169.72, 169.28, 166.03, 155.00, 154.87, 152.60, 152.18, 150.85, 147.95, 144.62, 143.75, 142.76, 142.59, 141.30, 131.59, 131.01, 130.86, 130.24, 126.83, 126.34, 124.90, 123.37, 122.90, 117.05, 116.89, 113.05, 112.79, 42.07. **ESI-MS** (*m/z*, CH_3CN): $[M]^+$ = 752; $[M]^-$ = 145 (PF_6^-).

[Ir(O_2N-PPy)$_2$(PTZ-Me)][PF_6]: Y = 63.4 % (MW = 896.72 g/mol, 90.8 mg, 0.101 mmol).

^{1}H-NMR, 400 MHz, d_6-DMSO δ (ppm): 8.63 (dt, J = 7.9, 1.1 Hz, 1H), 8.54 (m, 2H), 8.36 (td, J = 7.8, 1.5 Hz, 1H), 8.26 (d, J = 8.7 Hz, 1H), 8.23 – 8.15 (m, 3H), 8.15 – 8.08 (m, 1H), 8.00 – 7.86 (m, 3H), 7.84 (dd, J = 8.6, 2.4 Hz, 1H), 7.77 (ddd, J = 7.8, 5.5, 1.5 Hz, 1H), 7.43 (tdd, J = 7.2, 5.7, 1.4 Hz, 2H), 6.83 (d, J = 2.3 Hz, 1H), 6.82 (d, J = 2.3

Hz, 1H), 4.52 (s, 3H). **^{13}C-NMR**, 100 MHz, d_6-DMSO δ (ppm): 165.96, 163.93, 163.64, 151.39, 151.13, 150.97, 150.85, 150.62, 147.64, 147.60, 147.11, 144.41, 143.55, 141.35, 140.25, 140.13, 130.33, 126.44, 126.29, 126.02, 125.50, 124.93, 124.45, 124.12, 122.47, 122.32, 118.73, 118.34, 42.20, 29.54. **ESI-MS** (*m/z*, CH_3CN): $[M]^+$ = 752; $[M]^-$ = 145 (PF_6^-).

[Ir(F_2-PPy-NO_2)$_2$(PTZ-Me)]: Y = 75.46 % (MW = 968.68 g/mol, 104.7 mg, 0.1081 mmol).

^{1}H-NMR, 400 MHz, d_6-DMSO δ (ppm): 8.73 (dt, J = 8.3, 2.9 Hz, 1H), 8.64 (d, J = 8.0 Hz, 1H), 8.51 – 8.31 (m, 1H), 8.07 (d, J = 6.4 Hz, 0H), 7.94 (d, J = 5.1 Hz, 0H), 7.92 – 7.81 (m, 1H), 7.78 (dd, J = 6.5, 2.5 Hz, 0H), 7.17 (ddd, J = 12.3, 9.4, 2.3 Hz, 0H), 7.08 (ddd, J = 12.0, 9.4, 2.4 Hz, 0H), 5.86 (ddd, J = 11.0, 8.3, 2.3 Hz, 1H), 4.55 (d, J = 2.6 Hz, 2H). **ESI-MS** (*m/z*, CH_3CN): $[M]^+$ = 824; $[M]^-$ = 145 (PF_6^-).

[Ir(PPy-NO_2)$_2$(PTZ-^{t}Bu)][PF_6]: Y = 89.73 % (MW = 938.8 g/mol, 121.5 mg, 0.1294mmol).

^{1}H-NMR, 400 MHz, d_6-DMSO δ (ppm): 8.92 (dd, J = 5.9, 2.5 Hz, 2 H), 8.64 (dt, J = 7.8, 1.1 Hz, 1 H), 8.36 (td, J = 7.8, 1.6 Hz, 1 H), 8.24 (dd, J = 7.9, 1.4 Hz, 1 H), 8.20 – 8.14 (m, 2 H), 8.01 (dd, J = 6.5, 0.6 Hz, 1 H), 7.87 – 7.74 (m, 4 H), 7.12 (td, J = 7.6, 1.2 Hz, 1 H), 7.07 – 6.96 (m, 2 H), 6.91 (td, J = 7.5, 1.4 Hz, 1 H), 6.25 (dd, J = 7.7, 1.2 Hz, 1 H), 6.21 (dd, J = 7.6, 1.2 Hz, 1 H), 1.73 (s, 9 H). **^{13}C-NMR**, 100 MHz, d_6-DMSO δ (ppm): 169.72, 169.14, 166.07, 154.94, 154.85, 152.48, 152.12, 150.73, 147.49, 144.71, 143.99, 142.75, 142.57, 141.19, 131.60, 130.87, 130.83, 130.22, 126.78, 126.34, 125.01, 123.43, 122.88, 117.30, 117.01, 113.02, 112.83, 68.46, 40.20, 40.15, 39.99, 39.94, 39.78, 39.73, 39.63, 39.57, 39.52, 39.31, 39.10, 38.89, 28.57. **ESI-MS** (*m/z*, CH_3CN): $[M]^+$ = 794; $[M]^-$ = 145 (PF_6^-).

[Ir(O_2N-PPy)$_2$(PTZ-^{t}Bu)][PF_6]: Y = 72.42 % (MW = 938.8 g/mol, 108.5 mg, 0.1167 mmol).

^{1}H-NMR, 400 MHz, d_6-DMSO δ (ppm): 8.65 (d, J = 7.9 Hz, 1H), 8.54 (t, J = 8.8 Hz, 2H), 8.40 – 8.32 (m, 1H), 8.26 (d, J = 8.7 Hz, 1H), 8.20 (dd, J = 8.7, 4.8 Hz, 3H), 8.07

(d, J = 5.8 Hz, 1H), 7.97 (s, 2H), 7.95 – 7.88 (m, 2H), 7.88 – 7.80 (m, 2H), 7.77 (s, 1H), 7.44 (dt, J = 14.2, 6.8 Hz, 2H), 6.81 (dd, J = 8.6, 2.3 Hz, 2H), 1.73 (s, 2H), 1.71 (s, 9H). **^{13}C-NMR**, 100 MHz, d_6-DMSO δ (ppm): 166.02, 163.93, 163.51, 151.25, 151.14, 150.82, 150.53, 147.57, 147.24, 147.08, 144.49, 143.78, 141.23, 140.24, 140.15, 130.29, 126.48, 126.36, 126.01, 125.46, 125.06, 124.46, 124.07, 122.47, 122.29, 118.78, 118.35, 68.54, 28.51. **ESI-MS** (*m/z*, CH_3CN): $[M]^+$ = 794; $[M]^-$ = 145 (PF_6^-).

[Ir(F_2-PPy-NO_2)$_2$(PTZ-^{t}Bu)][PF_6]: Y = 81.44 % (MW = 1010.8 g/mol, 117.9 mg, 0.1167 mmol).

^{1}H-NMR, 400 MHz, d_6-DMSO δ (ppm): 8.74 (m , 2 H), 8.70 – 8.60 (m, 1 H), 8.40 (td, J = 7.9, 1.6 Hz, 1 H), 8.20 (d, J = 6.5 Hz, 1 H), 8.04 (d, J = 6.5 Hz, 1H), 7.95 – 7.80 (m, 4 H), 7.17 (ddd, J = 11.9, 9.4, 2.3 Hz, 1 H), 7.08 (ddd, J = 12.0, 9.5, 2.3 Hz, 1 H), 5.84 (ddd, J = 12.8, 8.3, 2.4 Hz, 2 H), 1.74 (s, 9 H). **^{13}C-NMR**, 100 MHz, d_6-DMSO δ (ppm): 166.01, 164.92, 164.85, 164.61, 154.99, 154.93, 153.01, 152.79, 151.53, 151.08, 151.01, 148.42, 148.35, 143.56, 141.71, 130.69, 127.00, 125.24, 117.90, 117.79, 115.80, 115.58, 100.06, 99.81, 68.80, 28.56. **ESI-MS** (*m/z*, CH_3CN): $[M]^+$ = 866; $[M]^-$ = 145 (PF_6^-).

General procedure for the synthesis of the anionic [Ir((C^N)-NO_2)$_2$(1.2-BTB)][Et_3NH] type complexes.

[Ir(PPy-NO_2)$_2$Cl]$_2$, **[Ir(F_2-PPy-NO_2)$_2$Cl]$_2$** or **[Ir(O_2N-PPy)$_2$Cl]$_2$** respectively (100 mg, 1 eq) and $AgPF_6$ (2 eq) were combined in 30 mL of a 1:1 v/v DCM/EtOH solution in a 50 mL round-bottom flask protected from light. The reaction mixture was heated at reflux under nitrogen atmosphere for 6 hours. The solution was allowed to cool down to room temperature and filtered through a celite plug, then **1,2-BTB-H_2** (1.25 eq) and Et_3N (2.5 eq) were added. The reaction mixture was heated at reflux under nitrogen atmosphere overnight. The desired complexes were eventually precipitated by addition of diethyl ether and isolated via vacuum filtration.

[Ir(PPy-NO_2)$_2$(1,2-BTB)][Et_3NH]: Y = 65.2 % (MW = 904.97 g/mol, 94.2 mg, 0.104 mmol).

^{1}H-NMR, 600 MHz, 253 K, $CDCl_3$ δ (ppm): 9.40 (d, *J* = 6.4 Hz, 1H), 8.69 (d, *J* = 2.5 Hz, 1H), 8.29 (d, *J* = 6.4 Hz, 1H), 8.22 (d, *J* = 2.5 Hz, 1H), 7.84 (d, *J* = 7.8 Hz, 1H), 7.74 (d, *J* = 7.7 Hz, 1H), 7.67 (dd, *J* = 6.5, 2.5 Hz, 1H), 7.58 (t, *J* = 7.5 Hz, 1H), 7.56 – 7.54 (m, 1H), 7.46 (d, *J* = 3.1 Hz, 1H), 7.36 (t, *J* = 7.6 Hz, 1H), 7.32 (d, *J* = 7.6 Hz, 1H), 6.93 – 6.85 (m, 2H), 6.85 (s, 2H), 6.73 (t, *J* = 7.3 Hz, 1H), 6.63 – 6.59 (m, 1H), 6.17 (d, *J* = 7.6 Hz, 1H). **^{13}C-NMR**, 151 MHz, 253 K, $CDCl_3$ δ (ppm): ^{13}C NMR (151 MHz, $cdcl_3$) δ 172.36, 171.73, 161.73, 160.49, 153.75, 153.55, 153.32, 153.23, 152.86, 152.41, 143.02, 141.74, 133.25, 131.41, 131.29, 131.15, 131.08, 130.69, 130.42, 129.97, 129.92, 128.43, 125.62, 125.09, 123.93, 122.02, 114.32, 111.86, 111.38, 110.85. **ESI-MS** (*m/z*, CH_3CN): $[M]^-$ = 803; $[M]^+$ = 102 (Et_3NH^+).

[Ir(F_2-PPy-NO_2)$_2$(1,2-BTB)][Et_3NH]: Y = 83.16 % (MW = 976.93 g/mol, 120.1 mg, 0.133 mmol). **ESI-MS** (*m/z*, CH_3CN): $[M]^-$ = 875; $[M]^+$ = 102 (Et_3NH^+).

[Ir(O_2N-PPy)$_2$(1,2-BTB)][Et_3NH]: Y = 79.32 % (MW = 904.97 g/mol, 111.0 mg, 0.1336 mmol). **ESI-MS** (*m/z*, CH_3CN): $[M]^-$ = 803; $[M]^+$ = 102 (Et_3NH^+)

6.6 References

[1] K. Yang, K. G. Leslie, S. Y. Kim, B. Kalionis, W. Chrzanowski, K. A. Jolliffe, E. J. New; *Org. Biomol. Chem.*, **2018**, 16, 619.

[2] J. Biddlestone, D. Bandarra, S. Rocha; *International Journal of Molecular Medicine*, **2015**, 35, 859-869,

[3] M. Najaf, B. Farhood, K. Mortezaee, E. Kharazinejad, J. Majidpoor, R. Ahadi, *Journal of Cancer Research and Clinical Oncology*, **2020**, 146,19 – 31.

[4] K. Y. Zhang, P. Gao, G. Sun, T. Zhang, X. Li, S. Liu, Q. Zhao, K. Lo, W. Huang, *J. Am. Chem. Soc.*, **2018**, 140, 7827−7834.

[5] N. Miyaura, A. Suzuki, *J. Chem. Soc., Chem. Commun.*, **1979**, *0*, 866 - 867.

[6] M. Nonoyama, *Bull. Chem. Soc. Jpn.*, **1974**, *47*, 767.

[7] V. Fiorini, I. Zanoni, S. Zacchini, A. L. Costa, A. Hochkoeppler, V. Zanotti, A. M. Ranieri, M. Massi, A. Stefan, S. Stagni; *Dalton Trans*., **2017**, 46, 12328.

[8] V. Fiorini, S. Zacchini, P. Raiteri, R. Mazzoni, V. Zanotti, M. Massi, S. Stagni; *Dalton Trans.*, **2016**, 45, 12884 - 12896.

[9] M V. Werrett, S. Muzzioli, P. J. Wright, A. Palazzi, P. Raiteri, S. Zacchini, M. Massi, S. Stagni; *Inorg. Chem.*, **2014**, 53, 229-243.

[10] a) A. Juris, S. Campagna, I. Bidd, J. M. Lehn, R. Ziessel; *Inorg. Chem*., **1988**, 27, 4007-4011. b) M. S. Wrighton, D. L. Morse; *J. Am. Chem. Soc.*, **1974**, 96, 998 - 1003. c) M. Chen, D. Chen, P. Chou; *ChemPlusChem*, **2020**, 85, 1–18.

[11] D. Septiadi, A. Aliprandi, M. Mauro, L. De Cola, *RSC Adv.*, **2014**, 4, 25709–25718.

[12] a) M. Mauro, A. Aliprandi, D. Septiadi, N. S. Kehr and L. De Cola; *Chem. Soc. Rev.*, **2014**, 43, 4144–4166. b) J. A. G. Williams; *Top. Curr. Chem.*, **2007**, 281, 205–268. c) J. Mei, Y. Hong, J. W. Y. Lam, A. Qin, Y. Tang and B. Z. Tang; *Adv. Mater.*, **2014**, 26, 5429–5479

[13] A. Aliprandi, M. Mauro and L. De Cola, Nat. Chem., 2016, 8, 10–15.

[14] N. K. Allampally, C. A. Strassert and L. De Cola, Dalt. Trans., 2012, 41, 13132–13137

[15] a) W. Che, G. Li,aX. Liu, K. Shao, D. Zhu, Z. Su, M. R. Bryce; *Chem. Commun.*, **2018**, 54, 1730-1733. b) C. Jin, J. Liu, Y. Chen, R. Guan, C. Ouyang, Y. Zhu, L. Ji, H. Chao; *Scientific Reports*, **2016**, 6, 22039.

[16] L. Flamigni, A. Barbieri, C. Sabatini, B. Ventura, F. Barigelletti, *Top. Curr. Chem*., **2007**, *281*, 143–203.

[17] K. Koguro, T. Oga, S. Mitsui and R. Orita, *Synthesis*, **1998**, 910-914.

[18] W. G. Finnegan, R. A. Henry and R. Lofquist; *J. Am. Chem. Soc.*, **1958**, 15, 3908.

[19] a) R. A. Henry, *J. Am. Chem. Soc.*, 1951, **73**, 4470–4470. b) C. Femoni, S. Muzzioli, A. Palazzi, S. Stagni, S. Zacchini, F. Monti, G. Accorsi, M. Bolognesi, N. Armaroli, M. Massi, G. Valenti, M. Marcaccio, *Dalton. Trans.*, **2013**, *42*, 997; c) U. Sheridan, J. McGinley, J. F. Gallagher, A. Fleming, F. Kelleher, *Polyhedron*, **2013**, *59*, 8-16.